A novel methodology for high strain rate testing using full-field measurements and the virtual fields methods

Haibin Zhu

Thèse de doctorat de l'UTT

Haibin ZHU

A Novel Methodology for High Strain Rate Testing using Full-field Measurements and the Virtual Fields Methods

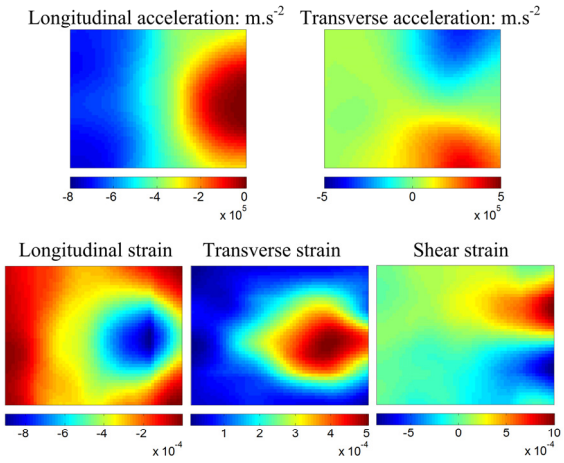

Systèmes Mécaniques et Matériaux

2015TROY0007

Année 2015

utt
université de technologie
Troyes

THESE

pour l'obtention du grade de

DOCTEUR de l'UNIVERSITE DE TECHNOLOGIE DE TROYES

Spécialité : SYSTEMES MECANIQUES ET MATERIAUX

présentée et soutenue par

Haibin ZHU

le 10 mars 2015

A Novel Methodology for High Strain Rate Testing using Full-field Measurements and the Virtual Fields Methods

JURY

Mme N. BAHLOULI	PROFESSEUR DES UNIVERSITES	Président
M. M. FRANÇOIS	PROFESSEUR DES UNIVERSITES	Examinateur
M. B. LANGRAND	INGENIEUR DE RECHERCHE - HDR	Rapporteur
M. P. LAVA	ASSISTANT PROFESSOR	Examinateur
M. E. MARKIEWICZ	PROFESSEUR DES UNIVERSITES	Examinateur
M. F. PIERRON	PROFESSOR	Directeur de thèse
M. H. ZHAO	PROFESSEUR DES UNIVERSITES	Rapporteur

Acknowledgements

During the journey to win this Ph.D., many supportive people have helped me in various aspects. This is the moment I have been dreaming to express my deep gratitude in words to individuals from my heart. The experience of working and studying in the *Université de Technologie de Troyes*, *Arts et Métiers ParisTech* in Chalons-en-Champagn and *University of Southampton* is unforgettable memory. I have been lucky to build up the memorable relationship and friendship with people I have encountered there.

First, I am deeply indebted to my supervisor, Professor Fabrice Pierron. Without his encouragement, tremendous patience and expert advices, this journey would not be so great. His big horizon, diligence and strict attitude have been exemplifying.

My sincere thanks go to my colleague Dr. Cédric Devivier. He provided many invaluable help and suggestions during the experimental data processing. I am also grateful to have Dr. Clive Siviour who acted as my collaborator of this Ph.D. project and provided help and facilities in a part of experimental work. I would also like to acknowledge Mr. Brian Speyer from *Speyer Photonics Ltd.* and Dr. Markus Ortlieb from *Shimadzu Europa GmbH* for the lending of Shimadzu HPV-X camera and help in the experimental work. My acknowledgements are also to Dr. Nicola Symonds and Dr. Liam Goodes for their help with the impact rig in the nCATS group of the *University of Southampton*.

I also want to express my thanks to the other jury members for my Ph.D. dissertation. They are: Professor Nadia Bahlouli from the *Université of Strasbourg*, Professor Manuel Francois from the *Université de Technologie de Troyes*, Dr. Bertrand Langrand from *L'Office National d'Etudes et de Recherches Aérospatiales*, Dr. Pascal Lave from the *Katholieke Universiteit Leuven*, Professor Eric Markiewicz from the *Université de Valenciennes et du Haut-Cambrésis* and Professor Han Zhao from *L'Ecole Normale Supérieure de Cachan*.

During this journey, I would like to thank Dr. Aymen Ben Soussia from *Arts et Métiers ParisTech*, Dr. Marco Longana and Mr. Wei Wang from the *University of Southampton* and my friends in the *Université de Technologie de Troyes*.

A special acknowledgement goes to the *China Scholarship Council* (CSC) who covers my maintenance in France for this PhD project. I also acknowledge the *University of Southampton* for providing me a Postgraduate Research visiting program with a studentship for two years.

Finally, I would like to appreciate my parents, my wife and my sisters for their patience and encouragement.

To all involved in this GREAT journey, thank you very much!

Haibin

Contents

List of Figures

Abbreviations

CCD	Charge Coupled Device
CEGM	Constitutive Equation Gap Method
CFRP	Carbon Fibre Reinforced Polymeric
CMOS	Complementary Metal Oxide Semiconductor
DIC	Digital Image Correlation
EGM	Equilibrium Gap Method
FE	Finite Element
FEMU	Finite Element Model Updating
FP	Full Pixels
FPS	Frames Per Second
HP	Half Pixels
HS	High-speed
ISIS	*in situ* Storage Image Sensor
MI	Moiré Interferometry
SHPB	Split Hopkinson Pressure Bar
SPI	Speckle Pattern Interferometry
UHS	Ultra-high Speed
VFM	Virtual Fields Method
WDFT	Windowed Discrete Fourier Transform.

"The best way to get something done is to begin."

Chapter 1

General introduction

1.1 Background

In the engineering area, materials experience high strain rate deformation when structures suffer impact, crash, blast, etc. Reliable material models capturing the physics of dynamic material response are required for numerical simulations of these structures. Only considering materials models under quasi-static conditions might lead to very conservative designs or designs that fail prematurely and unexpectedly [1], due to the fact that the mechanical behaviour of many materials at high strain rates is significantly different from that under quasi-static loading [2–6]. Therefore, it is essential to conduct substantial experimental tests at different strain rates. Most materials have been characterised accurately under quasi-static conditions. However, related work under dynamic conditions is still an open problem due to difficulties in characterising the high-rate behaviour of materials. In practice, inertial effects at high strain rates lead to the difficulty in measuring the impact forces. Moreover, at high strain rates, it is not easy to achieve homogeneous deformation in the specimen. High strain rate testing of materials is also limited by technological challenges. For instance, it is difficult to acquire real-time visualisation of the deformation of the specimen like for quasi-static conditions.

Nevertheless, different strategies to characterise the mechanical behaviour of materials at different strain rate ranges have been developed in the scientific community. A review of the conventional experimental techniques for high rate testing is available in [7]. Among these techniques the most popular is the so-called split Hopkinson pressure bar (SHPB). The original idea was proposed a century ago by Hopkinson [8], while the current split bars system was designed by Kolsky [9]. This technique has been widely used to perform high strain rate testing of a number of materials, as evidenced in [7]. However, the

SHPB procedure suffers from a number of shortcomings. First, it is based on the one-dimensional wave theory; therefore, it strictly relies on the assumption of uniaxial and homogeneous stress state. Then, another stringent assumption is the fact that the standard SHPB analysis based on the strain gauges readings on the input and output bars requires quasi-static loading conditions, *i.e.*, no inertial effects. As a consequence, specimens usually have to be very short to minimize the time over which stress waves travel back and forth within the specimen and fade away. This is even worse for materials with low wave speeds like soft materials and biological tissues. Although some authors proposed improvements to address some of these issues [10, 11], the derivation of impact force still requires some imperative assumptions for the SHPB tests.

Recently, owing to the dramatic advances in digital imaging and memory technology coupled to the available digital image processing algorithms (e.g. digital image correlation (DIC) [12] and the grid method [13]), it is possible to perform ultra-high speed (UHS) full-field measurements. Unlike conventional strain measurement techniques such as extensometers or strain gauges, full-field measurements are non-contact and can provide heterogeneous deformation of the specimen surface. The full-field data enables one to perform further analysis and processing such as characterising material constitutive parameters. In the past few years, DIC has been used to acquire the quantitative full-field deformation of specimens in SHPB tests [14–16]. In these examples, the assumption of uniform stress/strain state in the SHPB proved to be reasonably fulfilled. However, in these examples full-field deformation measurements were mainly used to provide average strain value over a certain area like a non-contact strain gauge, which did not take full advantages of full-field measurements.

All of the previous examples only involve simple nominally-uniform tests. More general case is to identify material parameters from heterogeneous tests using some inverse solutions, e.g. the finite element model updating (FEMU) method [17–19], the virtual fields method (VFM) [20], etc. However, it is important to note that in these examples the external force measurement is always required. Under quasi-static conditions, the external force used to identify material parameters is easy to measure through load sensors, as in [20], whereas at high strain rates, the force measurement is strongly affected by inertial effects. This is the reason why inertial effects generally represent a hindrance in current high strain rate testing techniques.

However, in some vibrating tests, it has been shown that inertial forces can be used to identify the material parameters. For instance, Grédiac *et al.* [21] and Giraudeau *et al.* [22, 23] reported the identification of stiffness and damping parameters using the acceleration of vibrating plates without the need for excitation force measurement. In these cases indeed, the acceleration can be simply obtained through measuring dynamic

deformation of the plate with the knowledge that the imposed excitation is harmonic. More recently, Othman *et al.* [24, 25] used high-speed (HS) imaging to obtain full-field acceleration in rubber specimens loaded at high rates in an SHPB apparatus through second order differentiation of time-resolved full-field displacement over time, although their work still involved the measurement of the external impact force. It is expected that cameras with higher frame rates will be required to acquire correct acceleration in stiff materials, because of the very large wave speeds. For instance, Pierron *et al.* [26] used the VFM to identify the Young's modulus of a concrete material from uniaxial tests, with ultra-high speed (UHS) imaging taking into account the acceleration without the need for external force measurement. All of these examples make use of inertial forces to identify material parameters at high strain rates. Some completely avoid the need for any external force measurement. In this case, the limitations (e.g. no inertial effects, uniform stress state, etc.) of current high strain rate testing techniques can be potentially relieved. This exciting progress leads one to believe that a new era of high strain rate testing is at hand.

1.2 Aims and objectives

The primary aim of this PhD work is to develop a novel experimental procedure using full-field strain and acceleration measurements and the VFM to identify the constitutive parameters of materials at high strain rates. This idea has already been initially validated using nominally heterogeneous tests on composites and concrete [26, 27], which renders it as an attractive methodology for high strain rate testing of materials. However, to deliver the full potential of this idea, it is necessary to develop better test configuration design and more robust program for identifying the material parameters. Moreover, more complex constitutive models (e.g. strain rate dependence of materials, elasto-visco-plastic behaviour of materials, etc.) are required to be explored. In this work, UHS cameras coupled to the grid method are used to perform full-field deformation measurements at high strain rates. To achieve the primary aim, four fundamental objectives are addressed as follows:

- To design appropriate experimental tests for UHS imaging.
- To adapt the VFM to the case of high strain rates.
- To investigate uncertainty in parameter identification at high strain rates.
- To explore novel methodologies to identify the strain rate dependence of materials.

In this project, linear elasticity is mainly considered as a first step. Before moving to the experimental tests, it is necessary to perform validation of the routines from simulated

data and to validate appropriate experimental configuration. The simulation is performed using ABAQUS/EXPLICIT. The related experimental tests are carried out on carbon/epoxy prepreg composite specimens, because composite materials exhibit limited plastic deformation but significant elastic deformation under a load. Moreover, with composite prepreg materials, it is convenient to stack quasi-isotropic and unidirectional composite specimens for identifying the isotropic and orthotropic elastic parameters respectively. The FE simulation and experimental procedures are presented in Figure 1.1.

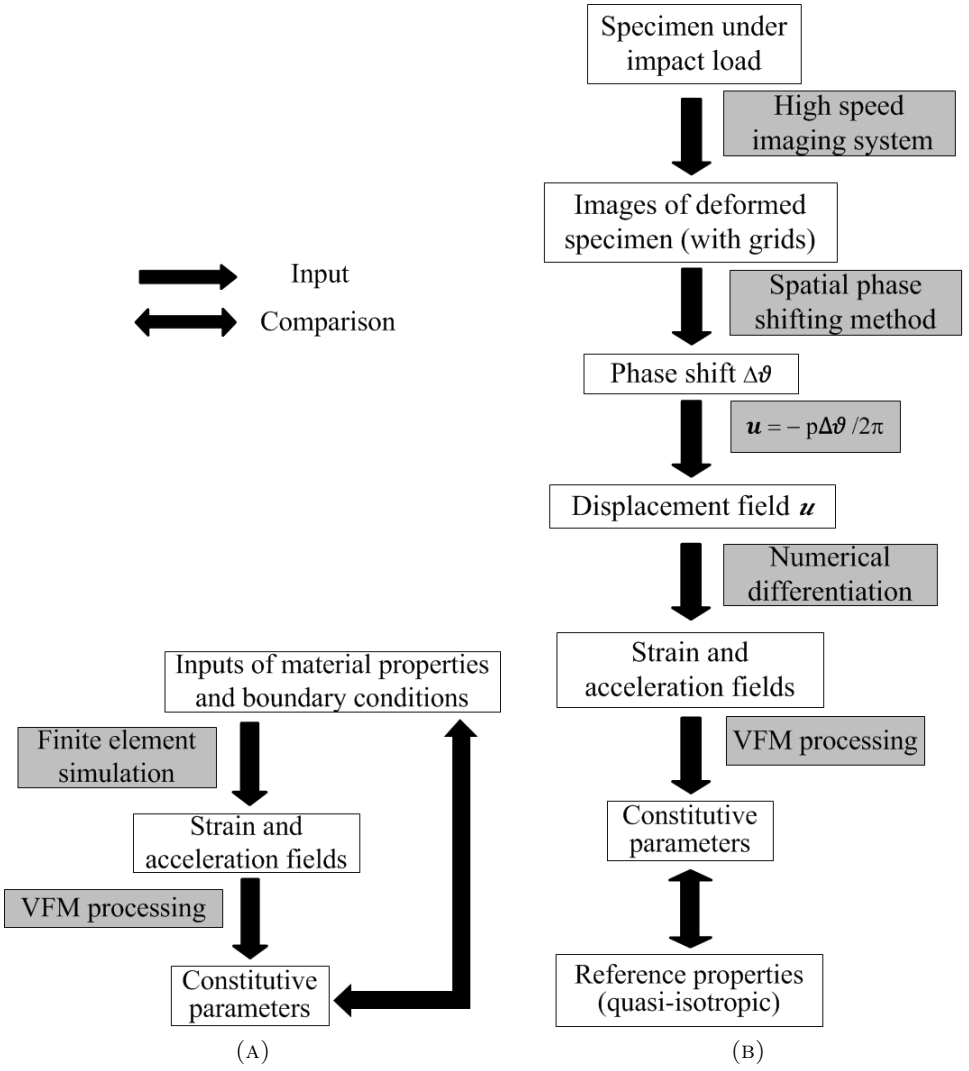

FIGURE 1.1: Flow charts of the finite element simulation and experimental implementation procedures in this PhD work. (A) Numerical validation. (B) Experimental implementation.

1.3 Novelty and contribution

A general experimental procedure to identify the constitutive parameters of materials at high strain rates is proposed in this PhD thesis. This original work covers the following aspects:

- Special optimized virtual fields in the case of high rate dynamics (*i.e.*, in the presence of inertial effects). The optimised virtual fields have been well applied to the identification of the material parameters under quasi-static conditions [28]. In this thesis, this procedure has been extended to the case of high rate dynamics for the first time.
- New purely inertial tests for stiffness identification using the acceleration as a load cell. In the VFM, the applied resultant force is generally used as the force information in the principle of virtual work to identify the material parameters under quasi-static conditions. However, at high strain rates, it is difficult to accurately measure the impact force due to inertial effects. In this work, inertial forces have been used as an alternative load cell to identify the constitutive parameters at high strain rates without the need for any impact force measurement. This relieved the constraint of the external force measurement and the assumption of the uniform stress state for current high strain rate testing techniques. Thus, high strain rate testing of materials like soft and brittle materials can potentially be much easier to perform.
- Numerical validation on FE simulated data. The idea to identify parameters making use of inertial effects has been numerically validated before moving to the experimental tests. To do so, FE simulations were first carried out on the quasi-isotropic composite specimens, and then on the orthotropic unidirectional composites.
- Experimental implementation on both quasi-isotropic and unidirectional laminates using two different impact set-ups and two different ultra-high speed cameras. In the experimental tests, quasi-uniaxial and more heterogeneous stress/strain states have been achieved through a steel cylindrical and/or a ball-bullet projectiles respectively. The strain levels in the ball-bullet impact tests were only one tenth of that in the steel cylindrical impact tests, however, the identification with the two projectiles proved reasonably consistent. Two UHS cameras have been used in the steel cylindrical impact tests. The results from the two cameras are comparable, although the measurement performances of the two cameras are significantly different. The consistent identification from different experimental configurations and cameras confirms that the experimental procedure proposed in this thesis is reproducible and robust.

- Identification of orthotropic parameters at high strain rates from a single test. According to the numerical simulation and identification, it shows the capability to identify all four independent orthotropic stiffness components from heterogeneous tests at high strain rates. Experimentally, the four parameters have not been identified completely and accurately yet. For one thing, this means that experimental set-ups to produce more heterogeneous stress/strain states are required. Another potential reason is the strain rate dependence of materials leading to difficulty in identifying the parameters.
- First exploration of the use of heterogeneous strain rate maps, both numerically and experimentally. In this work, full-field strain rate maps exhibit very heterogeneous spatial distributions. This results in spatially variable stiffness values during a single test. Consequently, the previous VFM routine based on constant stiffness assumption over the specimen is invalid. Thus, a novel strain rate analysis methodology has been explored for the first time.
- First exploration of non-linear laws. The shear stress-strain behaviour of unidirectional composites is known to be significantly non-linear. In this PhD thesis, the non-linear shear stress-strain behaviour has been first numerically implemented and identified with the VFM using simulated data.

This work has already led to two journal papers and five international conferences. A complete list of publications is presented in Appendix A.

1.4 Structure of thesis

The thesis begins with a general survey of high strain rate testing of materials in Chapter 2. A review of the main high strain rate testing techniques is first provided. UHS cameras and full-field measurement techniques able to be used in high strain rate testing are then reviewed. Thereafter, inverse strategies for characterising the constitutive parameters from full-field measurements are recalled. Since this work focuses on carbon-epoxy composites, some bibliographic details on the high strain rate behaviour of these materials are the provided. This chapter finally justifies why the grid method and the VFM are selected to perform UHS full-field measurements and to identify the material parameters from full-field data respectively.

Chapter 3 provides the details of the VFM with inertial effects at high strain rates. Firstly, it explains why the acceleration can be used as a load cell in this study. Secondly, the VFM-based procedures to identify the linear elastic isotropic and orthotropic constitutive parameters are detailed. The optimized virtual fields are extended to the

case of high rate non-harmonic dynamics for the first time. For the orthotropic model, a novel methodology to identify the strain rate dependence of materials from heterogeneous strain rate maps is proposed. This chapter outlines the basic theory of the VFM with inertial effects used to identify the constitutive parameters of materials at high strain rates.

Chapter 4 mainly validates the idea described in Chapter 3 using FE simulated data. Two-dimensional FE simulations are first carried out. For the isotropic model, two projectiles with different shapes are used to provide the in-plane impact. One is a cylinder, which is used to produce quasi-uniaxial mechanical fields because of the uniform contact between the specimen and the projectile. The other is a ball bullet. Because of the nature of the point contact, the stress state of this model proved far more heterogeneous than the first one. For the orthotropic simulation, the strain rate dependence of the transverse and shear stiffness components is implemented using the user subroutine (VUMAT) of ABAQUS/EXPLICIT. Finally, three-dimensional FE simulation of the in-plane ball impact test is performed, because, in practice, a misalignment of the point contact is likely to happen, which leads to biased identification of the material parameters. It is therefore essential to conduct substantial investigation into this three-dimensional wave effect and to search for suitable solutions.

Chapter 5 and 6 present the experimental implementations to identify the material parameters at high strain rate making use of inertial effects without the need for any impact force measurement. Series of impact tests have been conducted on different types (quasi-isotropic and unidirectional laminates) of specimens using a steel cylindrical projectile and/or a small steel ball. The experimental procedure is detailed in Chapter 5. Chapter 6 mainly presents the experimental results including the full-field maps and the identification of material parameters using the approaches mentioned in the previous chapters.

The main outcomes of this PhD work and recommendations for future work are presented in Chapter 7.

Chapter 2

High strain rate testing of materials

Due to challenges in the physical and technological aspects, high strain rate testing of materials is difficult to perform. Nevertheless, many techniques have been developed and applied in the tests at high strain rates based on specific hypotheses (e.g. no inertial effects, uniform stress state, etc.). This chapter provides a review of current high strain rate testing techniques. With the development of ultra-high speed (UHS) imaging and computer power, UHS full-field measurements can be carried out to obtain time-resolved full-field kinematic fields on the specimen surface. These full-field data can be then processed by some inverse strategies to identify the material parameters. Thus, some critical issues of current high strain rate testing techniques are being solved, e.g. the visualisation of deformation at high strain rates, the assumption of uniform stress state, etc. Related techniques and methodologies are briefly introduced in this chapter.

2.1 High strain rate testing techniques

Figure 2.1 presents a schematic diagram of the different strain rate ranges (in s^{-1}) encountered in engineering applications. This schematic spans over 16 orders of magnitude from creep to shock. Conventional commercial servo-hydraulic testing machines only achieve the intermediate strain rate up to 10^2 s^{-1}. The drop-weight tower can be used to produce comparatively high strain rates of 10^3 s^{-1}. Higher strain rate magnitude of 10^4 s^{-1} can be obtained through the Taylor impact test and the split Hopkinson pressure bars (SHPB) system. It is well-known that at low strain rates, inertial effects can be neglected. However, for strain rates larger than 10 s^{-1}, inertia is pronounced,

which makes force measurement in conventional testing techniques such as the SHPB difficult. However, with specific assumptions (e.g. uniform and uniaxial stress, no inertial effects, etc.), these techniques have been widely applied to high strain rate testing of a large number of materials. In this section, the main high strain rate testing techniques are briefly introduced.

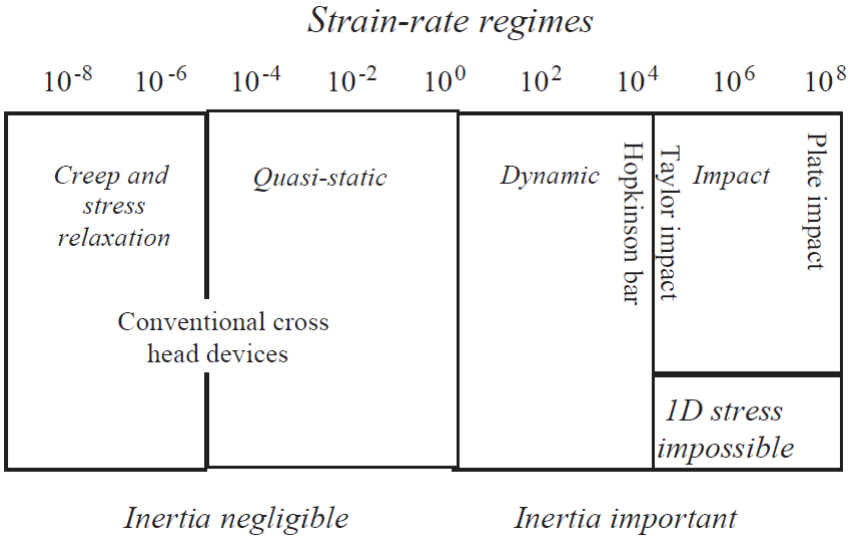

FIGURE 2.1: Schematic diagram of strain rate regimes (in s^{-1}) and related experimental techniques. [7].

2.1.1 Drop-weight tower

The drop-weight tower consists of a falling weight used as a striker, a massive base and a specimen placed at lower position, as seen in Figure 2.2. This instrument has been widely used in industry for research and quality control. Using strikers with varied impact noses together with adapted specimen holders, different tests (e.g. uniaxial compression, three-point bending, etc.) can be carried out using this instrument on specimens of different geometries. It is necessary to calibrate the system and to determine a factor between the force transducer and the output voltage signal before moving to the experimental tests. This machine can be used to acquire information such as forces, deflections and energies absorbed during the impact process [29]. However, this system is very sensitive to the contact conditions between the striker and the specimen [30]. Moreover, it is impossible to achieve constant loading and strain rates using this technique [31].

2.1.2 Servo hydraulic testing machine

The servo hydraulic testing machine is usually used to cover the intermediate strain rate range. Figure 2.3 shows the schematic of Instron VHS 1000, a typical high speed servo

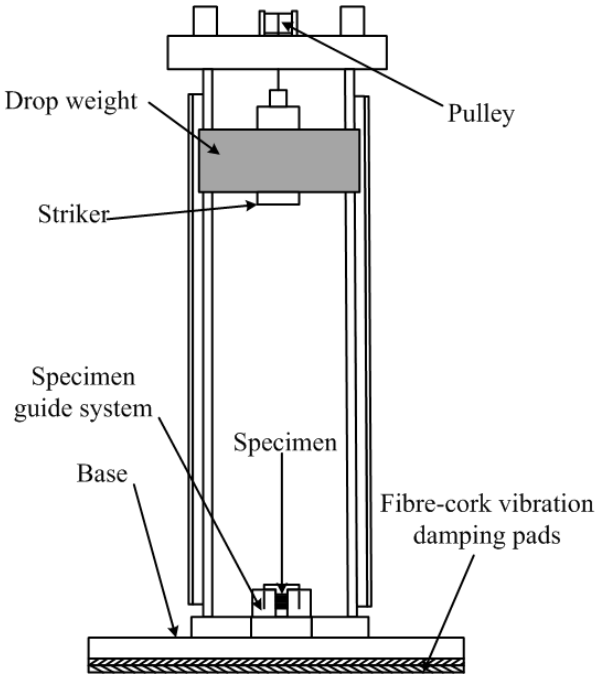

FIGURE 2.2: Schematic of the drop-weight tower [30].

hydraulic testing machine. This machine works through accumulating oil at a pressure of 280 *bars* in an pressure cylinder controlled by a proportional valve [32]. The advantage of the servo-hydraulic machines is that they can be used to perform mechanical tests from quasi-static to intermediate strain rates. The loading rate obtained by this kind of machine is quite stable, but usually less than 200 s^{-1}.

2.1.3 Cam plastometer

The application of the cam plastometer was first reported in the 1960*s* for dynamic compressive tests. A schematic of this equipment is shown in Figure 2.4. A cam is rotated at a specific velocity. The specimen is positioned on an elastic bar. The cam follower is engaged before compression, but after compression it must be removed for preventing repeated blows on the specimen. Thus, within one cycle the specimen is deformed. Strain rates between 0.1 and 100 s^{-1} have been obtained by this technique [33]. It is suitable for measuring the non-brittle materials during the dynamic deformation. It is capable of deforming specimens at constant strain rates [34]. It can also be used in high temperature environment [35].

2.1.4 Taylor impact

Taylor impact equipment consists in firing a cylinder made of the material of interest against a massive and 'rigid' plate as shown in Figure 2.5. The original purpose of this

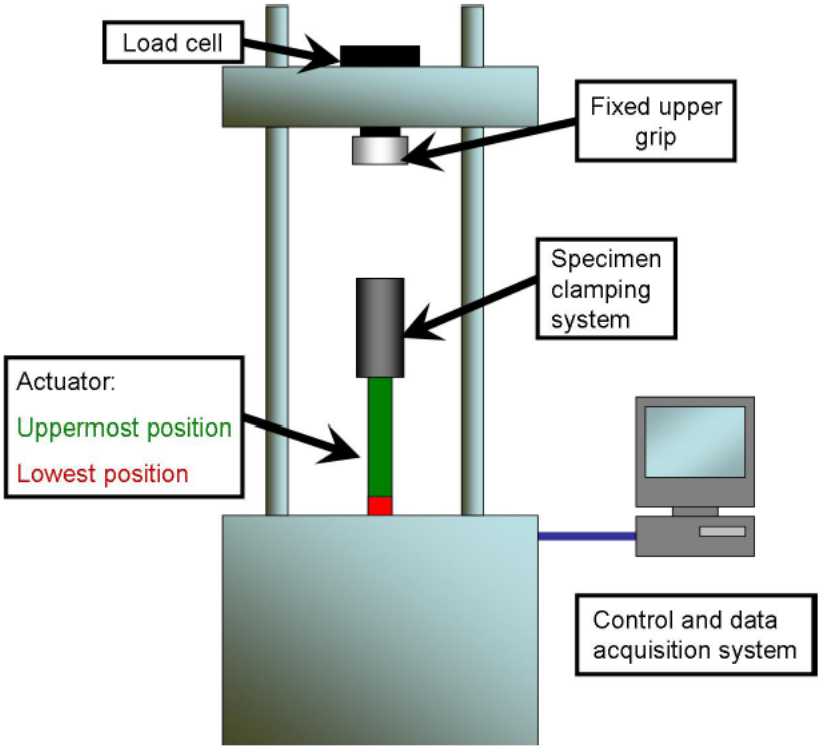

FIGURE 2.3: Schematic of the Instron VHS [32].

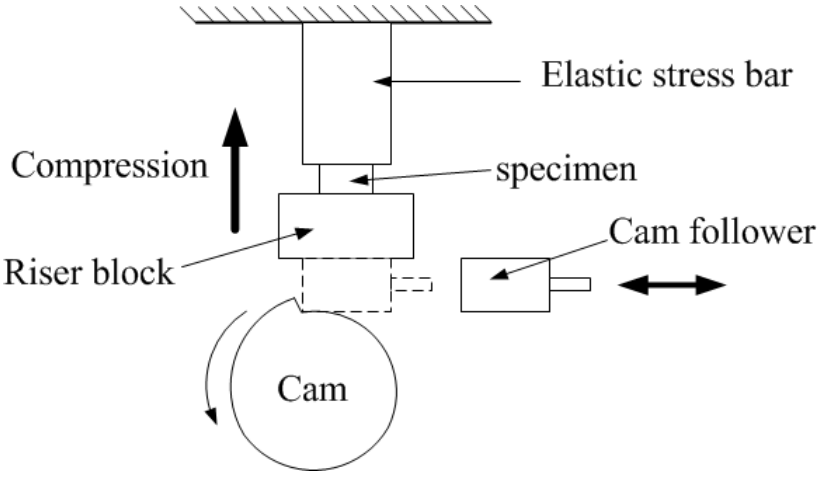

FIGURE 2.4: Schematic of the cam plastometer [33].

technique was to estimate the strength of ductile materials in compression. The flow stress of materials can be estimated with this test by measuring the overall length of the cylinder before and after impact [36–38]. However, this method is now often used to validate constitutive models of different materials through comparing the shape of the recovered cylinder with the computational prediction [39–41]. The advantage of Taylor impact tests is simple to perform. All that is required is a device to fire the cylinder at the desired velocity and the ability to measure the deformed shape of the cylinder. The Taylor impact test is a useful tool to check the constitutive equations at

high strain rates and large strains. However, one of the drawbacks of this technique is that the specimens used in this test are limited in size in order to fit in the gun barrel. Some improvements have been recently devised, e.g. the application of high speed (HS) imaging for measuring the progress of deformation and some techniques based on hardness variation measurements in regions of the deformed cylinder [42].

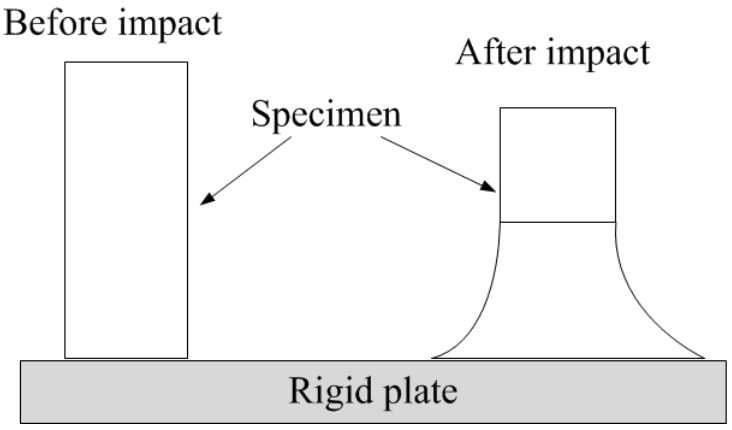

FIGURE 2.5: Schematic of the Taylor impact test showing the initial and final states of the cylindrical specimen [38].

2.1.5 Split Hopkinson pressure bar

Among these high strain rate testing techniques, the most popular is the so-called split Hopkinson pressure bar (SHPB) or Kolsky bar. The SHPB technique has become the standard method to characterise the mechanical behaviour of materials in the strain rate range of 1000 to 10000 s^{-1}. The basic idea of the SHPB is that the specimen is deformed between two elastic bars excited above their resonant frequency [7]. A schematic of the SPHB system is shown in Figure 2.6. This system consists of two elastic bars (input and output bars) and a specimen sandwiched between the two elastic bars. The free end of the input bar is impacted by a striker made of the same material as the input and output bars. The compressive wave propagates from the input bar to the specimen. A part of compressive wave is rebounded at the input bar/specimen interface and is then sent back to the input bar. The rest of the compressive wave is transmitted into the output bar. The strain gauges attached onto the two elastic bars can be used to record the signals including the incident, reflected and transmitted pulses in the two bars. Typical signals recorded in the SHPB test are shown in Figure 2.7. The compressive wave is represented as positive on this plot. Modified bar systems are now capable of performing the torsion and tension [43, 44].

The classic analysis using the SHPB technique is based on the assumption of uniform stress/strain state. Once equilibrium has been achieved (*i.e.*, the forces at the two ends

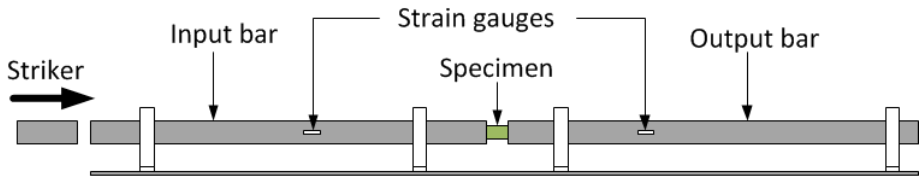

FIGURE 2.6: Schematic of the SHPB test.

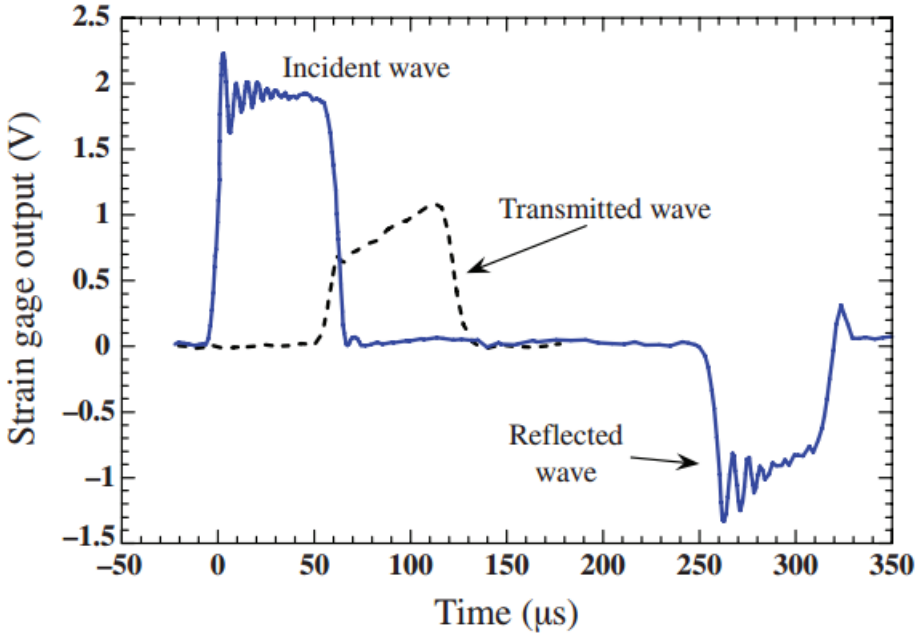

FIGURE 2.7: Typical signals in the input and output bars [45].

of the specimens are equal and opposed, or another words, inertia effects have vanished), the nominal strain rate $\dot{\varepsilon}$, strain ε and stress σ in the specimen can be estimated through:

$$\dot{\varepsilon}(t) = -\frac{2c_b}{L_s}\varepsilon_r(t) \tag{2.1}$$

$$\varepsilon = \int_0^t \dot{\varepsilon}(\tau)d\tau \tag{2.2}$$

and

$$\sigma(t) = \frac{E_b A_b}{A_s}\varepsilon_t(t) \tag{2.3}$$

where ε_r and ε_t represent the reflected and transmitted pulses measured by the strain gauges respectively, c_b the elastic wave speed in the bar defined by $c_b = \sqrt{\frac{E_b}{\rho_b}}$ with the knowledge of Young's modulus E_b and density ρ_b of the bars material, and A_s and L_s are the initial cross-sectional area and the length of the specimen, respectively. Combining Equations 2.2 and 2.3, a stress-strain curve can be obtained at a strain rate defined from Equation 2.1.

Series of typical stress-strain curves of Ti6A14V alloy specimens from the SHPB tests

at different strain rates are presented in Figure 2.8. One can clearly see that the stress-strain curves vary at different strain rates.

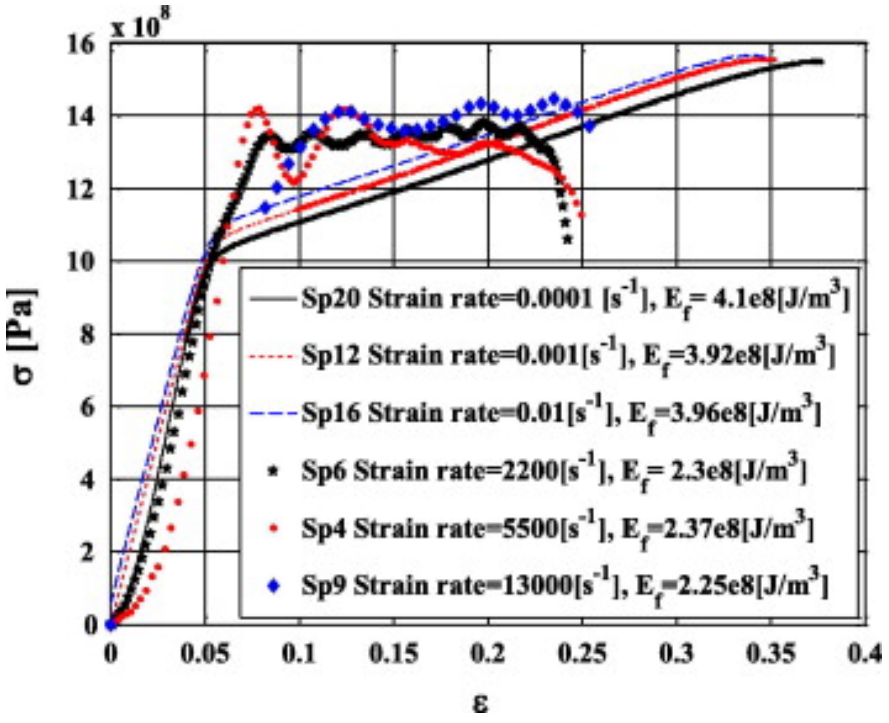

FIGURE 2.8: Typical stress-strain curves retrieved from the SHPB test [46].

The procedures for torsion and tension are similar to that for compression described above. It is worth noting that Equations 2.1∼2.3 are based on three major assumptions: *i*) the forces on both ends of the specimen are essentially identical at any instant of time. This means that one has to wait for the stress waves to fade away before the analysis can be used. As a result, initial elastic behaviour of test pieces is usually not attainable with this technique. This problem is worsened by long specimens and/or low speeds of sound (soft materials). *ii*) The specimen deforms at constant volume [7, 47]. *iii*) no dispersion happens during the test. Wave dispersion affects the measured stress-strain response. To minimise the effects of dispersion, a buffer or a shaper are usually placed between the striker and input bar [42]. If any of the three assumptions is false, these equations would be invalid. Therefore, the specimens tested in this technique are usually small. On the other hand, it is necessary to have about 1000 grains or crystals in a specimen for it to be mechanically representative of the bulk. The coarser the microstructure, the larger the specimen has to be to fulfil this condition and hence the lower the maximum strain rate achieved [7, 48]. Consequently, very large SHPB bar systems have to be built up in order to perform high strain rate testing of coarse-grained materials such as concrete.

The SHPB technique has been widely applied to high strain rate testing of different materials. However, for soft and brittle materials, the major assumptions for deriving

Equations 2.1∼2.3 are violated. For instance, brittle materials usually fail before stress equilibrium is achieved. In this case, strain gauges are often directly attached onto the specimen to measure the deformation. This has some disadvantages including: *i*) the strain gauge can be only used once; *ii*) only point-data can be obtained [7]. As for soft materials, it is not easy to achieve a uniform stress state in the specimen because of the low speeds of sound. Moreover, due to the low impedance of soft materials, the signal from the transmitted bar is too weak to accurately be measured by the strain gauge on the transmitted bar [49]. To circumvent this issue, different techniques have been applied. For example by the use of a tube instead of a solid rod for the output bar [50], or by using 'soft' materials (e.g. polycarbonate, nylon, polymer, etc.) instead of metal for the Hopkinson-bar systems [51–53]. Nowadays, optical measurement techniques are sometimes used to measure the deformation of the specimen. Indeed, these techniques are particularly useful for non-standard materials, such as the examples in [14, 54, 55].

After this brief introduction of the main high strain rate testing techniques, it can be seen that these techniques share some common features and an important one is that they are only capable of obtaining very limited experimental information. For instance, the Taylor impact test only involves measuring the permanent deformation of the tested cylinder although HS photography has been used more recently [41, 56]. When it comes to the SHPB test, strain gauges away from the test area are used to retrieve a global stress and strain response of the specimen. With this technique, stringent assumption of uniform stress/strain state in the specimen has to be fulfilled. Thus, only small specimens can be used to mitigate the equilibrium constraint. Although full-field measurement techniques have been used to obtain displacement fields throughout the impact event [6, 18, 54, 55], the data were only used either to check for strain uniformity and/or to provide a non-contact average strain measurement to use in conjunction with the classical SHPB analysis to derive the impact force.

In quasi-static tests, the constitutive parameters of materials can be identified from full-field heterogeneous fields with some inverse strategies [17, 28, 57]. This concept is being extended here to the case of high rate dynamic testing. To obtain full-field heterogeneous deformation of the specimen at high strain rates, high-speed (HS) even ultra-high speed (UHS) imaging is required, which will be reviewed in the next section.

2.2 Ultra-high speed imaging

HS imaging technology was started with the Manhattan project in which HS film cameras were devised to help the study of explosive events [58]. Its original purpose is to monitor what is happening during extremely short-scale events. In the last two decades, with the

progress of digital imaging sensors (CCD and CMOS sensors) coupled to the availability of digital image processing algorithms (e.g. DIC and the grid method), HS imaging has been capable of obtaining more quantitative information such as the deformation at a great number of points at the surface of a specimen, hence the terminology 'full-field' measurements. The full-field data acquired from the digital camera can be used to perform further analysis such as characterising the material constitutive parameters.

Full-field measurement techniques coupled to standard digital cameras have been extensively applied to quasi-static tests. However, extending this to high rate events is more difficult because of lower quality images and limited temporal resolutions among other reasons. To improve the performance of HS imaging, it is necessary to overcome challenges in aspects of camera sensor technology, frame rate and motion mitigation, etc. [59]. Currently, many commercial cameras are available to acquire dynamic images at different frame rates. An excellent review of the main techniques used in HS imaging is available in [60]. An overview of currently available HS digital cameras is displayed in Figure 2.9, where the horizontal and vertival axes represent the maximum frame rate and record length respectively while the rectangular area for each camera is proportional to the corresponding spatial resolution. The pie indicates the minimum exposure time of each camera. The cameras with a frame rate over 1 million frames per second (Mfps) are defined as ultra-high speed (UHS) cameras. As seen in Figure 2.9, it is clear that the available frame rates of HS cameras are only up to $100,000\ fps$ but with large record capacities (thousands of frames), whereas for UHS cameras the recording lengths drop to less than 150. To achieve ultra-high frame rates, the critical issue is the readout speed of data, *i.e.*, the number of pixels times the frame rate. Currently, this issue is being solved using different techniques, e.g. rotating mirrors, beam splitters and some special imaging sensors. The rest of this section is devoted to a review of these techniques.

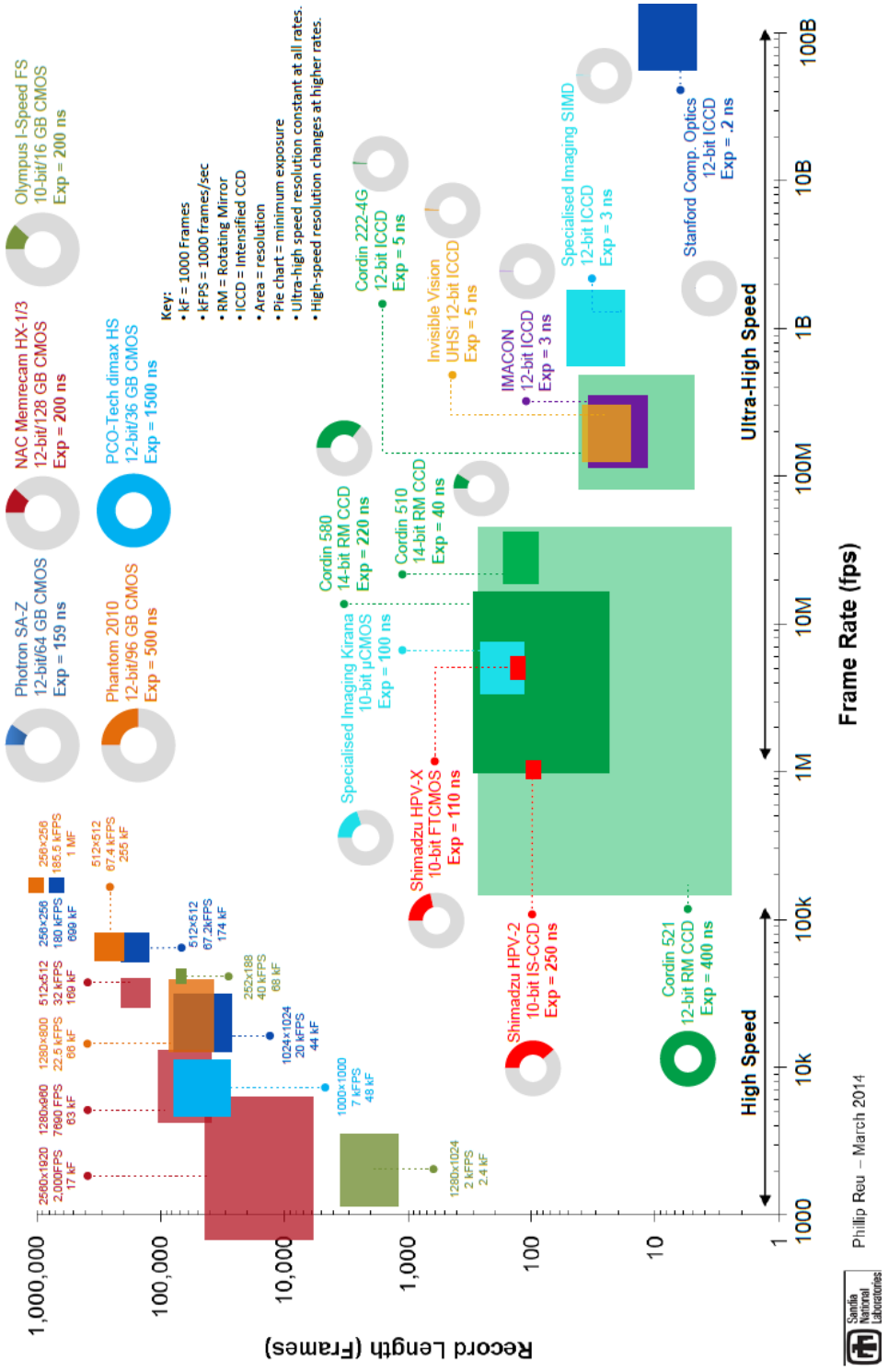

FIGURE 2.9: Survey of the high-speed imaging technology updated from [59].

2.2.1 Rotating mirror

The cameras (e.g. Cordin cameras mode 550 and 580) in this group rely on a rotating mirror to image the scene onto a number of distinct detectors. A schematic of this rotating mirror is shown in Figure 2.10. This mirror is driven by a turbine at high speed. The cameras based on this technology usually have good spatial resolution. The main disadvantage is that the physical size of this type of camera restricts its flexibility [60]. Moreover, this kind of camera usually involves image registration problems and image distortions due to the complex optical path and multi-sensor system [61].

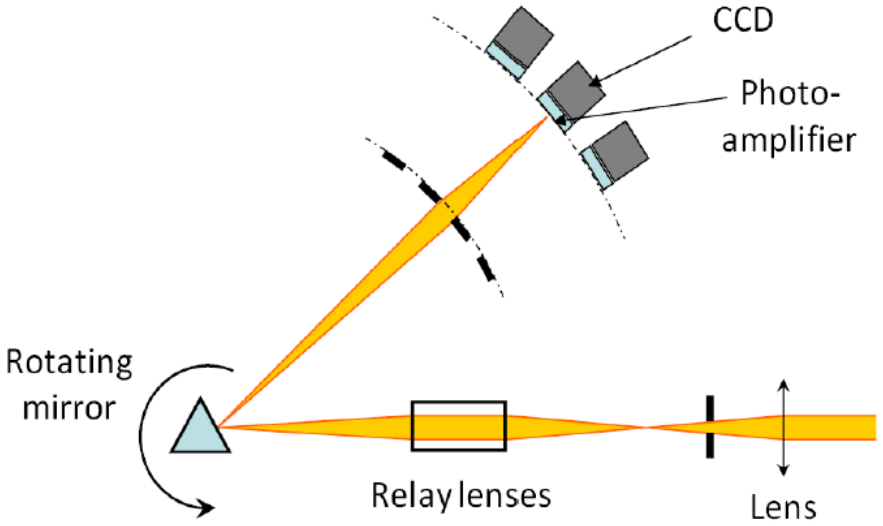

FIGURE 2.10: Schematic of the rotating mirror [62].

2.2.2 Beam splitter

In this technique, a beam splitter is used to divide the incoming light that is then directed onto multiple detectors. A schematic is displayed in Figure 2.11. Cameras (e.g. DRS IMACON or SIM series) using this technology require the additional application of image intensifiers to amplify the divided light. However, the usage of imaging intensifiers introduces some noise to the image. For instance, significant spatial correlation in the noise between two stationary images of the same scene was found using IMACON 200 in [62]. This issue largely degrades the accuracy of the DIC method due to the nature of the correlation calculation. From a metrological point of view, cameras using this technology were created for imaging rather than quantitative measurements [61]. The maximum frame rate for this kind of camera can reach 1 billion fps, but only a few

frames can be acquired, typically, only up to 16 or 32 frames, and this makes accurate triggering of the system critical.

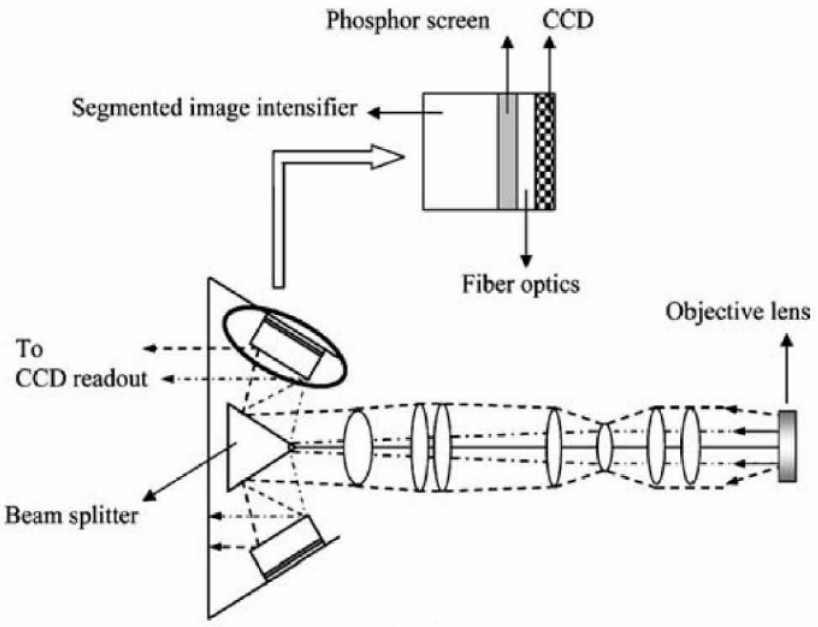

FIGURE 2.11: Schematic of the beam splitter [63].

2.2.3 On-board solid-state memory storage sensor

The concept of placing memory storage in each pixel element of the image sensor was proposed in [64]. However, a more practical UHS image sensor was developed by Kosonocky *et al.* in 1996 [65]. They overcame the difficulty in multi-transfer-direction changes of CCD register described in [64]. The camera with on-board memory storage sensors in [65] was capable of recording 30 consecutive images at 833,000 fps. In the recent years, this concept has been developed into different branches. This concept removes the problem of imaging distortion introduced by beam splitters, rotating mirrors and intensifiers. The rest of this subsection will be dedicated to a review of the latest on-board memory storage image sensors.

2.2.3.1 ISIS CCD

The representative of this type of camera is Shimadzu HPV-1 and 2 [66]. This kind of camera uses *in situ* storage image sensor CCD (ISIS-CCD) which has memory integrated onto the detector itself. The basic structure of this ISIS-CCD sensor is shown in Figure 2.12. When each image is recorded, the electrons are transferred from the photodiode to the storage unit, and then from one storage unit to the next one through 100

linear locations until they reach the CCD drain. More details about the ISIS CCD sensor can be found in [67, 68]. The maximum frame rate of this kind of camera is 1 Mfps. The theoretical maximum frame rate of this kind of sensor is expected to be more than 100 Mfps [68]. The recording capacity of the HPV-2 camera is up to 100 frames with a spatial resolution of 312×260 pixels. The main shortcomings of this kind of camera are: *i*) mounting the on-board memory occupies a lot of space of the pixel, consequently, the photo-active area of each pixel is small, which leads to low fill factors compared to standard CCD or CMOS sensors, especially in the horizontal direction (only 14 % [61]). Low fill factors distort images, especially in the case of high spatial frequencies. *ii*) With the ISIS-CCD sensor, the power consumption is comparatively high. Thus, the generated heat potentially spoils the imaging performance, even damages the sensor [69]. *iii*) Due to the nature of the ISIS-CCD sensor, the exposure time of this type of camera depends on its imaging speed. In other words, at low and/or intermediate frame rates, it is impossible to set short exposure times, which potentially blurs the image [69].

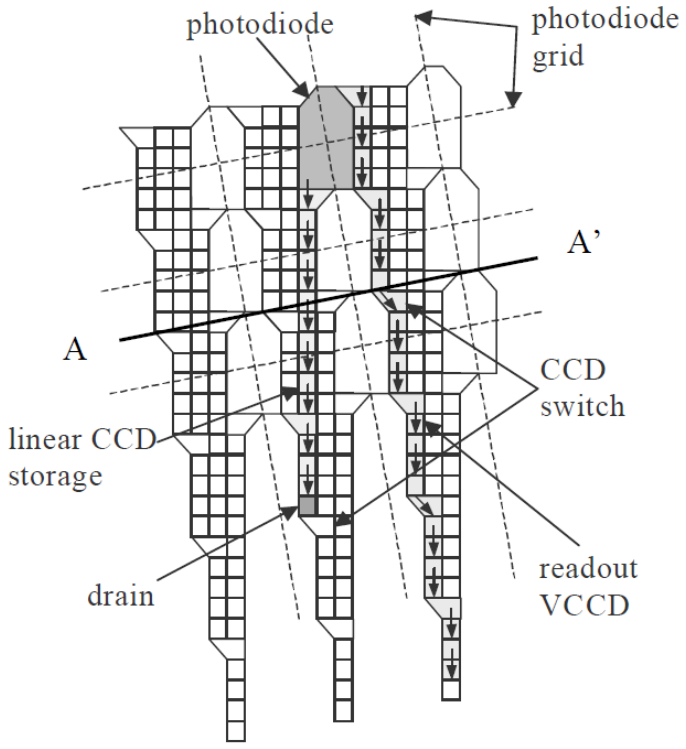

FIGURE 2.12: Schematic of the ISIS-CCD layout [67].

2.2.3.2 FTCMOS

The Shimadzu HPV-X camera is a representative of this technology [70]. This kind of camera uses a dedicated sensor called FTCMOS which is a special type of CMOS sensor.

The maximum frame rate of the FTCOMS camera has been improved significantly. The full spatial resolution of this kind of camera is 400×256 pixels. The sensor arrangement of the FTCMOS camera is different from the ISIS-CCD camera, as displayed in Figure 2.13. The sensor consists of one pixel array and two on-chip memory arrays which are spatially separated. This design allows one to cover the memory region with a light shield. Thus, signal degradation on the memory caused by high illumination does not occur. Each pixel has 128 on-chip memories corresponding to the recording capacity. In order to

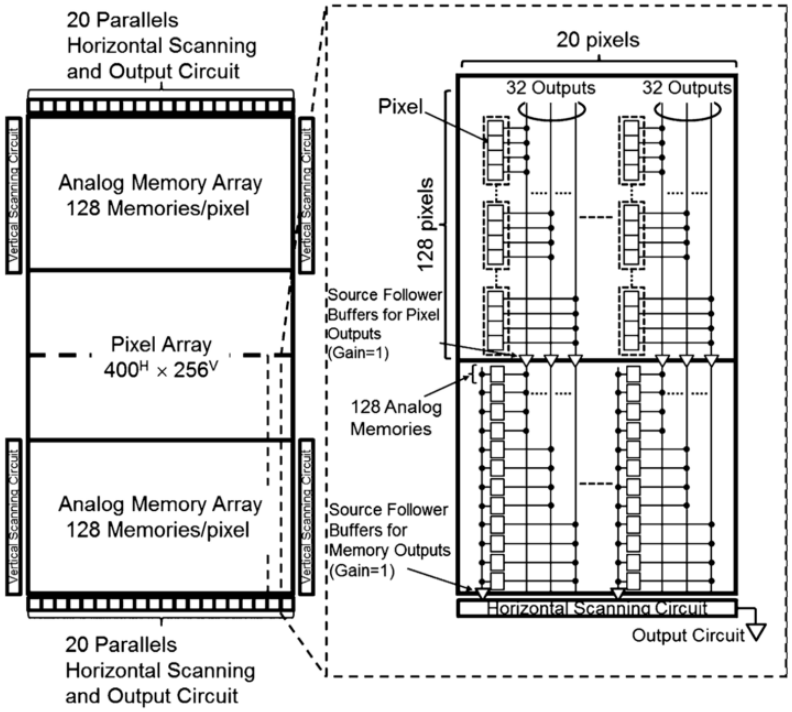

FIGURE 2.13: Schematic of the FTCMOS layouts [71].

achieve high readout speed, the parallel unit is applied, which reads the signal from the pixel to the memory region in parallel corresponding to the number of pixel output wires in each column. For instance, the parallel number in Figure 2.13 is 32. In order to obtain high fill factors, 4 pixels share one output wire. Thus, the fill factor of the HPV-X camera is up to 37 % [69]. Due to the nature of CMOS sensors, it is possible to set any variable exposure time starting from 200 nanoseconds with an increment of 10 nanoseconds in a frame rate range from 60 fps to 2 Mfps. However, exposure times are fixed at 110 nanoseconds for the frame rate of 5 Mfps and 50 nanoseconds for 10 Mfps. Thus, the images will not be blurred. It is worth noting that this kind of camera provides two recording modes. One is the full-pixel (FP) mode with full resolution. The maximum frame rate with this mode is up to 5 Mfps. The other is the half-pixel (HP) mode which is speed-priority (maximum frame rate of 10 Mfps) but only half spatial resolution. With the HP mode, the signal output is reduced so that only two

(four with the FP mode) pixels share one output wire. Although only half the spatial resolution is output at each frame with the HP mode, the full-pixel format is restored through reading the signal from the pixels in a zigzag pattern and then interpolating between them during the post-processing. This mode is therefore not usable for full-field measurements because of this interpolation. The disadvantages of this type of camera are: *i*) the spatial resolution is still low compared to the cameras using beam splitters and rotating mirrors. *ii*) The fill factor is still low compared to standard digital cameras, although better than the ISIS CCD sensors.

2.2.3.3 Kirana

The readout process of CCD sensors is implemented serially [72, 73]. The data from each pixel is passed through a single readout, whereas CMOS sensors can read the data at multiple pixels simultaneously because each pixel has a circuitry. Thus, the readout speed of CCD sensors is comparatively limited. Moreover, the power consumption of CCD sensors is higher compared to CMOS sensors. However, in terms of dynamic range, imaging quality (noise level) and light sensitivity, CCD sensors enjoy significant advantages over CMOS sensors [74, 75]. Additionally, CMOS sensors cannot physically bear too many pixels on the plane of the chip, which leads to lower spatial resolutions. A new sensor named 'Kirana' combining the advantages from both CCD and CMOS techniques has recently been developed [73, 76]. This technique is similar to that used in the ISIS-CCD and FTCMOS sensors. The representative of this technique is the Kirana camera from Specialised Imaging [77]. Figure 2.14 (A) shows the layout of a single pixel in the sensor and (B) presents its block diagram. Each pixel consists of five components: i) a fully pinned photodiode; ii) the input structure from the photodiode to the memory storage (MS); iii) the 2D MS array; iv) the output structure from the MS to the floating diffusion and v) the pixel readout circuit. The MS has a total of 180 memory cells organized as follows:

- A vertical entry (VEN) storage with 10 cells.
- 10 rows of lateral (LAT) storages, each with 16 cells.
- A vertical exit (VEX) storage with 10 cells .

The MS is based on three phase operations. This is considered a good compromise between the number of pixel control lines and the memory cell density per unit area. More details about the principle of this image sensor can be found in [76, 78]. With this kind of sensor, larger spatial resolutions (7 times larger than that of the HPV-2 and HPV-X) and recoding capacity (180 frames) with full pixels are achieved. However, the

photodiode is fully pinned and designed with a graded doping to improve the transfer speed, which leads to low fill factor (only 11 %) [79]. This issue significantly affects the full-field measurements performance. It should be noted that this camera is very new on the market and little feedback if any has been reported on its use for full-field measurements.

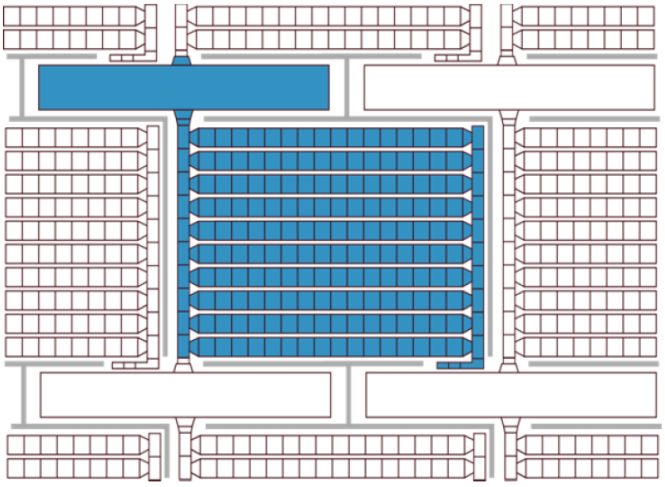

(A)

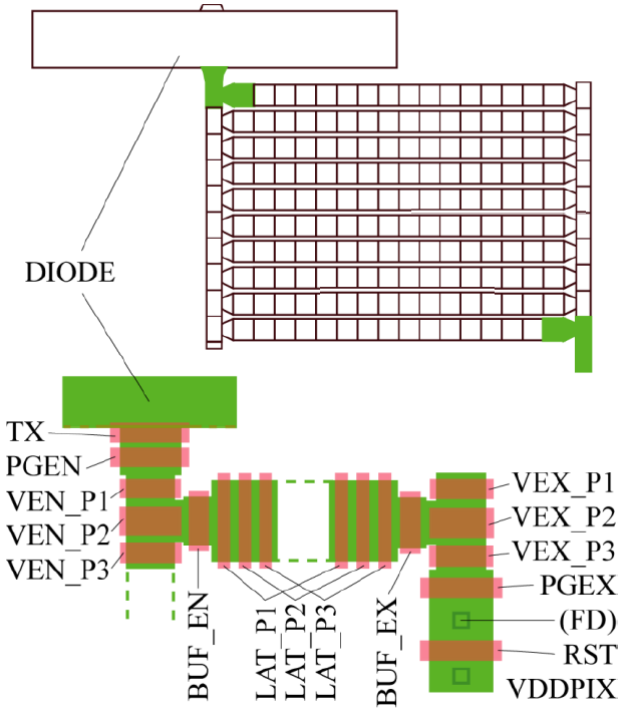

(B)

FIGURE 2.14: Layout of the Kirana sensor. (A) Highlighted single Kirana pixel [79]. (B) Single pixel diagram [78].

According to the brief review above, it is clear that fill factor, spatial resolution and frame rate of the camera are the bottlenecks of current UHS imaging techniques. However,

this area is currently experiencing rapid growth and further progress is expected in the coming years. For instance, with a backside illuminated image sensor, a fill factor of 100 % has been obtained recently [80]. An image sensor with multiple collection gates placed at the centre of each pixel can achieve a much higher frame rate. The theoretical maximum frame rate of a multi-collection-gate image sensor is 1 Gfps [81]. Of course, to obtain high quality images in UHS imaging, aside from the intrinsic issues of these techniques, it is necessary to pay attention to problems such as lighting and camera protection which are usually not very critical for standard digital imaging. In UHS imaging, it is essential to bring appropriate lighting so as to minimise the camera gain, which in turn reduces the noise in the images. Lighting in UHS imaging is not easy because not only is the intensity of the light important but also the distribution. For instance, the highlights in the image are particularly difficult to avoid if the specimen is curved or become curved during the tests. Camera protection proved necessary in some impact or explosion tests. The images are usually recorded by UHS camera through a transparent protective window. The distortion caused by the transparent window can lead to high displacement measurement errors if no measure to account for this is taken [61].

2.3 Full-field measurement techniques

In order to acquire quantitative information from images recorded by digital cameras, digital image processing algorithms are required. Under quasi-static conditions, full-field measurements have been widely used in the experimental mechanics community. A panel of full-field deformation measurement techniques is available. These techniques can be classified into interferometric and non-interferometric categories according to a criterion based on the nature of the physical phenomenon involved [82]. Interferometric methods include speckle pattern interferometry (SPI) [83, 84], moiré interferometry (MI) [85, 86] and holography [87], for the most common. Non-interferometric techniques mainly include digital image correlation (DIC) [12, 88] and the moiré/grid method [13, 89]. Interferometry requires a coherent light source, and the measurements are very susceptible to environment disturbances like vibrations [84]. Thus, they are normally conducted on a vibration-proof optical table. Moreover, the measured results from the interferometric techniques are often presented in the form of fringes. Further fringe processing and phase analysis techniques are necessary to obtain kinematic information like displacement. On the contrary, the non-interferometric techniques do not require coherent lighting. These techniques generally have less strict experimental requirements and determine the deformation through comparing the light intensity changes from the specimen surface before and after deformation.

Although the techniques mentioned above have been extensively applied to quasi-static tests, not all of them can be applied to at high rates. For instance, interferometric techniques require time for phase-shifting which compromises their use in dynamic events. They can be used in time-average format but this is only applicable to repeated harmonic excitation (*i.e.*, vibrations) [90, 91]. In high rate impact testing, real-time measurements are necessary. For this purpose, Bell [92] used a direct diffraction grating method to measure the strains in specimens tested in a SHPB set-up. However, this technique is quite time-consuming and requires skilled technicians. The authors are the only ones ever to use this method [7]. On the contrary, two non-interferometric techniques, *i.e.*, DIC and the grid method, have been successfully used in high rate testing by a range of authors [14, 15, 26, 27, 54, 93]. Therefore, the rest of this section will be devoted to a review of these two techniques.

2.3.1 Digital Image Correlation

DIC has been widely applied to full-field deformation measurements since it was proposed in the 1980*s* [94]. DIC is based on the correlation processing of patterns before and after deformation. The pattern can be applied to the specimen surface using white and black painting or it may be the natural texture of the material. Figure 2.15 presents a schematic of the data-acquisition system for 2D DIC measurements. A version using two cameras, called stereo-image correlation, is now currently used in experimental mechanics [95].

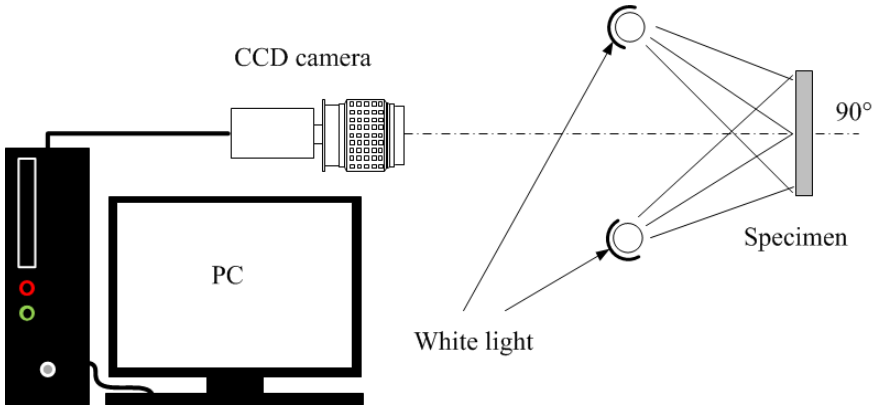

FIGURE 2.15: Schematic of the data-acquisition system for 2D DIC and grid method [12].

The basis of 2D DIC in UHS full-field measurements is same as that in quasi-static tests, except for more stringent requirements in terms of lighting and triggering, as well as using specific routes to mitigate the spurious effects of the particular UHS camera used. The correlation processing between undeformed and deformed images with random patterns is performed to extract the in-plane displacement of the specimen. However, in

order to obtain sub-pixel accuracy, it is necessary to reconstruct a continuous intensity function before the correlation processing. In practice, this continuous intensity is reconstructed using interpolation functions. Another important aspect of DIC is that the displacements are parameterised using shape functions and the coefficients of these functions are obtained through minimisation of a matching criterion. More details can be found in [96].

The sensitivity of DIC is typically much lower than that of interferometric techniques. Also, its spatial resolution is not very good, typically a few hundred pixels, compared to one pixel for interferometric techniques. The accuracy of full-field displacement measured using this method reaches sub-pixel level. The displacement resolution reported in [97] was less than 0.02 pixels with a subset of 41 by 41 pixels. Strain is usually the major interest of researchers and engineers in experimental mechanics. The reported strain resolution in [97] was around 127 microstrains with a window of 21 by 21 displacement data points to provide smoothing of the noisy raw data, at the cost of spatial resolution. Of course, aside from the intrinsic factors such as the correlation algorithm, the resolution also relies on some extrinsic conditions, e.g. image contrast, lighting conditions, performance of the camera, etc. These intrinsic and extrinsic factors almost affect all of the full-field measurement techniques, e.g. the grid method. Nevertheless, the flexibility and apparent ease of use of DIC has made it the preferred technique for most researchers and engineers in experimental mechanics.

2.3.2 The grid method

The grid method is based on the use of a regular grid pattern as opposed to a random speckle pattern. In practice, grids consisting of white and black contrasted lines are bonded onto the specimen surface so as to follow its deformation. Figure 2.16 shows a photo of an aluminium disc specimen on which a 300 μm grid pitch has been bonded.

The image-acquisition system described in Figure 2.15 can also be used to record the images of the undeformed and deformed specimen with grids. As mentioned above, this technique determines the object displacement through comparing the light intensity changes before and after deformation. In the undeformed state, the diffusively reflected light intensity digitised at a given pixel M_0, that corresponds to a material point M determined by the position vector $\vec{R}(x, y)$ in the Cartesian frame, can be written as:

$$I(\vec{R}) = I_0\{1 + \gamma frng[2\pi\vec{F} \cdot \vec{R}]\} \tag{2.4}$$

where

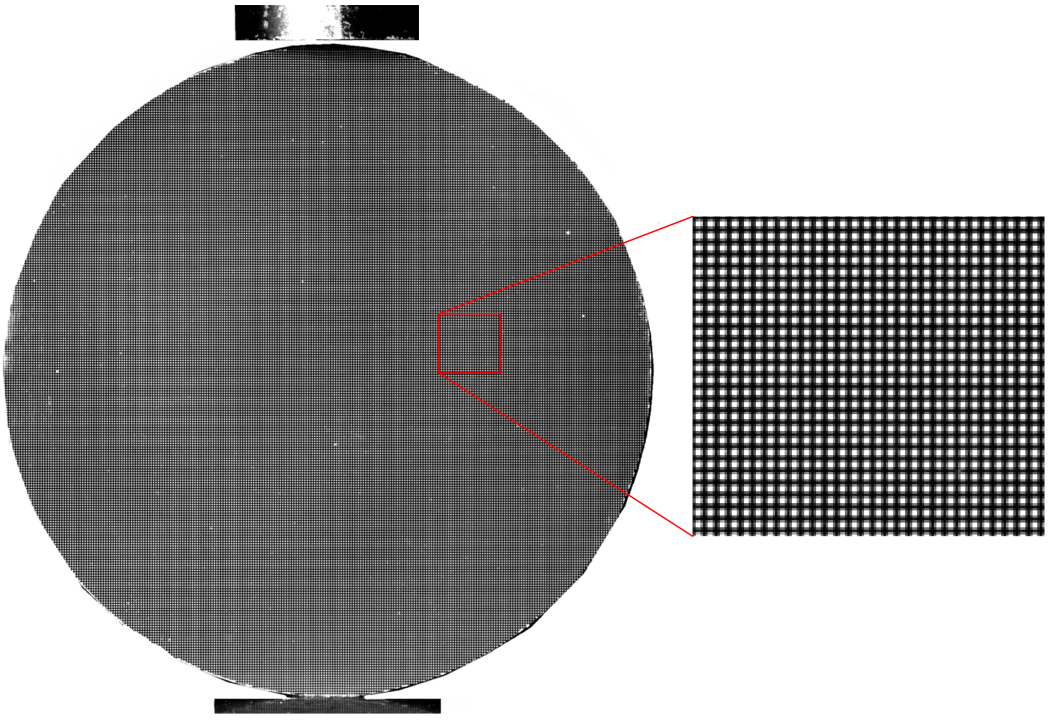

FIGURE 2.16: Photo of the aluminium disc with the grids. Grid pitch: 300 μm.

- I_0 is the intensity bias (or mean intensity);
- γ is the contrast;
- $frng$ is a 2π-periodic continuous function, for instance, a cosine in the simplest case;
- $2\pi\vec{F}\cdot\vec{R}$ contains the phase of function $frng$;
- $\vec{F}$ is the spatial frequency vector. It is orthogonal to the grid lines and its amplitude is the spatial frequency of the grid.

When a load is applied to the specimen, it deforms and so does the grid. The light reflected by point M_0 becomes the light reflected by another point M'. The phase variation of the function $frng$ from the undefromed state to the deformed one is denoted as $-2\pi\vec{F}\cdot\vec{u}(\vec{R})$. $\vec{u}(\vec{R})$ represents the displacement vector including the horizontal $u_x(x,y)$ and vertical $u_y(x,y)$ components. The phase shift can be extracted by the spatial phase shifting method [98, 99]. The relationship between the phase shift and the corresponding displacement is expressed as:

$$u_x(x,y) = -\frac{p}{2\pi}\Delta\phi_x(x,y) \tag{2.5}$$

$$u_y(x,y) = -\frac{p}{2\pi}\Delta\phi_y(x,y) \tag{2.6}$$

where p is the pitch size of the grid and $\Delta\phi$ the phase shift. From the displacement vector, strain components can be computed by spatial differentiation. Correspondingly, for fully time-resolved displacements in dynamics, acceleration fields can be calculated through

second order numerical differentiation over time from the displacements. Similarly, strain rate fields can be obtained through first order differentiation over time from the time-resolved strains. However, these numerical differentiations amplify the noise contained in the measured displacement [100]. Therefore, spatial and temporal smoothing are usually necessary for strain, strain rate and acceleration calculation. To perform spatial smoothing, different methods are available, e.g. polynomial fitting [101, 102], diffuse approximation [103, 104], Gaussian filter [105, 106], etc. For temporal smoothing, a local least-squares algorithm can be applied on a sliding window with fixed number of images to reconstruct the displacement and strain in the form of a polynomial function, for instance. These time-resolved kinematic fields can be further processed with some inverse strategies to identify the material parameters, which will be introduced in the following section.

Many works have been devoted to the reliable estimation of the displacement and strain fields using the grid method [107–111]. A strategy used for deducing the strain without the need for any differentiation of the displacement has been proposed and applied in [107, 110]. Thus, the differential errors can be effectively avoided. However, in some cases, the displacement fields are required. For instance, in this work the displacement is used to calculate the acceleration though double temporal differentiation. As for the achieved resolution using the grid method, Pierron *et al.* reported the resolution of raw displacement with the grid pitch of 0.6 mm (sampling is 5 pixels/pitch) was only 0.15 % of the grid pitch, less than 0.01 pixel [112], which is only a half of the resolution reported in [97]. Using appropriate spatial smoothing, the strain resolution reported in [112] was around 30 microstrains, which is only a fourth of that in [97]. In high strain rate testing, the strains vary from very low to extremely high levels. If the measurement resolution is not good enough, small deformation during the impact events cannot be acquired. Moreover, high noise spoils the further processing and analysis of the full-field data. According to the performance comparison between DIC and the grid method, the later one presents a better compromise between spatial resolution and resolution. In this work, the grid method is used to perform UHS full-field measurements.

2.4 Strategies to identify material parameters based on full-field measurements

Full-field deformation measurements can be used in practice to solve many different types of experimental mechanics problems. As listed in [113, 114], such measurements can be used for non-destructive testing and inspection, verification of boundary conditions, fracture characterisation, reconstruction of residual stresses and identification of

the constitutive parameters among others [113, 114]. This PhD work focuses on the identification of the constitutive parameters of materials.

Unlike conventional strategies relying on statically determinate tests like the uniaxial tensile test, there is no direct link between the full-field strains and the material parameters anymore when more complex test configurations are used. As a consequence, it is necessary to resort to some so-called 'inverse resolution'. With the exponential increase in computational power, a number of strategies based on full-field data have been proposed in the past. Among these methods, the Constitutive Equation Gap Method (CEGM) and the Finite Element Model Updating (FEMU) method do not require full-field data, whereas full-field data is necessary for the Virtual Fields Method (VFM) and the Equilibrium Gap Method (EGM). The rest of this section will be dedicated to a review of these methods.

2.4.1 First group: CEGM & FEMU

The principle of the CEGM is to minimise the gap between the numerical stress field and the stress field computed with the measured strain field and the unknown constitutive parameters. The materials parameters minimising the gap of the two stress fields are considered as the correct ones. This method requires measured displacements, forces and *a priori* information on the stress-free boundaries [115], but full-field data is not necessary because the CEGM can be applied to any kind of over-determined data [116]. FEMU consists in building a finite element model of the mechanical test under study using the information of geometry and boundary conditions. The basis of this method is to minimise the difference between the measured and FE calculated displacements or strain fields through an appropriate cost function. Initial estimated values are used to initiate the optimization process and iterations which is then run until a minimum of the cost function is reached. This method has been used to identify different material models. For instance, linear elastic examples can be found in [117, 118]. Cugnoni *et al.* [119] and Pagnacco *et al.* [120] reported some non-elastic examples of this method. Some applications of this method at high strain rates can also be found in [18, 121, 122], though in [18], no full-field measurement was used for the identification. The main drawback of this method is that it is rather CPU-intensive, as each iteration requires a complete FE analysis [17], particularly for non-linear and high rate dynamic problems where a single FE computation may take tens of minutes or more.

2.4.2 Second group: VFM & EGM

The VFM is suitable for the cases in which the mechanical kinematic fields are available in the region of interest. This method is based on the principle of virtual work which in dynamics and in absence of body forces can be expressed as [28, 57]:

$$-\int_{V_m} \underline{\underline{\sigma}} : \underline{\underline{\varepsilon}}^* dV + \int_{\partial V_m} \vec{T}.\vec{u}^* dS = \int_{V_m} \rho \frac{\partial^2 \vec{u}}{\partial t^2}.\vec{u}^* dV \tag{2.7}$$

where $\underline{\underline{\sigma}}$ represents the Cauchy stress tensor, $\vec{T}$ the Cauchy stress vector acting at the boundary surface ∂V_m, $\vec{u}^*$ a C^0 vectorial function referred to as 'virtual displacement field', $\underline{\underline{\varepsilon}}^*$ the virtual strain tensor derived from $\vec{u}^*$ and ρ the density of the material. '.' denotes the scalar product between vectors whereas ':' represents the contracted product between matrices (or scalar product for matrices). This equation is the integral form of local stress equilibrium. Under quasi-static conditions, the first item at the right-hand side of Equation 2.7 is null.

The basis of the VFM is to exploit Equation 2.7 with particular virtual fields. In the case of linear elasticity, elastic parameters can be identified directly from a linear system which is built up through rewriting Equation 2.7 with as many independent virtual fields as unknowns, provided that the measured kinematic fields are heterogeneous. In the non-linear case, the identification strategy relies on minimising a residual constructed with Equation 2.7 [57]. An important feature of this method is that no iterative finite element calculations are required. Computation times are therefore remarkably low compared to FEMU. This method requires full-field data in the region of interest, which are now more readily available thanks to the specular progress of full-field measurement techniques. As for the force information, the second integral at the left-hand of Equation 2.7 can be written as the product of a resultant force and a constant virtual displacement defined along the boundary where the external force is applied. In other words, the knowledge of the load distribution is by no means necessary. Many examples can be found in the literature (e.g. [123–125] for linear elasticity, [126–129] for elasto-plasticity, etc.). More promisingly, the VFM can be applied to identify the material parameters in dynamics making use of inertial forces without the need for any external measurement [26, 27], which connects to the current work.

As for the EGM, its basis is to build up the constitutive matrix in the form of the product of a scalar contrast which represents the isotropic damage (or the local reduction of stiffness) and an elementary stiffness matrix without damage consideration [116, 130, 131]. If equilibrium is not strictly satisfied, a residual force arises. Finally, the scalar contrast related to the constitutive matrix can be extracted through minimising

the residual force from the knowledge of displacement. The EGM requires full-field displacement measured at a regular grid so that the nodes set up in FE computation are consistent with the measurement points. It is worth mentioning that in EGM is similar to the VFM with particular piecewise virtual fields [132]. More details can be found in [131, 133, 134].

A detailed comparison of the methods mentioned above can be found in [116]. According to this review paper, it was found the identified parameters using these methods were reasonably consistent with the references. Although the identification using the updating methods such as the CEGM and FEMU proved less sensitive to noise, the two methods generally require very large computing times. As for FEMU, the load distribution must be known to feed into the FE model whereas in practice only the global force can be measured. Therefore, it is necessary to predict the loading distribution based on some assumptions. If the assumptions are violated a bias on the identification is likely to happen. Although the displacement from full-field measurements can be used as an alternative boundary conditions in FE simulations, to identify the stiffness components some equations involving force information are still required [57]. The related examples [18, 121, 122] at high strain rates all involved measuring impact forces, meaning that the assumptions necessary to obtain the force from the strain gauge on the Hopkinson bars readings still had to hold. Moreover, some intrinsic uncertainties (e.g. mesh size, time increment, etc.) of the FE calculations will affect the accuracy of the identification as well. Basically, in [135], it was found that FEMU and VFM were equivalent in elasticity. However, the VFM is much faster. The VFM is therefore selected to perform the identification of the material parameters in this PhD work. In the VFM, as in Equation 2.7, under quasi-static conditions, the measured kinematic fields and resultant force are used to identify the material parameters as long as a constant virtual displacement is defined along the boundary where the external force is applied. In dynamics, inertial forces can be used as an alternative load cell to identify the material parameters without the need for any external forces measurement. This methodology will be detailed in the next chapter.

2.5 Strain rate dependence of CFRP

As mentioned in Chapter 1, CFRP composite specimens have been selected here to perform the experimental tests to validate the idea of material parameters identification at high strain rates using inertial forces. In many areas of engineering, composites have been widely used in structures subjected to dynamical loadings, ranging from very low to extremely high loading rates. The response of structures designed with related static

properties might be too conservative or not be safe enough due to the strain rate dependence of composites. Unlike metals which have been investigated extensively over a wide range of strain rates, only limited information is available for fibrous composites. Therefore, more and more studies are being devoted to the investigation of the mechanical behaviour of composites at different strain rates. For quasi-isotropic composites, the stiffness strain rate dependence is very limited [136], whereas for unidirectional composites the mechanical behaviour is significantly strain rate dependent, particularly for stiffness components involving the matrix response, *i.e.*, shear and transverse stiffness components. This section summarises some published work related to the strain rate dependence of CFRP composites.

According to the strain rate dependence of CFRP composites investigated so far, it is widely accepted that the matrix dominated properties (e.g. transverse and shear properties) are more significantly strain rate dependent than the fibre dominated properties (e.g. longitudinal properties). This conclusion is supported by most researchers related to the strain rate effects in CFRP composites. For instance, Gilat *et al.* [6] carried out series of tensile dynamic tests using carbon/epoxy specimens with fibre orientations of 10°, 90°, 45° and $[\pm 45°]_s$. In that work, more significant strain rate dependence on the maximum stress was observed in the tests with the 45° and $[\pm 45°]_s$ specimens. The maximum strain at all strain rates for the $[\pm 45°]_s$ specimens was much higher than that of all the other types of specimens. They concluded that the composite sensitivity to strain rates is driven by the resin behaviour. More published work is summarised in Table 2.1. Here only conclusions about the strain rate dependence of the stiffness/modulus of CFRP composites are summrised.

TABLE 2.1: Summary of published work on strain rate effects of CFRP composites.

References	Materials tested	Strain rates range	Strain rate dependence of stiffness/modulus
Harding *et al.* [137]	0° unidirectional CFRP composites Woven-roving GFRP (0° and 45° respect to the principle reinforcement direction)	Tensile tests between 10^{-4} and 10^{3} s^{-1}	The **longitudinal modulus** were not strain rate dependent A dramatic increase in the initial modulus was observed for 0° GFRP specimens.
Daniel *et al.* [138]	Unidirectional CFRP specimens	Tensile dynamic tests using thin specimens at strain rates up to 500 s^{-1}, expanding ring tests	The **longitudinal modulus** increased moderately (20 % over the quasi-static value) with strain rate, while the **transverse modulus** increased sharply over the related quasi-static values; the **shear modulus** increased moderately (up to 30 % over the quasi-static value) with strain rate.
		Compressive dynamic tests using thin specimens at strain rates up to 210 s^{-1}, modified expanding ring tests	The **longitudinal modulus** increased moderately (30 % over the static value) with strain rate; the **transverse modulus** was significantly strain rate dependent; the **shear modulus** increased moderately (30 % over the quasi-static value) as the strain rate increased.
		Compressive dynamic tests using thick specimens at strain rates up to 80 s^{-1}, drop tower	The **transverse modulus** moderately (18 % over the static value) increased with strain rate.

TABLE 2.1: Summary of published work on strain rate effects of CFRP composites (continued).

References	Materials tested	Strain rates range	Strain rate dependence of stiffness/modulus
Hsiao *et al.* [30, 139]	Unidirectional CFRP and cross-ply composites	Compressive tests from 10^{-4} to 1800 s^{-1}, drop tower and SHPB	For unidirectional composites, the initial **longitudinal modulus** slightly increased with strain rate; the **transverse** properties showed an significantly increase (twofold) in the **modulus** over the quasi-static value; the **shear modulus** showed significant strain rate dependence and the shear stress-strain exhibited high non-linearity. For cross-ply composites, the strain rate sensitivities of the initial modulus was similar to that of longitudinal compression.
Koerber *et al.* [15, 55]	Unidirectional CFRP specimens	Compressive tests from 4.10^{-4} to 367 s^{-1}, SHPB	The **longitudinal modulus** was independent of strain rate, whereas the **transverse** and **shear modulus** both increased as the strain rate increased.
Longana [32]	Unidirectional CFRP specimens	Tensile tests, strain rates up to 62.5 s^{-1}, hydraulic testing machine	The **longitudinal modulus** was slightly strain rate dependent, whereas the **transverse** and **shear moduli** moderately increased by 35 % over the quasi-static values.
Hosur *et al.* [140]	Unidirectional (0°, 90°) and cross-ply CFRP specimens	Compressive tests at quasi-static, 82, 164 and 817 s^{-1}, modified SHPB	The **longitudinal** and **transverse moduli** at high strain rates both considerably increased compared to the quasi-static values
Melin *et al.* [141]	Unidirectional CFRP specimens	Transverse tensile tests from the quasi-static to 800 s^{-1}, SHPB	The average **transverse modulus** was independent of strain rate, and the **initial transverse modulus** decreased slightly with strain rate

For high rates tensile testing of fibre reinforced polymeric (FRP) composites, significant longer test specimens are required making the attainment of stress equilibrium across the specimen more difficult. Moreover, because the failure strain of composites is significantly smaller than that of metallic materials, the accurate determination of strain is more critical. For these reasons, Harding *et al.* added an input bar to the standard tensile Hopkinson bar [137]. Three strain gauges were attached at different positions (two were on the input bar and one was on the output bar) to monitor the incident and reflected waves. Reconstructed stress at two ends of the specimen proved identical and confirmed the validity of equilibrium across the specimen. Finally, the modulus, fracture strength and strain were obtained. To performed high rates tensile tests using Hopkinson bar, Melin *et al.* connected specimens to two split bars using steel bolts. Thus, a compensation signal must be considered for changes in the mechanical impedance which occurred at the capings and the steel bolts [141].

Aside from the Hopkinson bar approach, Daniel *et al.* used (modified) expanding ring tests to perform compressive and tensile tests at high strain rates [138]. In this example, they used thin ring specimens under internal (for tensile tests) and external (for compressive tests) pressure to minimise the wave propagation in the specimens. However, expanding ring tests is expensive and complex and cannot be used for thick specimens. More details about the expanding tests can be found in the cited paper. Hsiao *et al.* [30, 139] employed drop-tower and SHPB to perform high rates compression tests. In drop-tower tests, in order to obtain accurate signal, they placed rubber sheets over the top end cap of specimens to minimise ringing due to impact. Moreover, a fibre-cork vibration damping system (as seen in Figure 2.2) was placed between the floor and the drop-tower set-up to attenuate the transmitted waves. In SHPB tests, they placed a small rubber sheet at the striker/bar interface to increase the pulse rise time and the uniformity of loading. Moreover, this rubber sheet reduced oscillations and provided more uniform strain rates. To minimise frictional effects in SHPB tests, the specimen/bar interface was lapped to facilitate stress wave transmission and lubricated. For transverse and in-plane shear tests, similar to Hsiao's work, Koerber *et al.* [15] used copper pulse shapers to obtain constant strain rates, meanwhile, to minimise dispersion effects and establish dynamic equilibrium throughout the impact tests. High-speed camera was used to obtain the full-field deformation on the specimen surface. Using appropriate configuration, they verified the basic assumptions of SHPB tests described in Section 2.1 were fulfilled. For longitudinal high rates compression tests, Koerber *et al.* [55] used a special dynamic compression fixture to align and stabilise the thin rectangular specimens of thickness 1.5 mm. They observed the strain measured directly from strain gauges on the specimen was better than that from SHPB analysis.

In the conventional SHPB technique, if the specimen does not fail during the loading by the initial compressive pulse, it will be subjected to repeated loading by the wave in the incident bar, leading to difficulty in post-processing of experimental data, especially the microscopic analysis. To avoid repeated loading, Hosur *et al.* proposed a SHPB set-up in which the incident bar with transfer flange at the loading end was combined with an incident tube and a reaction mass. After the initial compression loading, the incident bar was loaded by the reflected wave in tension to avoid repeated loading on the specimen, more details about this modified set-up can be found in [140].

As summarised in Table 2.1, most of these examples conclude that the longitudinal modulus is slightly (or not) sensitive to strain rate, and the transverse and shear moduli are more strain rate dependent, although Hosur *et al.* and Melin *et al.* reported opposed conclusions to the majority. The discrepancy might be attributed to different testing conditions, experimental techniques and strain rate ranges covered in these examples. Another thing is the specimen size effects and fibre diameters [142–145], Kim *et al.* [146] reported that the size of the fibre diameter affected the strain rate dependence of the tensile strength of E-glass. The size effect is expected to affect the mechanical properties of other fibrous composites as well. In the previous examples, different set-ups (hydraulic machines, drop-tower and SHPB) were used to perform the mechanical tests, however, the identification of material parameters and other analysis in these examples were all based on the stress-strain curves, stringently relying on uniform strain assumption in the specimen. Additionally, to reconstruct stress/strain histories accurately in SHPB, the assumptions of no inertial effects and no wave dispersion are required. These assumptions are more easily violated in high strain rate testing of composites. Although different modifications and improvements (e.g. pulse shaper, special compression fixture, etc.) have been carried out in the these examples, only simple uniaxial tests with small specimens were involved. These modified set-ups cannot be used to carry out high strain rate testing of materials with complex shapes or non-uniform loading. This motivates the present work to develop a more general experimental procedure for high strain rate testing, which allows to identify the material parameters from heterogeneous tests making use of inertial effects as a load cell without the need for any impact force measurement. This will be detailed in the following chapters.

2.6 Summary

In this chapter, the main high strain rate testing techniques were first recalled. Advantages and disadvantages of these techniques can be clearly seen. Owing to the dramatic advances in full-field measurements and UHS imaging, it is now possible to perform

UHS full-field measurements. The available full-field measurement techniques and UHS cameras were then comparatively reviewed. The grid method presents a better compromise between spatial resolution and strain resolution. Some available inverse strategies used to identify the material parameters from full-field heterogeneous data were sequentially reviewed. Among these inverse strategies, considering the computational time and availability of full-field information, the VFM was used to identify the parameters. Here, kinematic quantities measured at very high rates using the grid method were fed into the VFM to identify material parameters. This procedure does not require any external force measurement, which potentially relieves the limitations (e.g. no inertial effects, uniform stress/strain state, etc.) of current high strain rate testing techniques. In this PhD work, linear elasticity is considered as a first step to validate this methodology. It should be underlined that low strain linear elasticity is where current SHPB techniques are lacking because of inertia effects, although the SHPB has often been applied to the plasticity where inertial effects are not a problem anymore. As the strains are small, it is also a challenging task to measure displacements and derive strains and acceleration in a quantitative way to feed into the identification procedure. So this is an excellent test case to validate the present methodology before moving on to non-linear constitutive models. Here, CFRP composite specimens have been selected to perform experimental tests for validating the identification of isotropic/orthotropic linear elastic parameters at high strain rates. Therefore, the high-strain-rate mechanical behaviour of CFRP composites investigated so far was briefly surveyed at the end of this chapter. The following chapters present the identification method in more detail before moving on to numerical validation and experimental implementation.

Chapter 3

The Virtual Fields Method with inertial effects

In this chapter, a new methodology based on the principle of virtual work (the so-called Virtual Fields Method or VFM) is introduced, which makes use of inertial forces (acceleration) to identify the material parameters at high strain rates from heterogeneous fields without the need for any impact forces measurement. This methodology potentially relieves the constraints and assumptions of current test approaches. This chapter first explains why acceleration can be used as an alternative load cell. Then, the VFM equations are presented for simple linear elastic problems. Extensions to strain rate dependent and non-linear models are then provided. Finally, a particular VFM resolution based on a general over-determined system of equations is proposed.

3.1 Acceleration as a load cell

In order to explain the concept of using acceleration as a load cell in the material identification process, a simple test configuration is considered as in Figure 3.1. A time-dependent external force is applied on the right end of a thin specimen of thickness h, supposing the material is homogeneous and its density is denoted as ρ. L and b are the length and width of the specimen respectively. A load cell used to measure the external force is mounted at the other end.

According to Newton's law, one can write:

$$F_x(t) + F_x^{'}(t) = \rho h \int_0^L \int_{-b/2}^{b/2} a_x(x, y, t) dx dy \tag{3.1}$$

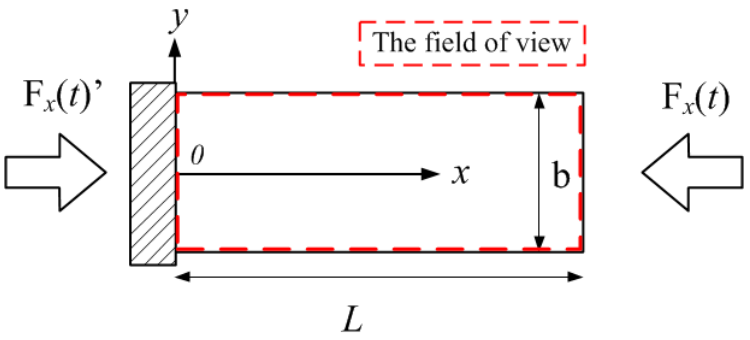

FIGURE 3.1: Schematic of the dynamic test with a load cell. L and b are the length and width of the specimen respectively.

where x and y are the coordinates of the field of view, F_x and $F_x^{'}$ are the applied external force and the force measured through the load cell at a certain time respectively, a_x is the longitudinal acceleration at the same time. The two forces at the left-hand side in Equation 3.1 can be expressed as:

$$\begin{aligned} F_x(t) &= h \int_{-b/2}^{b/2} \sigma_x(x = L, y, t) dy \\ F_x^{'}(t) &= -h \int_{-b/2}^{b/2} \sigma_x(x = 0, y, t) dy \end{aligned} \tag{3.2}$$

In order to simplify the writing of the equations, the time variable will be omitted in the rest of this PhD thesis but all mechanical fields in dynamics do depend on time even if time is not mentioned. In practice, full-field deformation of the specimen is measured at a large number of spatially discrete areas of identical sizes. Thus, if the spatial density of these discrete measurements is high enough, the right-hand item in Equation 3.1 can be approximated as:

$$\rho h \int_0^L \int_{-b/2}^{b/2} a_x(x, y, t) dx dy \approx \rho L b h \overline{a_x(x, t)} \tag{3.3}$$

where $\overline{a_x}$ is the spatial average of the x-component of acceleration over the region of interest. Consequently, Equation 3.1 can be rewritten as:

$$F_x + F_x^{'} = m\overline{a_x} \tag{3.4}$$

where m represents the mass of the specimen.

Combining Equations 3.2 and 3.4, if the force $F_x^{'}$ in Figure 3.1 and the full-field acceleration maps are measured simultaneously, at any transverse slice along the x-axis there

exists a local equation as:

$$bh\overline{\sigma_x(x,t)} = \rho x bh\overline{a_x(x,t)} - F_x^{'} \tag{3.5}$$

where $\overline{\sigma_x(x,t)}$ is the average longitudinal stress over the transverse slice of interest along the longitudinal axis of the specimen and $\overline{a_x(x,t)}$ represents the spatial average longitudinal acceleration over the area between the free end and the transverse slice of interest.

Equation3.5 means that as long as the force at either end (for instance, $F_x^{'}$ in Figure 3.1) and the full-field acceleration maps are measured simultaneously, the average longitudinal stress profiles can be constructed at any transverse slice along the x-axis, provided the material density is known. With the reconstructed stress and the corresponding average strain calculated from the measured strain over the same slice, local stress-strain curves can be plotted for each slice. In this way, the elastic modulus can be extracted from these curves without the need for any *a priori* constitutive model, hence the term 'non-parametric'. This concept was proposed by Othman *et al.* for the first time [25]. Pierron *et al.* [26] also used this concept to reconstruct the local stress-strain curves and to derive the tensile strength value with simple uniaxial spalling tests on concrete. In [26] the loading condition of the specimen is equivalent to that in Figure 3.1 with $F_x{}'(x=0)=0$. Thus, Equation 3.5 can be simplified as:

$$\overline{\sigma_x(x,t)} = \rho x\overline{a_x(x,t)} \tag{3.6}$$

Obviously, the average stress profiles at any position along the longitudinal axis of the specimen can be reconstructed from the acceleration field without the need for any force measurement. Consequently, the stress-strain curves at any position can be plotted and used to extract the elastic modulus. Although this method is simple, it is usually suitable for uniaxial tests. Moreover, if the loads at both ends of the specimen are unknown, Equation 3.4 would involve two unknowns, which would be useless. However, it is possible to extend this analysis by introducing the principle of virtual work.

3.2 The Virtual Fields Method with inertial forces

Equation 2.7 described the principle of virtual work in dynamics and in absence of body force for a given solid of volume V_m. However, most full-field measurement techniques only provide deformation over the external surface of the solid. Therefore, specimens need to be designed so that the surface response is representative of the volume response, which is however standard for material testing. Typically, a thin plate under plane stress

assumption is usually employed. In case of an in-plane test, if h is the thickness of the volume V_m and S the associated planar surface, Equation 2.7 reduces to a $2D$ situation as:

$$-h\int_S \underline{\underline{\sigma}}:\underline{\underline{\varepsilon}}^* dS + h\int_{\partial S} \vec{T}.\vec{u}^* dL = h\int_S \rho\vec{a}.\vec{u}^* dS \tag{3.7}$$

where $\vec{a}$ represents the acceleration vector ($\vec{a} = \frac{\partial^2\vec{u}}{\partial t^2}$). In above equation, the first item at the left-hand side of the equation is called the 'internal virtual work', the second item the 'external virtual work' and the first item at the right-hand side the 'acceleration virtual work'. From Equation 3.7, it is possible to produce Equation 3.4 considering the following virtual field:

$$VF\ 1: \quad \begin{cases} u_x^{*(1)} = 1 \\ u_y^{*(1)} = 0 \end{cases} \quad \begin{cases} \varepsilon_x^{*(1)} = 0 \\ \varepsilon_y^{*(1)} = 0 \\ \varepsilon_s^{*(1)} = 0 \end{cases} \tag{3.8}$$

Consequently, the internal virtual work in Equation 3.7 is zeroed out due to the null virtual strain field. Referring back to the case in Figure 3.1, the external virtual work produced by F_x and $F_x^{'}$ at both ends of the specimen equals to $F_x + F_x^{'}$ because $u_x^* = 1$ and the acceleration virtual work only depends on the longitudinal component because $u_y^* = 0$. Thus, the same expression as in Equation 3.4 can be obtained. Similarly, a shear force and moment profiles can also be reconstructed using virtual fields described in Equations 3.9 and 3.10 respectively (though these were not used in this work):

$$VF\ 2: \quad \begin{cases} u_x^{*(2)} = 0 \\ u_y^{*(2)} = 1 \end{cases} \quad \begin{cases} \varepsilon_x^{*(2)} = 0 \\ \varepsilon_y^{*(2)} = 0 \\ \varepsilon_s^{*(2)} = 0 \end{cases} \tag{3.9}$$

$$VF\ 3: \quad \begin{cases} u_x^{*(3)} = y \\ u_y^{*(3)} = -x \end{cases} \quad \begin{cases} \varepsilon_x^{*(3)} = 0 \\ \varepsilon_y^{*(3)} = 0 \\ \varepsilon_s^{*(3)} = 0 \end{cases} \tag{3.10}$$

The procedure of reconstructing the stress profiles from the acceleration for identifying Young's modulus E is simple, but it is only restricted in some simple uniaxial tests. For fully heterogeneous cases, this procedure will not enable direct identification of E. A more general procedure is therefore introduced below.

If a plane stress applied on an orthotropic material, according to Hooke's Law, the relationship between Cauchy stress and linear strain in the fibre orientation coordinate

system can be expressed by:

$$\begin{Bmatrix} \sigma_1 \\ \sigma_2 \\ \sigma_6 \end{Bmatrix} = \begin{bmatrix} Q_{11} & Q_{12} & 0 \\ Q_{12} & Q_{22} & 0 \\ 0 & 0 & Q_{66} \end{bmatrix} \begin{Bmatrix} \varepsilon_1 \\ \varepsilon_2 \\ \varepsilon_6 \end{Bmatrix} \tag{3.11}$$

where Q_{ij}'s are the stiffness matrix components in the fibre coordinate system, σ_i's and ε_i's the stress and strain components and subscripts 1, 2 and 6 represent the longitudinal, transverse and shear components (engineering shear component for strain) in the fibre orientation coordinate system, respectively. For the orthotropic constitutive model, one needs to define the global coordinate system. A schematic of the global and fibre orientation coordinates systems are shown in Figure 3.2. The $x-y$ plane is the global coordinate system and ϑ represents the off-axis fibre angle. If the material is isotropic, the following relations exist between the stiffness components:

$$\begin{cases} Q_{11} = Q_{22} \\ Q_{66} = \frac{Q_{11}-Q_{12}}{2} \end{cases} \tag{3.12}$$

Thus, the isotropic linear elastic constitutive equation only depends on two independent parameters Q_{11} and Q_{12}. In this work, the two isotropic stiffness components Q_{11} and Q_{12} are substituted by Q_{xx} and Q_{xy} respectively. The two components are related to Young's modulus E and Poisson's ratio ν through:

$$\begin{cases} \nu = Q_{xy}/Q_{xx} \\ E = Q_{xx}(1-\nu^2) \end{cases} \tag{3.13}$$

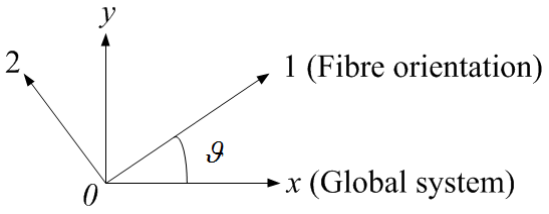

FIGURE 3.2: Global (specimen-related) and fibre orientation (material-related) coordinate systems.

For a $2D$ isotropic linear elastic model, supposing the stiffness component is constant in the specimen, and Equation 3.7 can be unfolded and simplified as:

$$Q_{xx}\int_S(\varepsilon_x\varepsilon_x^* + \varepsilon_y\varepsilon_y^* + \frac{1}{2}\varepsilon_s\varepsilon_s^*)dS + Q_{xy}\int_S(\varepsilon_x\varepsilon_y^* + \varepsilon_y\varepsilon_x^* - \frac{1}{2}\varepsilon_s\varepsilon_s^*)dS = \int_{\partial S} T_i u_i^* dL - \int_S \rho a_i u_i^* dS;\ i \in (x,y) \tag{3.14}$$

where stiffness components Q_{xx} and Q_{xy} are unknown, while strain and acceleration can be derived from the full-field displacement measurements through spatial and temporal differentiation respectively. The external forces T can be measured though load cells. However, at high strain rates the external force measurement is not easy to perform because of inertial effects. To identify the two unknowns in Equation 3.14, two independent virtual fields are necessary.

Considering the case in Figure 3.1 again, if the forces F_x and $F_x^{'}$ are unknown, the procedure described in Section 3.1 is invalid. However, in the VFM, if a virtual field is defined as:

$$VF\ 4: \quad \begin{cases} u_x^{*(4)} = x(x-L) \\ u_y^{*(4)} = 0 \end{cases} \quad \begin{cases} \varepsilon_x^{*(4)} = 2x - L \\ \varepsilon_y^{*(4)} = 0 \\ \varepsilon_s^{*(4)} = 0 \end{cases} \tag{3.15}$$

The virtual displacement components along the left and right boundaries ($x = 0$ and $x = L$) of the field of view are zeroed. Thus, the external virtual work in Equation 3.14 is cancelled out:

$$Q_{xx}\int_S (2x-L)\varepsilon_x dS + Q_{xy}\int_S (2x-L)\varepsilon_y dS = -\int_S \rho a_x x(x-L)dS \tag{3.16}$$

In Equation 3.16, the external forces are not involved, instead, the acceleration plays the role of 'load cell' to provide force information. To solve for the two unknowns Q_{xx} and Q_{xy}, a second independent virtual field has to be defined, for instance:

$$VF\ 5: \quad \begin{cases} u_x^{*(5)} = sin(\frac{x}{L}\pi) \\ u_y^{*(5)} = 0 \end{cases} \quad \begin{cases} \varepsilon_x^{*(5)} = \frac{\pi}{L}cos(\frac{x}{L}\pi) \\ \varepsilon_y^{*(5)} = 0 \\ \varepsilon_s^{*(5)} = 0 \end{cases} \tag{3.17}$$

Similarly, Equation 3.14 can be rewritten as:

$$Q_{xx}\int_S \frac{\pi}{L}cos(\frac{x}{L}\pi)\varepsilon_x dS + Q_{xy}\int_S \frac{\pi}{L}cos(\frac{x}{L}\pi)\varepsilon_y dS = -\int_S \rho a_x sin(\frac{x}{L}\pi)dS \tag{3.18}$$

Combining Equations 3.16 and 3.18, a linear system can be built up as:

$$\mathbf{AQ} = \mathbf{B} \tag{3.19}$$

$$\mathbf{A}: \begin{bmatrix} \int_S (2x-L)\varepsilon_x dS & \int_S (2x-L)\varepsilon_y dS \\ \int_S \frac{\pi}{L}cos(\frac{x}{L}\pi)\varepsilon_x dS & \int_S \frac{\pi}{L}cos(\frac{x}{L}\pi)\varepsilon_y dS \end{bmatrix}$$

$$\mathbf{Q}: \left\{ \begin{array}{c} Q_{xx} \\ Q_{xy} \end{array} \right\}; \quad \mathbf{B}: \left\{ \begin{array}{c} -\int_S \rho a_x x(x-L) dS \\ -\int_S \rho a_x sin(\frac{x}{L}\pi) dS \end{array} \right\};$$

Since **A** and **B** can be evaluated from the full-field strain and acceleration measurements, **Q** can be directly obtained by inversion of the system (if the virtual fields are selected so that **A** is invertible), without the need for any iterative scheme as would be necessary with FEMU. This is one of the strengths of the VFM.

To deliver the potential of this methodology, the case described in [26] is recalled here, as seen in Figure 3.3. In this case, the left end of the specimen is free and an unknown impact load is applied at the right end of the specimen to produce inertial impact excitation. As per the above discussion, this analysis does not need to measure the impact force only acceleration (inertial force) and strains.

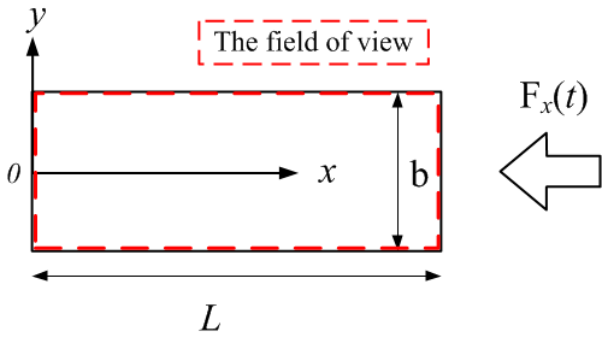

FIGURE 3.3: Schematic of the dynamic inertial impact test.

Similarly, to identify the two isotropic stiffness components, two independent virtual fields are necessary where the virtual displacement at the right boundary of the field of view must be zeroed so that the virtual work of the unknown impact force can be cancelled out. For instance, two virtual fields for this case can be defined as follows:

$$VF\ 6: \quad \left\{ \begin{array}{l} u_x^{*(6)} = x - L \\ u_y^{*(6)} = 0 \end{array} \right. \quad \left\{ \begin{array}{l} \varepsilon_x^{*(6)} = 1 \\ \varepsilon_y^{*(6)} = 0 \\ \varepsilon_s^{*(6)} = 0 \end{array} \right. \tag{3.20}$$

$$VF\ 7: \quad \left\{ \begin{array}{l} u_x^{*(7)} = cos(\frac{x}{2L}\pi) \\ u_y^{*(7)} = 0 \end{array} \right. \quad \left\{ \begin{array}{l} \varepsilon_x^{*(7)} = -\frac{\pi}{2L} sin(\frac{x}{2L}\pi) \\ \varepsilon_y^{*(7)} = 0 \\ \varepsilon_s^{*(7)} = 0 \end{array} \right. \tag{3.21}$$

The impact case described in Figure 3.3 is reasonably easy to perform in practice. It does not require cumbersome devices like the SHPB system, neither does it require

impact force measurement. It just requires the strain and acceleration at the surface of the specimen derived from the displacement measured using digital cameras with sufficient spatial and temporal resolution. Fortunately, recent ultra-high speed cameras can provide the required level of performance to use this analysis in practice, as is demonstrated in Chapter 6.

Actually, there is infinite of virtual fields can be defined to solve unknown stiffness components in Equation 3.14. If the strain and acceleration data are exact, any set of virtual fields will lead to the same identification. However, if the data are corrupted by noise, which is unavoidable in experimental tests, different virtual fields will provide varied results. In this case, if these virtual fields are selected intuitively, it is impossible to ensure that the selected virtual fields are the best ones. However, a special optimised virtual fields procedure proposed in [147, 148] can automatedly select the virtual fields which lead to the unique maximum likehood solution based on some special conditions. In Equation 3.19 if matrix $\mathbf{A}$ equals the identity matrix $\mathbf{I}$, the solution to the linear system can be straightforward since $\mathbf{A^{-1}} = \mathbf{I}$. This is so-called 'special conditions', as shown below:

$$\mathbf{Q} = \mathbf{A}^{-1}\mathbf{B} = \mathbf{B} \tag{3.22}$$

The virtual field can be expanded using various types of functions such as polynomials or piecewise functions. Under quasi-static conditions, an automated optimised piecewise virtual fields relying on the application of the VFM with the special virtual fields has been developed in [148], which enables to minmise noise effect and to select the best virtual fields. The present work attempts to extend this optimised procedure to the case of dynamics. The detailed derivations for different constitutive models is presented in the rest of this section.

3.2.1 Noise minimization: the Isotropic linear elastic case

For the sake of simplicity, an isotropic linear elastic model is first considered. In practice, the strain and acceleration fields are both noisy. For the strain, the noise level is amplified by spatial differentiation from the displacement, while the noise of acceleration is amplified by double temporal differentiation. However, the noise in strain proved more critical than that in acceleration. This was investigated numerically: a simulated displacement field was produced by ABAQUS. Then, a Gaussian white noise was added into the (simulated) exact displacement field. The acceleration and strain fields were both calculated from the exact and noisy displacement fields. It was found that the virtual work produced by the noise in the strain was significantly higher than that in

the acceleration. This is not a general result however, it arises from the fact that acceleration levels are very high in the presently considered tests. Therefore, in the rest of this PhD thesis, only noise in the strain is considered.

The measured strain components can be written as the sum of their exact values and a noise component. Particular virtual fields are selected here so as to cancel out the virtual work of the external forces. This is referred to as 'virtual boundary conditions' in the rest of the text. Supposing the material is homogeneous, thus, Equation 3.7 becomes:

$$\begin{aligned} Q_{xx}\int_S[(\varepsilon_x-\gamma\mathfrak{N}_x)\varepsilon_x^*+(\varepsilon_y-\gamma\mathfrak{N}_y)\varepsilon_y^*+\frac{1}{2}(\varepsilon_s-\gamma\mathfrak{N}_s)\varepsilon_s^*]dS+... \\ Q_{xy}\int_S[(\varepsilon_x-\gamma\mathfrak{N}_x)\varepsilon_y^*+(\varepsilon_y-\gamma\mathfrak{N}_y)\varepsilon_x^*-\frac{1}{2}(\varepsilon_s-\gamma\mathfrak{N}_s)\varepsilon_s^*]dS=-\int_S\rho a_i u_i^* dS \end{aligned} \tag{3.23}$$

where $\mathfrak{N}_i$'s represent the zero-mean normalised Gaussian noise for the three strain components, ε_i are the measured strain components and γ is the standard deviation of the strain noise. As stated before, the noise effect of acceleration has been neglected.

To identify the two parameters in Equation 3.23, two independent virtual fields satisfying the virtual boundary conditions and the special conditions are necessary. In this work, bilinear finite elements are used to expand the virtual fields. More details can be found in [28, 132]. For instance, a special virtual field $u^{*(1)}$ provides Q_{xx}:

$$\begin{aligned} Q_{xx}=\gamma[Q_{xx}\int_S(\mathfrak{N}_x\varepsilon_x^{*(1)}+\mathfrak{N}_y\varepsilon_y^{*(1)}+\frac{1}{2}\mathfrak{N}_s\varepsilon_s^{*(1)})dS+... \\ Q_{xy}\int_S(\mathfrak{N}_x\varepsilon_y^{*(1)}+\mathfrak{N}_y\varepsilon_x^{*(1)}-\frac{1}{2}\mathfrak{N}_s\varepsilon_s^{*(1)})dS]-\int_S\rho a_i u_i^{*(1)}dS \end{aligned} \tag{3.24}$$

Similarly, Q_{xy} can be determined by another special field $u^{*(2)}$:

$$\begin{aligned} Q_{xy}=\gamma[Q_{xx}\int_S(\mathfrak{N}_x\varepsilon_x^{*(2)}+\mathfrak{N}_y\varepsilon_y^{*(2)}+\frac{1}{2}\mathfrak{N}_s\varepsilon_s^{*(2)})dS+... \\ Q_{xy}\int_S(\mathfrak{N}_x\varepsilon_y^{*(2)}+\mathfrak{N}_y\varepsilon_x^{*(2)}-\frac{1}{2}\mathfrak{N}_s\varepsilon_s^{*(2)})dS]-\int_S\rho a_i u_i^{*(2)}dS \end{aligned} \tag{3.25}$$

If the noise source is not taken into account in Equations 3.24 and 3.25, the identified stiffness components are not exact and are denoted Q_{xx}^{app} and Q_{xy}^{app}. According to Equations 3.19 and 3.22, the two approximate components are defined by:

$$\begin{cases} Q_{xx}^{app}=-\int_S\rho a_i u_i^{*(1)}dS \\ Q_{xy}^{app}=-\int_S\rho a_i u_i^{*(2)}dS \end{cases} \tag{3.26}$$

The standard deviation of noise, γ, is assumed to be much smaller than the norm of the strain components. Thus, the actual values of stiffness components can be substituted by their approximate counterparts. The variance of each stiffness components can expressed

as follows:

$$V(Q_{ij}) = E([Q_{ij} - E(Q_{ij})]^2) \tag{3.27}$$

In practice, the measured data are discrete. Therefore, integral above must be discretized at each data point. Because of the autocorrelation of functions $\mathfrak{N}_i$ $(i = x, y, s)$, finally, the variances of Q_{xx} and Q_{xy} can be simplified and written as:

$$\begin{cases} V(Q_{xx}) = \gamma^2(\frac{S}{n})^2 \mathbf{Q^{app}}.\mathbf{G^{(1)}}\mathbf{Q^{app}} \\ V(Q_{xy}) = \gamma^2(\frac{S}{n})^2 \mathbf{Q^{app}}.\mathbf{G^{(2)}}\mathbf{Q^{app}} \end{cases} \tag{3.28}$$

where S is the area of the specimen, n the number of strain data points and $\mathbf{G}^{(i)}$ $(i = 1, 2)$ is a square matrix detailed in Appendix B.

Variable η is defined as follows:

$$(\eta^{(i)})^2 = (\frac{S}{n})^2 \mathbf{Q^{app}}.\mathbf{G^{(i)}}\mathbf{Q^{app}} \tag{3.29}$$

Thus, the variances of Q_{xx} and Q_{xy} becomes:

$$\begin{cases} V(Q_{xx}) = (\eta^{(1)})^2\gamma^2 \\ V(Q_{xy}) = (\eta^{(2)})^2\gamma^2 \end{cases} \tag{3.30}$$

This equation is interesting as it linearly connects the variances of the identified parameters, $V(Q_{xx})$ and $V(Q_{xy})$, to the variance of the noise gamma. The coefficients of proportionality, $\eta^(1)$ and $\eta^(2)$ can be seen as noise sensitivity factors. The lower the η parameters, the lower the variances of the identified parameters for a same noise level. Therefore, the best virtual fields are those for which the η parameters are minimal. This requires the minimization of the quantity defined in Equation 3.29. The $\mathbf{G}$ matrix depends on the virtual fields. If expanded over a given set of functions, here, piecewise finite elements, then the virtual degrees of freedom appear in matrix $\mathbf{G}$. The objective is therefore to find the set of virtual degrees of freedom minimizing η in Equation 3.29. This is a minimization problem under the constraints imposed by virtual boundary conditions and specialty conditions. To solve this problem here, the method of Lagrange multipliers is used [149, 150]. With these virtual fields minimising the variances, the stiffness components can be calculated according to Equations 3.19 and 3.22. More detailed derivations of the optimized virtual fields for the isotropic linear elastic model can be found in Appendix B and in [28] where a tutorial is provided on specific examples.

This optimised procedure provides not only the the stiffness components but also the minimum η which indicates the noise sensitivity of each identified stiffness component

[148]. However, in practice, the ratios of the different η_{ij}'s by their corresponding stiffness components Q_{ij}'s are considered. This corresponds to dimensionless coefficients of variation which make it easier to compare scatter on the different stiffness components which can be of very different magnitudes, particularly in the orthotropic case next. To validate the noise minimisation procedure, simulated strain components are disturbed by an additive Gaussian white noise with increasing standard deviation γ. The coefficients of variation of the identified stiffness components at different noise levels can be plotted as a function of the standard deviation of strain noise. This plot should provide a straight line for each stiffness components of which slope should be equal to the η/Q values provided by the noise optimization procedure. This validation will be presented in Chapter 4.

3.2.2 Noise minimization: the orthotropic linear elastic case

For the orthotropic linear elastic model, an off-axis lamina is more general case. The global and fibre orientation coordinate systems has been shown in Figure 3.2. In global coordinate system, the relationship between stress and strain can be expressed as:

$$\begin{Bmatrix} \sigma_x \\ \sigma_y \\ \sigma_s \end{Bmatrix} = \begin{bmatrix} Q_{xx} & Q_{xy} & Q_{xz} \\ Q_{xy} & Q_{yy} & Q_{yz} \\ Q_{xz} & Q_{yz} & Q_{ss} \end{bmatrix} \begin{Bmatrix} \varepsilon_x \\ \varepsilon_y \\ \varepsilon_s \end{Bmatrix} \tag{3.31}$$

where $\mathbf{Q}$ represents the stiffness matrix in the global system and the subscripts x, y and s describe the three stress/strain components in the global system. The main difference with Equation 3.11 is the well-known shear-extension coupling arising from Q_{xz} and Q_{yz} in Equation 3.31, leading to difficulty in identifying the six stiffness components. In practice, the identification of the orthotropic parameters often happens in the fibre coordinate system. As in Equation 3.11, the relationship of stress and strain in the fibre coordinate system only involves four independent stiffness components.

To identify the four independent stiffness components in the fibre orientation system, all quantities in Equation 3.7 must be transformed to the fibre coordinate system. It is worth emphasising that virtual fields must be built up in the global system first and then transformed into the fibre orientation system, because the virtual boundary conditions are defined in the global system.

If $\vec{D_g}$ and $\vec{D_f}$ are vectors representing the force (or displacement or acceleration) vectors in the global and fibre systems respectively, the relationship between them can be

expressed as:

$$\vec{D}_f = C\vec{D}_g \tag{3.32}$$

where C is the transformation matrix from the global system to fibre system:

$$C = \begin{bmatrix} c & s \\ -s & c \end{bmatrix} \; with \; c = cos(\vartheta) \; and \; s = sin(\vartheta) \tag{3.33}$$

In the fibre orientation coordinate system, the external virtual work in Equation 3.7 can be written as:

$$\begin{aligned} h\int_L \vec{T}_f.\vec{u}_f^* dL &= h\int_L [(c^2+s^2)T_{1g}u_{1g}^* + (c^2+s^2)T_{2g}u_{2g}^*]dL \\ &= h\int_L (T_{1g}u_{1g}^* + T_{2g}u_{2g}^*)dL \\ &= h\int_L \vec{T}_g.\vec{u}_g^* dL \end{aligned} \tag{3.34}$$

Similarly, the acceleration virtual work in Equation 3.7 can be expressed as follows:

$$h\int_S \rho\vec{a}_f.\vec{u}_f^* dS = h\int_S \rho\vec{a}_g.\vec{u}_g^* dS \tag{3.35}$$

Thus, if the orthotropic stiffness components are not strain rate dependent, with particular virtual fields to cancel out the virtual work of the external forces, Equation 3.7 can be unfolded and simplified in the fibre orientation system as:

$$\begin{aligned} Q_{11}\int_S \varepsilon_1\varepsilon_1^* dS + Q_{12}\int_S (\varepsilon_1\varepsilon_2^* + \varepsilon_2\varepsilon_1^*)dS + Q_{22}\int_S \varepsilon_2\varepsilon_2^* dS + Q_{66}\int_S \varepsilon_6\varepsilon_6^* dS \\ = -\int_S \rho a_i u_i^* dS \end{aligned} \tag{3.36}$$

All quantities in Equation 3.36 are expressed in the fibre orientation system, however, as in Equation 3.35, the virtual work of acceleration in the fibre orientation system equals that in the global system. To identify four independent orthotropic stiffness components, four independent virtual fields are required and expanded here using bilinear finite elements as well. Similarly, if only the strain noise is considered here, Equation 3.36 can be rewritten as:

$$\begin{aligned} Q_{11}\int_S (\varepsilon_1 - \gamma\mathfrak{N}_1)\varepsilon_1^* dS + Q_{12}\int_S [(\varepsilon_1 - \gamma\mathfrak{N}_1)\varepsilon_2^* + (\varepsilon_2 - \gamma\mathfrak{N}_2)\varepsilon_1^*]dS + \\ Q_{22}\int_S (\varepsilon_2 - \gamma\mathfrak{N}_2)\varepsilon_2^* dS + Q_{66}\int_S (\varepsilon_6 - \gamma\mathfrak{N}_6)\varepsilon_6^* dS = -\int_S \rho a_i u_i^* dS \end{aligned} \tag{3.37}$$

The general procedure to identify the four orthotropic parameters is the same as that for the isotropic linear elastic model except that there are more parameters. The details of the noise optimization for the virtual fields selection is provided in Appendix C. However, in practice, some stiffness components are strain rate dependent, especially the transverse and shear stiffness components [30, 139]. For instance, if we only consider the strain rate dependence of the transverse and shear stiffness components, a model has to be selected a priori for this strain rate dependence. For instance [4, 151, 152]:

$$\begin{cases} Q_{22} = Q_{22}^0 + \beta_2 ln(|\dot{\varepsilon_2}| + 1) \\ Q_{66} = Q_{66}^0 + \beta_6 ln(|\dot{\varepsilon_6}| + 1) \end{cases} \tag{3.38}$$

where Q_{22}^0 and Q_{66}^0 represent the quasi-static transverse and shear stiffness components respectively and β_2 and β_6 are parameters of the model driving the strain rate dependence of the transverse and shear stiffness components respectively. Thus, the transverse and shear stiffness components in Equation 3.36 cannot be moved outside the integral sign. This is because the strain rate maps will be heterogeneous in the general case. Therefore, the strain rate dependence of the stiffness components implies that the stiffness varies spatially over the specimen according to the heterogeneous strain rate maps. However, it is possible to substitute Q_{22} and Q_{66} using the model in Equation 3.38 and move Q_{22}^0 and Q_{66}^0 and β_2 and β_6 out of the integrals as these parameters are now constant spatially.

$$\begin{aligned} &Q_{11}\int_S \varepsilon_1\varepsilon_1^* dS + Q_{12}\int_S (\varepsilon_1\varepsilon_2^* + \varepsilon_2\varepsilon_1^*) dS + Q_{22}^0\int_S \varepsilon_2\varepsilon_2^* dS + Q_{66}^0\int_S \varepsilon_6\varepsilon_6^* dS \\ &+\beta_2\int_S ln(|\dot{\varepsilon_2}| + 1)\varepsilon_2\varepsilon_2^* dS + \beta_6\int_S ln(|\dot{\varepsilon_6}| + 1)\varepsilon_6\varepsilon_6^* dS = -\int_S \rho a_i u_i^* dS \end{aligned} \tag{3.39}$$

Because only the transverse and shear stiffness components Q_{22} and Q_{66} are strain rate dependent, the other two components Q_{11} and Q_{12} are the same as in quasi-static situations. For the sake of simplicity, it is supposed that these quasi-static parameters (*i.e.*, Q_{11}, Q_{12}, Q_{22}^0 and Q_{66}^0) are known or measured in advance in the case when strain rate dependence is studied (see Chapters 4 and 6). Thus, in Equation 3.39, only β_2 and β_6 are unknown in this case. The procedure to identify two parameters is the same as that for the isotropic linear elastic model. More details are provided in Appendix D. In order to examine the robustness of the strain rate dependent models considered here, a model involving only one strain-rate dependent stiffness component has also been studied here. The identification procedure is same but only one unknown is sought instead of two.

3.2.3 Non-linear shear stress-strain behaviour

As mentioned in Section 2.5, the shear stress-strain relationship for unidirectional composite specimens exhibits significant non-linearity. Therefore, this work attempts to identify this non-linear behaviour at high strain rate. Even though this non-linearity is generally less important than in quasi-static situations [32], it is significant and should be looked at. It should be noted that such a non-linear stress-strain model has already been identified with the VFM in the past [153, 154] in quasi-static situations. To obtain simulated data for validation, the non-linear relationship between the shear stress and strain is numerically simulated by the user subroutine in ABAQUS to produce fully time-resolved strain and acceleration fields, which will be described in the next chapter. To do so, a non-linear shear stress-strain relationship model is considered as [154, 155]:

$$\sigma_6 = Q_{66}\varepsilon_6 - K{\varepsilon_6}^3 \tag{3.40}$$

where K is a parameter describing the strain softening. Thus, with particular virtual fields to cancel out the virtual work of external forces, Equation 3.36 can be rewritten as:

$$Q_{11}\int_S \varepsilon_1\varepsilon_1^* dS + Q_{12}\int_S (\varepsilon_1\varepsilon_2^* + \varepsilon_2\varepsilon_1^*)dS + Q_{22}\int_S \varepsilon_2\varepsilon_2^* dS + Q_{66}\int_S \varepsilon_6\varepsilon_6^* dS - ... \\ K\int_S \varepsilon_6^3\varepsilon_6^* dS = -\int_S \rho a_i u_i^* dS \tag{3.41}$$

It can be seen that the fourth and fifth items at the left-hand side of Equation 3.41 both contain the multiplier $\varepsilon_6\varepsilon_6^*$. Thus, it is not convenient to identify the stiffness components with the optimised virtual fields procedure described above because of the unfulfilled specialty conditions. However, these stiffness components can be identified with another approach, the over-determined resolution, which is introduced in the next section.

3.3 Over-determined resolution

In practice, the kinematic fields are usually measured in the global reference frame. For the isotropic linear elastic model, referring back to Equation 3.11, it is possible to calculate the global stress field σ_x from the strain fields with the stiffness components as:

$$\sigma_x = Q_{xx}\varepsilon_x + Q_{xy}\varepsilon_y \tag{3.42}$$

The stress and strain components in this equation can also be expressed in the form of average values. The average longitudinal stress can be reconstructed by the acceleration at each transverse slice along the longitudinal axis of the specimen as in Equation 3.6, and the strains averaged over the same slice. Combining Equations 3.6 and 3.42, the following relationship is obtained:

$$\rho x\overline{a_x(x,t)} = Q_{xx}\overline{\varepsilon_x(x,t)} + Q_{xy}\overline{\varepsilon_y(x,t)} \tag{3.43}$$

As for the orthotropic linear elastic model, according to Equation 3.11 with required transformation marix, it is also possible to calculate the global longitudinal stress field σ_x from the strain fields with the stiffness components as:

$$\sigma_x = Q_{11}c^2\varepsilon_1 + Q_{12}(c^2\varepsilon_2 + s^2\varepsilon_1) + Q_{22}s^2\varepsilon_2 - 2Q_{66}sc\varepsilon_6 \tag{3.44}$$

where the Q_{ij}'s represent the unknown stiffness components, the ε_i's the three strain components in the material axes and s and c are the sine and cosine of the fibre orientation ϑ. Similarly, according to Equation 3.6, Equation 3.44 can be expressed in the form of average values as:

$$\rho x\overline{a_x(x,t)} = Q_{11}c^2\overline{\varepsilon_1} + Q_{12}(c^2\overline{\varepsilon_2} + s^2\overline{\varepsilon_1}) + Q_{22}s^2\overline{\varepsilon_2} - 2Q_{66}sc\overline{\varepsilon_6} \tag{3.45}$$

Considering the non-linear shear stress-strain relationship as in Equation 3.40, Equation 3.45 can be rewritten as:

$$\begin{aligned}\rho x\overline{a_x(x,t)} = Q_{11}c^2\overline{\varepsilon_1} + Q_{12}\overline{c^2\varepsilon_2 + s^2\varepsilon_1} + \ldots \\ Q_{22}s^2\overline{\varepsilon_2} - 2Q_{66}sc\overline{\varepsilon_6} + 2Ksc\overline{\varepsilon_6^3}\end{aligned} \tag{3.46}$$

Experimentally, the acceleration and strain fields can be calculated from the fully time-resolved displacement fields through temporal and spatial numerical differentiations respectively. In FE simulation, these fields can be output from ABAQUS directly at n (n is greater than the number of unknowns) different frames. Equations 3.43, 3.45 and 3.46 can be used for each transverse slice along the longitudinal axis of the specimen at all frames when strain and acceleration maps are available. So, at each slice, an over-determined system consisting of n equations (from the n data frames) with unknowns Q_{ij}'s (and K) can be built up for the corresponding model. This can be solved for unknowns by a least-squares solution. The process will be demonstrated with FE simulated data in the following chapters.

3.4 Summary

This chapter first introduced why the acceleration (inertial forces) can be used as a load cell and recalled how to reconstruct the stress profiles at any transverse slice along the longitudinal axis of the specimen from the acceleration field. This concept can lead to a non-parametric approach able to identify elastic moduli of materials without the need to formulate a model *a priori*. However, this non-parametric method is restricted to purely uniaxial stress states. It is possible to extend it to multi-axial cases or non-linear behaviour by using an over-determined system approach. This was derived for a non-linear shear stress-strain relationship. The alternative is a full Virtual Fields Method approach. The identification of isotropic and orthotropic linear elastic parameters at high strain rates with the VFM was detailed in Section 3.2, introducing special optimized virtual fields. This approach is similar to the quasi-static case except that the virtual work of external forces is replaced by the virtual work of acceleration forces. It is the first time that such optimized virtual fields are applied in high rate dynamics. Finally, a first attempt at a very simple strain rate dependence model was introduced to see if heterogeneous strain rate maps could be used to identify a strain rate dependence model on a test at a single impact speed. The different models mentioned above are numerically investigated for validation by series of FE simulations. The details pertaining to FE simulation and related identification are presented in Chapter 4.

Chapter 4

Validation based on finite element simulated measurements

Chapter 3 has described how acceleration could be used as an alternative load cell to identify the material parameters at high strain rates. In this chapter, this concept is explored by series of FE simulations to generate perfect data for validation. The dynamic response of different models are simulated using ABAQUS/EXPLICIT to produce time-resolved strain, strain rate and acceleration fields which are then processed using the VFM to extract the material parameters. Simple thin isotropic specimens impacted by either a steel cylinder or a steel ball are first simulated, assuming that the mechanical behaviour is purely linear elastic. For the orthotropic model, the strain rate dependence on the transverse and shear stiffness components discussed in Section 3.2.2 is implemented in the user subroutine VUMAT of ABAQUS/EXPLICIT. Because of the limitations of current full-field measurement techniques, only the deformation at one (or two if two cameras are used) of the lateral specimen surfaces can be acquired in practice. Generally, thin specimens are used in experimental tests so that the deformation in the solid can be analytically related to that on the surface. However, through-thickness strain heterogeneity in the specimen is likely to happen due to possible non-uniform contact between the specimen and the projectile. A worse situation may happen in the ball impact tests, *i.e.*, if the contact point between the ball and the specimen is not in the midplane of the specimen, the through-thickness strain in the specimen would be very heterogeneous. The strain heterogeneity through the thickness will be detrimental to accurate identification of the material parameters as the volume integrals in Equation 2.7 will be falsely evaluated from the surface ones in Equation 3.7. Therefore, this complex $3D$ wave propagation in the specimen has been simulated and is described in Section 4.3, and some solutions to mitigate the 3D effects are proposed as well.

4.1 2D isotropic model

In this PhD work, the isotropic impact tests were carried out using quasi-isotropic carbon/epoxy laminated composite specimens. As reviewed in Section 2.5, Young's modulus and Poisson's ratio of this kind of laminate are not significantly strain rate dependent. Therefore, strain rate dependence was not considered for the isotropic model in FE simulation. In this section, the identification of the isotropic material parameters is demonstrated with different simulations.

4.1.1 Steel cylinder

For the isotropic model, the projectile was first considered as a steel cylinder. A schematic is shown in Figure 4.1. The thicknesses of the specimen and the projectile are both 4 mm. In practice, the projectile is a steel cylinder of diameter 35 mm and length 50 mm. In this FE simulation, the steel cylinder was simulated as a thin plate of thickness 4 mm with the same mass as a cylinder of diameter 35 mm and length 50 mm (density was adjusted accordingly), as seen in Figure 4.1, so that a simple plane stress simulation could be used. Due to the quasi-uniform contact forces between the two solids, the stress wave propagation in the specimen is expected to be quasi-uniaxial. The mechanical response of this model was simulated using ABAQUS/EXPLICIT to produce full-field strain and acceleration maps which were then processed by the VFM. The FE simulation details are provided in Table 4.1. The mesh density is the result of a convergence study.

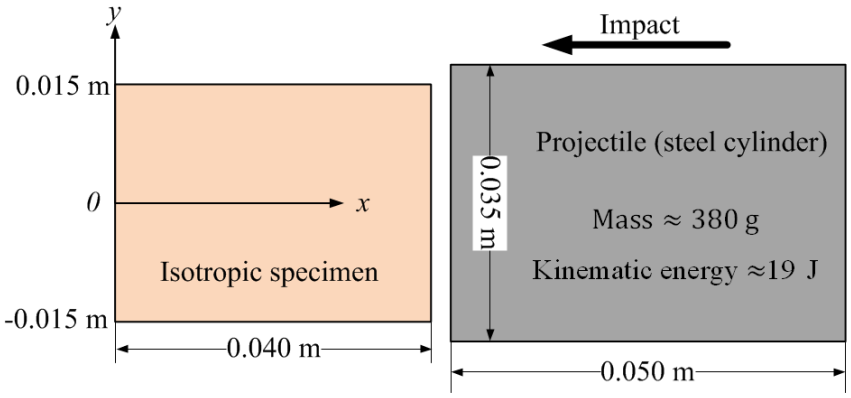

FIGURE 4.1: Schematic of the impact test with the steel cylinder projectile (rectangular block here). Isotropic specimen: $\rho = 2.2.10^3\ kg.m^{-3}$, $E = 47.5\ GPa$, $\nu = 0.3$, thickness= 4 mm. Projectile: adjusted $\rho = 5.24.10^4\ kg.m^{-3}$, $E = 210\ GPa$, $\nu = 0.3$, thickness=4 mm, length=50 mm, width=35 mm.

TABLE 4.1: Details of the ABAQUS/EXPLICIT model: cylindrical projectile.

Mesh size (mm)	0.5 (for the specimen and projectile)
Element type	$CPS4R$ *
Inter-frame time (microsecond)	1
Time increment	Auto increment (around 80 nanoseconds)
Contact type	Hard contact
Impact speed ($m.s^{-1}$)	10

* CPS4R: 4-node linear plane stress, reduced integration, hourglass control.

From the FE simulation, it was found that the contact time between the specimen and the projectile is about 17 microseconds for this model, which corresponds to the time needed for a return travel of the stress wave along the impactor, as expected. Full-field strain and acceleration maps have been output from ABAQUS. Figure 4.2 presents the full-field strain and acceleration maps at 10 microseconds. It can be seen that the spatial frequency content of these maps is very high. One of the potential reasons for this is that no damping was considered in the FE simulation. The effect of a small amount of damping on the stability of the solution is examined later for the $3D$ simulations. Here, the results proved good enough to validate the VFM approach. From Figure 4.2, one can clearly see that the patterns of these full-field maps are not exactly unidirectional. Moreover, the acceleration levels in the specimen are very high. This feature will be used to extract the constitutive parameters with the VFM.

As mentioned in Section 3.2, bilinear piecewise functions are used to expand the virtual fields. The simulated strain and acceleration fields are (nearly) exact, and different virtual mesh densities should therefore provide very similar results. Thus, the virtual mesh is not critical for the VFM identification from simulated data. Here the virtual mesh has been chosen to be composed of 4 elements in the x-direction and 3 elements in the y-direction. This proved to provide a sufficient number of virtual degrees of freedom to solve the problem efficiently. The virtual displacement vector along the contact boundary is set to 0 so that the virtual work of the impact forces is cancelled out from the VFM equation. The time-resolved full-field strain and acceleration fields are then processed using the VFM. The results are expressed as Young's modulus and Poisson's ratio, related to the stiffness components Q_{xx} and Q_{xy} through Equation 3.13. For instance, Figures 4.3 and 4.4 show the maps of virtual displacement and strain used to identify the two parameters at 10 microseconds. It can be seen these virtual fields are different from the actual fields shown in Figure 4.2. However, they satisfy the virtual boundary conditions and special conditions mentioned previously. The results of the

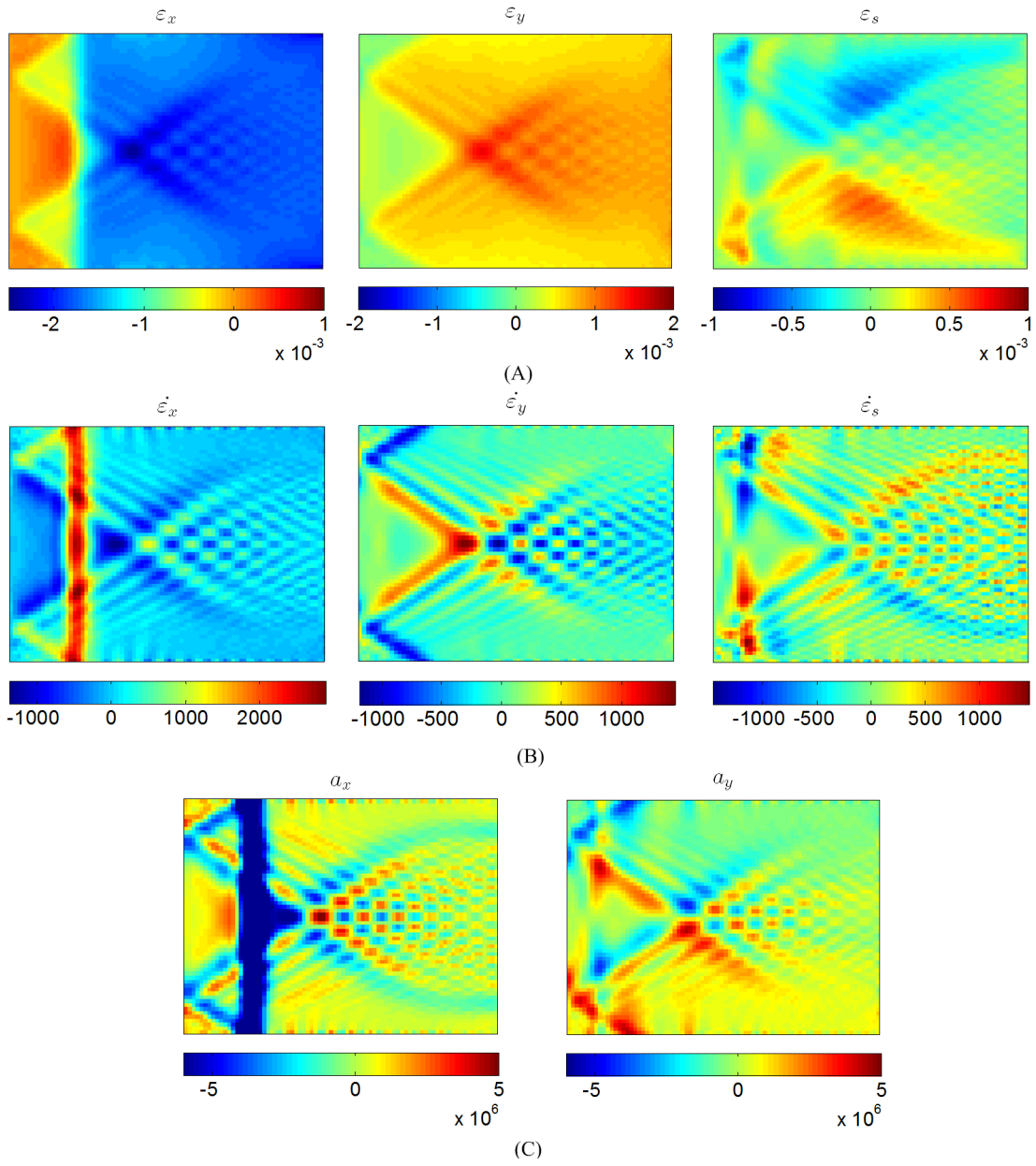

FIGURE 4.2: Maps of full-field strain and acceleration at 10 microseconds. Cylindrical projectile. (A) Strain. (B) Strain rate (in s^{-1}). (C) Acceleration (in $m.s^{-2}$).

identified Young's modulus and Poisson's ratio are shown in Figure 4.5. The identified parameters are within 1 % of the reference, which validates the VFM programme as well as the forward FE calculations. It is worth noting that the error on the identified Poisson's ratio at 1 microsecond is much higher. This is because at that time, the stress wave is concentrated in a very small area close to the contact end, increasing the effects of numerical noise.

The optimised nature of the virtual fields defined in Section 3.2.1 has been validated as follows. The FE strain maps have been polluted with Gaussian white noise of increasing standard deviations, with a maximum level of 10 % of the average strain over the field of

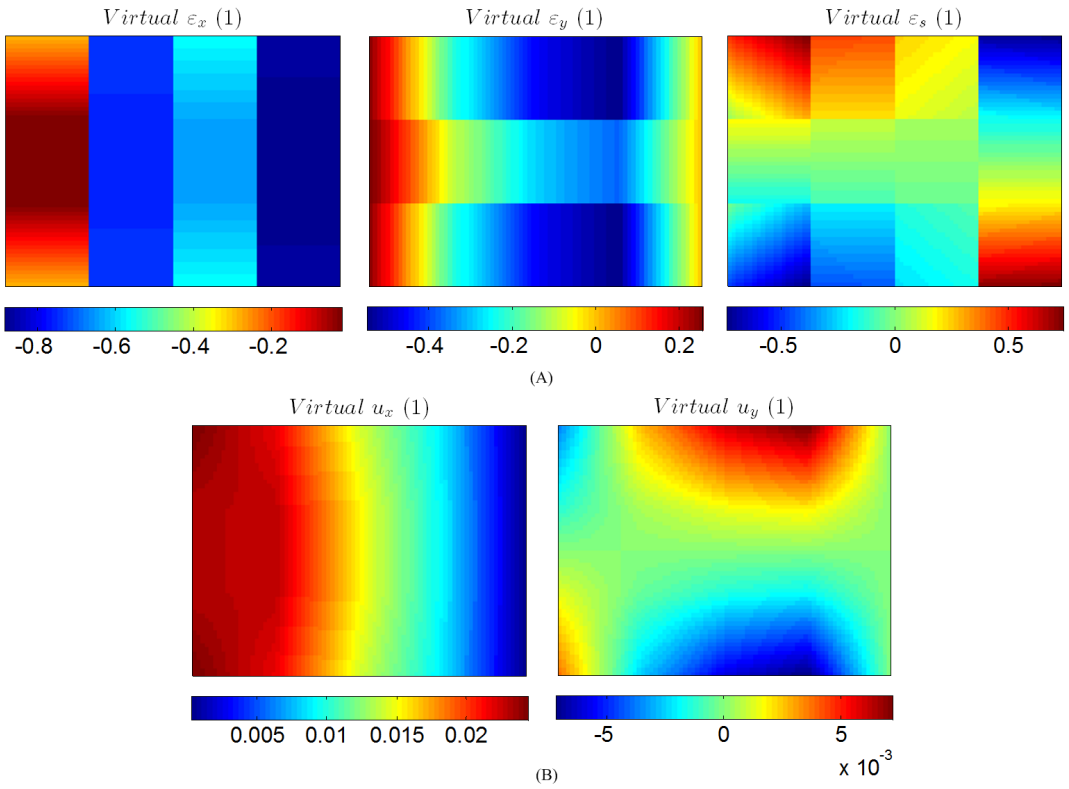

FIGURE 4.3: Maps of virtual strain and displacement for identifying Q_{xx} at 10 microseconds. Virtual meshes: 4×3. (A) Virtual strain. (B) Virtual displacement (in meter).

view and all frames. The calculated average strain is around 3.10^{-4}. Thus, the standard deviation of noise is set from 3.10^{-6} to 3.10^{-5} by an increment of 1.10^{-6}, providing 30 increasing values of noise. For each level, 20 identifications have been performed using 20 different random copies of the same noise level. It is therefore possible to plot the coefficient of variation of each identified stiffness component as a function of the noise standard deviation. This is reported in Figure 4.6 in the form of a cloud of points of linear tendency fitted by a linear approximation. The slope of this approximation is an experimental evaluation of η/Q provided by the optimised virtual fields routine, as mentioned in Section 3.2.1. It is reported at the bottom of the plot as the 'fitted' value, which is compared to the 'theoretical' one directly issued from the virtual field optimisation procedure. As seen in Figure 4.6, at different time steps, it is clear that the value of η_{xy}/Q_{xy} is significantly higher than that of η_{xx}/Q_{xx}. This means that the identification of Q_{xy} is more sensitive to noise. This is reasonable because Q_{xy} has a smaller influence on the strain field than Q_{xx}. Moreover, it can be seen that the values of η/Q vary at different time steps. These values proved inversely proportional to the corresponding strain levels, as expected since the optimized virtual fields rely on strain signal to noise ratios. The higher the strains, the lower the η parameters. For instance, Figure 4.7 presents the strain profiles during this impact simulation. Analyzing the plots

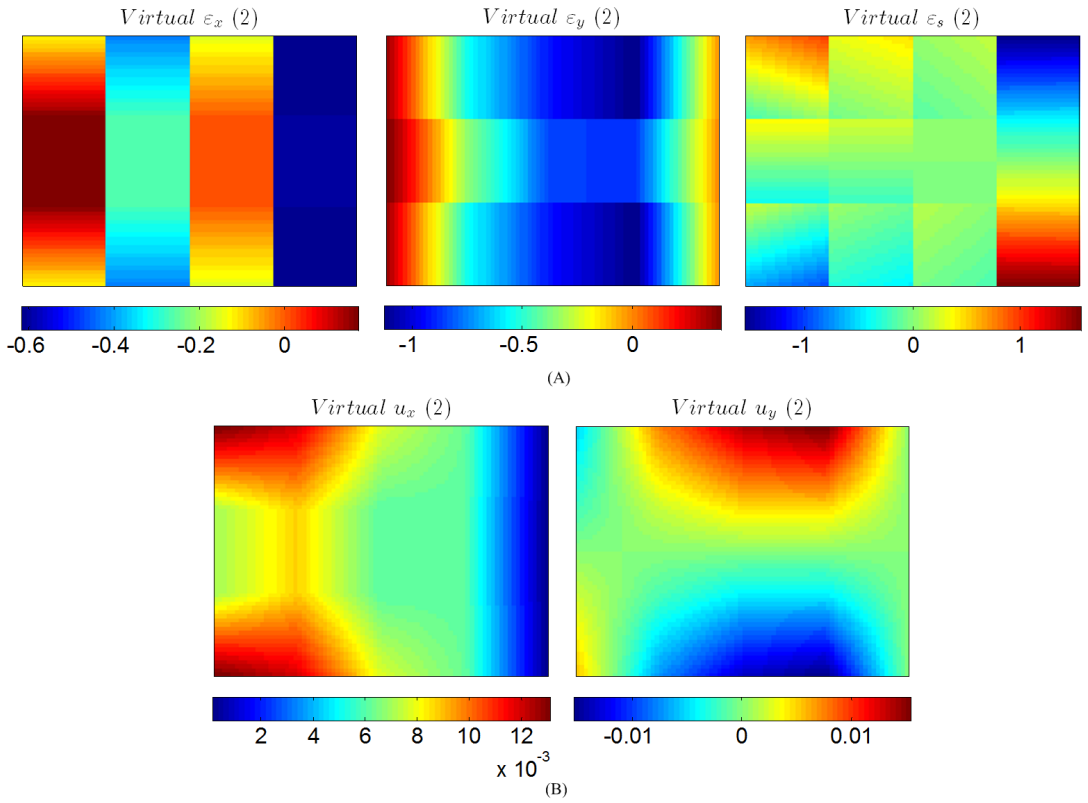

FIGURE 4.4: Maps of virtual strain and displacement for identifying Q_{xy} at 10 microseconds. Virtual meshes: 4×3. (A) Virtual strain. (B) Virtual displacement (in meter).

at different time steps in Figure 4.6 in light of the strain profiles in Figure 4.7, it can be seen that the strain level at 11 microseconds is the highest (among the steps reported in Figure 4.6), while the related value of η/Q in Figure 4.6 is the lowest. Finally, at the bottom of these plots in Figure 4.6, the 'fitted' and 'theoretical' values match very well, validating the optimised virtual fields program. According to [148], these coefficients of variations are the smallest possible among the virtual fields expanded over the current set of piecewise functions (4×3 virtual mesh).

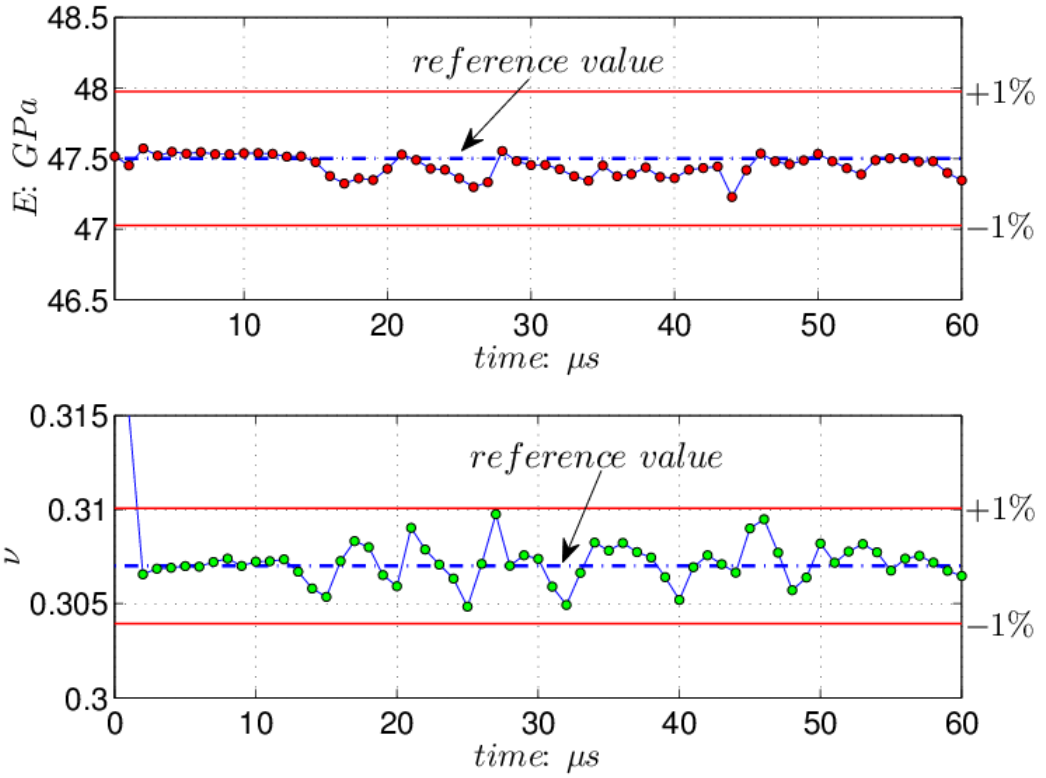

FIGURE 4.5: Identification of Young's modulus and Poisson's ratio from the simulated data. Cylindrical projectile. Data points: 80×60. Virtual meshes: 4×3.

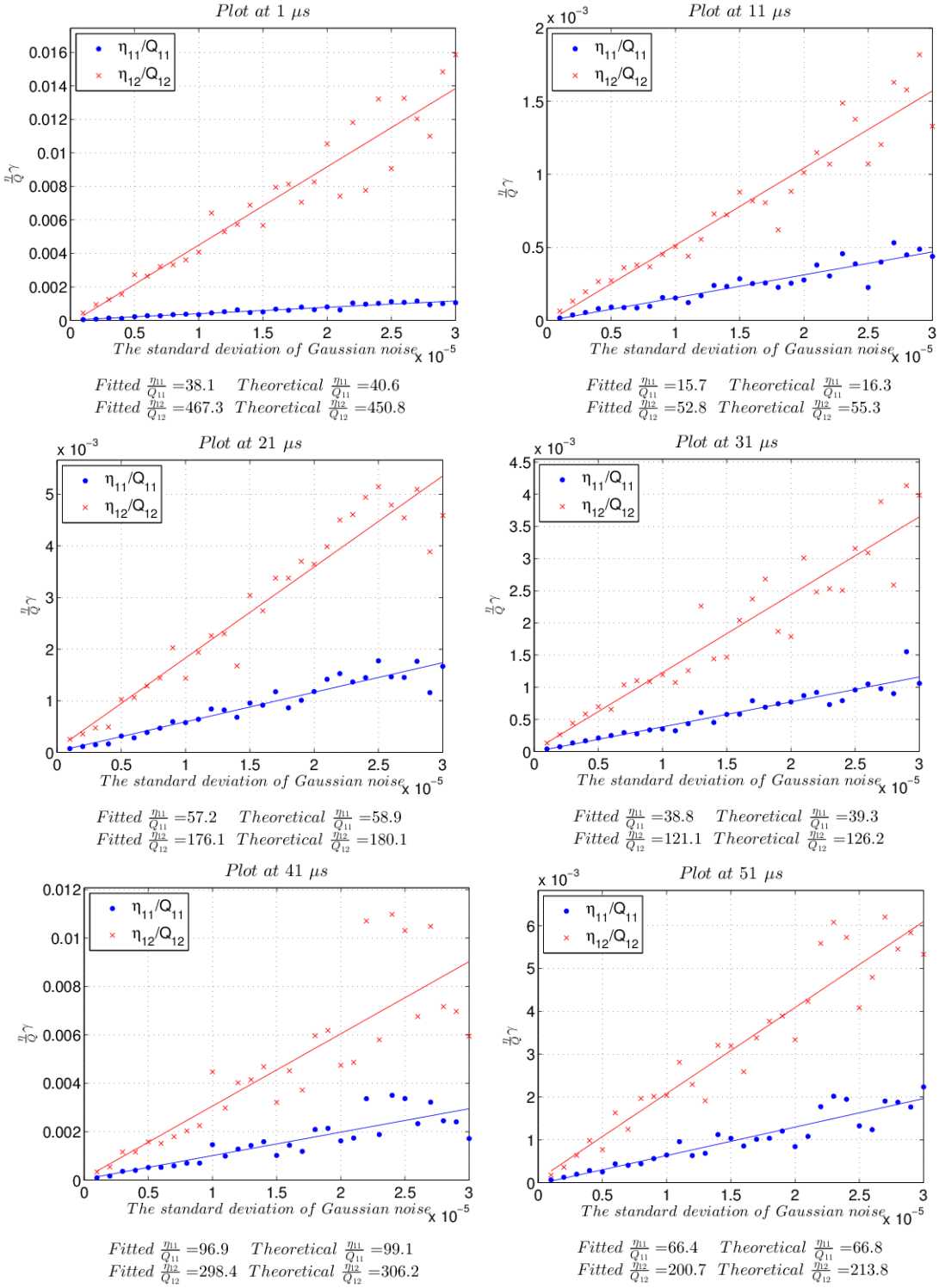

FIGURE 4.6: Plots of the coefficients of variations of the identified stiffness components for the cylindrical impact model. Data fitted by linear regression. Data points: 80×60. Virtual meshes: 4×3.

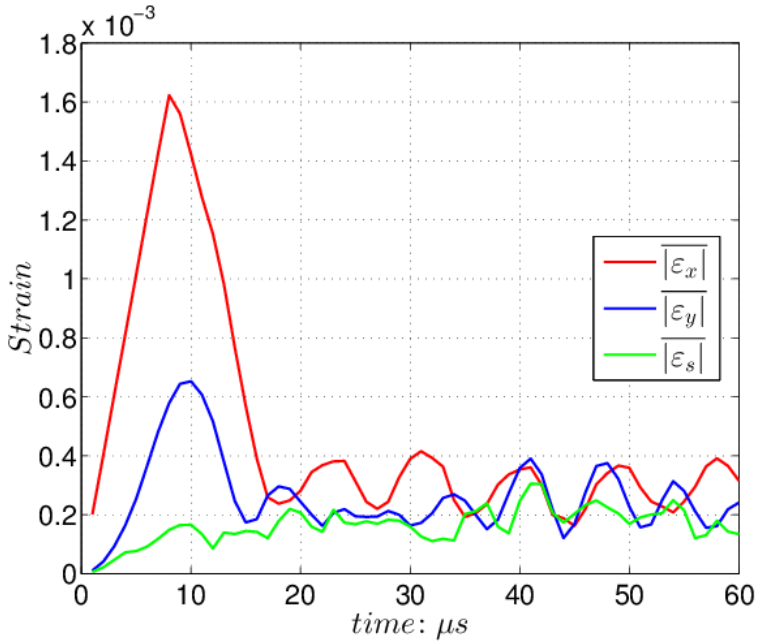

FIGURE 4.7: Strain profiles for the impact simulation with the cylindrical projectile.

4.1.2 Ball impact

As demonstrated in Section 4.1.1, the wave propagation in the specimen impacted by a cylindrical projectile tended to be quasi-uniaxial. The longitudinal strain is predominant among the three strain components, as shown in Figure 4.7. To characterise isotropic materials, this simple uniaxial test is good enough. However, to characterise anisotropic materials, more heterogeneous states of stress/strain are necessary to activate all stiffness components. Therefore, in this subsection, a steel ball impactor is used as the projectile. It is expected that more heterogeneous strain and acceleration states can be achieved because the contact between the specimen and the projectile is not nominally uniform. A schematic is shown in Figure 4.8. The specimen is same as that in Figure 4.1 but the projectile is a ball. The thickness of this model is 4 mm. Similarly to the previous case, a 2D model is considered here for the sake of simplicity. Therefore, the real steel ball has been simulated by a 2D cylinder of the same mass.

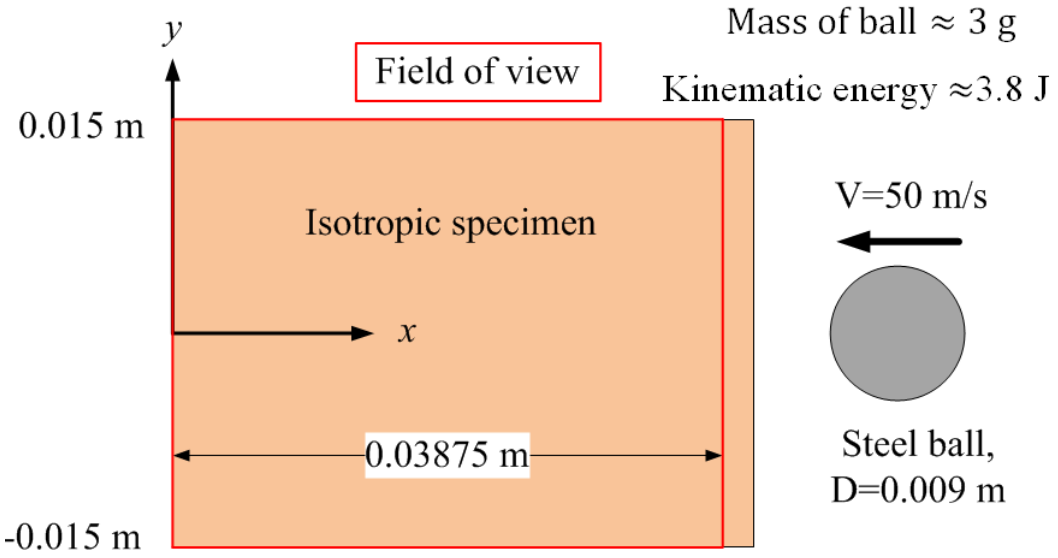

FIGURE 4.8: Schematic of the impact test with the ball projectile. Isotropic specimen: $\rho = 2.2.10^3\ kg.m^{-3}$, $E = 47.5\ GPa$, $\nu = 0.3$, thickness= 4 mm. Projectile: adjusted $\rho = 1.2.10^4\ kg.m^{-3}$, thickness=4 mm, diameter= 9 mm, $E = 210\ GPa$, $\nu = 0.3$.

In this case, the stress wave is introduced at the contact point and propagates in the circular patterns. This impact model was run using ABAQUS/EXPLICIT as well. The FE parameters are the same as that in Table 4.1 except for the element size which has been selected at 0.25 mm to ensure that the FE calculation close to the contact area is accurate enough. The projectile speed is 50 $m.s^{-1}$. Damping was not considered in this simulation either. As in the previous example, strain, strain rate and acceleration have been output for post-processing. The contact time between the two solids is around

17 microseconds as well. The full-field maps at 10 microseconds are presented in Figure 4.9. The stress concentration at the contact point can be clearly seen, as expected. The patterns of these maps are symmetric or antisymmetric about the longitudinal axis of the specimen. The strain and acceleration maps are clearly more heterogeneous than that in Figure 4.1, which was the objective here. Additionally, the circular patterns of the wave propagation can clearly be observed in the acceleration and strain rate maps, and the spatial frequency content is higher than that in Figure 4.1. Here, the region of interest was selected as the area marked by the red rectangular in Figure 4.8 to avoid using the data close to the contact point which suffers from high strain concentrations and therefore, larger computational errors. This is enhanced by the fact that the optimized fields will try to enhance the contribution of this area since the strains are large, introducing unwanted errors in the VFM identification. More precisely, the data from the 5 columns (the total number of columns of data is 160) from the right end of the specimen have been removed from the analysis. This is easily done with the piecewise VFM by setting zero virtual displacements over this new boundary. The strain and acceleration data over this slightly reduced field of view are then processed using the optimised virtual fields. The virtual mesh consists of 5 elements in the x-direction and 3 elements in the y-direction. The number of virtual elements has been slightly increased in the x-direction because of the more heterogeneous state of strain compared to the previous case. The results of the identification of Young's modulus and Poisson's ratio is shown in Figure 4.10. It can be seen that the results are very good with a relative error of the identified Young's modulus and Poisson's ratio lower than 1 % again. However, it is clear that the identified results fluctuate periodically, especially Poisson's ratio. This might be because of the wave rebound over the lateral edges of the specimen which potentially affects the precision of the FE calculation. Comparing the results from Figures 4.10 and 4.5, it is clear that the fluctuations of the identified parameters for the ball impact simulation is more important than for the cylinder impact, although the identification errors are very small in both cases. Figure 4.11 plots the strain profiles in the ball impact simulation. One can clearly see that for the ball impact simulation the wave rebounds (the wave peaks) are more important than for the cylinder impactor and that the strain levels after contact (after 17 microseconds) are still high, whereas for the cylinder impact model, as seen in Figure 4.7, the first strain peak was remarkably higher than the following strain peaks. Moreover, for the ball impact simulation, the three strain components are comparable throughout the first 17 microseconds, whereas in Figure 4.7, the longitudinal strain component was predominant. Due to better ratios of signal to noise, the coefficients of variations of the identified results for the ball impact model are expected to be lower than that of the cylinder impact model. Similarly, the processing shown in Figure 4.6 was also performed for the ball impact model. Figure 4.12 presents the plots of the coefficients of variations of the identification at different frames.

Indeed, the coefficients of variations for the ball impact model are systematically lower than that for the cylinder impact model, even though the maximum strain is lower than for the cylinder impact.

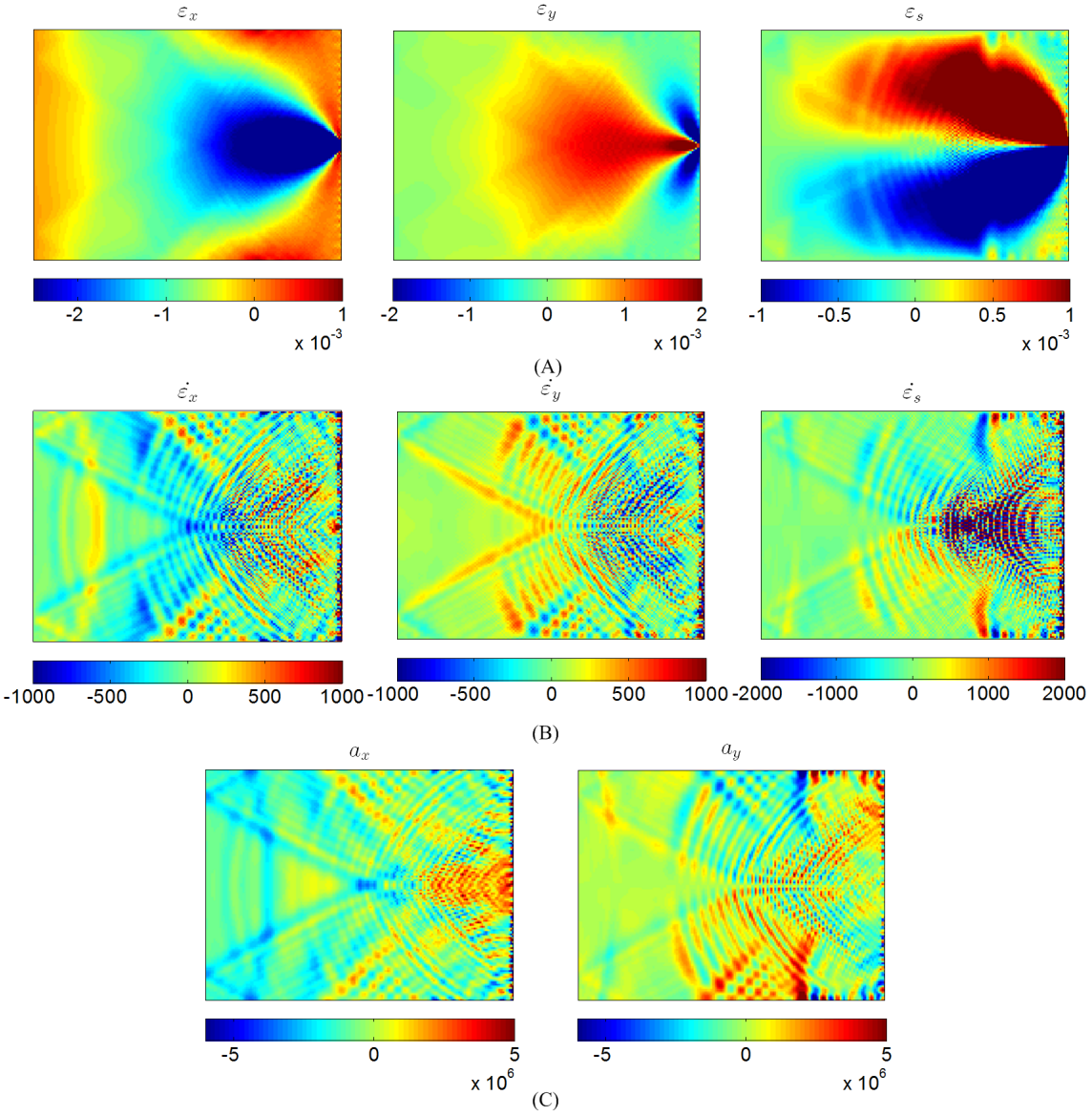

FIGURE 4.9: Maps of full-field strain and acceleration fields at 10 microseconds. Ball projectile. (A) Strain. (B) Strain rate (in s^{-1}). (C) Acceleration ($m.s^{-2}$).

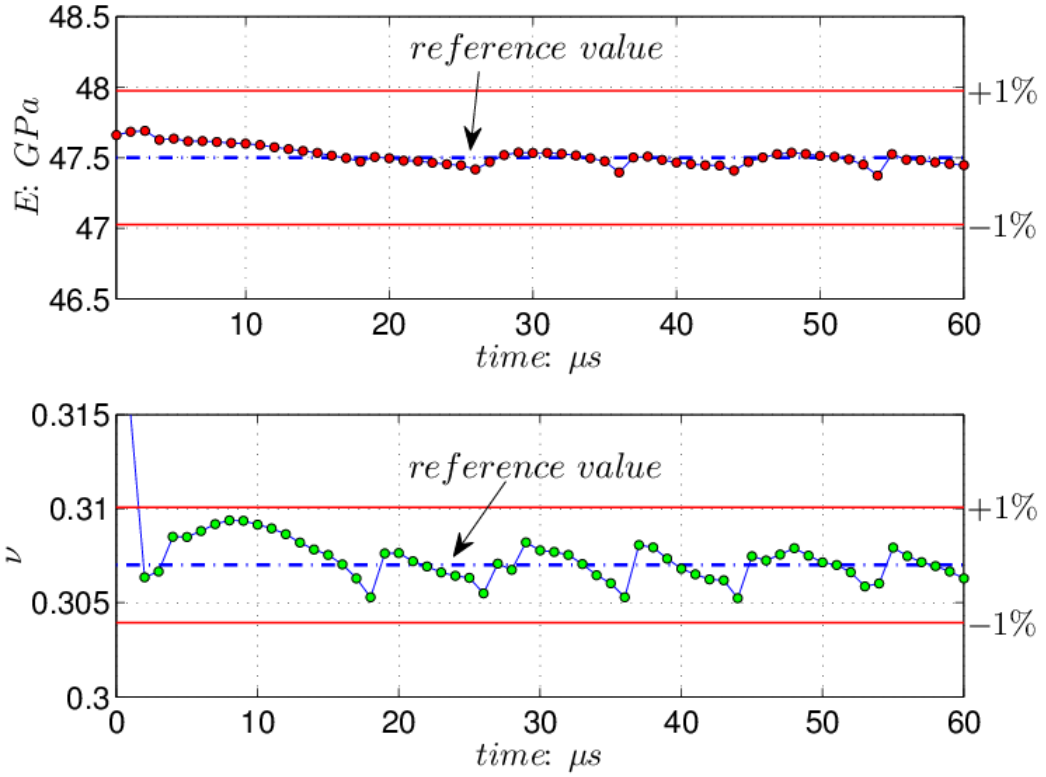

FIGURE 4.10: Identification of Young's modulus and Poisson's ratio from the simulated data. Ball projectile. Data points: 155×120. Virtual mesh: 5×3.

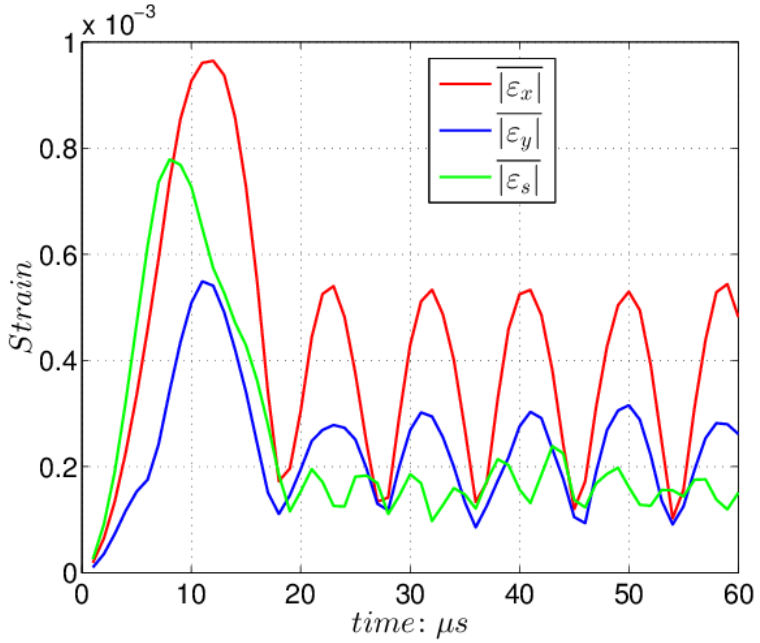

FIGURE 4.11: Strain profiles for the impact simulation with the ball projectile.

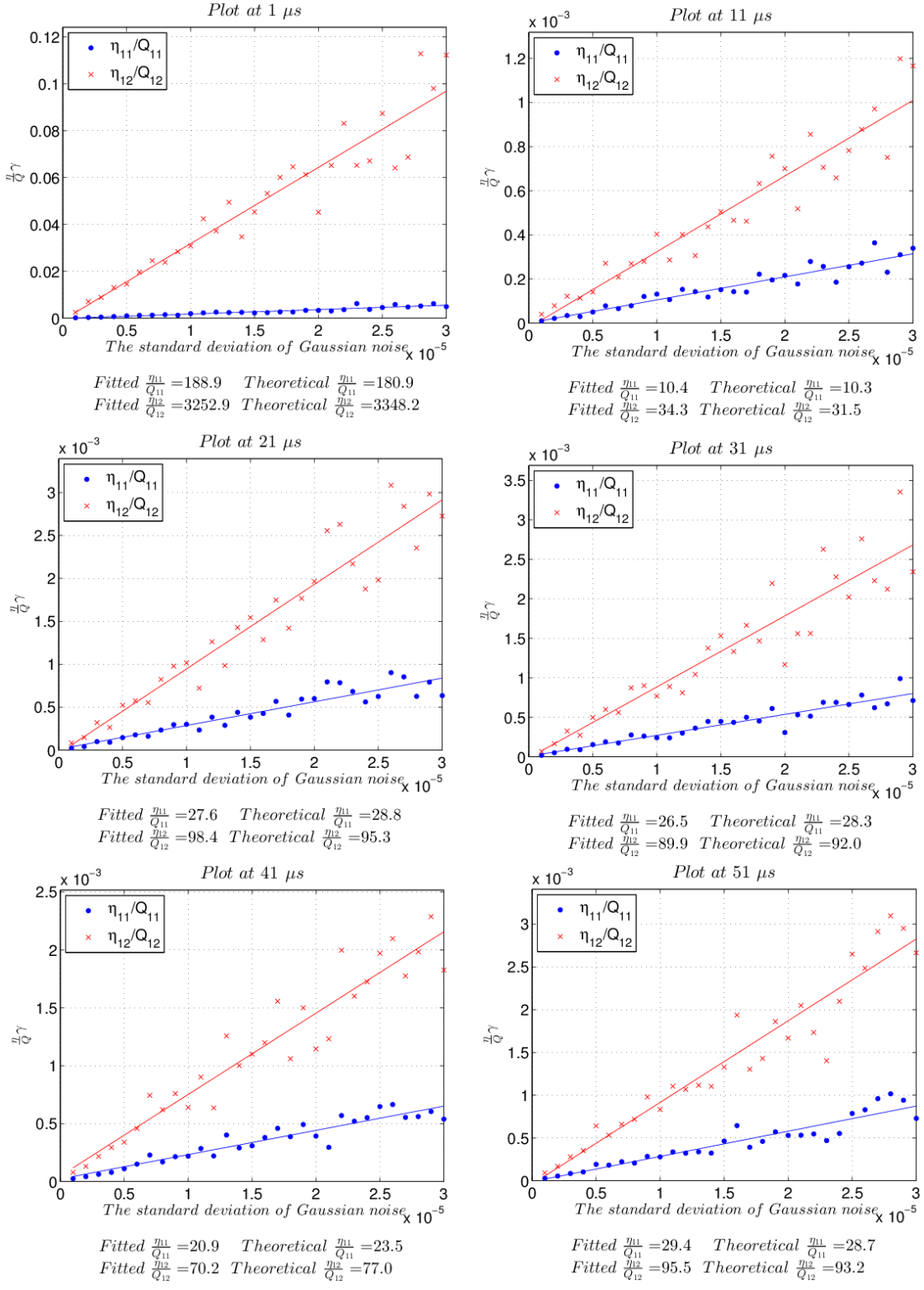

FIGURE 4.12: Plots of the coefficients of variations of the identified stiffness components for the ball impact model. Data fitted by linear regression. Data points: 155×120. Virtual meshes: 5×3.

4.2 2D orthotropic model

Section 4.1 validated the identification of the constitutive parameters making use of inertial effects based on two isotropic linear elastic models. The results were very good. The relative errors were both less than 1 %. The identification of orthotropic constitutive parameters is however more challenging due to the larger number of unknown parameters, as discussed in Section 3.2.2. In the section, the VFM procedure based on the orthotropic linear elastic model is demonstrated. The schematic is the same as that in Figure 4.1 but the specimen is orthotropic. The orthotropic material properties are as follows: $Q_{11} = 124.0\ GPa$, $Q_{22} = 7.5\ GPa$, $Q_{12} = 2.3\ GPa$ and $Q_{66} = 4.0\ GPa$, which represents typical values for the carbon/epoxy material used in the experimental tests.

4.2.1 No strain rate dependence

As reviewed in Section 2.5, the strain rate dependence of unidirectional composite materials is very significant. However, as the first step, the strain rate dependence of the materials was not considered explicitly in the identification process. Orthotropic models with different off-axis fibre orientations (from $\vartheta = 0°$ to $90°$ with a step of $5°$) were simulated using ABAQUS to produce full-field strain, strain rate and acceleration maps. Damping was not considered in this FE simulation. Figure 4.13 presents the full-field maps of this orthotropic simulation with fibre orientation $\vartheta = 30°$. It is clear that the spatial frequency in the maps is high, especially the strain rate and acceleration maps, which would be reduced with a small amount of numerical damping.

These time-resolved full-field maps were then processed by the VFM procedure detailed in Appendix C. In the VFM processing, the virtual mesh consists of 4 elements in the direction of x and 6 elements in the direction of y. The virtual displacement vector along the right-hand side boundary of the specimen is set to zero so as to cancel out the virtual work of the impact forces. Full-field data was processed by the VFM routine described in Appendix C. For instance, the results of the identification of four stiffness components are shown in Figure 4.14. One can clearly see that the identification is very good, especially Q_{22} and Q_{66} within 1 % of the reference. Worse Q_{11} is because of comparatively low longitudinal stress in this off-axis case leading to unreliable identification of Q_{11}. As for Q_{12}, it is difficult to be correctly identified due to its small value, and it does not depend on the strain level and can only be reasonably identified if both Q_{11} and Q_{22} are correctly identified. To check for the simultaneous identifiability of the different stiffness components, the variations of the sensitivity to noise ratios with off-axis angle have studied first. From this investigation, it is possible to plot the relationship between the

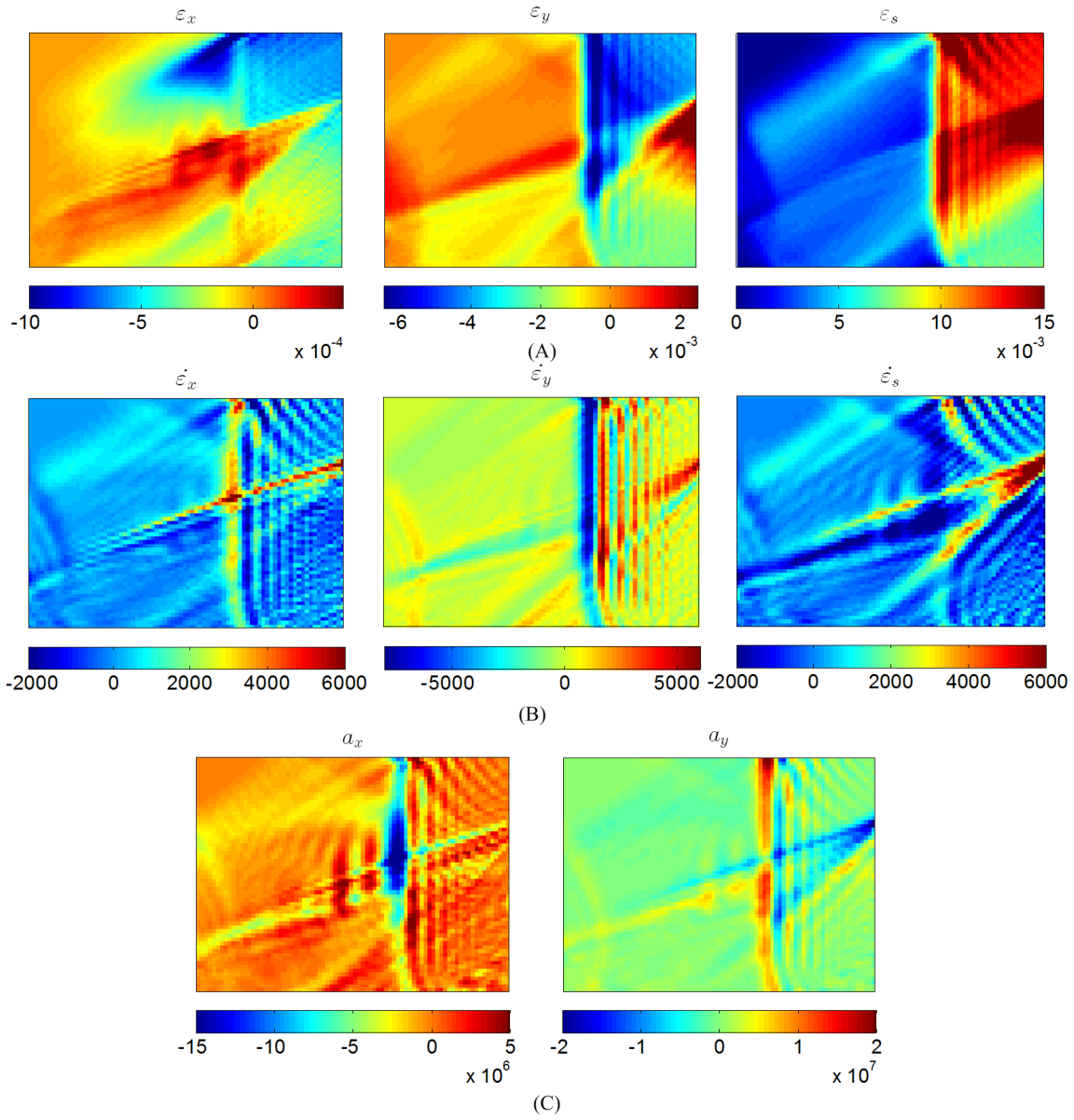

FIGURE 4.13: Maps of full-field strain and acceleration fields at 10 microseconds. Cylindrical projectile. Fibre angle: $\vartheta = 30°$. (A) Strain. (B) Strain rate (in s^{-1}). (C) Acceleration (in $m.s^{-2}$).

η/Q values of the corresponding identified parameters and the off-axis fibre orientations, as shown in Figure 4.15. One can clearly see that the values of η_{11}/Q_{11} (for Q_{11}) increase with the off-axis fibre orientation, and the opposite for η_{22}/Q_{22} (for Q_{22}). This is because at low fibre orientation angles the longitudinal stress in the fibre direction is high, which leads to good signal to noise ratios for the longitudinal stiffness component. When this angle increases, the stress in the fibre direction decreases and the identification quality sharply decreases. The opposite trend is seen for η_{22}/Q_{22} for the same reason. As for Q_{12} and Q_{66}, they share a similar tendency, *i.e.*, the values of η_{12}/Q_{12} and η_{66}/Q_{66} are lower at intermediate off-axis fibre angles than at small and large fibre angles. However, the magnitude of η_{12}/Q_{12} is significantly higher than that of η_{66}/Q_{66}. This was expected

because of the low value of Q_{12}. From these profiles in Figure 4.15, it seems that the off-axis test at a intermediate fibre angle is a good compromise for the identification of the four independent stiffness components.

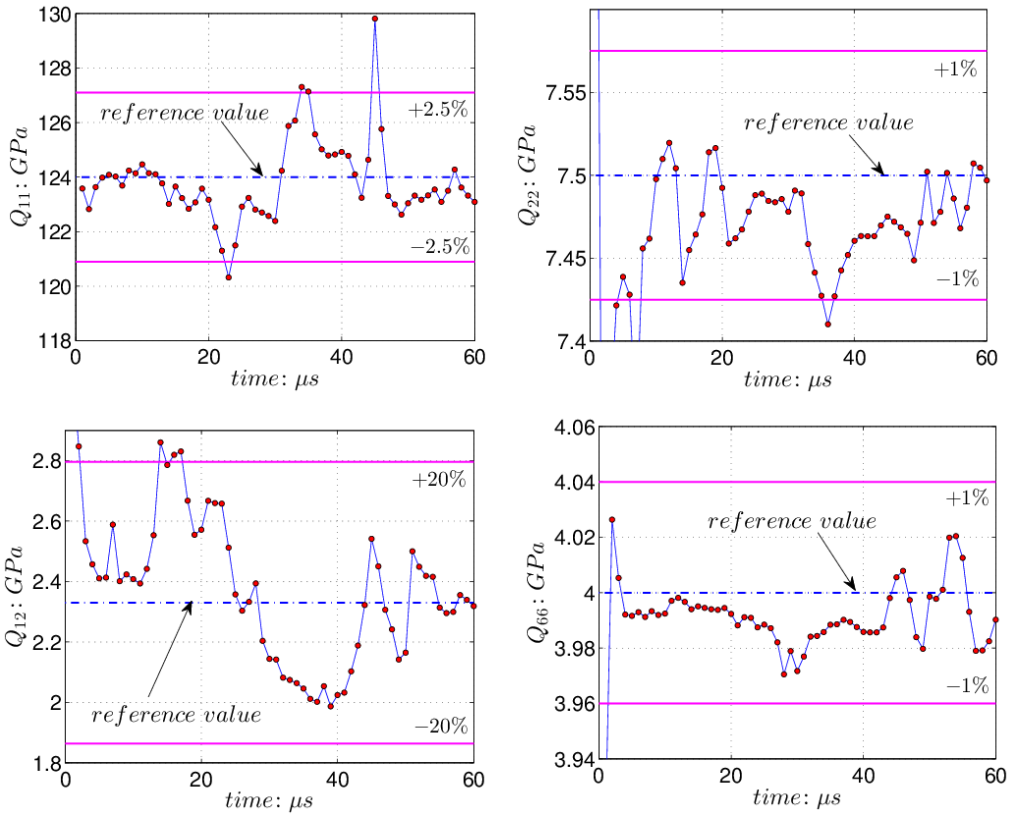

FIGURE 4.14: Identification of four stiffness components with the VFM without strain rate dependence. Data points: 80×60. Virtual meshes: 4×4.

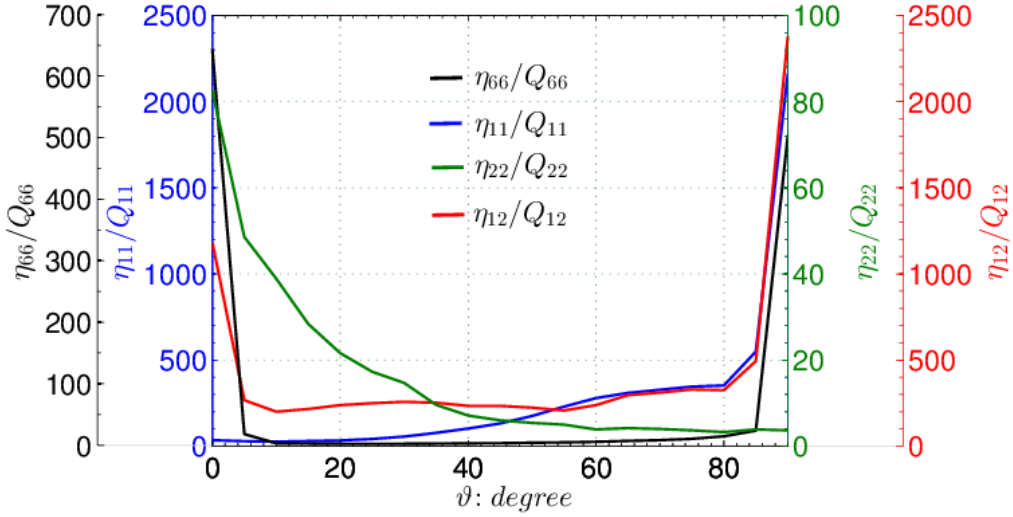

FIGURE 4.15: Profiles of the coefficients of variations of the related identified stiffness components vs. the fibre orientations at 10 microseconds.

4.2.2 Strain rate dependence

The above orthotropic simulation without the strain rate dependent consideration only validated the capability to identify the four independent orthotropic parameters from time-resolved strain and acceleration maps using the VFM. However, in practice, for the orthotropic tests at high strain rates, the strain rate dependence of the material parameters is pronounced, especially the transverse and shear stiffness components, as reviewed in Section 2.5. Therefore, it is necessary to consider this strain rate dependence in the orthotropic simulation. For the sake of simplicity, here only the strain rate dependence on the transverse and shear stiffness components is considered. The strain rate dependence model has been described in Equation 3.38. A schematic of the orthotropic simulation with strain rate dependence is shown in Figure 4.16. In this simulation, the specimen is loaded by a constant and instantaneous pressure. The detailed configuration in the FE simulation is shown in Table 4.2. Among the stiffness components, stiffness components Q_{11} and Q_{12} are same as for quasi-static loading. As in Equation 3.38 parameters Q_{22}^0 and Q_{66}^0 are the quasi-static transverse and shear stiffness components respectively, while for β_2 and β_6 represent the strain rate dependence of Q_{22} and Q_{66} respectively. Based on the results in [32], the values of β_2 and β_6 have been chosen as the values are around 0.6 GPa and 0.35 GPa, respectively.

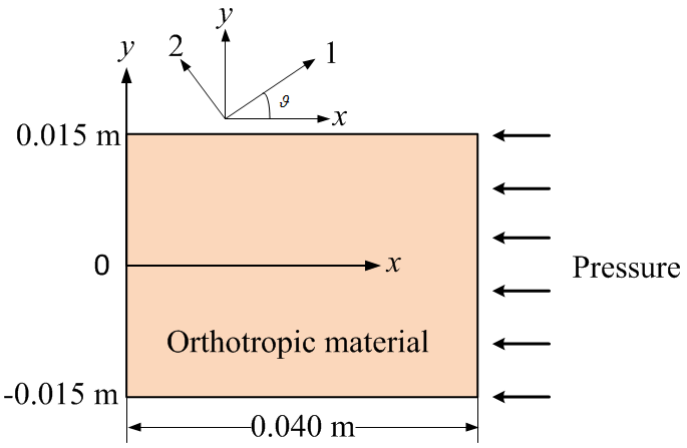

FIGURE 4.16: Schematic of the strain rate dependent simulation. Density of the material: $2.2 \times 10^3\ kg.m^{-3}$. $Q_{11} = 124.0\ GPa$, $Q_{22}^0 = 7.5\ GPa$, $Q_{12} = 2.3\ GPa$ and $Q_{66}^0 = 4.0\ GPa$, $\beta_2 = 0.6\ GPa$ and $\beta_6 = 0.35\ GPa$.

TABLE 4.2: Details of FE configuration for the strain rate dependent model

Mesh size (mm)	0.5
Element type	$CPS4R$ *
Inter-frame time (microsecond)	1
Time increment (nanosecond)	50
Impact pressure (instantaneous)	50 MPa for the first 10 microseconds

* CPS4R: 4-node linear plane stress, reduced integration, hourglass control.

4.2.2.1 Validation of VUMAT code

The strain rate dependent model in Equation 3.38 was implemented through the user defined material model in ABAQUS/EXPLICIT (VUMAT). Before moving to the strain rate dependent simulation, it is necessary to validate the feasibility of the defined model in VUMAT. Thus, an orthotropic linear elastic constitutive model described in VUMAT without any strain rate dependent consideration (*i.e.*, $\beta_2 = 0\,GPa$ and $\beta_6 = 0\,GPa$) was compared to the internal orthotropic linear elastic constitutive model in ABAQUS/EXPLICIT with the same inputs. Here an off-axis case with $\vartheta = 15°$ is taken as an example. The FE configuration is the same as that in Table 4.2. The average longitudinal stress and acceleration over each transverse slice along the longitudinal axis of the specimen at different time steps are plotted, as shown in Figure 4.17. One can clearly see that the profiles from the VUMAT routine are completely consistent with those from the internal model in ABAQUS/EXPLICIT. This shows that the defined orthotropic linear elastic constitutive model in VUMAT is correct. The strain rate dependence on the transverse and shear stiffness components has then been implemented using a modified VUMAT routine, as presented in Appendix E. The identification is discussed in the rest of this section.

4.2.2.2 Identification with strain rate effect

In the strain rate dependent simulation, full-field strain, strain rate and acceleration maps were output from ABAQUS and then processed by the VFM procedure described in Appendix D. In this section, only parameters β_2 and β_6 will be considered. Indeed, it was found that the strain rate heterogeneity was not sufficient in this test to identify both Q_{22} and β_2 on one side, and Q_{66} and β_6 on the other. The alternative is to identify Q_{22} and Q_{66} at this rate and use the counterparts obtained from quasi-static tests to fit the strain rate dependence model. This is attempted later on with experimental

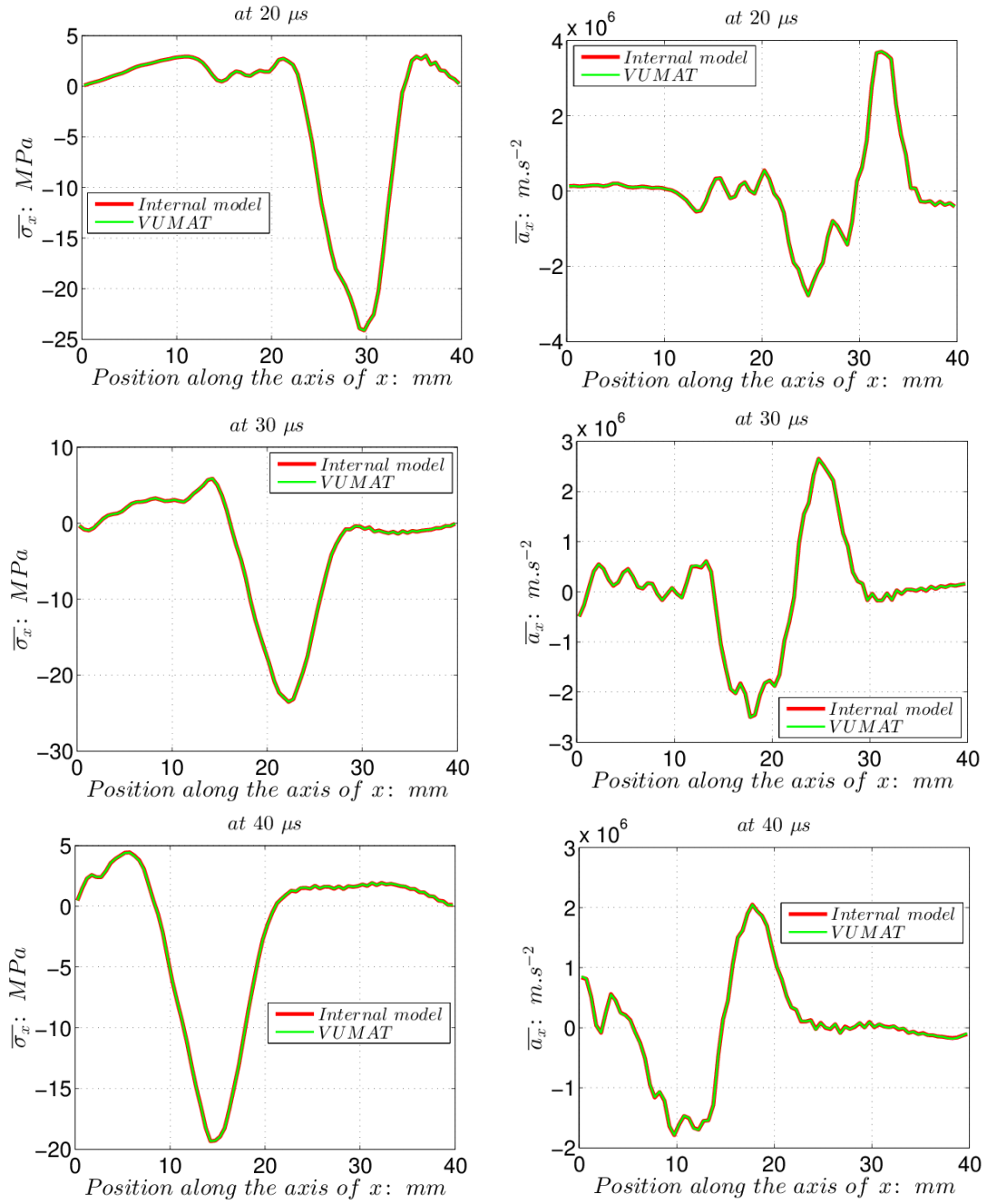

FIGURE 4.17: Profiles of the longitudinal stress and acceleration in the global system using the internal model and VUMAT at different time steps. $\vartheta = 15°$. Time increment: 50 nanoseconds.

data in Chapter 6 where the identification concentrates on the four stiffness components without strain rate dependence. It will be shown that this approach leads to similar value for β_6 (for the experimental data, only the strain rate dependence on the shear stiffness component was considered as a first step), in other words, the strain rate can be considered constant even in the current test and represented by an average value. This is because the strain rate dependence is not very high. Things would probably be very different in polymers, for instance. The virtual displacement in the x-direction along the right-hand side boundary of the specimen is set to 0 so that the virtual work of the instantaneous pressure can be cancelled out, although the instantaneous pressure is known in this FE simulation. The identified values of β_2 and β_6 from the simulations with different off-axis fibre orientations are shown in Figures 4.18∼4.21, with a virtual mesh of 4 by 6 elements (in the x and y directions respectively). It can be seen that the identified parameters are systematically higher than the reference values. Moreover, the identification of β_2 and β_6 is not stable, and the identification varies at different fibre orientations. The relative errors of these identifications are more than 20 %.

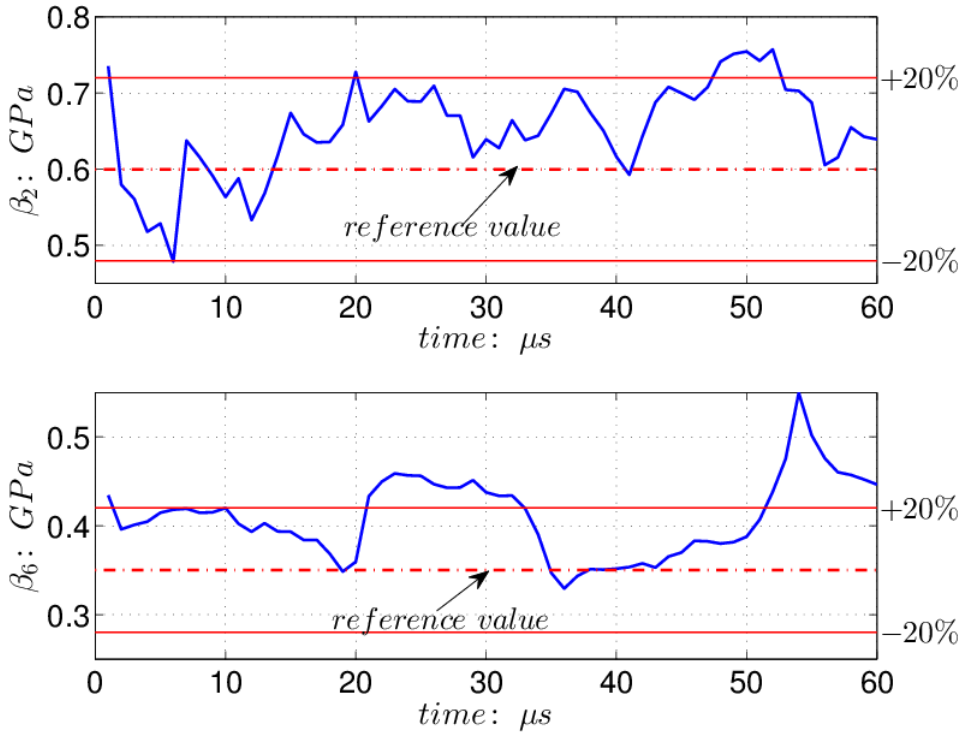

FIGURE 4.18: Identification of β_2 and β_6 with the VFM. Virtual mesh: 4×6. Data points: 80×60. $\vartheta = 10°$.

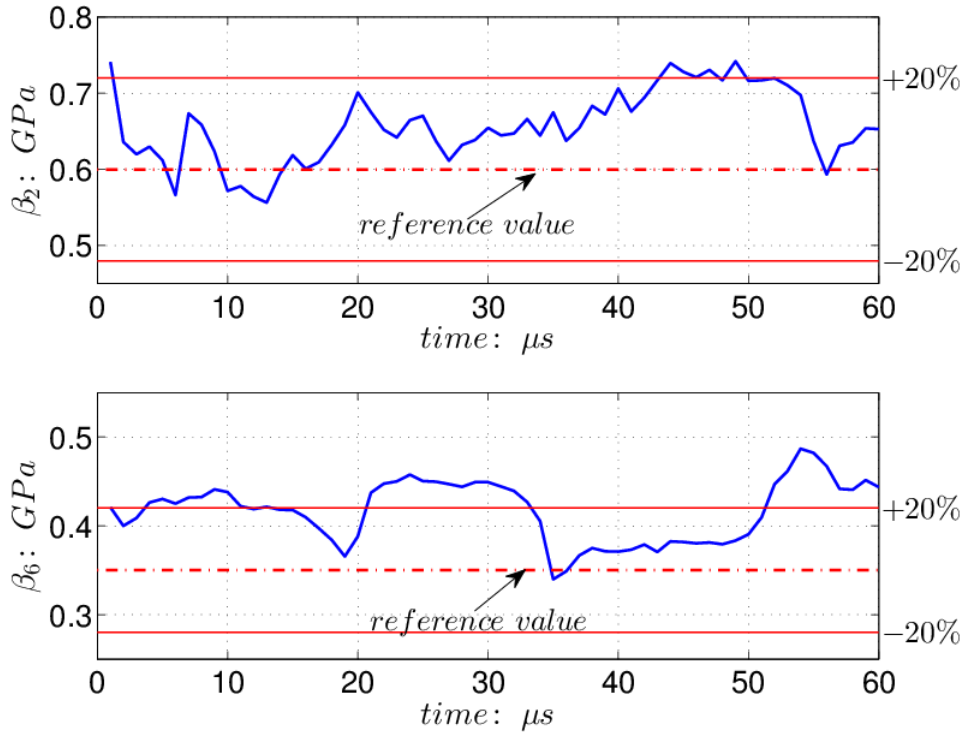

FIGURE 4.19: Identification of β_2 and β_6 with the VFM. Virtual mesh: 4×6. Data points: 80×60. $\vartheta = 15°$.

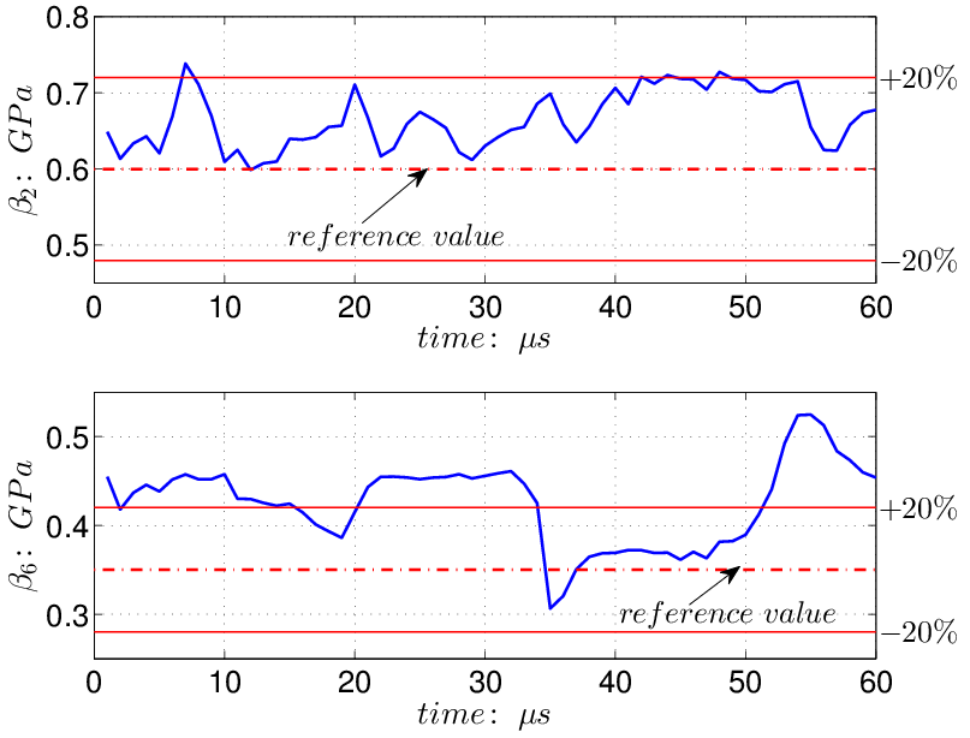

FIGURE 4.20: Identification of β_2 and β_6 with the VFM. Virtual mesh: 4×6. Data points: 80×60. $\vartheta = 20°$.

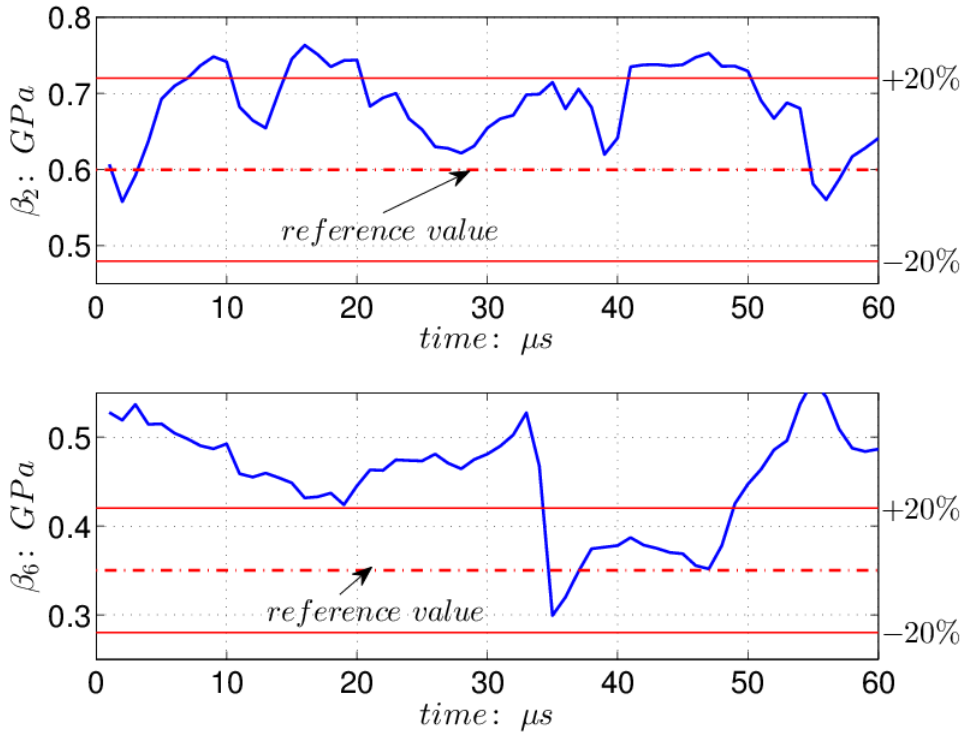

FIGURE 4.21: Identification of β_2 and β_6 with the VFM. Virtual mesh: 4×6. Data points: 80×60. $\vartheta = 30°$.

A first item to investigate is the relationship between the errors and the off-axis fibre orientations. The mean values of β_2 and β_6 over all time steps in different off-axis situations are presented in Table 4.3. It can be seen that the relative error on β_2 increases as the fibre angle increases (except between 0° and 10°), whereas β_6 tends to exhibit a more or less constant error with the fibre angle. Moreover, the identification for $\vartheta = 90°$ is completely off. To investigate the error source, simulations with different time increments were performed. Here only the strain rate dependence on the transverse stiffness component is considered for the sake of simplicity. Time-resolved full-field stress, strain and strain rate maps were output in fibre orientation coordinate system from ABAQUS. According to Equations 3.11 and 3.38, the stress can be reconstructed from the strain fields with the stiffness components, which can be compared to the FE stress output from ABAQUS. Thus, it is easy to calculate the gap between the reconstructed stress and the FE stress maps.

$$G = \sigma_{rec} - \sigma_{FE} \tag{4.1}$$

where σ_{rec} and σ_{FE} represent the reconstructed stress from strain and the FE stress maps respectively. Figure 4.22 presents shows G for $\vartheta = 15°$ with different FE time increments. It is clear that the gaps of longitudinal and shear stresses are significantly lower than that of the transverse one. Moreover, G decreases with decreasing time increment for σ_1 and σ_6, whereas the transverse stress gap is not reduced by refined time increment. To further quantify this issue, a relative gap is defined as:

$$G_{rel} = \frac{\overline{|G|}}{\overline{|\sigma_{FE}|}} \times 100\ \% \tag{4.2}$$

The relative stress gaps G_{rel} are calculated frame by frame with time increments of 50, 25, 10, 5, 2.5 and 1 nanoseconds respectively. The profiles of the relative stress gaps throughout the dynamic simulation with different time increments are shown in Figures 4.23∼4.25. It is clear that, for the longitudinal and shear stress components, the relative gap significantly decreases as the time increment decreases. Moreover, it can be seen that the relative gap of the longitudinal stress is higher than that of the shear component. This is because in the case of $\vartheta = 15°$ the shear strain is significantly higher than the longitudinal strain, leading to better signal to noise ratios for the shear components. In contrast, it can be seen that the profiles of the transverse component with different time increments are consistent with each other. The refined time increments do not mitigate the relative gap of this strain rate dependent component.

TABLE 4.3: Mean values of β_2 and β_6 with different fibre orientations (with relative error in brackets).

ϑ	$\beta_2 : GPa$	$\beta_6 : GPa$
0°	0.79 (31.7 %)	0.45 (28.5 %)
10°	0.65 (8.3 %)	0.41 (17.1 %)
15°	0.66 (10.0 %)	0.42 (20.0 %)
20°	0.67 (11.7 %)	0.43 (22.9 %)
30°	0.68 (13.3 %)	0.45 (28.6 %)
45°	0.71 (18.3 %)	0.42 (20.0 %)
60°	0.78 (30.0 %)	0.39 (11.4 %)
70°	0.85 (41.7 %)	0.41 (17.1 %)
80°	1.03 (71.7 %)	0.40 (14.2 %)
90°	1.55 (158.0 %)	-0.16 (145.7 %)

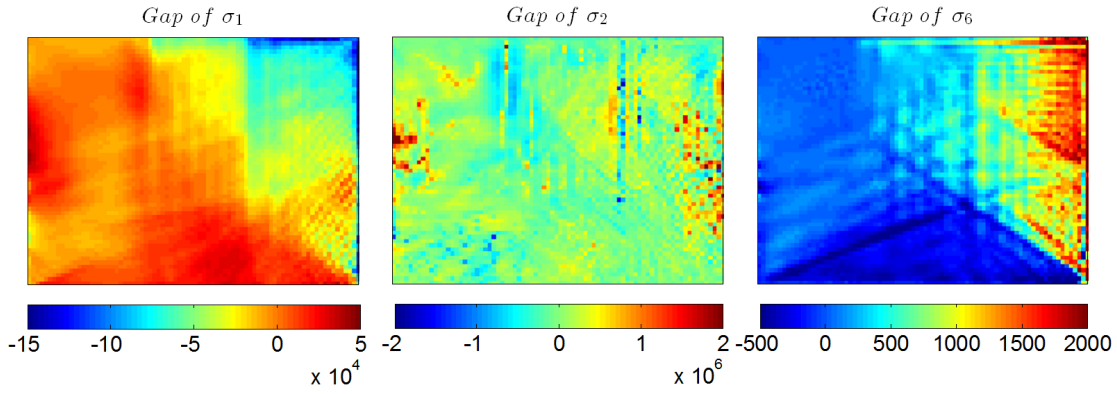

(A)

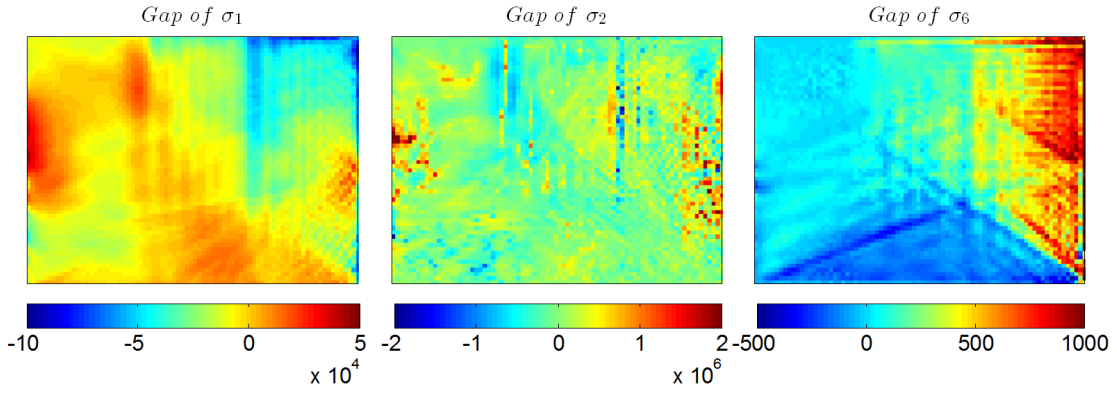

(B)

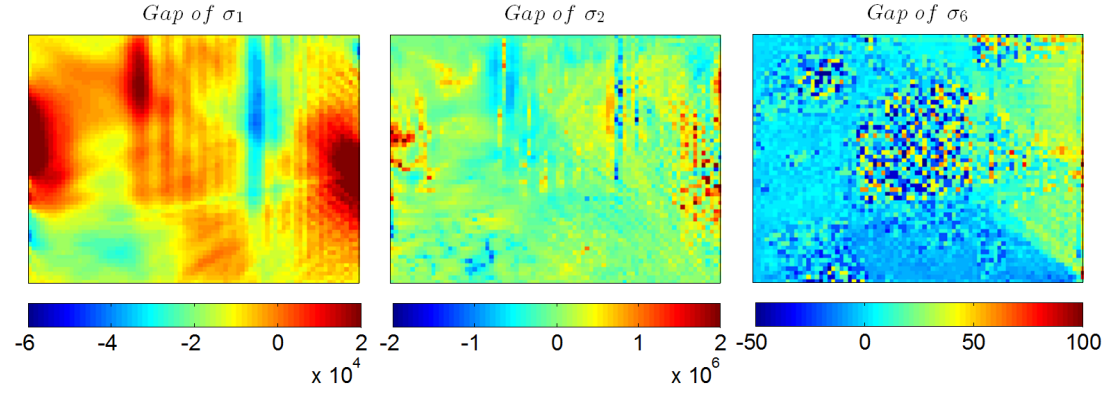

(C)

FIGURE 4.22: Gaps (in Pa) between the reconstructed and FE stress at 20 microseconds in fibre orientation system with different time increments. $\vartheta = 15°$. $\beta_2 = 6.10^8\ Pa$, $\beta_6 = 0\ Pa$. (A) 50 nanoseconds. (B) 25 nanoseconds. (C) 1 nanosecond.

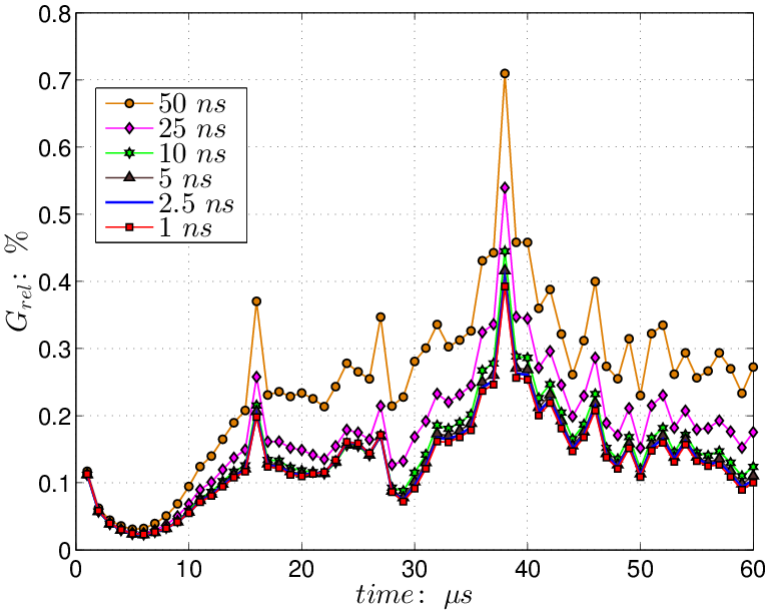

FIGURE 4.23: Relative gap of σ_1 with different time increments. $\vartheta = 15°$.

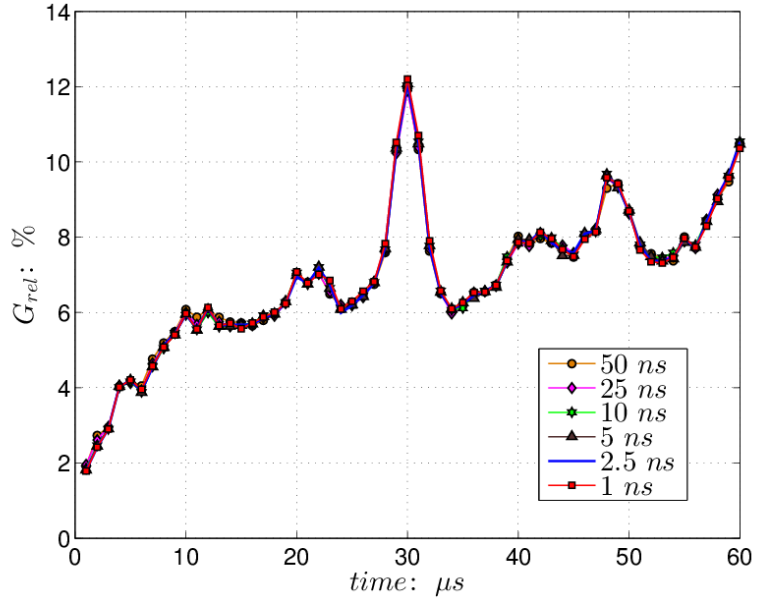

FIGURE 4.24: Relative gap of σ_2 with different time increments. $\vartheta = 15°$.

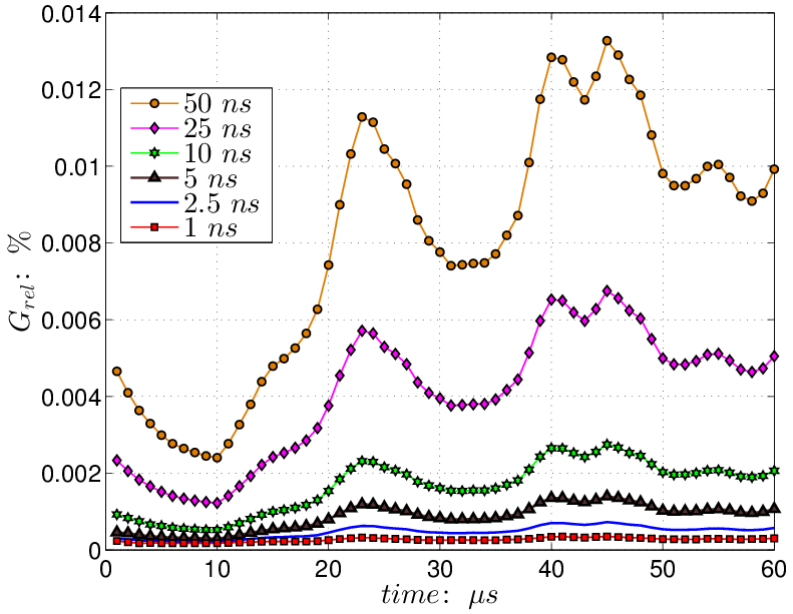

FIGURE 4.25: Relative gap of σ_6 with different time increments. $\vartheta = 15°$.

Returning to the VUMAT validation in Section 4.2.2.1, let us look again at the case where $\beta_2 = \beta_6 = 0\ GPa$ and $\vartheta = 15°$. The stress gaps at 20 microseconds are presented in Figure 4.26. It can be seen the transverse stress gap is significantly smaller than that in Figure 4.22 (A). Among the three components, the gap of the shear stress is the lowest, whereas the longitudinal stress gap is the highest. According to Equation 4.2, the relative longitudinal stress gap is 0.29 %, 0.09 % and 0.01 % for the transverse and shear components respectively. With this fibre orientation, if the strain rate dependence is only considered on the transverse stiffness component ($\beta_6 = 0\ GPa$), it is possible to perform strain rate dependent simulations with different values of β_2 and the relative stress gaps at 20 microseconds are presented in Table 4.4. It can be found that the relative gap of the transverse component increases with increasing values β_2, whereas for the longitudinal and shear components (non-strain-rate-dependent components) the relative gaps are small and stable. This comparison is also carried out when only the shear stiffness component is strain rate dependent ($\beta_2 = 0\ GPa$). Similarly, the relative gap for the strain rate dependent component (the shear component) increases as the parameter β_6 increases, in contrast to the other two non-strain-rate-dependent relative gaps which are very stable, as shown in Table 4.5. Based on the verification results presented above, the identification errors evidenced in Table 4.3 seem to arise from FE computation errors related to the VUMAT routine. Indeed, it has been stated before that in explicit FE simulation, accurate time estimation is very difficult, leading to erroneous calculation of the strain rate [156–158]. Because of the present difficulties, this attempt was put aside and direct identification of the four in-plane stiffness components without any explicit strain rate dependence was attempted instead. Future work will have to concentrate on the computation of reliable stress and strains in FE orthotropic models.

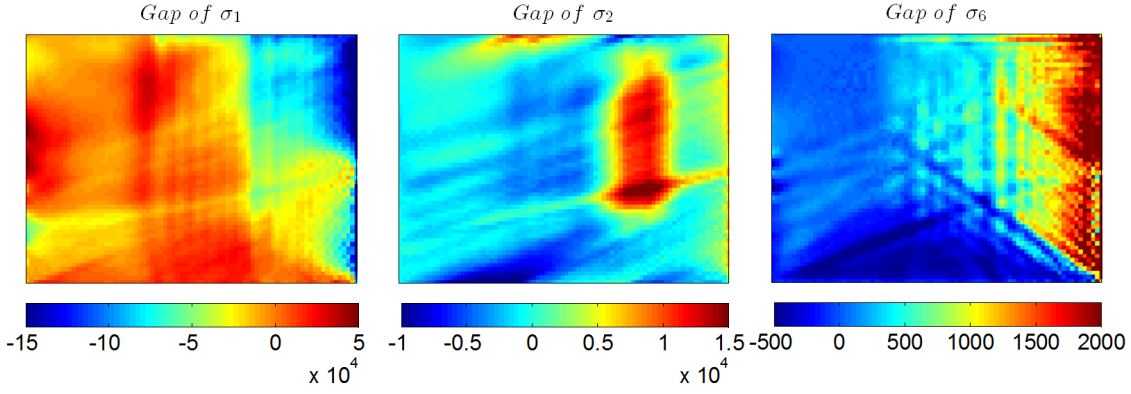

FIGURE 4.26: Gaps (in Pa) of the reconstructed and FE stress at 20 microseconds in fibre orientation system. $\vartheta = 15°$. Time increment: 50 nanoseconds. $\beta_2 = 0\ Pa$, $\beta_6 = 0\ Pa$.

TABLE 4.4: Relative gap with different values of β_2 at 20 microseconds: $\vartheta = 15°$, $\beta_6 = 0\ Pa$.

β_2: Pa	Gap of σ_1: %	Gap of σ_2: %	Gap of σ_6: %
0	0.29	0.09	0.01
1.10^4	0.29	0.09	0.01
1.10^6	0.29	0.09	0.01
5.10^6	0.29	0.12	0.01
1.10^7	0.29	0.18	0.01
5.10^7	0.28	0.78	0.01
1.10^8	0.28	1.52	0.01
6.10^8	0.23	7.01	0.01
1.10^9	0.23	10.05	0.01
5.10^9	0.17	16.29	0

TABLE 4.5: Relative gap with different values of β_6 at 20 microseconds: $\vartheta = 15°$, $\beta_2 = 0\ Pa$.

β_6: Pa	Gap of σ_1: %	Gap of σ_2: %	Gap of σ_6: %
0	0.29	0.09	0.01
1.10^4	0.29	0.09	0.01
1.10^6	0.29	0.09	0.04
5.10^6	0.29	0.09	0.17
1.10^7	0.28	0.09	0.33
5.10^7	0.26	0.08	1.56
1.10^8	0.26	0.08	2.99
$3.5.10^8$	0.22	0.02	11.55
1.10^9	0.08	0.09	16.11
5.10^9	0.10	0.15	19.48

4.3 Investigation of the effect of strain heterogeneities through the thickness

For both cylindrical and ball impacts, the quality of the through-thickness contact between the specimen and the projectile is crucial because of the need to evaluate the volume integrals in the VFM from surface data. This problem is clearly more crucial for the ball impact as even a perfect contact leads to nominally heterogeneous through-thickness data. The objective of this section is to investigate this issue and look at ways to mitigate these effects. The ball impact configuration is investigated here as it is the more sensitive to this effect of the two impact configurations. Experimentally, it is difficult to perfectly align the specimen with the gun barrel. Figure 4.27 shows photos of the tested specimens and steel tabs (of thickness 1 mm) used to protect the impact end of the specimens in the ball impactor tests. Different offsets in contact can be seen

potentially leading to additional non-uniform strain distributions through the thickness of the specimen. Therefore, it is essential to conduct substantial investigation of the $3D$ wave effects on the identification of the material parameters and to search for effective ways to mitigate these effects.

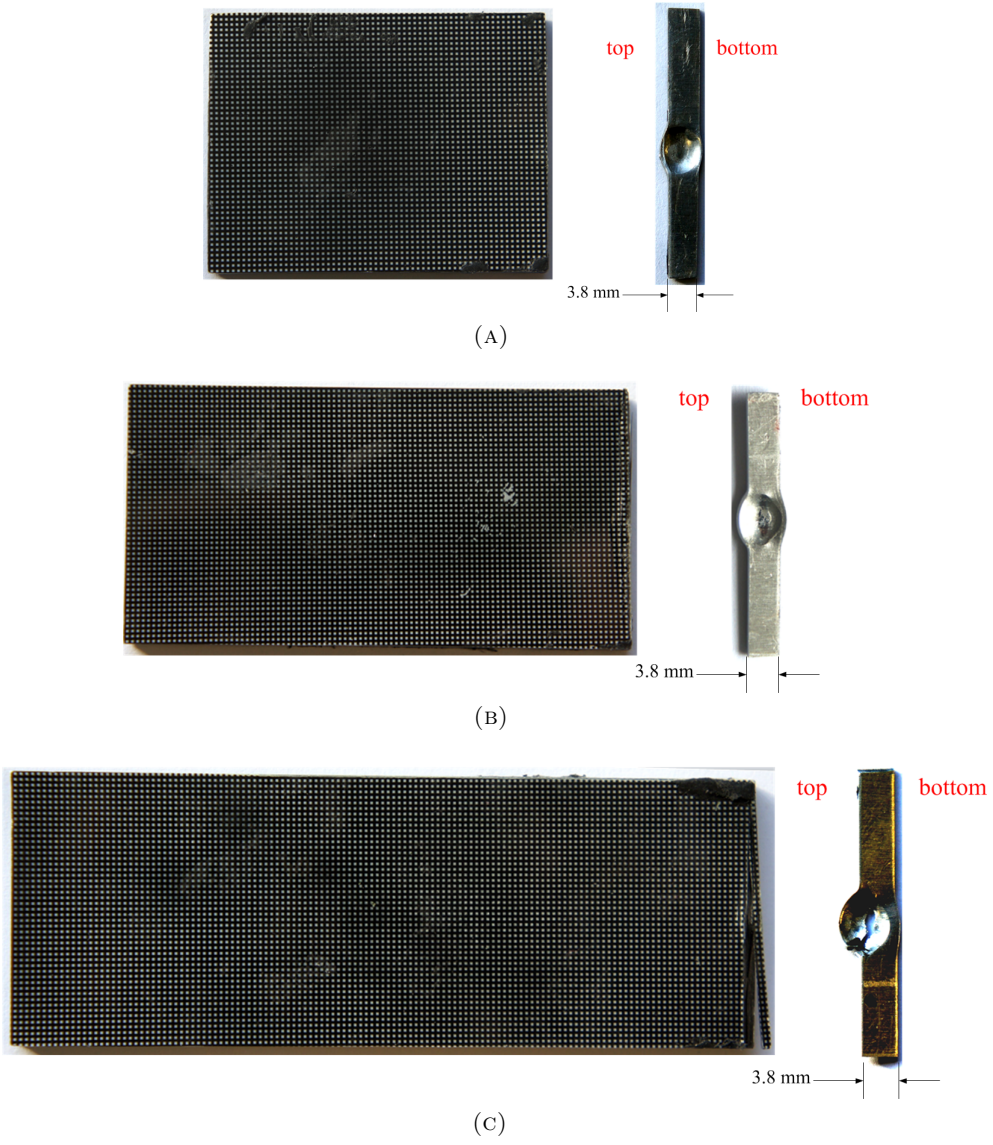

FIGURE 4.27: Pictures of the tested specimens and associated steel tabs. (A) Specimen QI-1, misalignment: 1 *mm* (B) Specimen QI-2, misalignment: 0.5 *mm*. (C) Specimen QI-3, misalignment: 1.5 *mm*

4.3.1 Simulated full-field maps

In this section, the $3D$ wave propagation in the specimen was systematically simulated. It is worth emphasising that only the full-field data at the top and bottom surfaces were processed, because this is the information available experimentally. However, the average

fields over the thickness were output as well and used as reference in the following. A schematic of the $3D$ model is shown in Figure 4.28. It is composed of an isotropic specimen of dimensions $40 \times 30 \times 4$ mm (length $\times$ width $\times$ thickness) impacted by a steel ball of diameter 9 mm. A steel tab of thickness of 1 mm is attached at the impact end of the specimen to protect its cross-section. In this simulation, the input Young's modulus for the specimen is 47.5 GPa and 0.3 for its Poisson's ratio. For the steel material, the input Young's modulus is 210 GPa and 0.3 for the Poisson's ratio, provided the values were used for the steel tab and for the steel ball. Specify the tab was considered linear elastic, even though experimental evidence shows it is not. However, plasticity will absorb energy but probably not change the effect of the tab in terms of contact distribution so much. This was to save computational time for such $3D$ models. The dynamic response was simulated using ABAQUS/EXPLICIT to produce full-field strain and acceleration maps which were then processed by the VFM. The details of the FE simulations are shown in Table 4.6. From this simulation, it was found that the contact time between the two solids is about 20 microseconds. Moreover, damping was used here to improve numerical stability. Here, classical Rayleigh damping was considered [159] as it is implemented in ABAQUS. It combines mass and stiffness damping through the mass-proportional and stiffness-proportional coefficients α and β, respectively. Figure 4.29 plots the stress-strain curves at $x = 20.75$ mm with different damping parameters, from Equation 3.6. One can clearly see that, without damping ($\alpha = 0$ s^{-1} and $\beta = 0$ s), the curve is linear only when the two solids are in contact, whereas after the contact phase, the data are inconsistent. With large damping (e.g. $\alpha = 0$ s^{-1} and $\beta = 1.10^{-6}$ s), this model experiences significantly non-linear behaviour, as expected for a visco-elastic material. Therefore, the damping coefficient should be small enough to respect the condition of elastic material behaviour but large enough to damp the numerical instabilities during computation. It can be seen from Figure 4.29 (C) that damping coefficients of $\alpha = 0$ s^{-1} and $\beta = 2.10^{-8}$ s are appropriate, because the curve throughout the impact simulation is linear. Therefore, this set of values will be kept for the simulations presented in this paper. It is also worth noting that the current approach enabling to calculate stress from acceleration is also a relevant method to check for the quality of dynamic explicit computations.

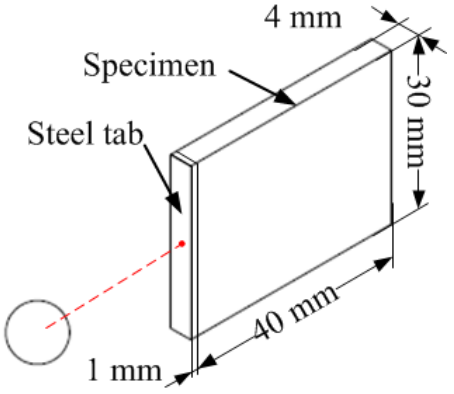

FIGURE 4.28: Schematic of the 3D finite element simulation of the ball impact test. Specimen properties: $E = 47.5\ GPa$, $\nu = 0.3$, $\rho = 2.2 \times 10^3\ kg.m^{-3}$. Steel ball impactor and tab properties: $E = 210\ GPa$, $\nu = 0.3$, $\rho = 7.8 \times 10^3\ kg.m^{-3}$.

TABLE 4.6: Details of the ABAQUS/EXPLICIT model.

Mesh size (mm)	0.5 for the steel tab, specimens and ball impactor
Element type	$C3D8R$ *
Time step (microsecond)	Automatic (around 0.01)
Inter-frame time (microsecond)	1
Contact type	Hard contact
Impact speed ($m.s^{-1}$)	30

* CPS8R: 8-node linear brick, reduced integration, hourglass control.

A first item to investigate is the effect of the point load. Indeed, this generates stress and strain states that are not uniform through the thickness, as opposed to the cylindrical impactor configuration in Section 4.1.1. This will result in an error when estimating the volume integrals from the surface measurements. Moreover, an offset in the contact point as shown on Figure 4.27 will make things worse. In order to investigate these issues, three contact models have been developed, as shown in Figure 4.30. Contact model (1) describes an ideal case where the full-field data at the top and bottom surfaces are symmetrical about the midplane. Contact model (2) represents a small misalignment of 0.5 mm (12.5 % of the thickness) from the midplane in the cross-section, and a larger misalignment of 1.5 mm (37.5 % of the thickness) is considered in contact model (3). Due to this misalignment, the stress wave propagation in the specimen tends to be three-dimensional. It is thought however that the metal tab used to protect the specimen can already act as a load spreader to mitigate this effect. Its dimension has been presented in Figure 4.28.

The ideal contact model (1) without the steel tab was simulated first. The strain and acceleration fields at the top and bottom surfaces were output. The average fields over the thickness were also output and used as the reference field as this is the data that will provide exact estimations of the surface integrals in Equation 3.7 from the volume integrals in Equation 2.7. For instance, Figure 4.31 presents the average full-field strain and acceleration maps at 14 microseconds. The strain concentration caused by the point load appears very clearly. The heterogeneity of the mechanical fields is far more pronounced than for the quasi-uniaxial case in Section 4.1.1. The spatial frequency of acceleration is higher than that of strain. The difference between the top surface strain and the average strain through the thickness in the longitudinal direction at 14 microseconds is shown in Figure 4.32 (A). The strain difference represents about 10 % of the global strain values. One can clearly see a wave pattern produced by the multiple reflections of the waves on the top and bottom surfaces. Figure 4.32 (B) shows the same data as in Figure 4.32 (A) but with the steel tab of thickness 1 mm. It is interesting to see that the curvature of the strain ripples is less pronounced with the tab, showing the load spreading effect of the tab. The top to average difference is also slightly smaller than without the tab, as expected. Finally, one can see that away from the loading point, the error fades away, illustrating a kind of Saint-Venant effect [160, 161] in dynamics. In practice however, the metal tab exhibits local yielding, thus absorbing some of the impact energy that will not be available to deform the specimen. Nevertheless, the tab will prevent local indentation damage in the material which is beneficial for the analysis presented here. Therefore, 1 mm thick steel tabs will systematically be used in the rest of the paper, for both simulations and experiments.

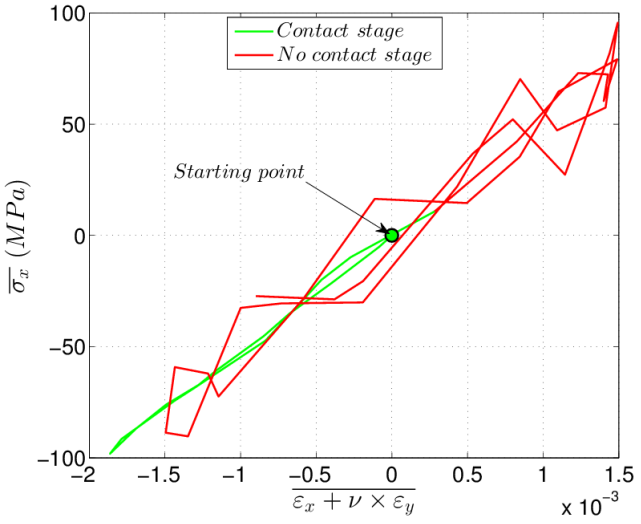

(A)

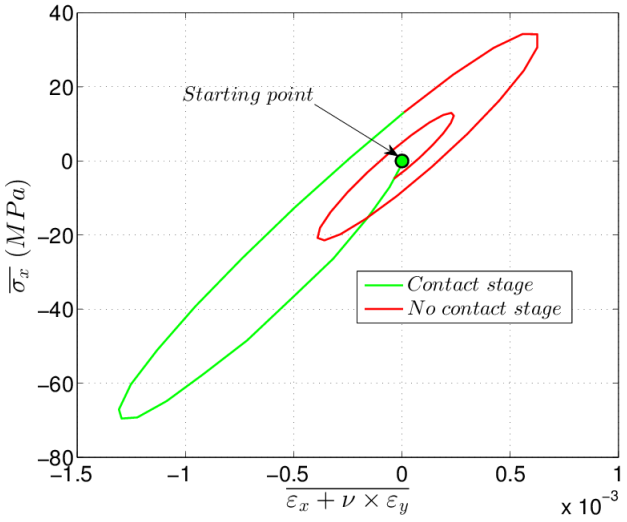

(B)

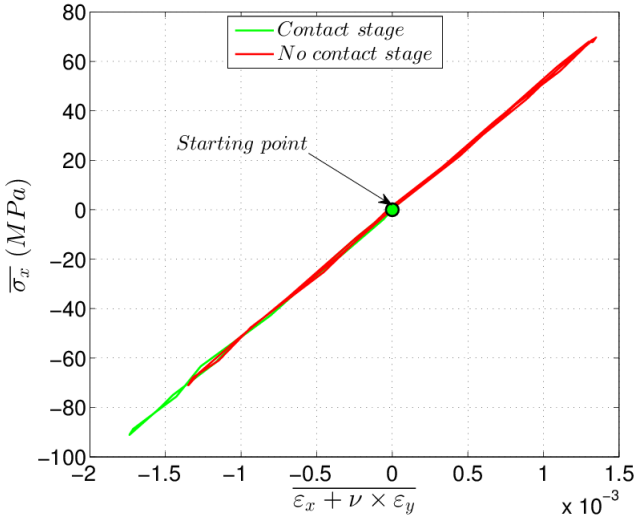

(C)

FIGURE 4.29: Stress-strain curve from data at the top surface at $x = 20.75\ mm$ with different damping parameters. Contact duration: 20 microseconds. (A) $\alpha = 0\ s^{-1}$, $\beta = 0\ s$. (B) $\alpha = 0\ s^{-1}$, $\beta = 1.10^{-6}\ s$. (C) $\alpha = 0\ s^{-1}$, $\beta = 2.10^{-8}\ s$.

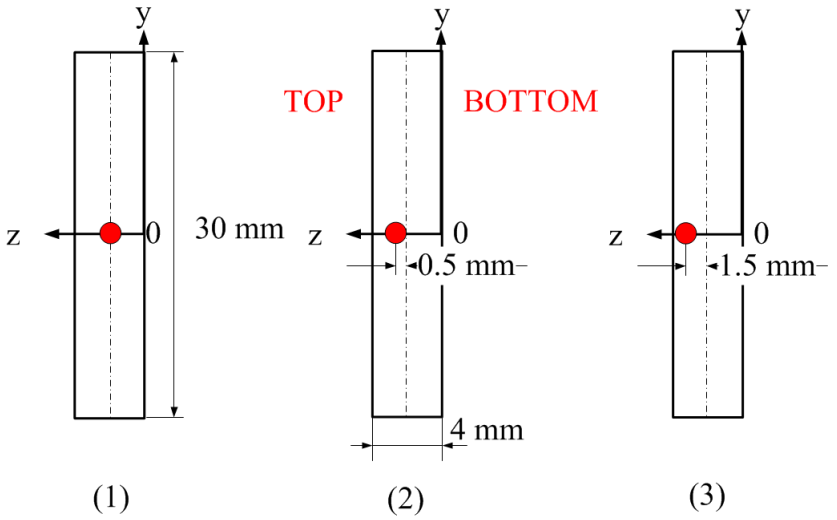

FIGURE 4.30: Schematic of the contact point models used in the FE simulation (the red points represent the contact points).

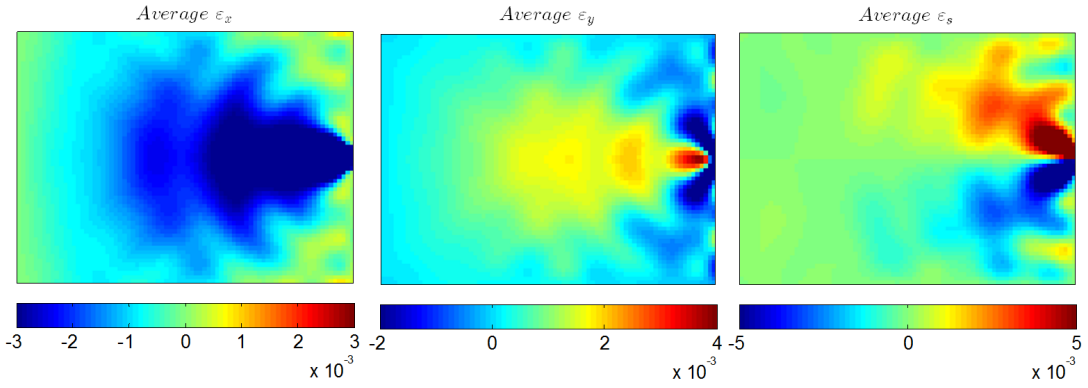

(A)

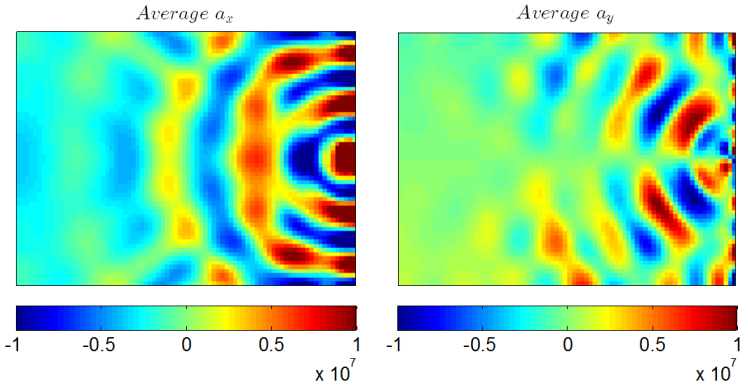

(B)

FIGURE 4.31: Maps of through-thickness average strain and acceleration at 14 microseconds without tab. (A) Strain. (B) Acceleration (in $m.s^{-2}$). $L = 40\ mm$.

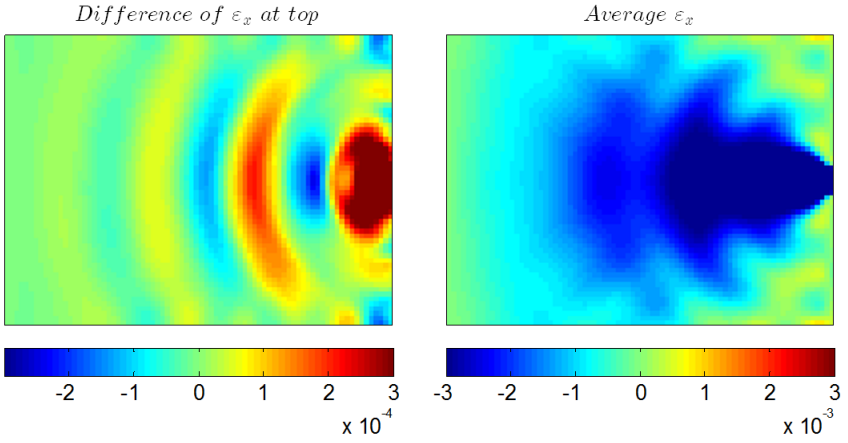

(A)

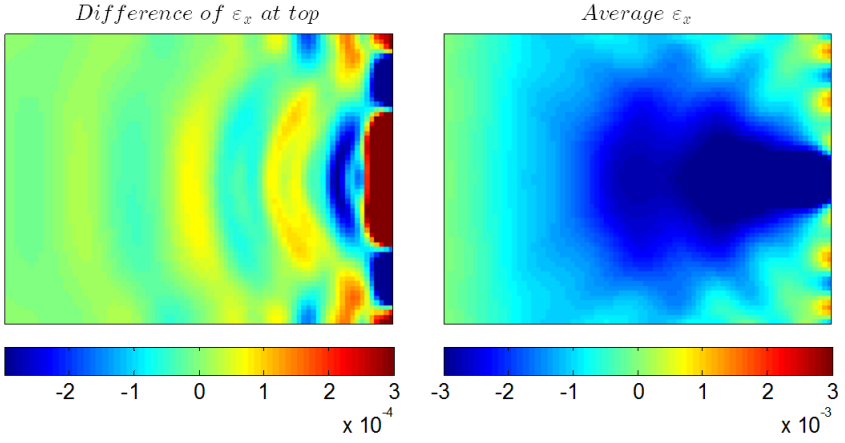

(B)

FIGURE 4.32: Differences between the top surface and through-thickness average strains in the longitudinal direction at 14 microseconds. (A) Without tab. (B) With tab. $L = 40\ mm$.

Contact model (2) with the tab was then simulated. The differences in longitudinal strain at the top and bottom surfaces at 14 microseconds are shown in Figure 4.33. It can be seen that the strains are much more heterogeneous through the thickness than that in Figure 4.32 (B). Because the average longitudinal strains are negative, the difference close to the impact end of the specimen tends to be negative at the top surface, whereas the bottom surface exhibits a positive strain difference in the same region. This problem will significantly disrupt the identification results as the volume integrals will be falsely evaluated from the surface ones. In addition to the tabs, another interesting idea to mitigate these $3D$ effects is to lengthen the specimen in order to benefit from Saint-Venant's principle. In this case, the field of view will be restricted to 40 mm from the free-end side of the specimen to be consistent with experimental conditions as imaging a longer field of view would compromise the spatial resolution of the measurements. Two models with specimen lengths of 60 and 80 mm for contact models (2) and (3) respectively were simulated with the same FE configuration as for the 40 mm specimen. Figure 4.34 presents the differences in longitudinal strains at the top and bottom surfaces for the two longer specimens at different time steps. Comparing Figures 4.33 and 4.34, one can clearly see that for the two longer specimens the strain differences at both surfaces in the field of view are significantly lower than that for the specimen of length 40 mm, although the average strains through the thickness of the three specimens are comparable. This means that lengthening the specimen mitigates the through-thickness strain heterogeneity in the specimen.

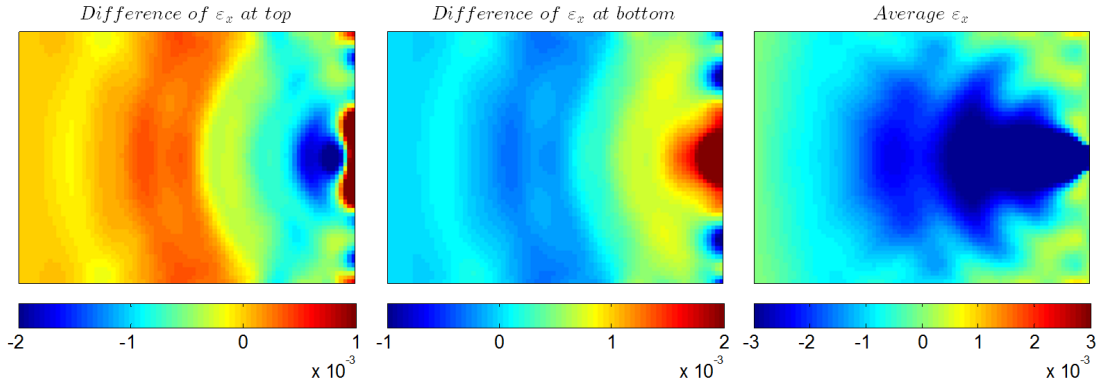

FIGURE 4.33: Relative longitudinal strains on top and bottom surfaces at 14 microseconds with pad. Contact model (2). $L = 40$ mm.

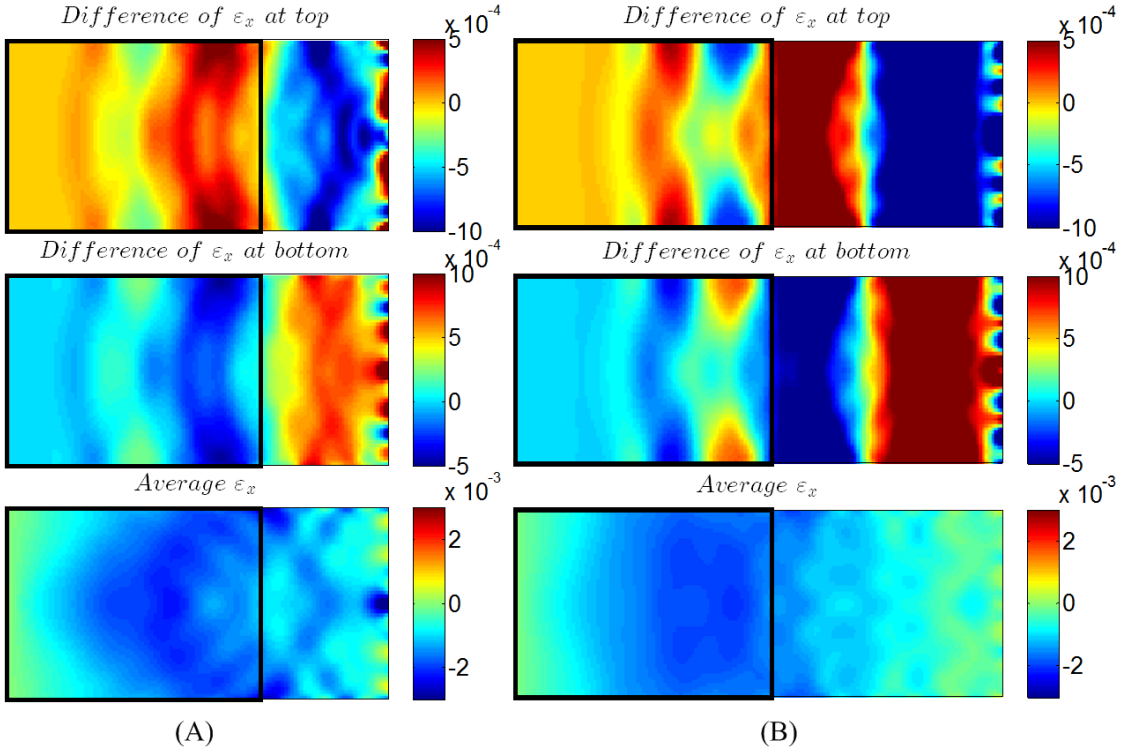

FIGURE 4.34: Differences in longitudinal strain at the top and bottom surfaces for longer specimens with tab. (A) $L = 60\ mm$, contact model (2) at 19 microseconds. (B) $L = 80\ mm$, contact model (3) at 23 microseconds. The black rectangular box represents the field of view.

4.3.2 Identification from simulated data

This section presents three different procedures to extract the elastic stiffness parameters from the simulated data, with increasing complexity. The first one assumes Poisson's ratio as known and investigates the identification of E through the plots of stress-strain curves using the non-parametric approach described in Section 3.2. The second one brings this one step further by using over-determined systems arising from the application of Equation 3.6, as introduced in Section 3.3. Finally, the full Virtual Fields Method approach is considered.

4.3.2.1 Stress-strain curves from simulated data

The influence of misalignment can also be quantitatively verified by the non-parametric method described in Section 3.2. Obviously, the stress/strain state in the ball impact simulation is not uniaxial. Figure 4.35 presents the average longitudinal stress as a function of the average $\varepsilon_x + \nu\varepsilon_y$ ($\nu = 0.3$, here) at $x = 20.75\ mm$ from the free end. The slope of the stress-strain curve provides the stiffness component Q_{xx} which relates to E through Equation 3.13. It is clear that the stress-strain curves from the top and bottom surfaces for contact model (1) are consistent with each other and linear, and the estimated Young's modulus for model (1) is around 47.2 GPa, very close to the input value of 47.5 GPa. For contact model (2) however, the curves from the top and bottom surfaces diverge, although the curve from the average data through the thickness matches that of contact model (1) very well, as expected.

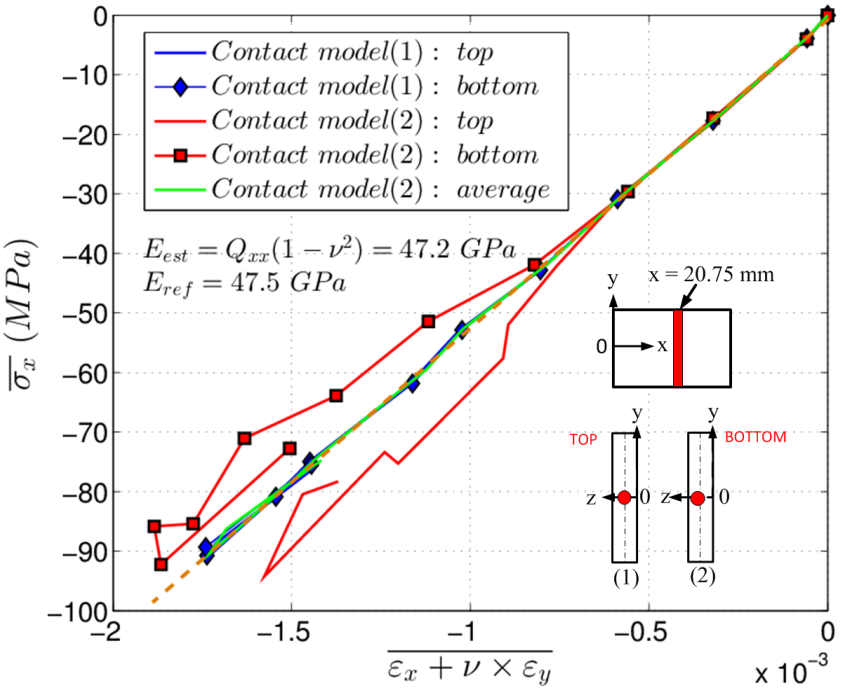

FIGURE 4.35: Stress-strain curves at the loading stage for contact models (1) and (2) at $x = 20.75\ mm$. $L = 40\ mm$.

To validate the Saint-Venant effect in the dynamic simulation, the stress-strain curves at $x = 20.75\ mm$ from the free end for all offset contact models mentioned previously are presented in Figure 4.36. It can clearly be seen that longer specimens lead to reduced discrepancies in the stress-strain curves from the top and bottom surfaces, even though larger misalignment was considered for the specimen of length 80 mm. The estimated E through fitting the first 20 points of the stress-strain curve on the top surface of the longest specimen is about 47.7 GPa. Young's modulus can also be identified for all transverse slices of the 40 mm long field of view along the longitudinal axis of the

specimen. Figure 4.37 presents the identified Young's modulus for all offset contact models. It seems that, for all specimens, the identified results from the top and bottom surfaces are symmetric about the reference value and tend to converge at the free (left) end. Moreover, with the increase of specimen length, the discrepancies of the identified Young's modulus from the top and bottom surfaces are reduced, even though a larger offset of the point contact was considered for the longest specimen. This means that lengthening the specimen reduces the stress/strain heterogeneity through the thickness at slices away from the impact. This solution was implemented experimentally to check for its practical validity (see Chapter 6).

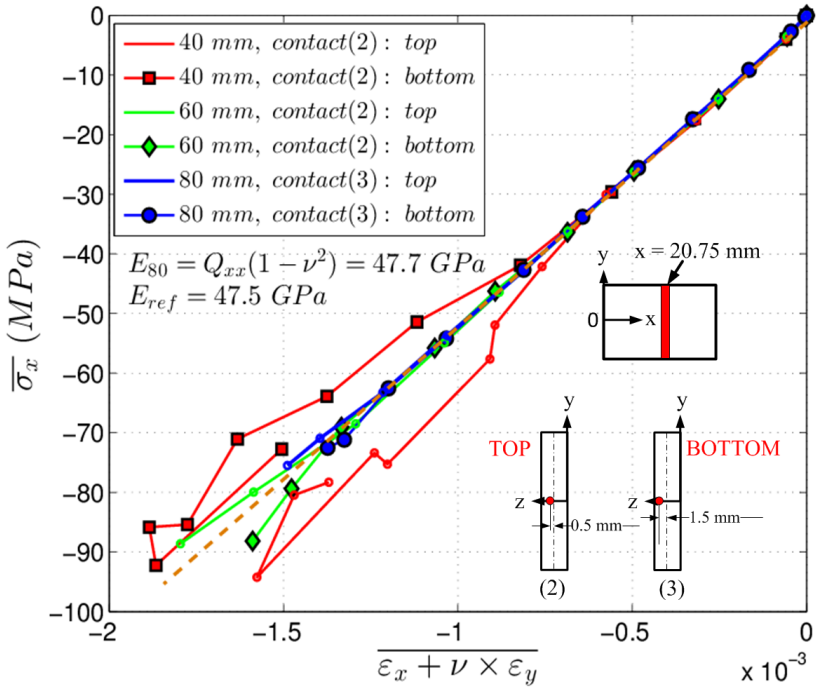

FIGURE 4.36: Stress-strain curves at the loading stage for contact models (2) and (3) with different lengths at $x = 20.75\ mm$.

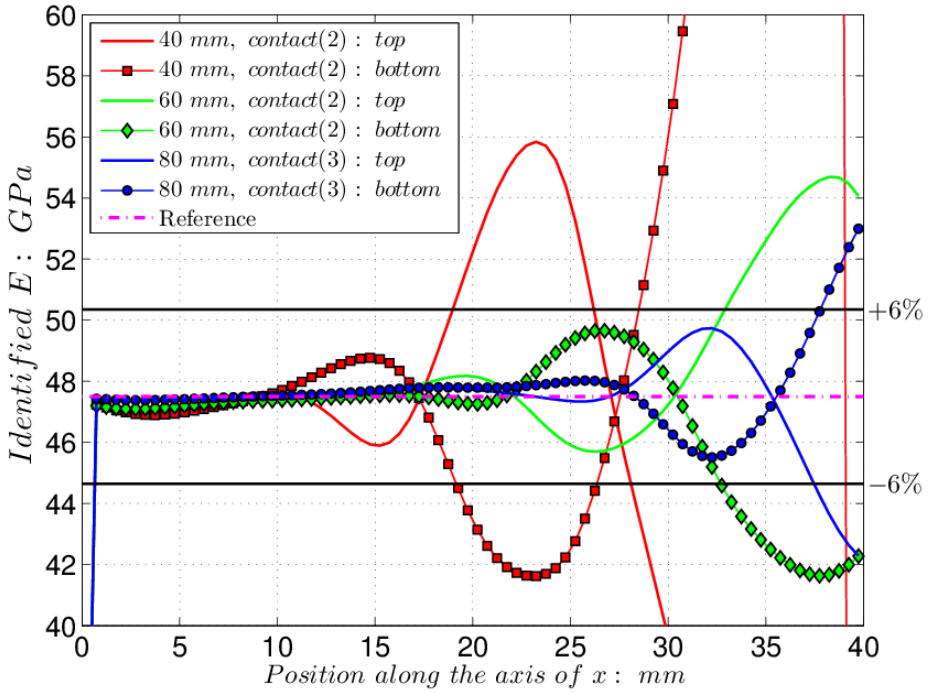

FIGURE 4.37: Identified Young's modulus from the stress-strain curves of specimens with different lengths with offset contact.

4.3.2.2 Over-determined system solution from simulated data

As mentioned in Section 3.3, Q_{xx} and Q_{xy} in Equation 3.43 are unknown. This equation can be used for each transverse slice at all times when strain and acceleration maps are available. In this FE simulation, 50 data frames containing the strain and acceleration maps were output from ABAQUS. So, at each slice, an over-determined system consisting of 50 equations (from the 50 data frames) with two unknowns Q_{xx} and Q_{xy} can be built up. This can be solved for Q_{xx} and Q_{xy} by a least-squares solution. However, for all offset contact models, the linearity of the stress-strain curves is only restricted to the loading stage. For instance, Figure 4.38 presents the stress-strain curve from the top surface of the specimen of length 80 mm at $x = 20.75$ mm. One can clearly see that within the loading stage (first 22 microseconds) the linearity is good, whereas during the unloading stage, the data are inconsistent. The reason for this is currently unknown but might be caused by erroneous FE calculation. In any case, in the rest of this paper, all of the over-determined system solutions only consist of data from the loading stage.

It must be emphasised that for contact model (1), Young's modulus is calculated through Equation 3.13 with the identified Poisson's ratio, whereas for contact models (2) and (3), E is calculated with $\nu = 0.3$ due to the inaccurate identification of Poisson's ratio. Firstly, the identified E and ν at each slice for the short specimen with contact model (1) are plotted in Figure 4.39. For the good contact model, it is clear that the identification

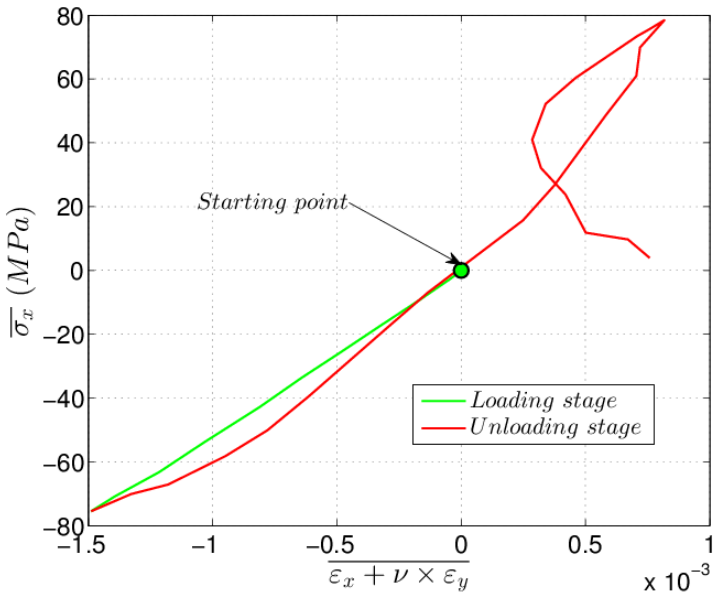

FIGURE 4.38: Stress-strain curve for the first 45 microseconds at $x = 20.75$ mm. $L = 80$ mm, contact model (3). Duration of the loading stage: 22 microseconds.

of Young's modulus is very good, except for the identification at slices close to the free and impact ends. This is not surprising for the free end as the stress values become very small. For the impact end, one would expect errors for the top and bottom data but not for the average. This is probably caused by errors in the FE data arising from the impedance difference between the steel tab and the tested material. As for the identification of Poisson's ratio, it is not as good as Young's modulus. For the offset contact models, the identified results are presented in Figure 4.40. It can be seen that the identification is significantly worse than that for contact model (1). For the same specimen, the identified Young's modulus from the top and bottom surfaces converges at the left part of the specimen. This tendency is consistent with that in Figure 4.37, however, the identification from the over-determined system is worse than that in Figure 4.37. The exact reason for this has not been established yet but it might be that at some time during the loading, each slice contains a low stress and low strain situation which generates some error in the lest-square inversion. This will need to be investigated in the future as this identification approach is very appealing because of its simplicity.

It is also possible to consider all slices at the same time to identify one overall value of E and ν. Since it has been shown that the data close to the impact and free ends are not reliable, only a central section away from the ends has been kept by discarding 4 and 12 columns of data from the free and impact ends respectively over a total of 80 columns of data. The identified overall Young's modulus and Poisson's ratio are shown in Table 4.7. The percentages in brackets represent the errors from the reference. It is clear that for

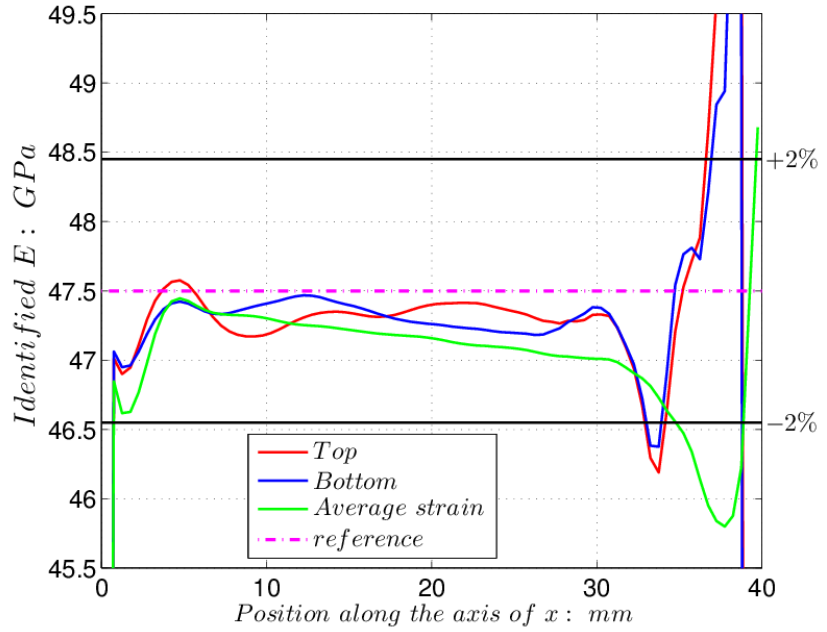

(A)

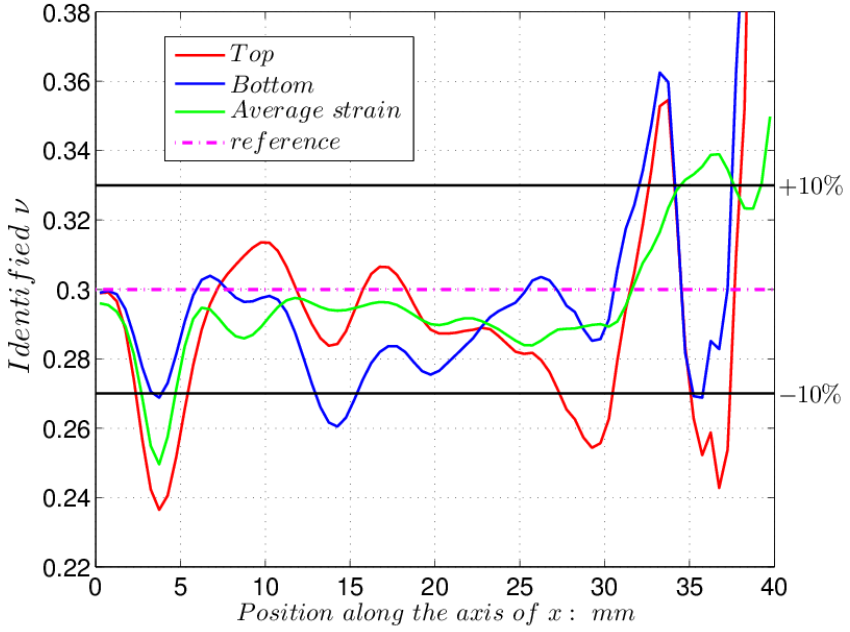

(B)

FIGURE 4.39: Identification of Young's modulus and Poisson's ratio from the over-determined system for the good contact model. $L = 40\ mm$. (A) Young's modulus. (B) Poisson's ratio.

all contact models the identified results from the average fields through the thickness are good. Moreover, the identification of Poisson's ratio is worse than that of Young's modulus. For the offset contact models (2) and (3), the identification is unsatisfactory, however, with increasing specimen length, the errors reduce, even for the larger offset considered for the longest specimen.

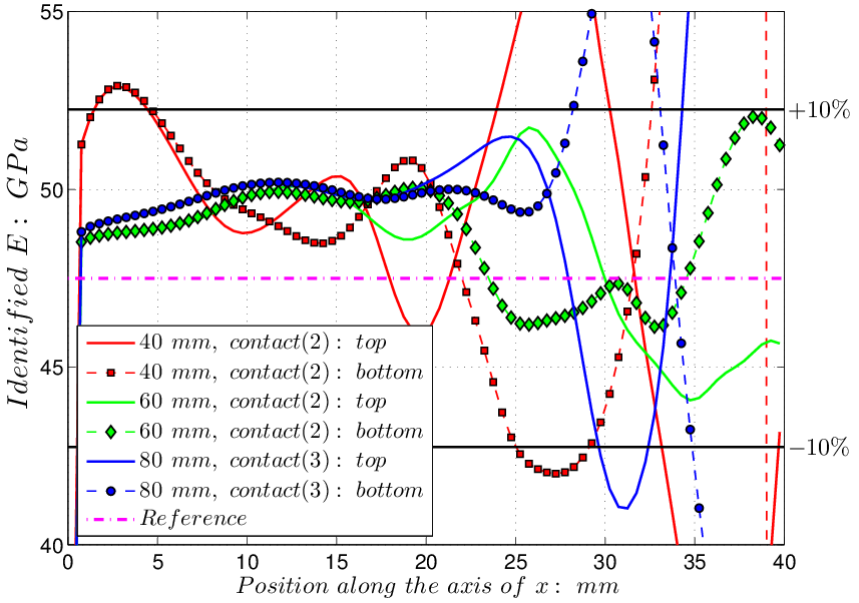

(A)

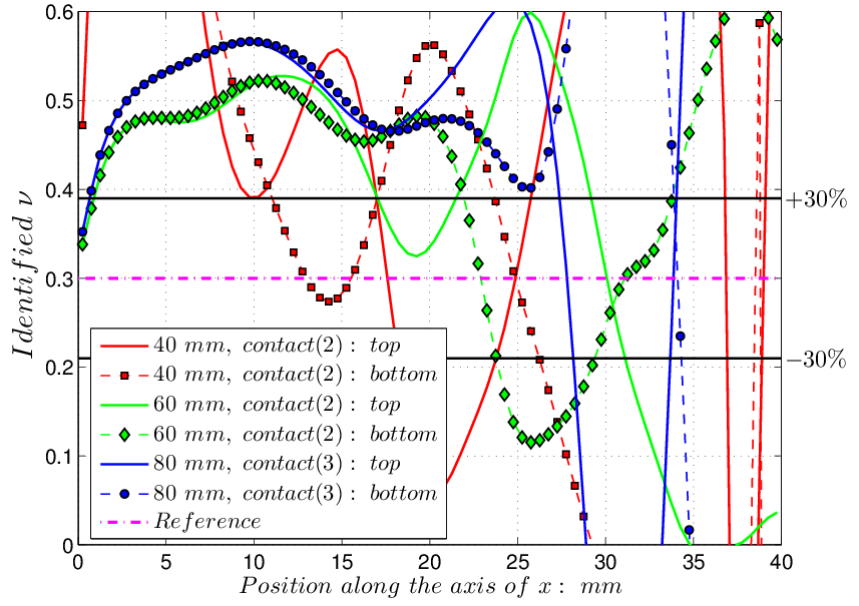

(B)

FIGURE 4.40: Identification of Young's modulus and Poisson's ratio from the over-determined system for the offset contact models. (A) Young's modulus. (B) Poisson's ratio.

TABLE 4.7: Identification of E and ν from the large over-determined system with data from the central area. Reference: $E = 47.5\ GPa$. $\nu = 0.3$.

	E: GPa			ν		
	Top	Bottom	Average field	Top	Bottom	Average field
$L = 40\ mm$, contact (1)	47.9 (0.8 %)	48.0 (1.1 %)	46.9 (1.3 %)	0.31 (3.3 %)	0.31 (3.3 %)	0.29 (3.3 %)
$L = 40\ mm$, contact (2)	38.0 (20.0 %)	41.5 (12.6 %)	46.9 (1.3 %)	0.02 (93.3 %)	0.10 (66.7 %)	0.29 (3.3 %)
$L = 60\ mm$, contact (2)	46.2 (2.7 %)	48.6 (2.3 %)	47.3 (0.4 %)	0.22 (26.7 %)	0.35 (16.7 %)	0.30 (0.0 %)
$L = 80\ mm$, contact (3)	48.3 (1.7 %)	49.4 (4.0 %)	47.4 (0.2 %)	0.34 (13.3 %)	0.44 (46.7 %)	0.30 (0.0 %)

4.3.2.3 VFM identification from simulated data

The same simulated sets of data were processed by the VFM. Firstly, the data from the whole field of view were considered. In this procedure, the virtual mesh used to expand the virtual fields is composed of 4 elements in the x-direction and 3 elements in the y-direction. The virtual displacement along the right-hand side boundary of the field of view is set to 0 so as to cancel out the virtual work of the impact forces at the right end. In the VFM, Q_{xx} and Q_{xy} are first identified. Young's modulus and Poisson's ratio are then calculated through Equation 3.13. The results for contact model (1) are shown in Figure 4.41. It can be seen that the identified results from the top and bottom surfaces match, even though they slightly diverge from that from the average data through the thickness, even for the good contact model. Moreover, the identified Young's modulus values from the top and bottom surfaces are significantly higher than that for the average data during the first 20 microseconds (within the contact stage), thereafter, they gradually converge to the reference value. This was expected because, for the good contact model, during the contact stage the strain levels at the top and bottom surfaces are always lower than the average value through the thickness, which leads to higher Young's modulus at the top and bottom surfaces. When contact is lost at around 20 microseconds, the strain state through the thickness tends to become more uniform as the waves bouncing between the top and bottom surfaces get damped, hence the converged values. In addition, as seen in Figure 4.41, some oscillations can clearly be observed at around 20 and 30 microseconds, especially for Poisson's ratio. It is still not clear what is causing this.

It has been shown that the identification at slices close to the free and impact ends of the specimen is not reliable, as seen in Figures 4.37 and 4.40. In the VFM processing, if only data from the central area is considered, for instance, removing data from 4 columns from the left (free) end and 12 columns from the right (impact) end of the specimen (the whole data set consists of 80 columns by 60 rows), the VFM results in Figure 4.42 are obtained. It is worth noting that in this case the virtual displacement vector along the left and right boundaries of the region of interest is necessarily set to zero so as to cancel out the virtual work of the unknown forces applied at both boundaries. As seen in Figure 4.42, it is clear that the identification errors are significantly reduced, and the results from the surfaces and the through-thickness average match very well. This is mainly because the through-thickness stress and strain heterogeneities are concentrated at the impact end, as already illustrated previously. However, some oscillations at 20, 30 and 40 microseconds persist and cannot be interpreted at the present time.

The simulated data for the offset contact models have also been processed with the VFM. The data over the complete field of view was kept here, since as the results were

much worse than for contact model (1), removing the end data did not significantly change the trends of the results. As shown in Figure 4.38 for the offset contact models, good linearity of stress-strain curves is only restricted to the loading stage. Moreover, in the experimental tests, the recording duration of the ultra-high speed camera is only 25.6 microseconds. Therefore, for all offset contact models, only the identification within the first 25 microseconds is presented in the following. The identification for the short specimen ($L = 40\ mm$) proved quite unsatisfactory, as shown in Figure 4.43. It is clear that the modulus identified from the top surface data is systematically lower than that from the bottom surface. The reason is the same as for the results in Figure 4.41. At the top surface, strains are larger than at the bottom surface within the first 25 microseconds for the short specimen, hence the identified Young's modulus at the top surface is lower. Figure 4.44 shows the VFM identification results for the longer specimens. It can be seen that the discrepancies of the identified Young's Modulus and Poisson's ratio are significantly reduced through lengthening of the specimen, even though a larger offset has been considered for the longest specimen. However, for these long specimens, the identification from the top surface seems to be higher than that from the bottom surface, which is opposed to the trend seen in Figure 4.43. This is thought to be caused by an inversion of the through-thickness strain distribution pattern as the wave propagates further down the longer specimens and bounces off the free lateral surfaces.

As a conclusion to this section on numerical simulations, all three identification strategies have confirmed that increasing the specimen length mitigates the effect of through-thickness strain heterogeneity and provides results closer to the reference. An experimental investigation of this effect will be described in the following chapter.

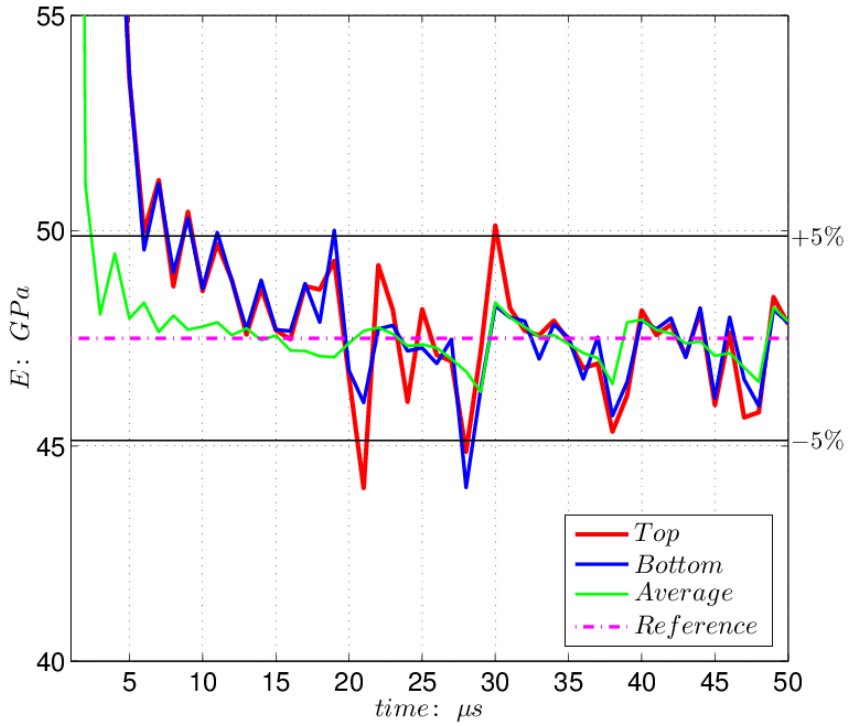

(A)

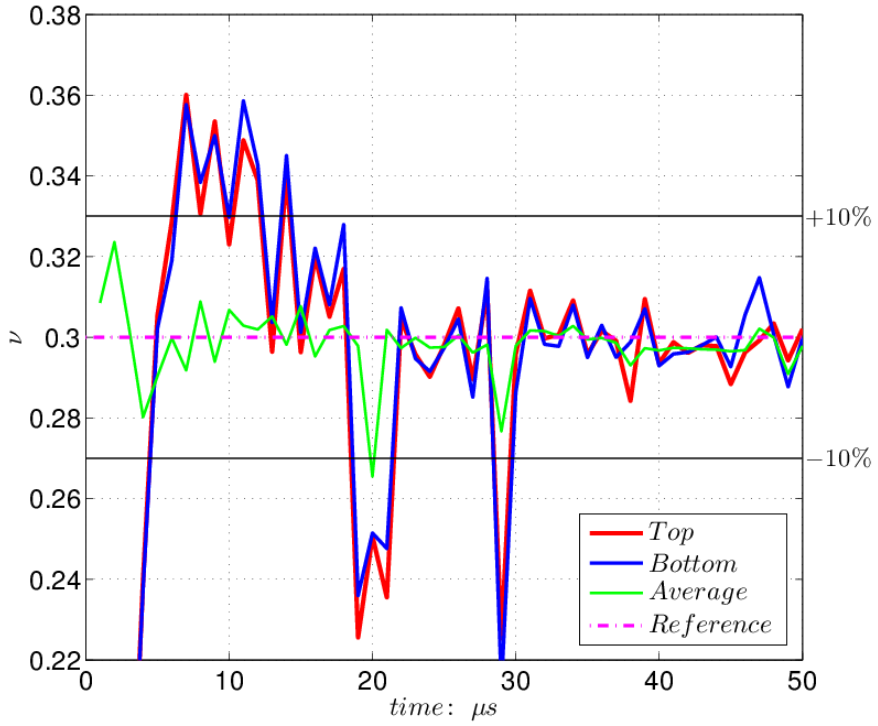

(B)

FIGURE 4.41: Identification of Young's modulus and Poisson's ratio from the whole field of view with the VFM. Data points: 80 by 60. Virtual mesh: 4 by 3. $L = 40\ mm$. Contact Model (1). (A) Young's modulus. (B) Poisson's ratio.

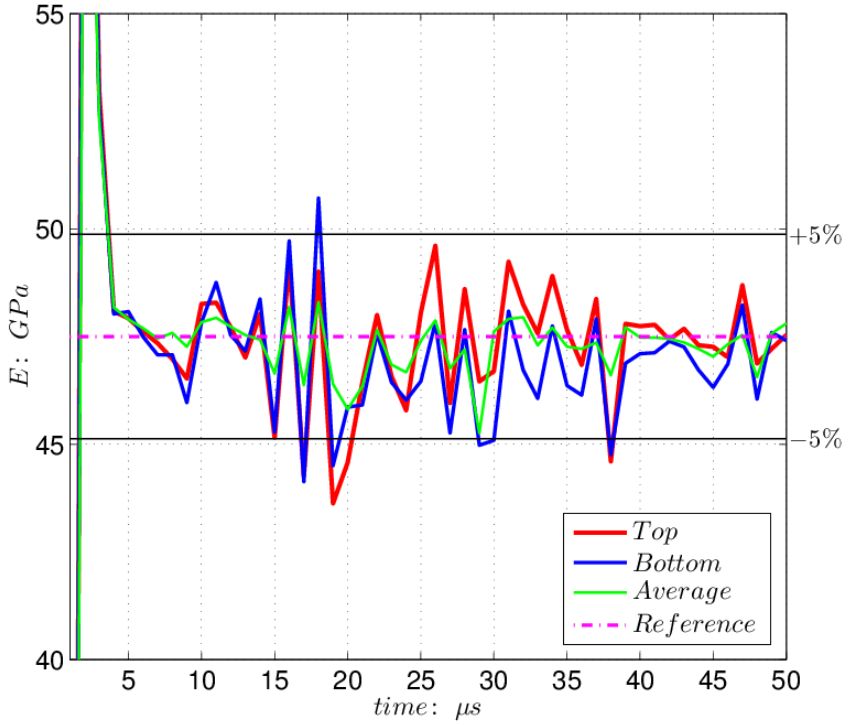

(A)

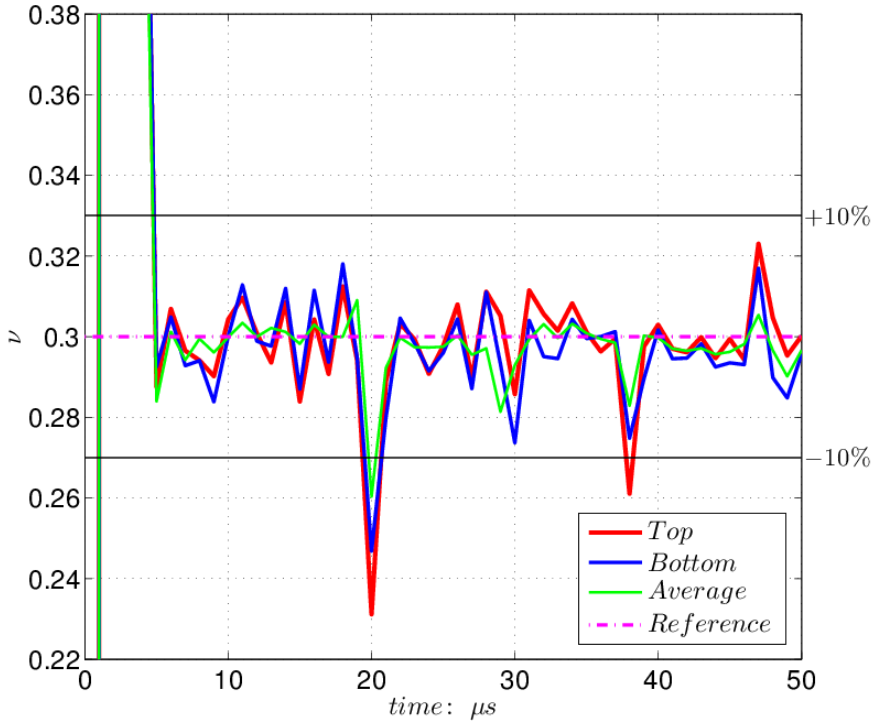

(B)

FIGURE 4.42: Identification of Young's modulus and Poisson's ratio from the central area with the VFM. Data points: 64 by 60. Virtual mesh: 4 by 3. $L = 40\ mm$. Contact Model (1). (A) Young's modulus. (B) Poisson's ratio.

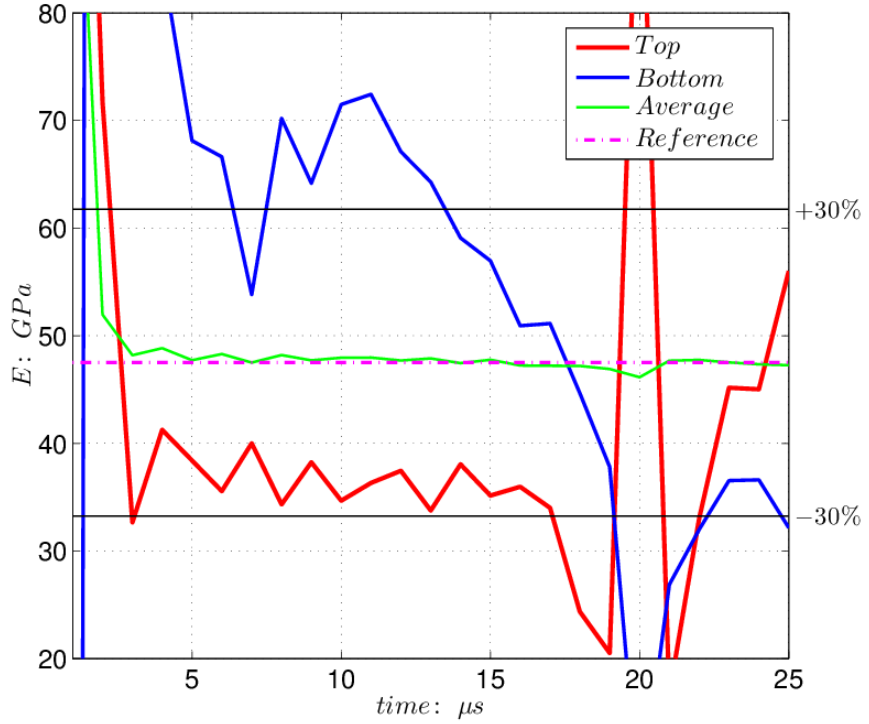

(A)

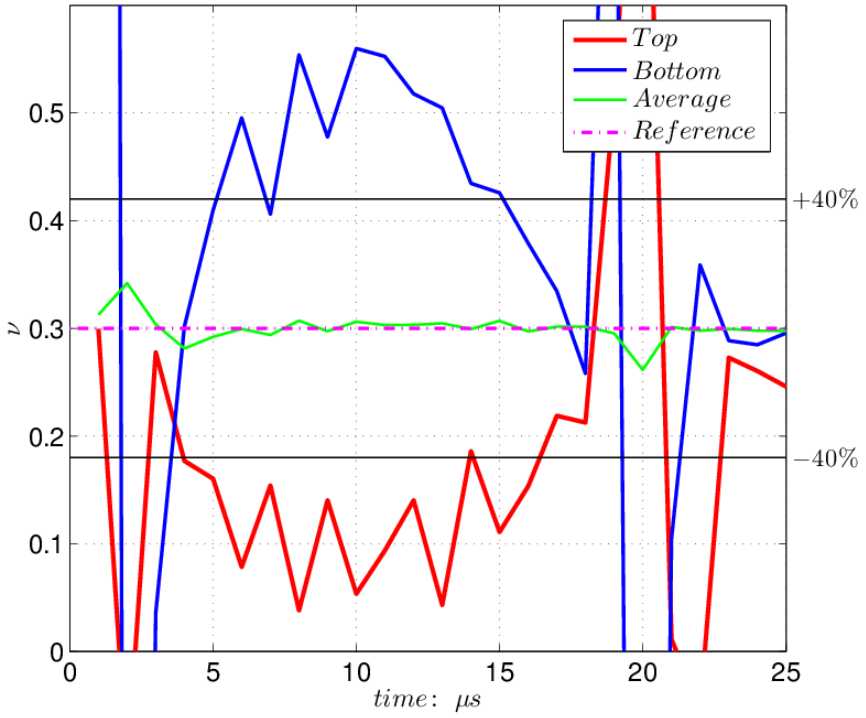

(B)

FIGURE 4.43: Identification of Young's modulus and Poisson's ratio with the VFM. Data points: 80 by 60. Virtual mesh: 4 by 3. $L = 40\ mm$. Contact Model (2). (A) Young's modulus. (B) Poisson's ratio.

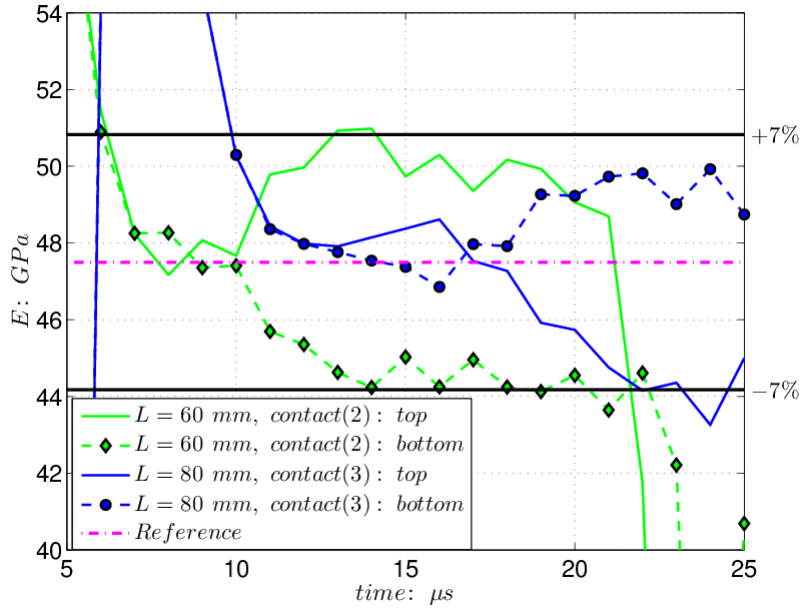

(A)

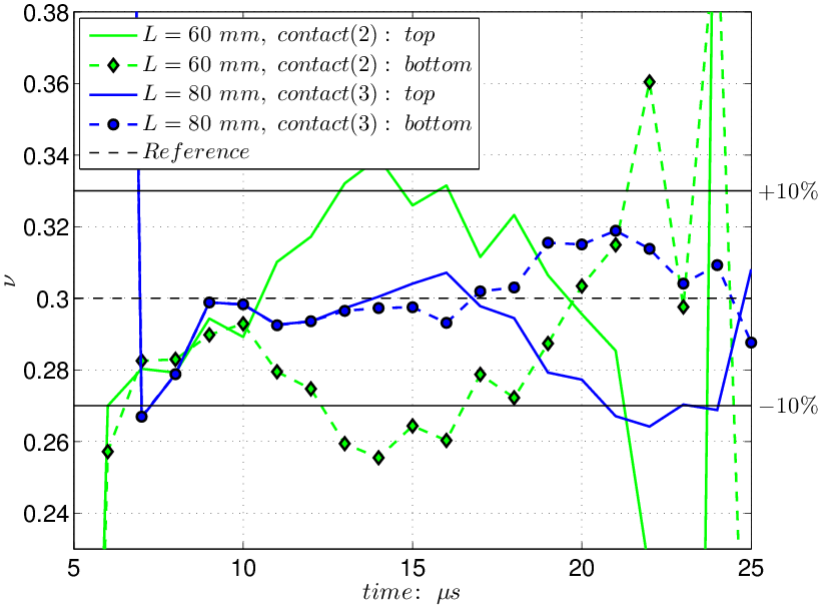

(B)

FIGURE 4.44: Identification of Young's modulus and Poisson's ratio with the VFM. Data points: 80 by 60. Virtual mesh: 4 by 3. Offset contact models & longer specimens. (A) Young's modulus. (B) Poisson's ratio.

4.4 Non-linear laws

As mentioned in Section 3.2.3, a non-linear shear stress-strain relationship as in Equation 3.40 was considered while the other two components remained linear elastic functions of the strain components. Fitting M. Longana's experimental data when $\vartheta = 11°$ [32] using the non-linear shear stress-strain model in Equation 3.40, the calculated Q_{66} is around 4 GPa and K is about 2.10^6 GPa. Thus, in this FE simulation, the input parameters were selected as: $Q_{11} = 124.0$ GPa, $Q_{12} = 2.3$ GPa, $Q_{22} = 7.5$ GPa, $Q_{66} = 4.0$ GPa and $K = 2.10^6$ GPa. Based on this non-linear parameter, the shear stress-strain relationship can be plotted as shown in Figure 4.45. It is clearly seen that with the present parameters the non-linear behaviour is significant when the strain level is higher than 1 %. The off-axis fibre orientation are from 5° to 85° with a step of 5°, hence 17 fibre orientations in total. The FE simulation details are shown in Table 4.2. The specimen geometry is the same as that in Figure 4.16, and the non-linear constitutive model was implemented using the user subroutine program of ABAQUS/EXPLICIT (see Appendix E) to produce full-field strain and acceleration maps. In Equation 3.46, only Q_{66} and K are now considered as unknown. For the sake of simplicity, it has been supposed that Q_{11}, Q_{12} and Q_{22} are known *a priori*. In this FE simulation, 60 data frames containing the strain and acceleration fields were output. Equation 3.46 can be used for each transverse slice at all frames. Thus, at each slice, an over-determined system consisting of 60 equations with only two unknowns can be built up. Finally, Q_{66} and K can be identified at each transverse slice by a least-squares solutions. In each off-axis case, the identified Q_{66} and K were averaged over all transverse slices. This procedure was implemented at each off-axis fibre angle. The results are reported in Figure 4.46. The relative error on Q_{66} is less than 1 %, whereas the error on K is more than 15 %. The exact reason is under investigation, and it might be because of the FE calculation again, similar to that in the strain rate dependent simulation in Section 4.2.2. Moreover, the identified Q_{66} and K at intermediate off-axis fibre orientations ($20° \sim 60°$) are better than that for low or high off-axis fibre angles. This is expected because for low or large off-axis fibre orientations, the shear stress is too low compared to the predominant normal stresses, leading to a bias in the identification probably arising from the uncertainties in the FE calculation. This could also be caused by bad conditioning of the over-determined system. This part of work was an exploratory attempt. Further investigation should be conducted to understand these issues. For instance, the optimized virtual fields is worth being extended to this case.

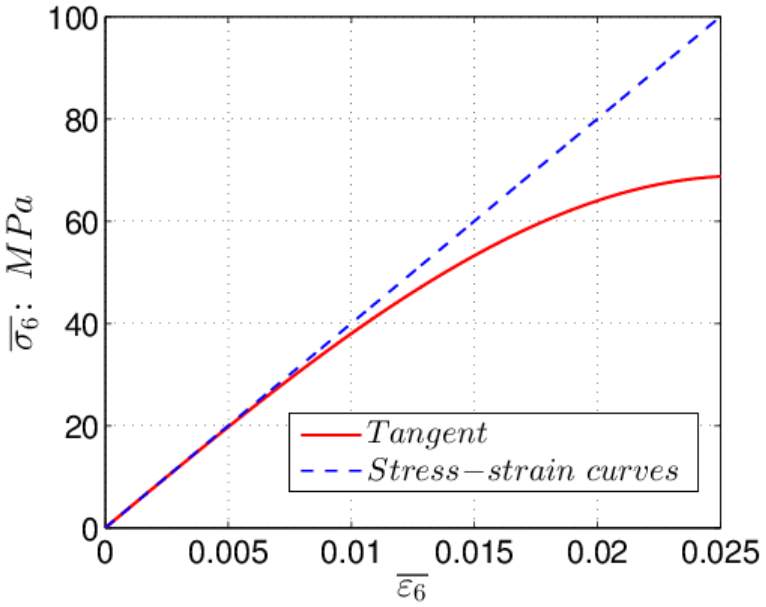

FIGURE 4.45: Non-linear relationship of the shear stress and strain with $Q_{66} = 4\ GPa$ and $K = 2.10^6\ GPa$.

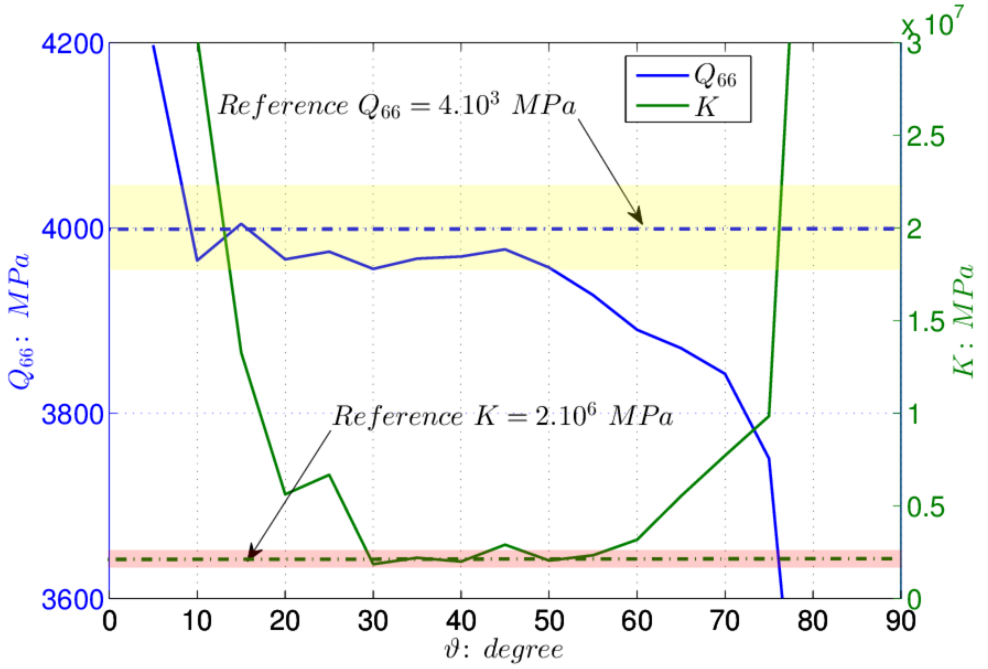

FIGURE 4.46: Relationship between the identified parameters and the fibre orientations. The error band of Q_{66} (yellow area) is 1 % and 15 % for K (pink area).

4.5 Summary

This chapter demonstrated substantial validations of new VFM-based procedures to identify the constitutive parameters of materials at high strain rates making use of inertial effects based on different FE models. A simple isotropic linear elastic model was first considered. Two types of projectiles were used to produce high-strain-rate deformation and inertial fields. Young's modulus and Poisson's ratio of this isotropic model were identified successfully. The relative errors were both less than 1 %.

The orthotropic linear elastic model including strain rate effect was then presented. Without strain rate dependence, series of orthotropic linear elastic models with different off-axis fibre orientations were run. Four independent orthotropic stiffness components were identified at each fibre angle. The relationship between the coefficients of variations of the identified stiffness components and the fibre orientation showed the identification of the longitudinal (transverse) stiffness component Q_{11} (Q_{22}) is worse (better) with the increasing fibre angles. This is expected because at low (high) off-axis fibre angles the longitudinal (transverse) stress in the fibre direction is higher, which leads to better ratios of signal to noise. As for the shear stiffness Q_{66}, the values of η_{66}/Q_{66} were large at low and high off-axis fibre angles, whereas at intermediate fibre angles the values were comparatively small. This is because at low and high fibre angles, the shear stress in the fibre coordinate system are too low to enable robust identification. The tendency for the identification of Q_{12} was similar to that of Q_{66}. The strain rate dependence of the transverse and shear stiffness components was then considered. The strain rate dependent model was implemented using the VUMAT user subroutine of ABAQUS/-EXPLICIT to produce time-resolved strain, strain rate and acceleration fields. A new VFM-based methodology for identifying the strain rate dependent parameters was developed. However, the identification errors were comparatively high. This was shown to be a consequence of the direct FE calculation and not the identification. The actual source of this computational errors is still unknown.

Current UHS full-field measurement techniques are only capable of acquiring the deformation at the specimen surface. However, depending on the nature and quality of the contact between the projectile and the test specimen, some through-thickness strain heterogeneity may take place which will introduce an error when evaluating the volume integrals from surface measurements in the VFM equations. Therefore, detailed $3D$ FE simulations consisting of firing a small steel ball impactor at a rectangular free standing isotropic specimen were performed. Different offset impact models and specimens with various lengths were considered. Full-field strain and acceleration fields were output at the top and bottom surfaces and then processed by different methodologies to identify the constitutive parameters. The results from different methodologies were consistent

and showed that the parasitic effects arising from non-uniform through-the-thickness loading can successfully be mitigated by the use of longer specimens, making use of Saint-Venant's principle in dynamics.

Lastly, it is well-known that the shear stress-strain relationship for a unidirectional composite is significantly non-linear. Therefore, this chapter explored the identification of this non-linear shear stress-strain behaviour based on FE simulated data from a user-defined constitutive model. The related FE simulation was implemented in VUMAT with different off-axis fibre orientations. Similarly, time-resolved fields were output and then processed by the over-determined system procedure. The results proved that the identification at intermediate off-axis fibre angles were better than that at low and high fibre angles, because the shear stress is higher at intermediate off-axis fibre angles.

All of these FE simulations validated that in the VFM processing inertial effects can be used to identify the material parameters without the need for any impact force measurement. The VFM procedures with different FE models described in this chapter have been implemented experimentally and are presented in the following chapters.

Chapter 5

Experimental procedure for ultra-high speed imaging

Chapter 3 demonstrated how to identify the material parameters using inertial effects at high strain rates, which was then numerically explored on different constitutive models in Chapter 4. The identified results from simulated data proved that inertial effects can be used as a load cell in the VFM to identify the material parameters at high strain rates. Chapters 5 and 6 describe the experimental implementations of this procedure. Chapter 5 mainly describes the detailed experiment procedures including the tested materials and the ultra-speed imaging configurations and reports the deformation measurement performances as a function of the camera and image processing parameters. Two types of UHS cameras (SIMX16 and Shimadzu HPV-X cameras, respectively) were used to record images at high strain rates. Two projectiles with different shapes (a steel cylinder and a steel ball, respectively) were used to provide inertial loading. Chapter 6 presents the full-field maps of the experimental tests and related identification results using the methodologies described in the previous chapters.

5.1 Tests and materials

In this work, two types of composites lay-ups were employed. The first one is an in-plane quasi-isotropic laminate lay-up used to validate the isotropic linear elastic model. The other one is a unidirectional laminate for the identification of orthotropic parameters. The quasi-isotropic specimens were laminated to the following $[0/45/-45/90]_s$ stacking sequence from CYTEC MTM58FRB carbon/epoxy prepreg, whereas the unidirectional lay-up used the same number of plies but all oriented in the same direction $[0]_8$. All laminates were laid up and autoclaved at the University of Southampton to a maximum

temperature of 120°C and pressure of 3.2 bar, according to the curing cycle recommended by the prepreg manufacturer. The thickness of these specimens was around 3.7 mm. The nominal quasi-static stiffness parameters of the carbon/epoxy prepreg are: $E_{11} = 123.7\ GPa$, $E_{22} = 7.5\ GPa$, $\nu_{12} = 0.31$, $G_{12} = 4.0\ GPa$ [32]. The moduli identified at different strain rates from [32] are shown in Table 5.1. For the quasi-isotropic specimens, due to the nature of such layup, the in-plane elastic stiffness components only depend on two parameters. Based on lamination theory, the in-plane Young's modulus of this quasi-isotropic laminate is 47.1 GPa and Poisson's ratio is 0.31. Additionally, the specimens are expected to exhibit low strain rate dependence because the behaviour of this quasi-isotropic lay-up is highly dominated by the fibres which do not show any significant strain rate dependence [136]. Therefore, the quasi-static Young's modulus and Poisson's ratio will be used as the reference values in this work. However, as reviewed in Section 2.5, the unidirectional laminate was shown to exhibit significant strain rate dependence in shear and transverse tension and compression, as reported in Table 5.1 (data from [32]). Unfortunately, the strain rates experienced here are much larger than that reported in [32], meaning that no effective reference values are available for the unidirectional lay-up. The model described in Equation 3.38 will be used for the strain rate dependence analysis in the following.

TABLE 5.1: Moduli summary in GPa at different strain rates [32].

Strain rate: s^{-1}	E_{11}	E_{22}	G_{12}
$1.25.10^{-4}$	123.7	7.5	4.0
$1.25.10^{-3}$	125.0	8.0	4.4
1.25	126.2	9.5	4.9
12.5	127.5	9.6	5.3
62.5	129.4	10.3	5.5

5.1.1 Cylindrical impact rig

Two different experimental set-ups were used to provide impact loading. The first one employs a cylindrical impactor of which diameter is slightly larger than the width of the specimens, ensuring an ideally uniform contact over the specimen impact area. The tests were performed at the University of Oxford in collaboration with Dr Clive Siviour at the Engineering Department. A simplified picture of the experimental set-up can be found in Figure 5.1. The projectile is a steel cylinder of diameter 35 mm and length of 50 mm. It is launched by a gas gun to reach a nominal speed of 30 $m.s^{-1}$ for these experiments. The specimen is positioned on a foam support at the exit of the gas barrel so as to provide free-free boundary conditions. The specimens were cut to the dimensions of

40×30 mm (length $\times$ width) from quasi-isotropic and unidirectional composite panels. As mentioned in Section 2.3, the grid method was used to perform full-field deformation measurements at high strain rates. The surface preparation procedure for the grid method can be found in [162]. The choice of the grid pitch depends on the spatial resolution of the camera used to record the images, which will be reported later on when describing the imaging configurations. Five specimens were tested on this impact rig. The information is shown in Table 5.2. Specimen SIMX-16 was tested using the SIMX16 camera, and the rest were tested using the Shimadzu HPV-X camera. The details of the cameras are introduced in the following section.

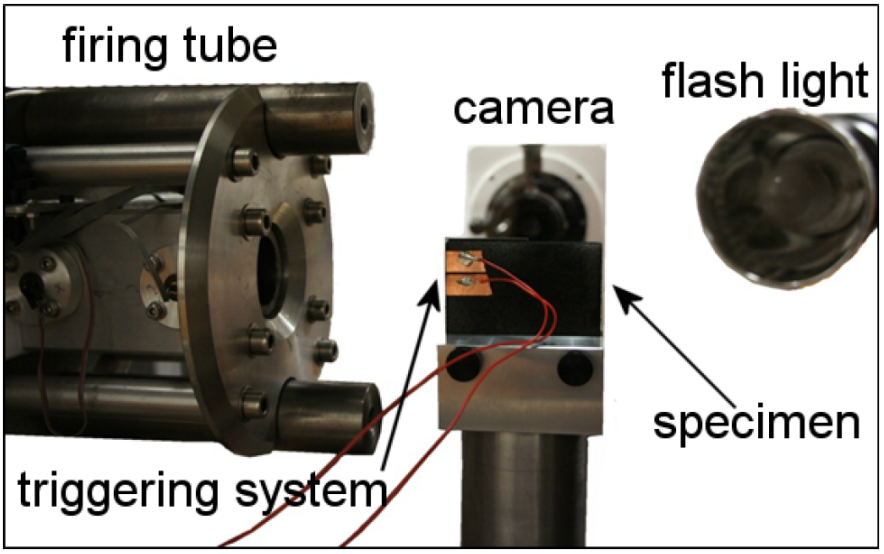

FIGURE 5.1: Schematic picture of the impact test set-up: cylindrical impactor.

TABLE 5.2: Dimensions and impact speeds for the different specimens tested on the cylindrical impact rig. Diameter of the cylindrical impactor: 35 mm, length: 50 mm, its density: $7.8.10^3$ $kg.m^3$. Kinematic energy of impactor: 171 J.

	Length: mm	Impact speed: $m.s^{-1}$	Fibre angle: degree
Specimen HPV-X	40	≈ 30	Quasi-isotropic
Specimen SIMX-16	40	≈ 30	Quasi-isotropic
Specimen 15-1	40	≈ 30	15
Specimen 40-1	40	≈ 30	40
Specimen 40-2	40	≈ 30	40

5.1.2 Ball-bullet impact rig

Series of in-plane ball impact tests were also carried out. The experimental set-up is shown in Figure 5.2. It is composed of a gun connected to an air pump and a 9 mm diameter steel ball used as the projectile. The specimen was positioned at the exit of

the gun barrel with the help of a foam support, so as to provide free-free boundary conditions. A thin steel tab of thickness 1 mm was bonded onto the impact end of the specimen so as to mitigate the stress concentration. This has the unfortunate effect of also absorbing some of the impact energy as the tab deforms plastically but tests without the tabs have proved worse with too much damage to the composite specimens at the impact end, which is detrimental to the present analysis. This is clearly a disadvantage of the ball impact when compared to the cylindrical impact. The specimen was enclosed in a chamber with transparent perspex walls at its top and front faces. A couple of quasi-isotropic and unidirectional specimens with different lengths but same width were tested using the grid method in this study. The dimensions and the impact speeds are shown in Table 5.3. The kinematic energy of the ball impactor is much lower than that of the cylindrical impactor, as presented in Tables 5.2 and 5.3.

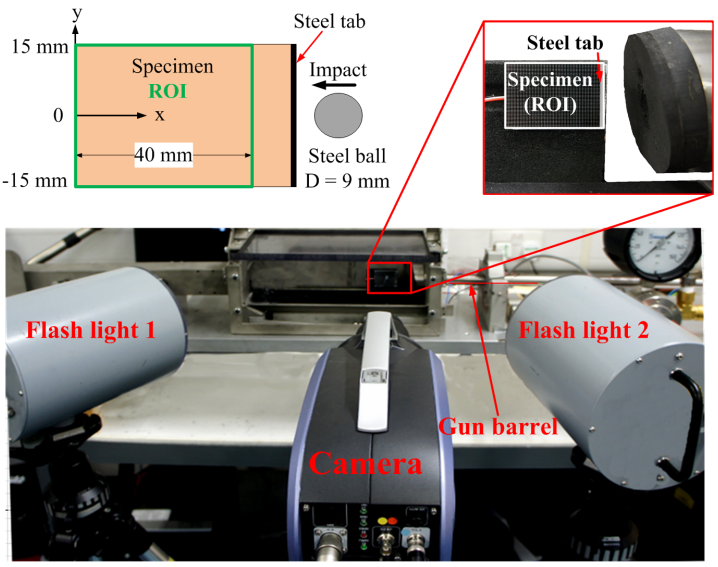

FIGURE 5.2: Schematic and picture of the impact test set-up: ball-bullet impactor.

TABLE 5.3: Dimensions and impact speeds for the different specimens in the ball impact tests. Diameter of ball: 9 mm, its density: $7.8.10^3$ $kg.m^3$. Kinematic energy of the ball impactor: 3 J for the speed of 45 m/s^{-1} and 1.8 J for the speed of 35 m/s^{-1}.

	Length: mm	Impact speed: $m.s^{-1}$	Fibre angle: degree
Specimen QI-1	40	≈ 35	
Specimen QI-2	60	≈ 45	Quasi-isotropic
Specimen QI-3	80	≈ 45	
Specimen UD-15-1	40	≈ 35	
Specimen UD-15-2	60	≈ 45	15
Specimen UD-15-3	80	≈ 45	
Specimen UD-60-1	40	≈ 35	60
Specimen UD-60-2	60	≈ 45	

5.2 Ultra-high speed imaging

As mentioned in Section 5.1, two types of experimental set-ups were used to implement these impact tests. Due to the differences between the two experimental set-ups, the UHS imaging systems were slightly different, as reported in the following.

5.2.1 Cylindrical impact tests

Because it is required to derive acceleration maps from displacements, it is necessary to grab images with very low inter-frame times, of the order of a microsecond. This is the range of what Reu & Miller [59] define as ultra-high speed imaging. Here, two different cameras with such frame rate performances have been used, which is interesting to check for the effect of image quality on the identification results. The first camera is a Specialised Imaging SIMX16. This is an intensified gated camera the principle of which relies on dividing the light into several optical paths, here 16, and recording at very high rates by electronically gating the corresponding 16 CCD sensors sequentially. The fact that light is divided by as many channels as there are CCD sensors leads to the need for light amplification. Unfortunately, this causes a number of issues, including 'leakage' of light over neighboring pixels, blurring the image and creating significant spurious strains. This is documented in [62, 63] for a similar camera using the same technology, the IMACON200, even if the current SIMX16 camera suffers slightly less from this problem. Finally, because of small misalignment of the different CCD sensors, displacements have to be calculated between images from each individual sensor. Therefore, a set of 16 images of the stationary specimen are first recorded before deforming the specimens and the first set of images is used as the undeformed reference for each sensor, as explained in [63, 163]. The second camera used here is a Shimadzu HPV-X, a recent version of the older HPV-1/2 series. This camera uses a dedicated sensor called FTCMOS which is a special type of CMOS sensor with on-board solid-state memory storage. The horizontal fill factor of the HPV-X camera is around 37 %, which is higher than that of the previous versions HPV-1/2 (only 14 % in the horizontal direction [26]). More details about this camera can be found in [69, 71]. For the versions of HPV-1 and 2, there are a number of issues with the ISIS CCD sensor, as summarized in [164], but when used with the correct settings (dark image, avoid 1 Mfps frame rate), very good images can be captured as evidenced in [26]. The new FTCMOS sensor used in the Shimadzu HPV-X seems to suffer much less, if at all, from the issues noted on the previous generation cameras. It is not the objective here to perform a full characterisation of the measurement performances using these cameras, only basic performance information is provided. Information concerning the two imaging systems and grids is

collated in Table 5.4. Because of very short inter-frame time, strong flash light proved necessary. The flash light was positioned opposite to the grided surface of the specimen, as shown in Figure 5.1. The flash duration is around 2 milliseconds. In order to acquire high quality images and to make full use of the recording capacity of the camera, the images should be acquired with full flash intensity (after the rising stage of the flash light), and the camera should be triggered at the instant the projectile contacts with the specimen. The rise time of flash light was 50 nanoseconds. Thus, two independent triggering systems are necessary. The triggering signal for the flash light was from the high pressure pump connected to the gas gun. An appropriate delay was selected to ensure the flash duration covered the imaging of the camera with full flash intensity. To trigger the camera, two pieces of thin copper film were bonded onto the impact end of the foam support so that when the projectile reached, it contacted both pieces of film which closed an electrical circuit, providing the triggering signal to the camera, as shown in Figure 5.1.

TABLE 5.4: Imaging and measurement performance information in the cylindrical impact tests.

	Specialised Imaging SIMX16
Pixel array size	1280×960
Inter-frame time (microsecond)	1
Number of images	16
Pitch of the grid (mm)	0.2
Sampling (pixel per period)	6
Field of view (mm)	32.4×24.0
Raw displacement resolution	10 % of grid pitch (0.6 pixel)
Displacement spatial smoothing	Gaussian, 16 × 16 data points
Displacement temporal smoothing	3^{rd} order polynomial over 5 images
Strain resolution (microstrain)	700
Acceleration resolution ($m.s^{-2}$)	5×10^5
	Shimadzu HPV-X
Pixel array size	400×250
Inter-frame time (microsecond)	0.2
Number of images	128
Exposure time (nanosecond)	110
Pitch of the grid (mm)	0.6
Sampling (pixel per period)	5
Field of view (mm)	32.0 ×25.2
Raw displacement resolution	0.15 % of grid pitch (0.0075 pixel)
Displacement spatial smoothing	Gaussian, 3 × 3 then 10 × 10 data points
Displacement temporal smoothing	3^{rd} order polynomial over 25 images
Strain resolution (microstrain)	30
Acceleration resolution ($m.s^{-2}$)	2×10^4

5.2.2 Ball-bullet impact tests

The UHS camera used in the ball impactor tests was the Shimadzu HPV-X again, though it was a different camera. The images of the deforming specimens were acquired by the camera through a transparent PMMA window. Two strong flash lights (Bowens Prolite 60, here) proved necessary. The output power of each flash light is 300 Joules. The rise time is around 50 microseconds and the flash duration is 1 millisecond. The main imaging configuration of Shimadzu HPV-X camera is similar to that in the cylindrical impact tests. However, the triggering systems used here consisted in two closing circuits. One was positioned between the exit of the gun barrel and the specimen and consisted of a piece of metallic wire wound around a cardboard frame and a thin metal strip fixed at the back of the frame. When the ball passed through the frame, it pushed at least one of the wires against the metal strip, closing the circuit and triggering the flash lights. Since the distance between the frame and the front end of the specimen was about 15 mm, this ensured that the imaging took place roughly midway through the lighting event. The other triggering system consisted of two small pieces of wire attached to the front end of the specimen but separated by about 1 mm. When the ball reached the specimens, it made contact with both wires, closing the circuit and triggering the camera. This was not 100 % accurate since before impacting the specimen, the ball had first to crush the wires but thanks to the built-in post-triggering of the camera, satisfactory triggering was eventually achieved.

5.3 Resolution

Before moving to the dynamic tests, it is necessary to assess the accuracy of the deformation measurements. For full-field measurements, the resolution can be evaluated as the standard deviation of kinematic fields obtained from stationary images. In this work, it has been qualified by capturing images of the stationary specimen just before the tests, using the same imaging conditions as in the impact tests. Theoretically, the displacement, strain and acceleration between two nominally stationary images should be uniformly null, but in practice, this is not the case because of the digital noise. For the SIMX16 camera, the noise is calculated between two series of stationary images whereas for the HPV-X, only one series is necessary and the first image is taken as the reference. For instance, Figure 5.3 presents the raw displacement between two stationary images in the ball impact tests. High spatial frequency uncorrelated noise can be seen on this map. The standard deviation is very low, 0.17 % of the grid pitch (or 0.085 pixel), which is better than for most standard CCD cameras. This is probably due to the very high sensitivity of this sensor. However, this is still not good enough to evaluate strain and

acceleration without any smoothing as small strains have to be measured here. Therefore, the displacement should be spatially smoothed before differentiation. In this work, spatial smoothing was performed with a Gaussian filter. The acceleration and strain rate fields were calculated from the displacement and strain fields respectively using temporal smoothing, as introduced in Section 2.3.2. To configure spatial and temporal smoothing, a sensitive study has performed.

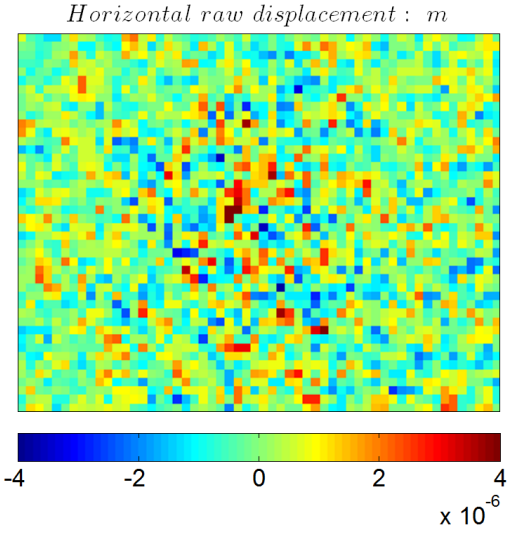

FIGURE 5.3: Example of raw horizontal displacement from two stationary images.

The standard deviation of displacement, strain and acceleration can be calculated at each frame. Average standard deviations of these kinematic fields over all frames are regarded as the measurement resolutions. For instance, Table 5.4 presents the measurement performance information in the cylindrical impact tests. It can be seen that the measurement performances from the HPV-X camera are far superior to that of the SIMX16. The only real advantage of the SIMX16 is its better spatial resolution, the limited total number of images being also a very stringent limiting factor.

In the ball impactor tests, a different Shimadzu HPV-X camera was used. The imaging configuration was the same as that in Table 5.4. However, the measurement performance was quantified again to validate the robustness of this particular camera. The results are shown in Table 5.5. Comparing the imaging information for the ball impactor tests (in Table 5.5) with that for the cylindrical impactor tests (in Table 5.4), it can be seen that the measurement performances are very similar, except for a slightly better acceleration resolution in the ball-bullet impact tests. This shows that the imaging performance of the Shimadzu HPV-X camera is quite robust. The deformed images have been smoothed using the same configurations in Tables 5.4 and 5.5 to extract full-field strain, strain rate and acceleration maps. Finally, these full-field data have been processed by the different approaches described in the previous chapters.

TABLE 5.5: Imaging and measurement performance information in the ball-bullet impact tests.

Pixel array size	400×250
Inter-frame time (microsecond)	0.2
Number of images (FP mode)	128
Exposure time (nanosecond)	110
Pitch of the grid (mm)	0.6
Sampling (pixel per period)	5
Field of view (mm)	33.6 ×26.4
Raw displacement resolution	0.17 % of grid pitch (0.0085 pixel)
Displacement spatial smoothing	Gaussian, 3 × 3 then 10 × 10 data points
Displacement temporal smoothing	3^{rd} order polynomial over 25 images
Strain temporal smoothing	3^{rd} order polynomial over 25 images
Strain resolution (microstrain)	34
Acceleration resolution ($m.s^{-2}$)	1.4×10^4

Chapter 6

Experimental results and identification

6.1 Experimental full-field maps

The consecutive raw grey-level grid images were acquired from the UHS cameras. As mentioned in Section 2.3, spatial phase maps relating to displacements can be obtained using spatial phase shifting. The algorithm implemented here is called WDFT (windowed discrete Fourier transform). The general procedure of the grid method was reviewed in Section 2.3.2. More details about the grid method can be found in [107]. These phase maps may contain phase jumps from π to $-\pi$ when the displacement range in one image is larger than the grid pitch. This is known as 'phase wrapping'. Here these maps have been unwrapped using the algorithm published by [165]. Finally, because of the rigid body motion accompanying the stress wave propagation, the mean displacement as a function of time also exhibits 'jump' each time if the rigid body translation goes above the grid pitch. Since the rigid body movement is monotonic, simple temporal unwrapping is performed by adding integer numbers of pitch size to the displacement maps so that the mean displacement is monotonic. This is essential in dynamics to derive the acceleration maps. It was found that a rigid 'jumps' happened in the cylindrical impactor tests but not in the ball impactor tests, not surprisingly as the latter provides significantly lower impact energy. The experimental full-field maps for quasi-isotropic and unidirectional composite specimens are presented in the following.

6.1.1 Quasi-isotropic composite specimens

6.1.1.1 Cylindrical impactor tests

These raw images were processed using the configuration in Tables 5.4 to obtain time-resolved kinematic fields. As mentioned previously, two types of cameras were used in the cylindrical impactor tests. Figure 6.1 shows the average longitudinal strain and acceleration profiles calculated over the whole field of view of the quasi-isotropic specimens in the cylindrical impactor tests. Even though these tests were performed independently on different days, these plots look very much alike, although the SIMX16 acceleration data are much nosier, as expected from the double temporal differentiation. One can see a shift of 2 microseconds between the two curves because of the difference in triggering. In order to get a feel for the results, displacement, strain and acceleration maps are provided at 8 microseconds for the SIMX16 and 10 microseconds for the HPV-X so that the data correspond to the same state of the test (Figures 6.2∼6.4). Videos of the whole set of data are provided as supplementary material to this PhD thesis. Again, the maps are really similar, showing the same localisation of the impact at the bottom. This illustrates the reproducibility of the set-up which uses a rigid foam stand for the specimen. This means that better alignment of the set-up could also be possible to generate a more even impact. From these images and videos, the superior data quality from the HPV-X camera is spectacular. Looking at the acceleration maps, one can see values going up to nearly one million g's, which corresponds to what was obtained from the FE calculation (Figure 4.31). As for the strain rate, Figure 6.5 shows the average strain rate over the field of view as well as the strain rate map at 6 microseconds for the HPV-X quasi-isotropic test. The strain rate reaches a maximum value close to 2000 s^{-1} at the beginning of the test but with highly heterogeneous strain rate maps. Here, this strain rate information is just used to provide an idea of the order of magnitude reached in this test but it will not be used in the identification.

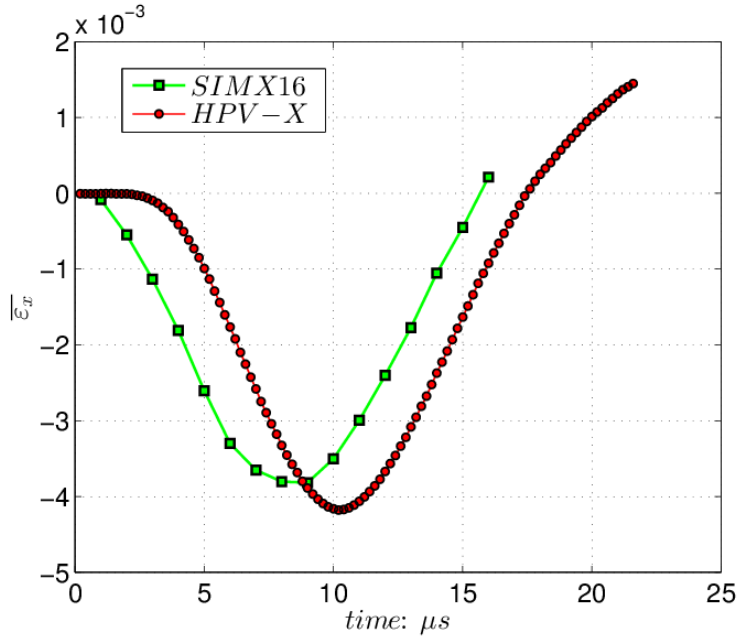

(A)

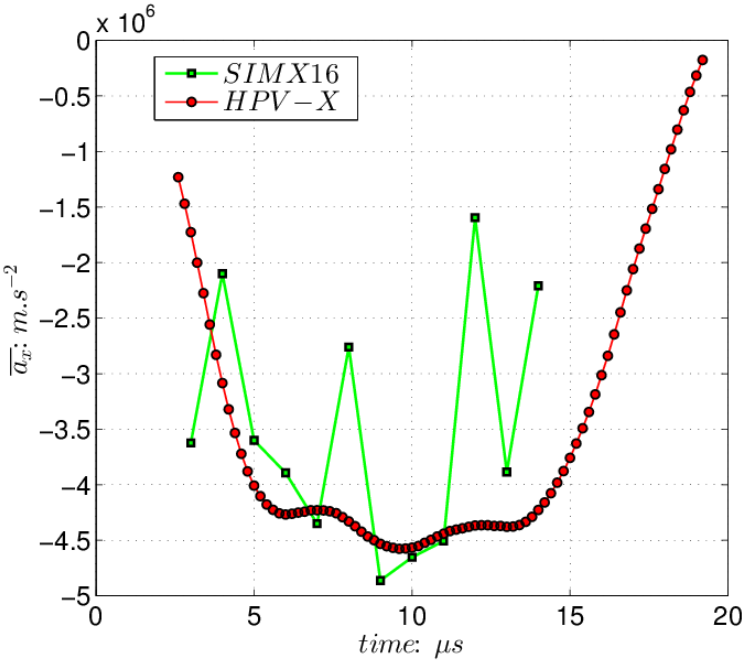

(B)

FIGURE 6.1: Average longitudinal strain and acceleration for SIMX16 and HPV-X cameras in quasi-isotropic cylindrical impact tests. (A) Average longitudinal strain $\overline{\varepsilon_x}$. (B) Average longitudinal acceleration $\overline{a_x}$.

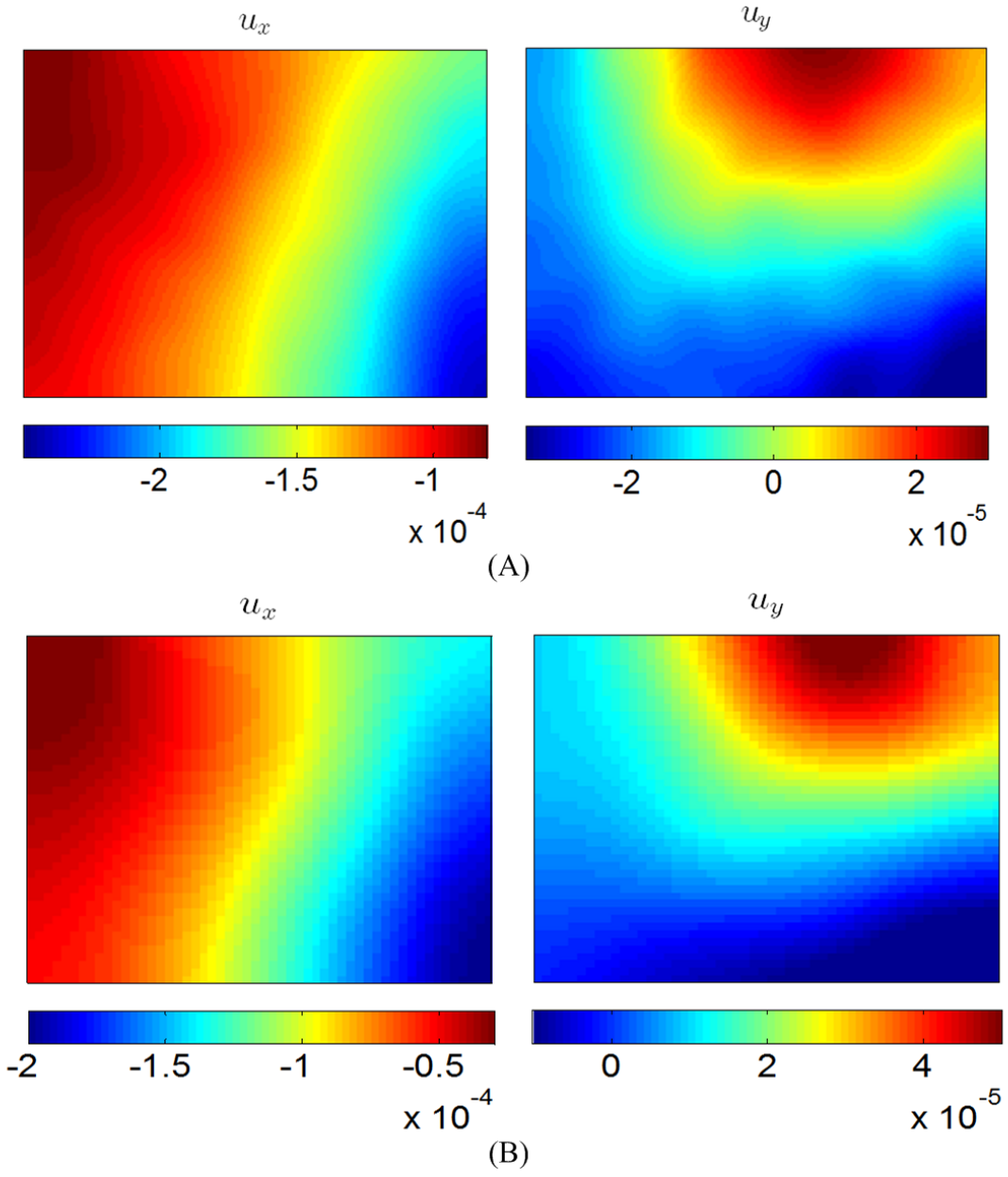

FIGURE 6.2: Displacement maps in meters for SIMX16 and HPV-X cameras at 8 and 10 microseconds in quasi-isotropic cylindrical impact tests. (A) Displacement at 8 microseconds, SIMX16. (B) Displacement at 10 microseconds, HPV-X.

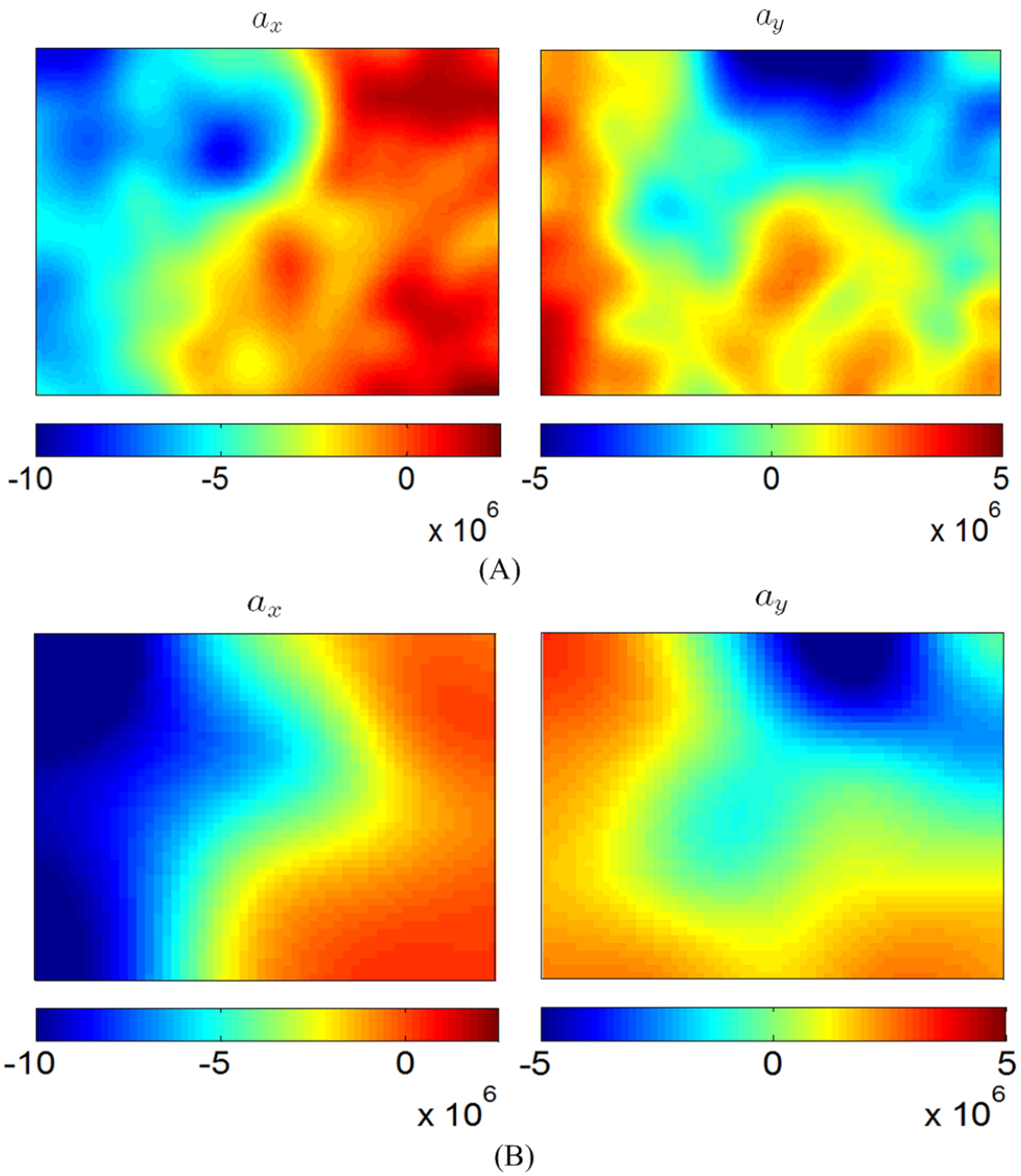

FIGURE 6.3: Acceleration maps in $m.s^{-2}$ for SIMX16 and HPV-X cameras at 8 and 10 microseconds in quasi-isotropic cylindrical impact tests. (A) Acceleration at 8 microseconds, SIMX16. (B) Acceleration at 10 microseconds, HPV-X.

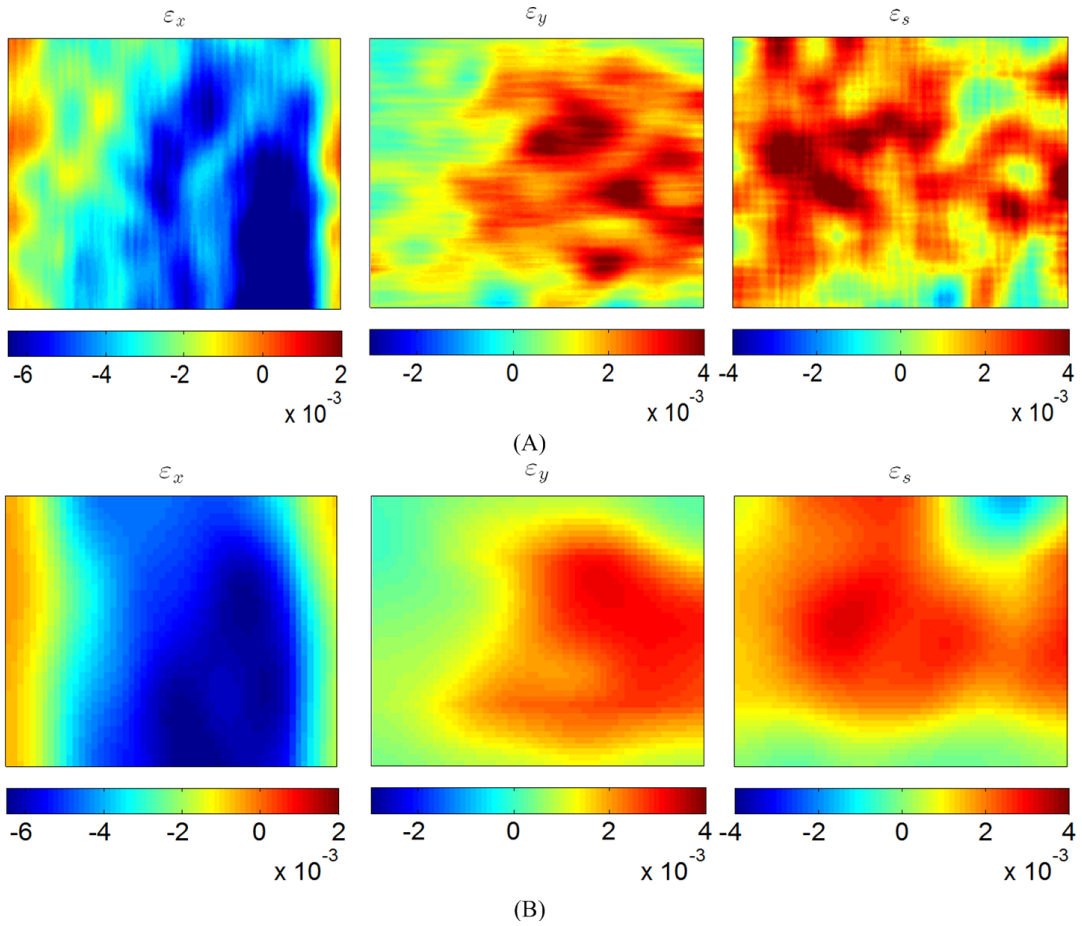

FIGURE 6.4: Strain maps for SIMX16 and HPV-X cameras at 8 and 10 microseconds in quasi-isotropic cylindrical impact tests. (A) Strain at 8 microseconds, SIMX16. (B) Strain at 10 microseconds, HPV-X.

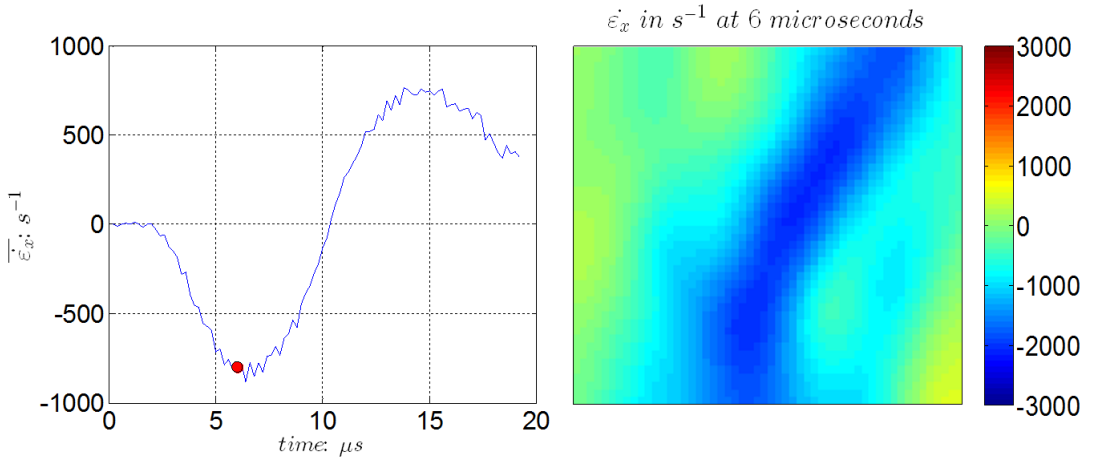

FIGURE 6.5: Longitudinal strain rate map at 6 microseconds for HPV-X cameras in quasi-isotropic cylindrical impact tests.

6.1.1.2 Ball impactor tests

Three quasi-isotropic composite specimens with different lengths were tested on the ball-bullet impact rig as shown in Figure 5.2. The dimensions of the specimens and the impact speeds are presented in Table 5.3. Figure 4.27 shows the photos of the three tested specimens and tabs in the experimental tests. One can clearly see that the contact point is not always perfectly centred. Aside from small discrepancies of the test specimen position in the impact chamber, it is thought that the wires used for triggering may also cause some slight deflection of the ball at the moment of impact. According to the $3D$ FE simulation in Section 4.3, the offset of the point contact in the cross-section leads to large errors in the identification procedure so it will be possible to experimentally assess the effect of lengthening of the specimen from the present tests. The acquired images were processed with the configuration presented in Table 5.5. For specimen QI-1 ($L = 40\ mm$), the maps of strain and acceleration at 9 microseconds with respect to the triggering of the camera are shown in Figure 6.6. It is worth emphasising that for this specimen, the surface used for data processing has been reduced from the image field of view by removing 6 mm from the impact end of the specimen in order to avoid the strain distortion due to the permanent damage caused by the localised impact point. It can be seen that these fields are symmetric or antisymmetric (for the shear components) with respect to the horizontal axis of the specimen, as expected. This confirms that the impact point is positioned at the middle of the impacted surface in the y direction. However, the spatial frequencies of the experimental maps are significantly lower than for the simulated counterpart in Figure 4.31. This is mainly due to the low pass filtering produced by the full-field measurements (including strong spatial smoothing necessary to measure the low strain levels reliably), as well as the fact that the small damped FE simulations result in spurious high frequency ringing, particularly on the acceleration maps. Finally, only elastic deformation was considered in the FE analysis whereas experimentally, tab plasticity and composite damage occur at the loading point. As shown in Figure 4.27, significant delamination at the impact end of specimen 3 was observed, in spite of the steel tab. This dissipates a significant amount of energy and leads to lower strain and acceleration levels, as can be seen when comparing the data from Figures 4.31 and 6.6.

The full-field maps for specimens QI-2 and QI-3 are shown at 13 microseconds in Figure 6.7 and at 17 microseconds in Figure 6.8 respectively. Different times were selected for the three specimens to show comparable strain and acceleration maps as the triggering time varied between the tested specimens. As seen in these figures, longer specimens lead to more uniaxial and unidirectional strain and acceleration maps. This was expected as a consequence of dynamic Saint-Venant's principle acting in the (x, y) plane:

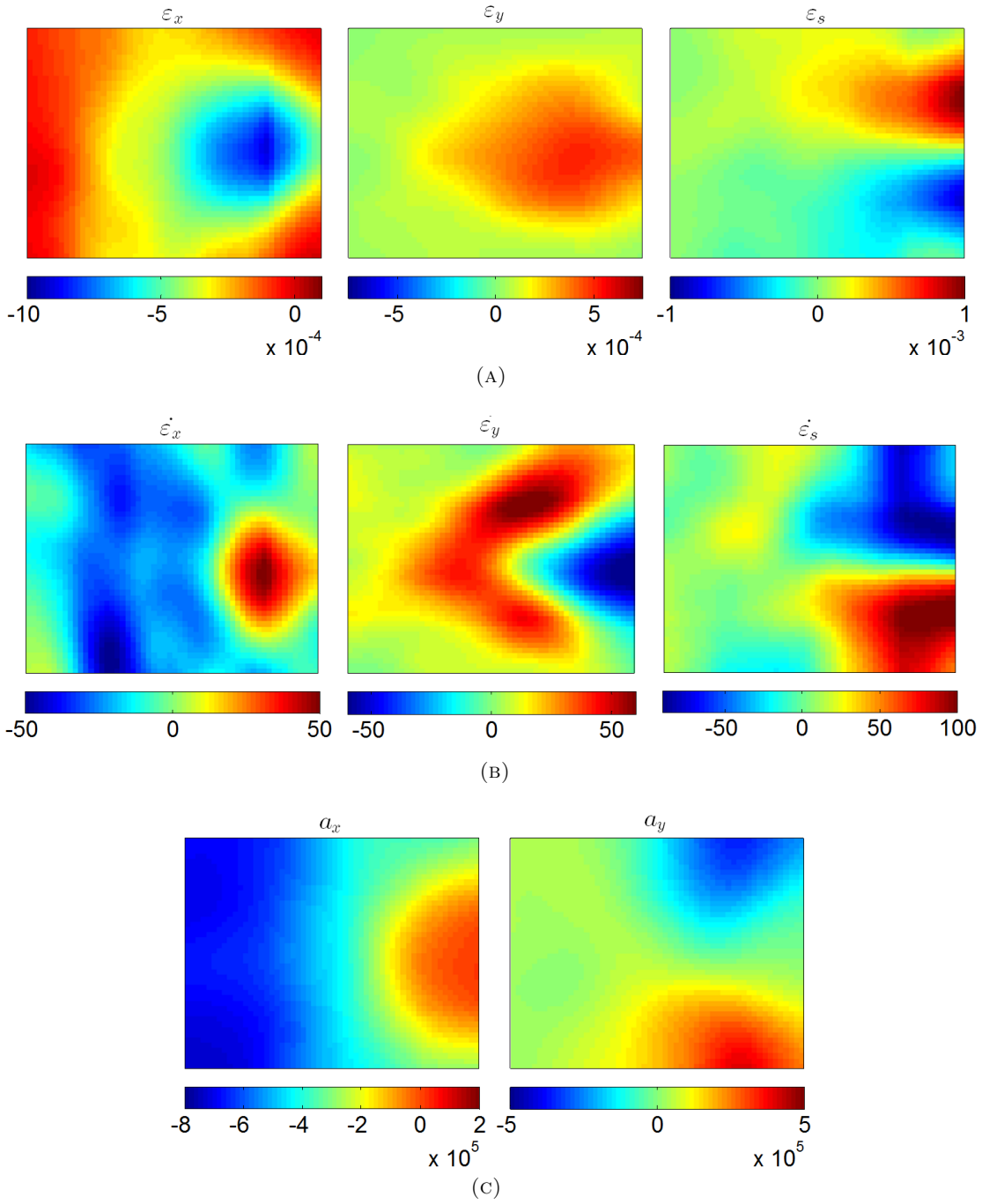

FIGURE 6.6: Strain, strain rate and acceleration maps for specimen QI-1 at 9 microseconds. Data points: 56 by 44. (A) Strain. (B) Strain rate (in s^{-1}). (C) Acceleration (in $m.s^{-2}$).

the deformation tends to become more like that generated by a uniform pressure as the waves travel along the test specimen.

Figure 6.9 shows the temporal evolution of the average of the longitudinal strain over the field of view. As seen in this figure, the strain profiles are consistent with the impact speeds reported in Table 5.3, as the 40 mm specimen was impacted at a lower ball

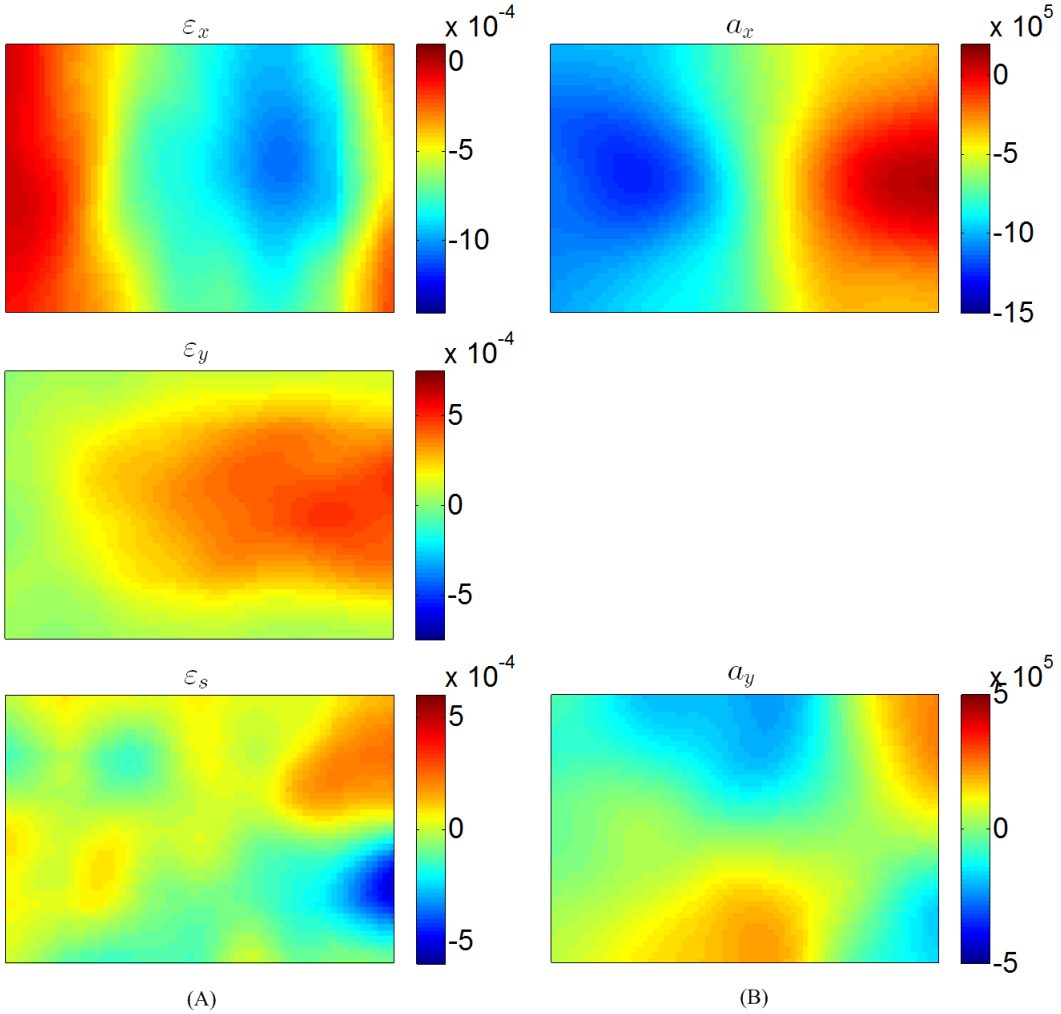

FIGURE 6.7: Strain and acceleration maps for specimen QI-2 at 13 microseconds. Data points: 68 by 47. (A) Strain. (B) Acceleration (in $m.s^{-2}$).

speed. In this quasi-isotropic ball impact test, the strain levels are only about a tenth of that shown in Figure 6.1 in the cylindrical impactor test. Complete wave rebounds are captured except for specimen QI-3 due to the limited recording capacity of the camera and slightly early triggering. The complete set of dynamic maps are provided as supplementary material to this thesis.

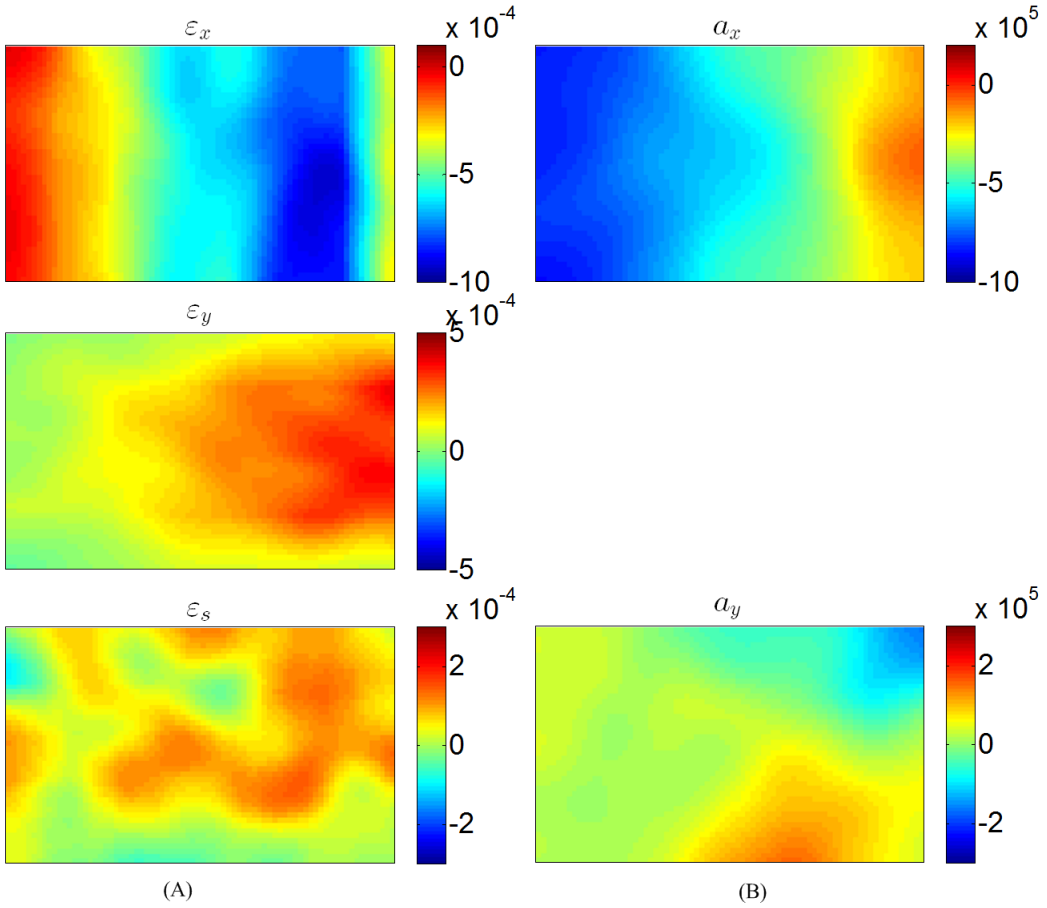

FIGURE 6.8: Strain and acceleration maps for specimen QI-3 at 17 microseconds. Data points: 76 by 46. (A) Strain. (B) Acceleration (in $m.s^{-2}$).

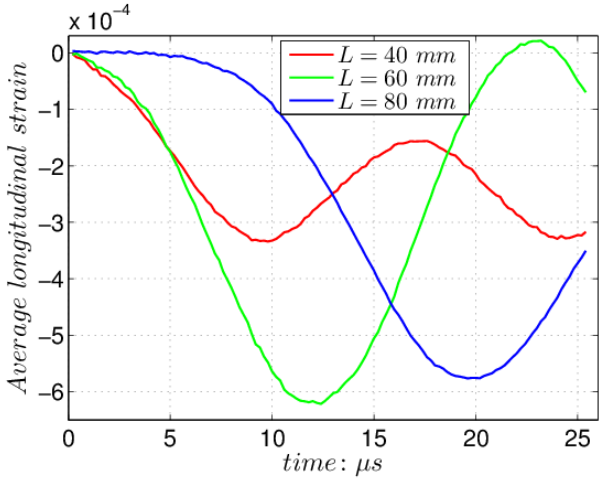

FIGURE 6.9: Average longitudinal strain levels for the three quasi-isotropic cylindrical impactor tests.

6.1.2 Unidirectional composite specimens

For the unidirectional impact tests, both cylindrical and ball impactors were employed to provide high rate loading. The Shimadzu HPV-X camera was used for both series of tests. The maps of kinematic fields are presented in the rest of this section.

6.1.2.1 Cylindrical impactor tests

In the unidirectional cylindrical impact tests, three specimens were tested and the information has been shown in Table 5.2. The details of image processing has been shown in Table 5.4. The maps of strain, strain rate and acceleration fields in the global system are presented in Figures 6.10∼6.12. One can clearly see that the bands of these maps follow the off-axis fibre angles, especially the strain rate and acceleration maps. However, it is worth noting that the angle of the band in Figure 6.10 is larger than the off-axis fibre angle. The exact reason has not been established yet. It might be because of the interaction between the matrix and the fibre. Comparing the maps in Figures 6.11 and 6.12 (with the same off-axis fibre angles), the consistent patterns in strain rate and acceleration maps confirm the reproducibility of this experimental set-up. However, the patterns of strain maps are different. It might be because of damage at the impact end, creating some permanent deformation.

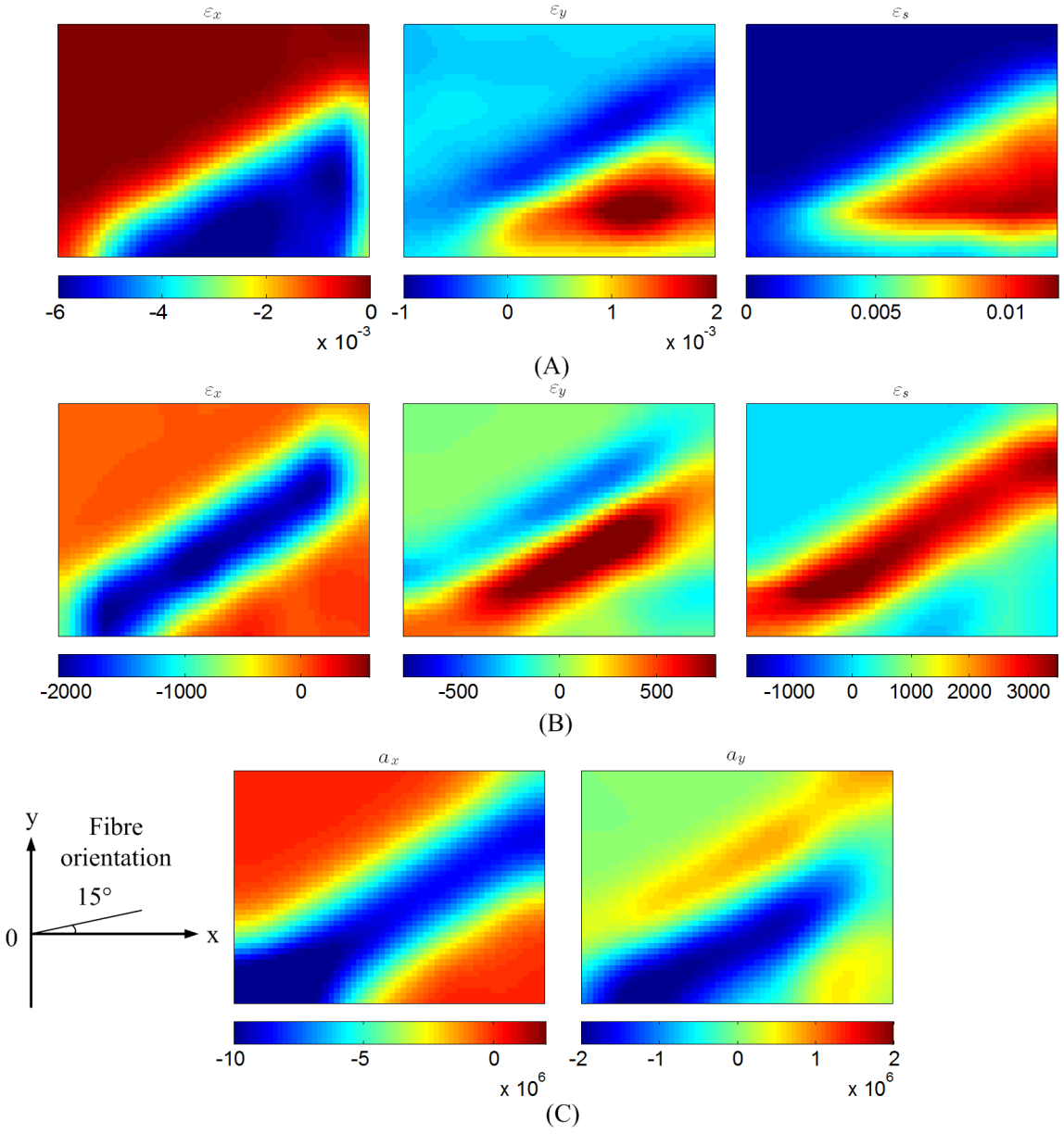

FIGURE 6.10: Strain, strain rate and acceleration maps in off-axis tests at 10 microseconds with the cylindrical impactor. Global coordinate system. Specimen 15-1, fibre angle: 15°. Data points: 52 by 45. (A) Strain. (B) Strain rate (in s^{-1}). (C) Acceleration (in $m.s^{-2}$).

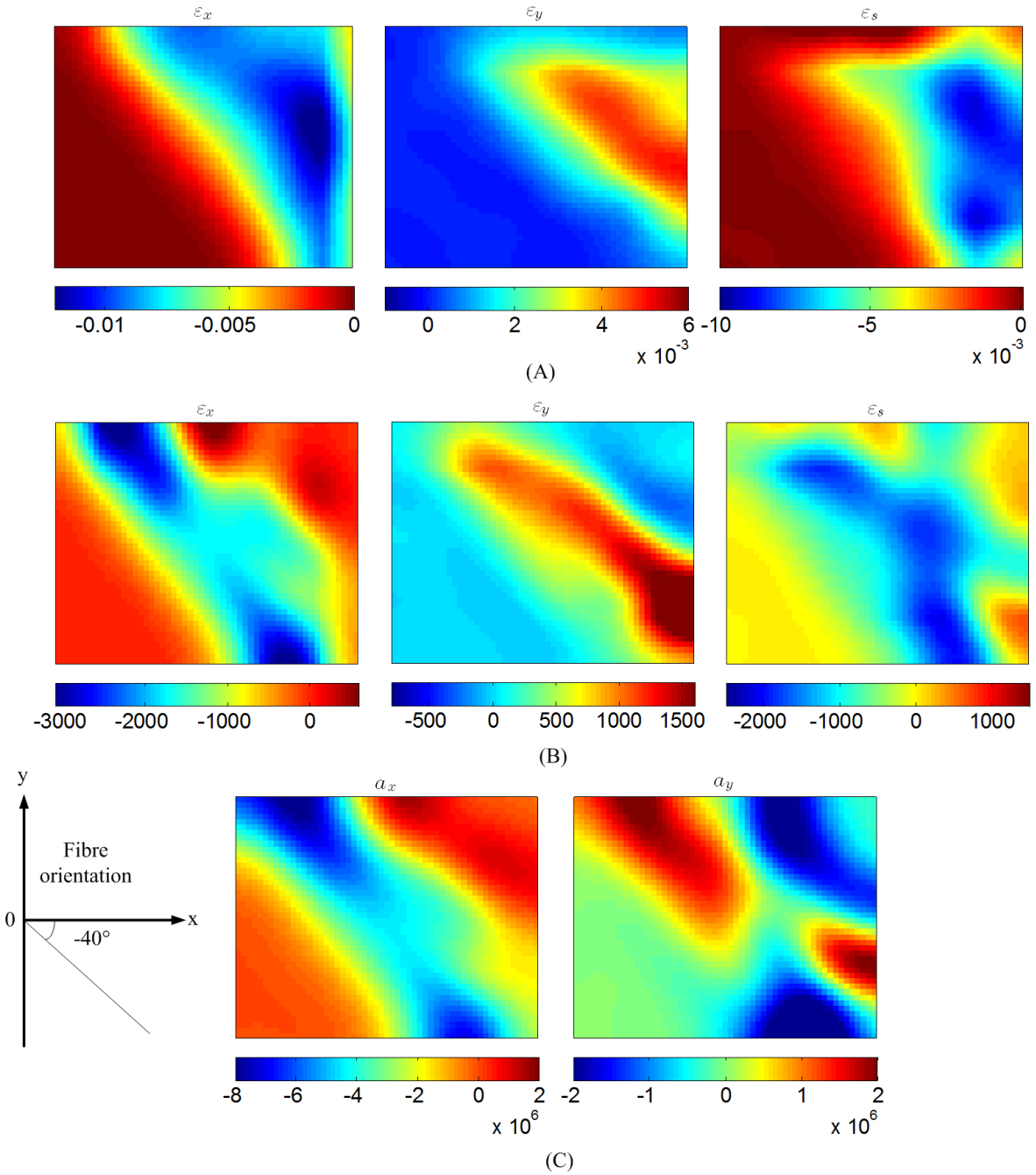

FIGURE 6.11: Strain, strain rate and acceleration maps in off-axis tests at 10 microseconds with the cylindrical impactor. Global coordinate system. Specimen 40-1, fibre angle: 40°. Data points: 55 by 45. (A) Strain. (B) Strain rate (in s^{-1}). (C) Acceleration (in $m.s^{-2}$).

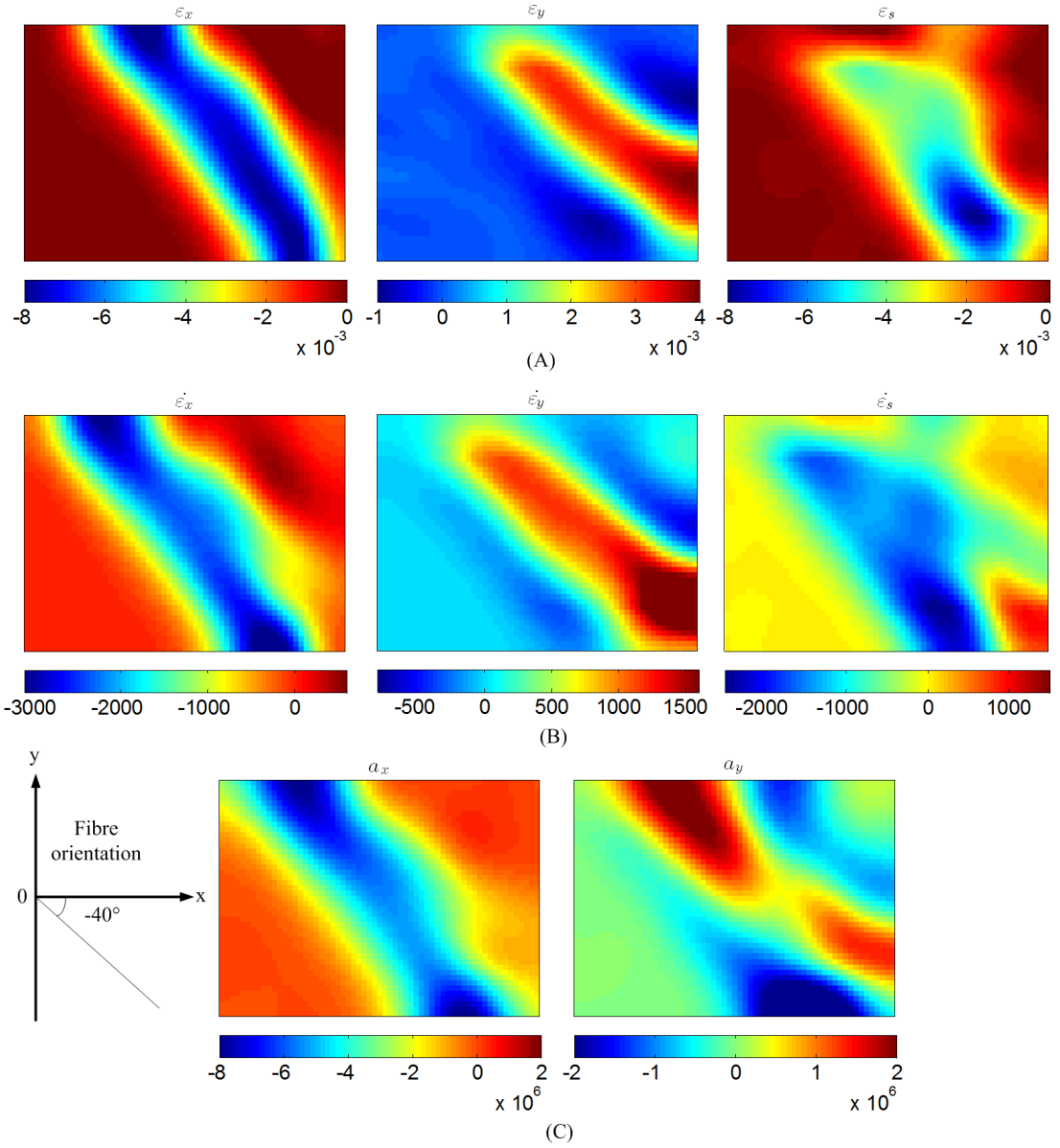

FIGURE 6.12: Strain, strain rate and acceleration maps in off-axis tests at 3 microseconds with the cylindrical impactor. Global coordinate system. Specimen 40-2, fibre angle: 40°. Data points: 61 by 45. (A) Strain. (B) Strain rate (in s^{-1}). (C) Acceleration (in $m.s^{-2}$).

6.1.2.2 Ball impactor tests

A couple of specimens with two types of off-axis fibre angles (60° and 15°) and three different lengths ($L = 40\ mm, 60\ mm$ and $80\ mm$, respectively) were employed. The details about the specimens are reported in Table 5.3. Full-field maps were obtained from the raw images using the image processing procedure from Table 5.5. Figures 6.13∼6.15 present full-field maps with three different specimens lengths for $\vartheta = 15^{\circ}$. One can clearly see that the strain levels in these tests are much lower than that in the cylindrical impactor tests, as expected from the lower energy and the energy absorbed by plastic deformation of the tab which acts as a pulse shaper. The patterns of these maps follow the fibre orientation as well except for the length of 80 mm. The angle of the pattern seems to be slightly larger than the fibre angle again. The exact reason is being investigated. With the increase of the specimen length, the stress concentration is less pronounced, as one could expect. For $\vartheta = 60°$, specimens with two different lengths were used. Figures 6.16 and 6.17 show the related full-field maps. It is clearly seen that for the short specimen the stress concentration is very significant, even though the steel tab was employed. For the longer specimen, the strain distribution is less heterogeneous. For all tests in this section, it can be seen the strain rate level is only one tenth of that in the cylindrical impactor tests.

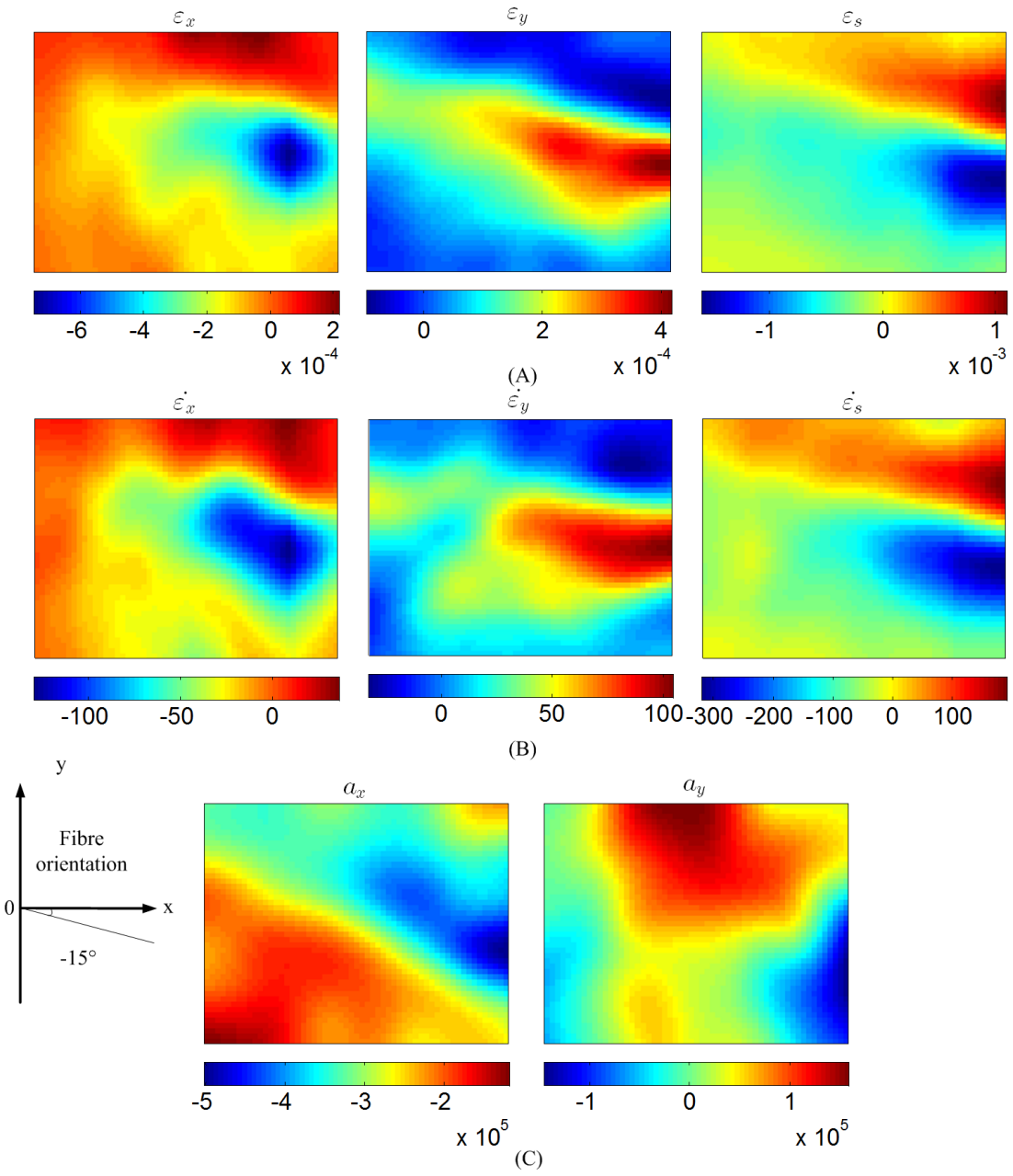

FIGURE 6.13: Strain, strain rate and acceleration maps in off-axis tests at 13 microseconds with the ball impactor. Global coordinate system. Specimen length: 40 mm. Specimen UD-15-1, fibre angle: 15°. Data points: 57 by 45. (A) Strain. (B) Strain rate (in s^{-1}). (C) Acceleration (in $m.s^{-2}$).

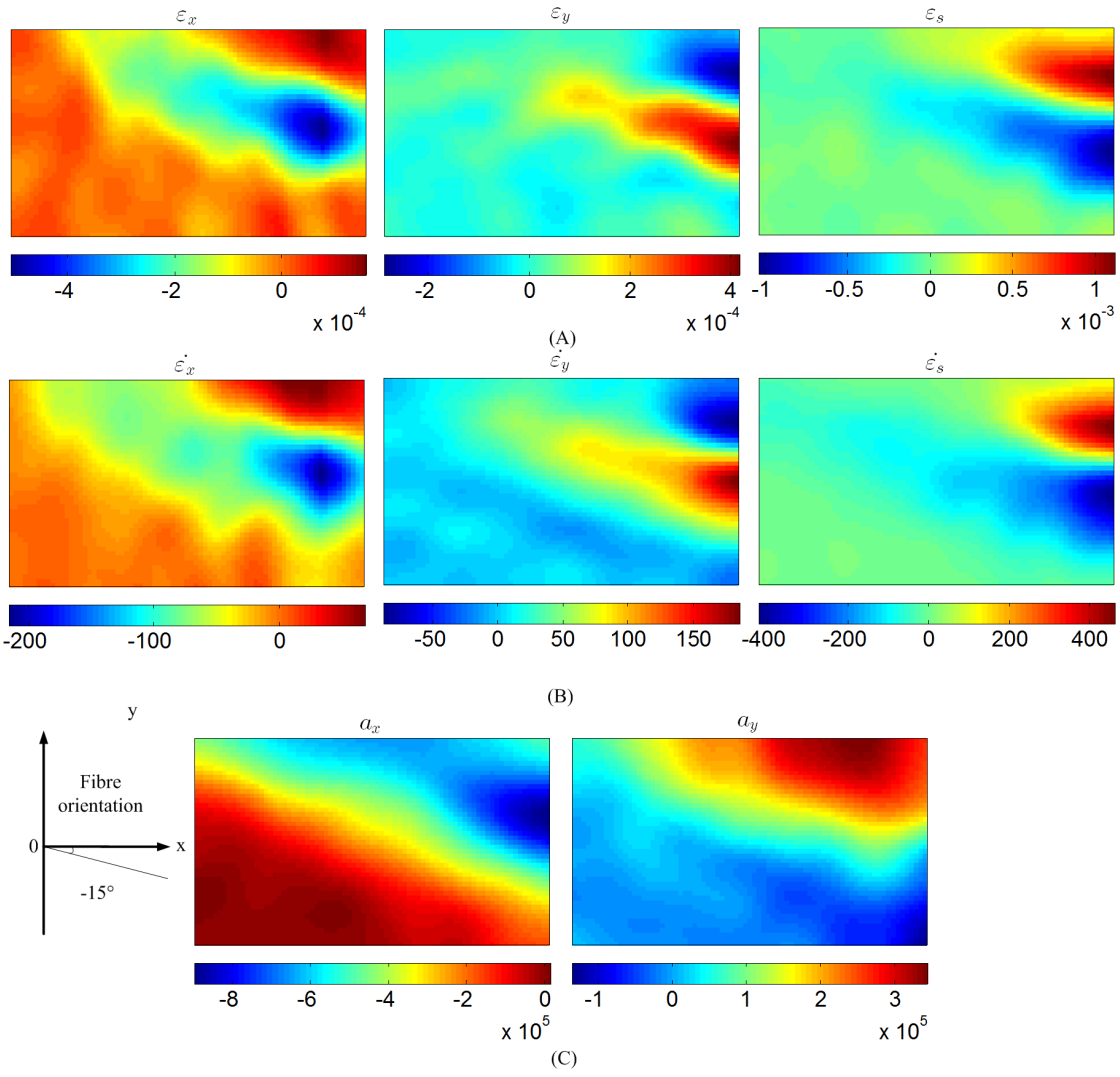

FIGURE 6.14: Strain, strain rate and acceleration maps in off-axis tests at 4 microseconds with the ball impactor. Global coordinate system. Specimen length: 60 mm. Specimen UD-15-2, fibre angle: 15°. Data points: 77 by 45. (A) Strain. (B) Strain rate (in s^{-1}). (C) Acceleration (in $m.s^{-2}$).

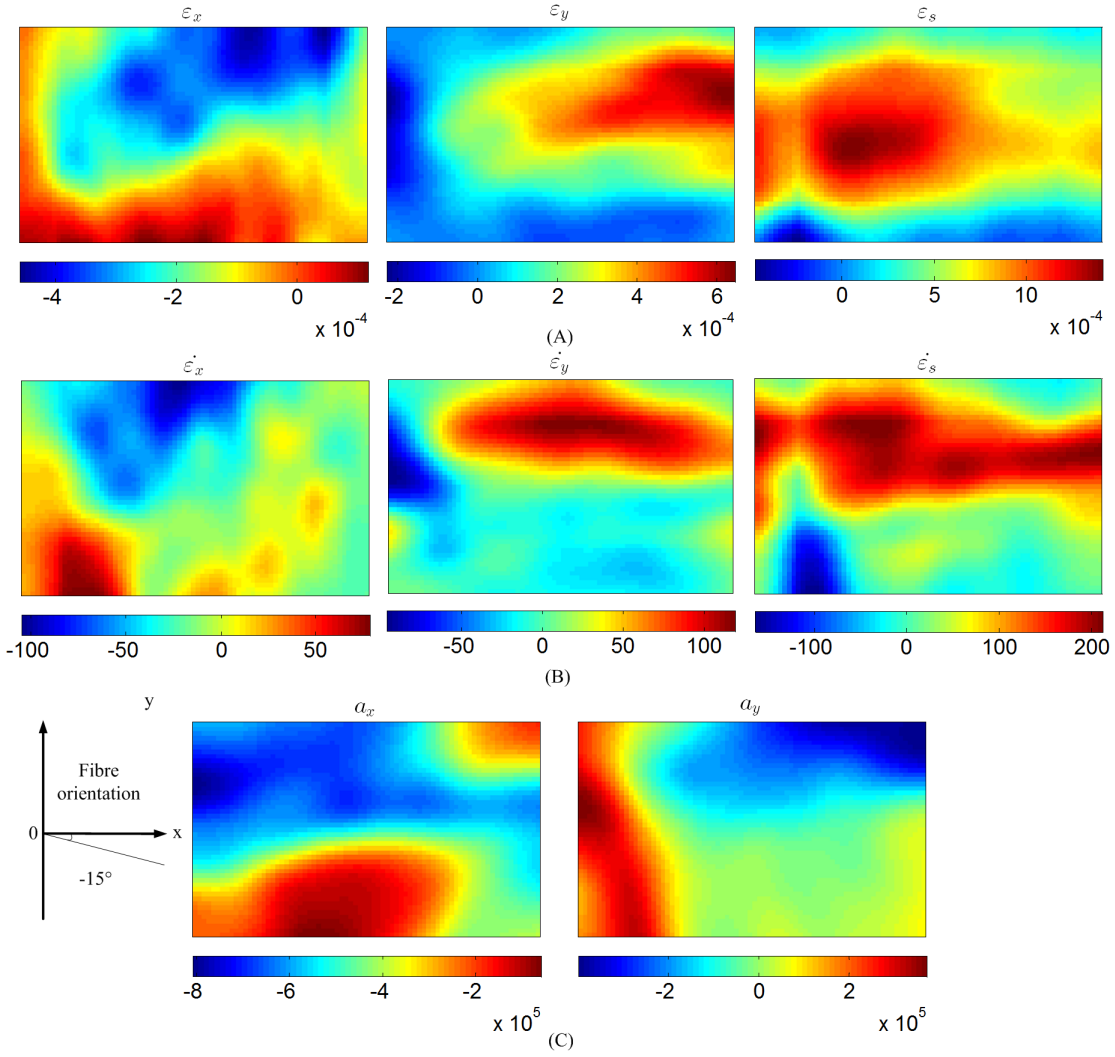

FIGURE 6.15: Strain, strain rate and acceleration maps in off-axis tests at 6 microseconds with the ball impactor. Global coordinate system. Specimen length: 80 mm. Specimen UD-15-3, fibre angle: 15°. Data points: 76 by 47. (A) Strain. (B) Strain rate (in s^{-1}). (C) Acceleration (in $m.s^{-2}$).

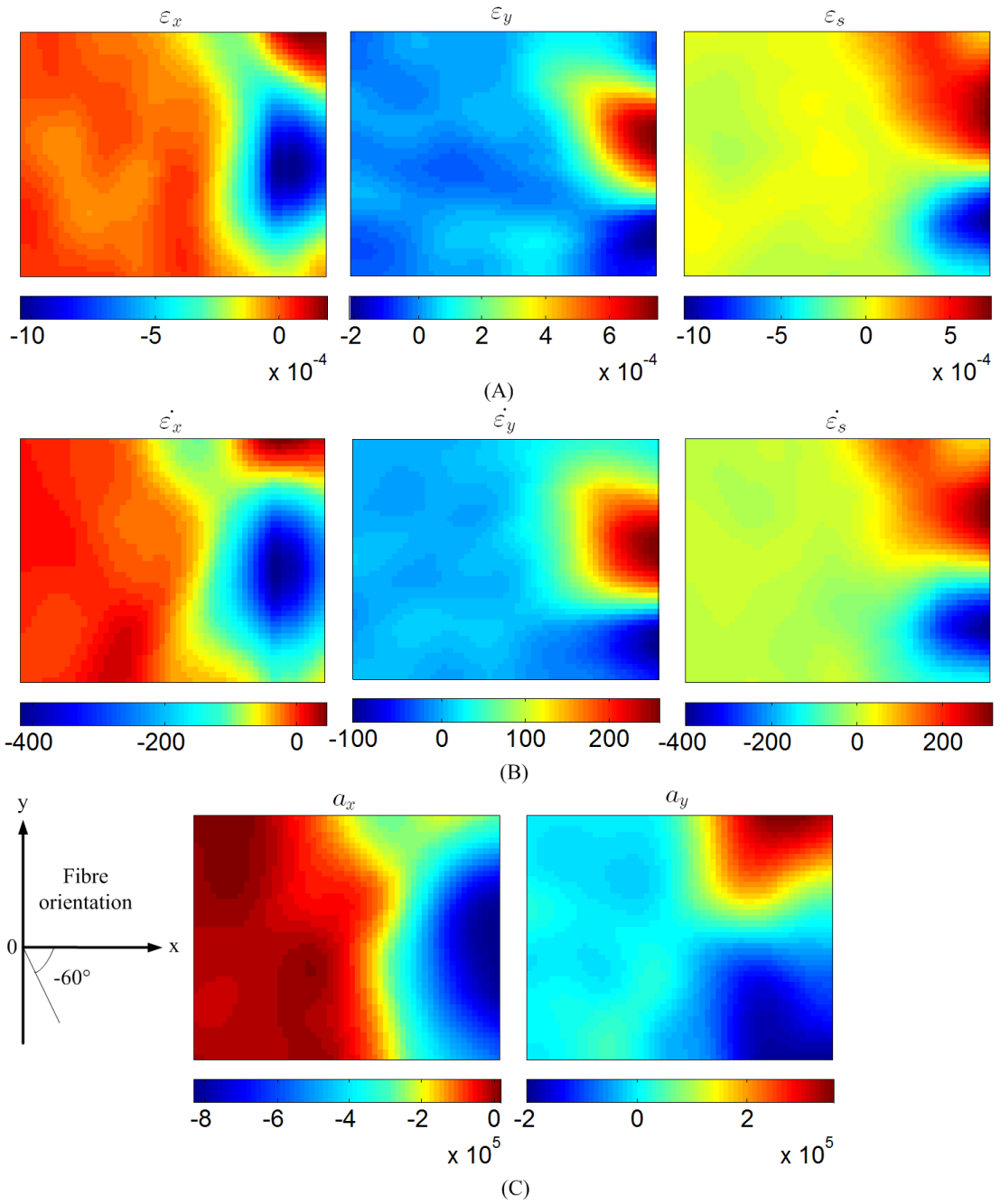

FIGURE 6.16: Strain, strain rate and acceleration maps in off-axis tests at 14 microseconds with the ball impactor. Global coordinate system. Specimen length: 40 mm. Specimen UD-60-1, fibre angle: 60°. Data points: 55 by 44. (A) Strain. (B) Strain rate (in s^{-1}). (C) Acceleration (in $m.s^{-2}$).

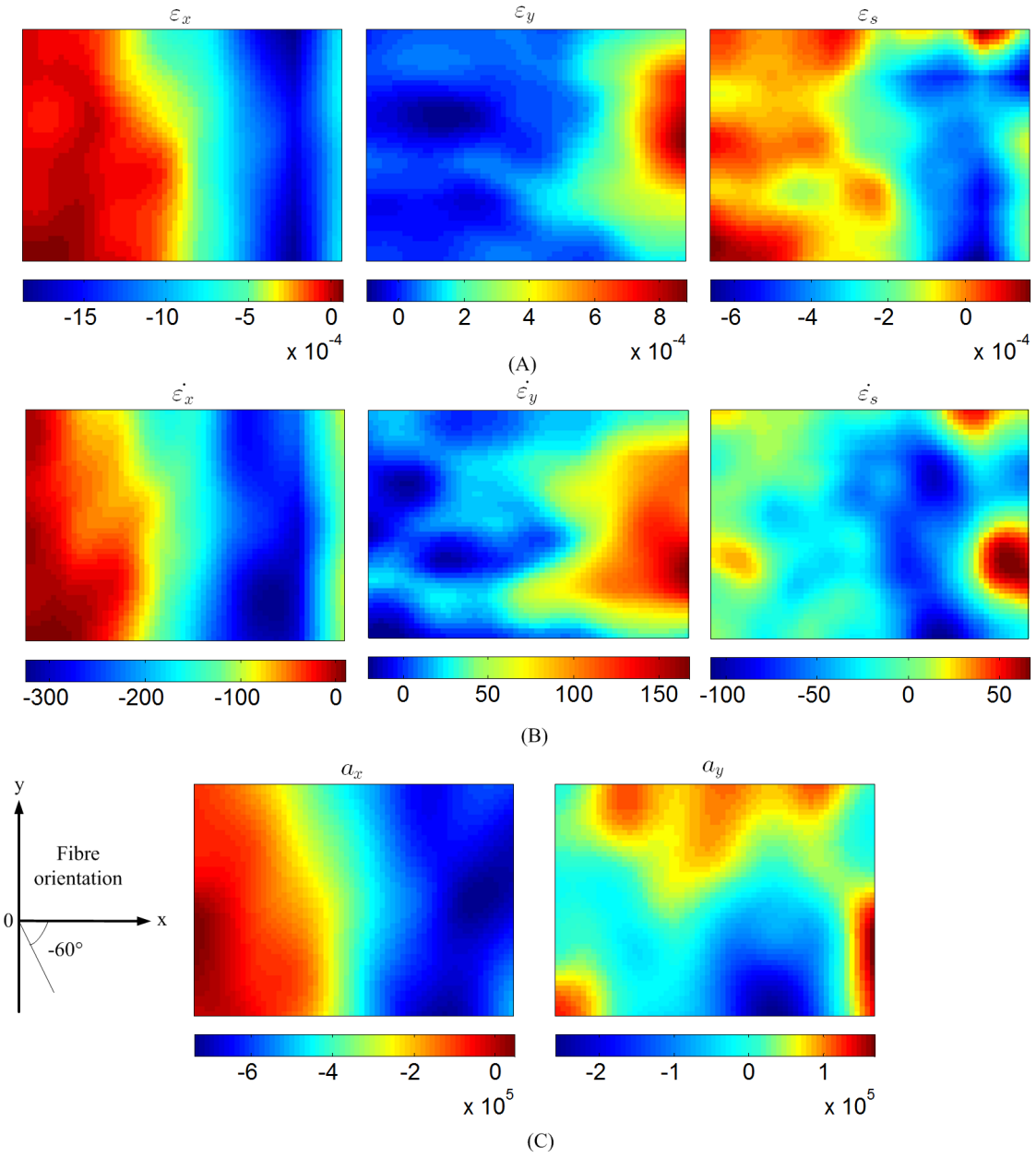

FIGURE 6.17: Strain, strain rate and acceleration maps in off-axis tests at 4 microseconds with the ball impactor. Global coordinate system. Specimen length: 60 mm. Specimen UD-60-2, fibre angle: 60°. Data points: 62 by 45. (A) Strain. (B) Strain rate (in s^{-1}). (C) Acceleration (in $m.s^{-2}$).

6.2 Simplified VFM identification

This section is dedicated to the identification of the material parameters from experimental tests using the simplified VFM approaches described in the previous chapters. Only the quasi-isotropic impact tests are discussed in the following.

6.2.1 Cylindrical impactor tests: quasi-isotropic composite specimens

The first approach used here is that introduced in Section 3.1. The average longitudinal stress σ_x along transverse slices has been reconstructed using Equation 3.6. This allows to plot the average σ_x against the average longitudinal strain ε_x at all transverse slices along the longitudinal axis of the specimen. As the cylindrical impact tests provide a dominantly unidirectional state of stress, the slope of this curve identifies Young's modulus of the quasi-isotropic specimen, as a first approximation. An example is provided in Figure 6.18 for the SIMX16 test and in Figure 6.19 for the HPV-X one, at 20.7 mm from the free edge (about two-thirds towards the right-hand side of the field of view). The first one is very noisy, as one would expect from the poor measurement performance in Table 5.4. Using a linear fit of the data, one recovers a value of 51.7 GPa for E, about 10 % higher than the expected value of 47.1 GPa. In Figure 6.19(A), one can see that the stress-strain curve from the HPV-X data is of much better quality and exhibits nice linearity except during the early stages of the test. This is caused by the temporal smoothing to obtain acceleration. It results in non-zero acceleration values before the wave reaches, leading to stress without any strain. After about 12 images (half the smoothing window of 25 images), correct data are recovered as seen in Figure 6.19(B). In this case, a linear fit of the data leads to a Young's modulus of 40.1 GPa. This is 14 % lower than the expected value of 47.1 GPa. In order to check for the consistency of these results, stress-strain curves have been plotted in Figure 6.20(A) for the unloading part of the response only, at three different locations in the field of view. The three curves are very similar, only the one at 20.7 mm exhibiting an offset caused by the problem mentioned previously, which tends to decrease in intensity when moving closer to the free end, probably because the wave front is less sharp there. From this, a modulus around 40 GPa is recovered from the three sets of data, showing good consistency.

A legitimate question is whether the unidirectional stress assumption is reasonable. In order to investigate this issue, Figure 6.20(B) represents the average longitudinal stress as a function of the average of $\varepsilon_x + \nu\varepsilon_y$, the slope of which provides the stiffness component Q_{11} which relates to E through Equation 3.13. This is plotted for $\nu = 0.31$ from the reference quasi-static data in [32]. One can also see good linearity of the response. One can then calculate E from Q_{11} and compare the results to those obtained using the

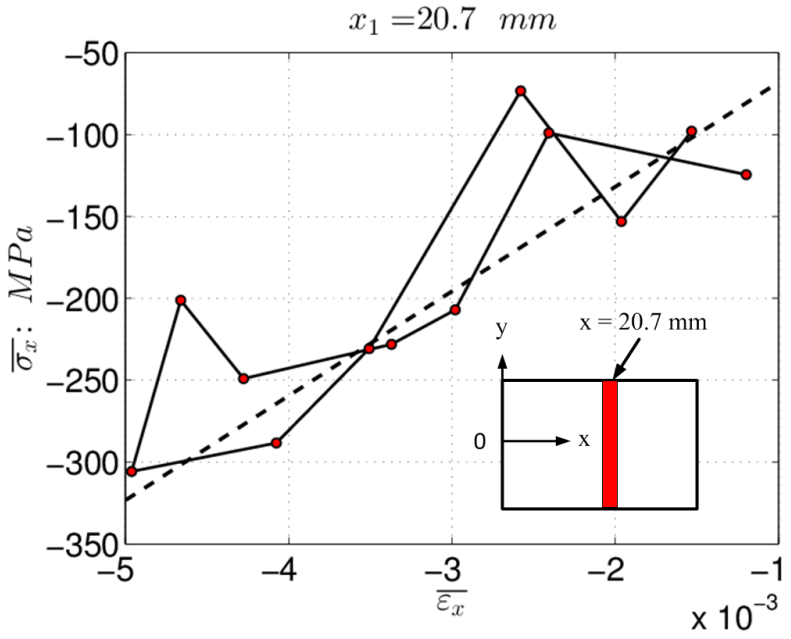

FIGURE 6.18: Stress-strain curves for the SIMX16 test at $x = 20.7\ mm$.

uniaxial stress assumption. This is shown in Figure 6.21, where data too close to both edges have been discarded. Indeed, close to the free edge, stress and strain become too low and close to the impact edge, issues with in-plane loading and damage may occur. The results show that the difference between the two values is about 15 % for about half the field of view, closer to the free end. The value extracted from Q_{11} is the closest to the quasi-static reference, showing the limitations of the uniaxial stress assumption, as could have been expected from the heterogeneous nature of mechanical fields in the test. However, both approaches converge to a lower value of E towards the impact end of the specimen. It is not clear why this is happening but it is thought that the contact between the projectile and the specimen is not perfect and may lead to some through-thickness strain heterogeneities. In this case, the strains may be too high on the front side where the measurements are performed but because the thickness of the specimen is small, the strains tend to average out through-the-thickness at a certain distance from the impact zone, a kind of Saint-Venant effect in dynamics, as evidenced numerically in Section 4.3. The results for the SIMX16 camera tests are shown in Figure 6.22. The variations in Young's modulus are much larger than for the HPV-X data and only the mean values over the field of view excluding the edges (shown in grey box in the figure) relate to the reference values. Clearly, the quality of the data is not good enough for this approach.

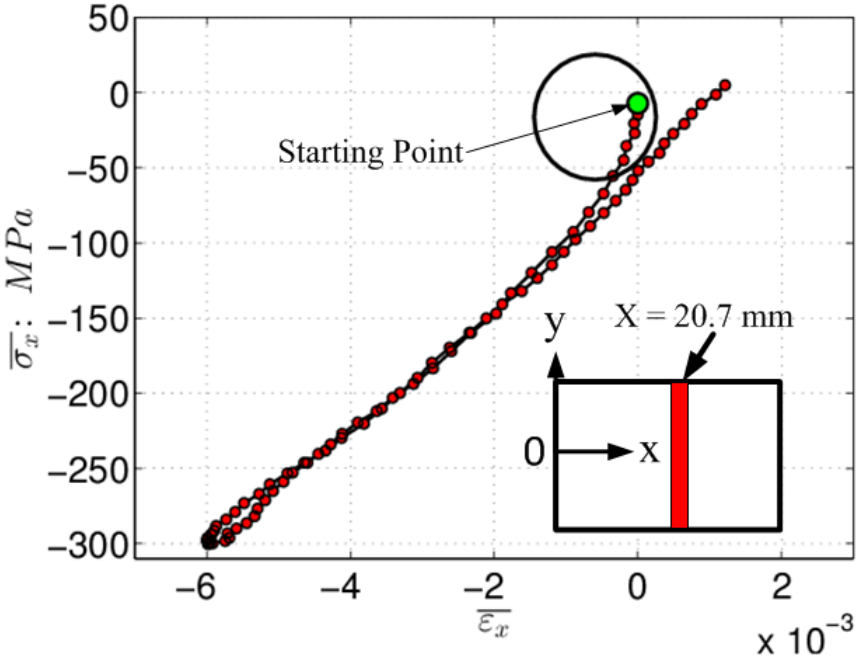

(A)

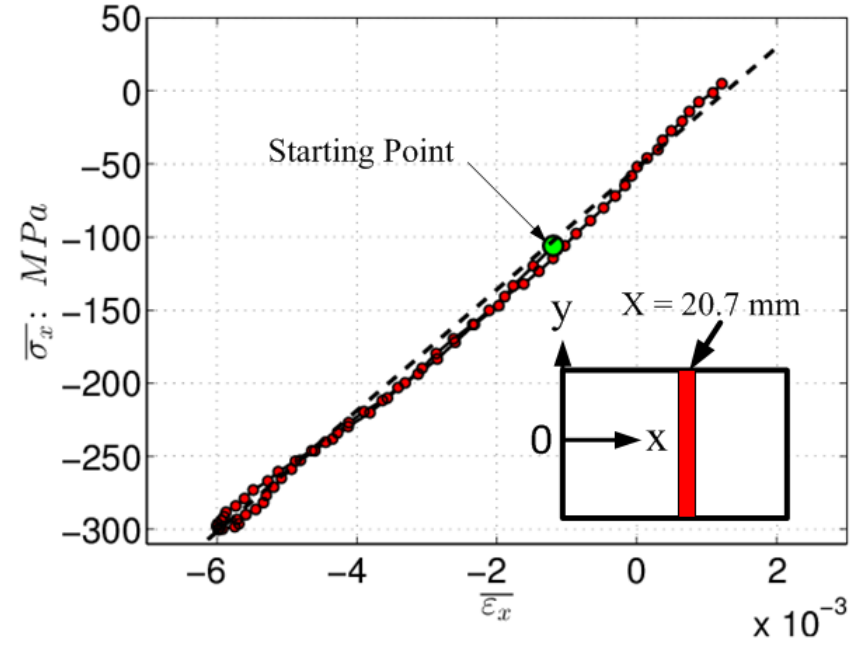

(B)

FIGURE 6.19: Stress-strain curves for the HPV-X test at $x = 20.7\ mm$. (A) Full stress-strain curve. (B) Stress-strain curve without initial part and with linear fit.

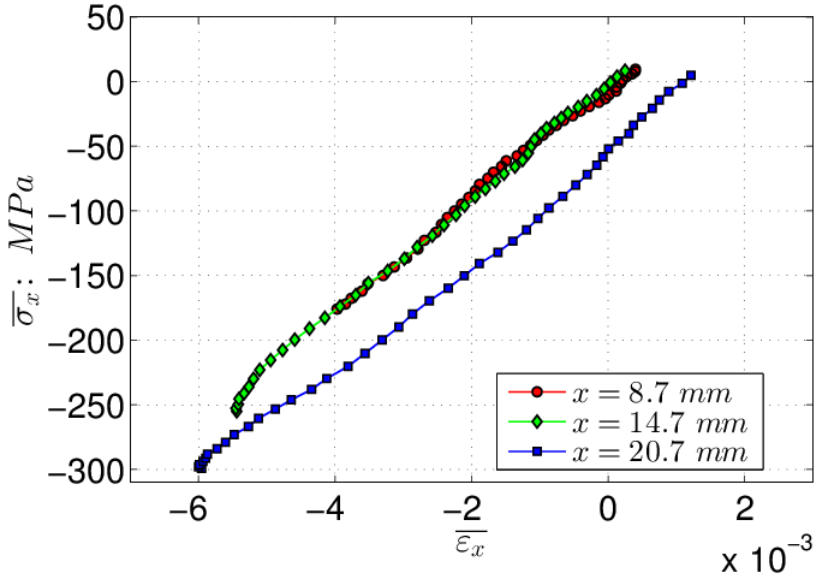

(A)

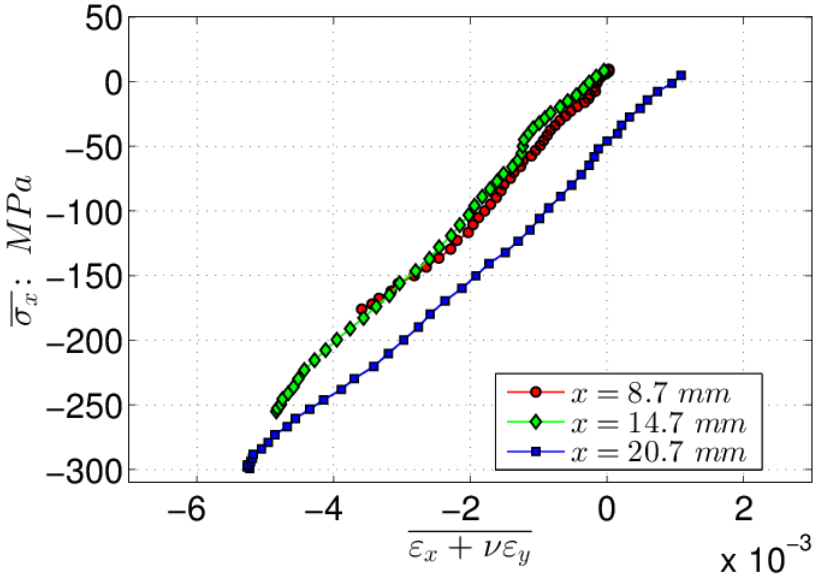

(B)

FIGURE 6.20: Stress-strain curves at different locations for the HPV-X test. (A) Uniaxial stress assumption. (B) No uniaxial stress assumption.

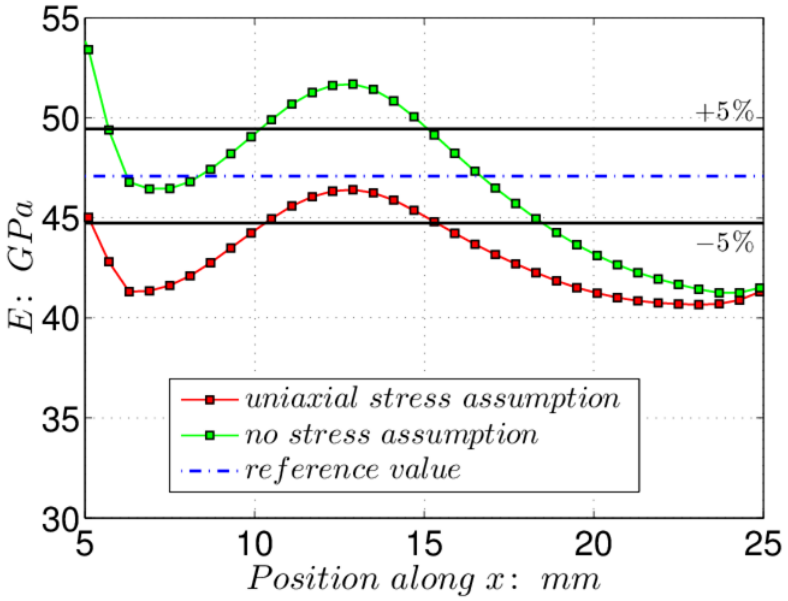

FIGURE 6.21: Modulus obtained from stress-strain curves with and without uniaxial stress assumption, HPV-X camera.

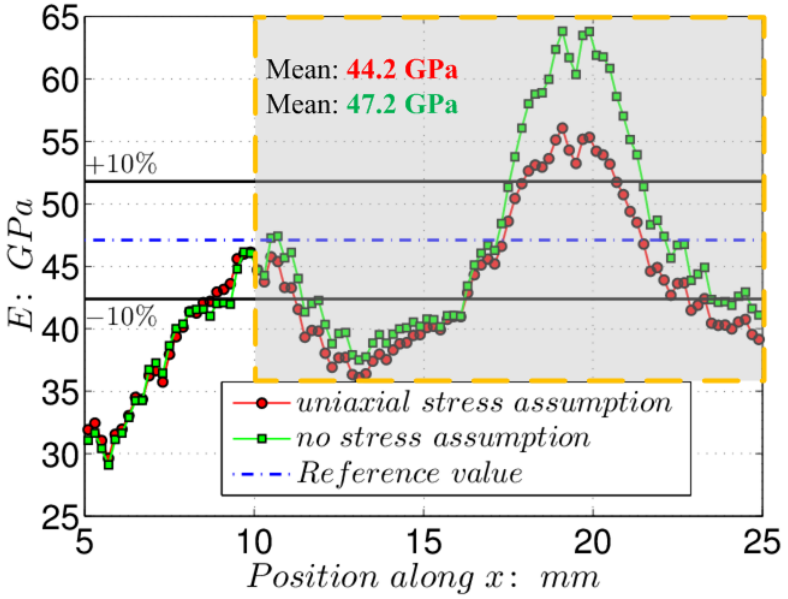

FIGURE 6.22: Modulus obtained from stress-strain curves with and without uniaxial stress assumption, SIMX16 camera. Mean value of Young's modulus with uniaxial stress assumption in the shaded area is 44.2 GPa, and 47.2 GPa for that without uniaxial stress assumption.

6.2.2 Ball impactor tests: quasi-isotropic composite specimens

It has been shown that the strain states in the ball impact tests were more heterogeneous than those in the cylindrical impact tests, as described in Section 6.1. Therefore, the stress-strain curves were plotted between the average longitudinal stress and average $\varepsilon_x + \nu\varepsilon_y$. The slope of the straight line used to fit the curve provided Q_{11} relating to Young's modulus E. The same value of Poisson's ratio, 0.31, was used to provide these results.

Young's modulus was extracted from stress-strain curves at each transverse slice along the longitudinal axis of the specimen. For instance, stress-strain curves from different specimens at $x = 17.7\ mm$ are shown in Figure 6.23. The impact speed for specimen QI-1 was lower than for the other two specimens, as already mentioned previously, explaining the 'truncated' stress-strain curve. The stress-strain curves for the three specimens are reasonably linear and consistent with each other. The estimated E from the curve of specimen QI-3 is 52.2 GPa (error of 11.1 %). It is worth noting that there are significant oscillations for specimen QI-2 and QI-3 marked by black circles. Figure 6.24 presents the profiles of displacement, velocity and acceleration for specimen QI-2 during the test. Even though the displacement curve is very smooth, a first differentiation to obtain velocity shows slight disturbances (magnification window). This is further enhanced by the next differentiation to obtain acceleration. The disturbance is now clearly visible, and will translate to the stresses obtained from Equation 3.6. This can be traced back to some artefacts in the imaging. The mean intensity profile of the raw images of specimen QI-2 during this dynamic test is shown in Figure 6.25. One can see an increase of the mean intensity as a function of time. This is a characteristic of the camera sensor and happens systematically. Fortunately, the phase extraction is not sensitive to the mean image intensity so this did not affect the displacement measurements. However, some oscillations can be observed there, especially early in the image series, as marked by the red circle. This is similar to the problem reported for the earlier version of this camera, the Shimadzu HPV-1 [164], although on a much smaller scale. Clearly here, the temporal smoothing used to derive acceleration reduces this effect but does not cancel it. Nevertheless, its impact on the global stress-strain curve is rather limited, as seen on Figure 6.23.

Young's modulus for each transverse slice along the longitudinal axis of the specimen is shown in Figure 6.26. One can clearly see that at slices close to both specimen ends, the results are not good. This trend is similar to that from the simulated data in Section 4.3.2.1. The estimated Young's modulus over the central part of the field of view is comparatively good. For specimen QI-1 ($L = 40\ mm$), the mean Young's modulus value over this central part is around $E = 48.6\ GPa$ with a coefficient of

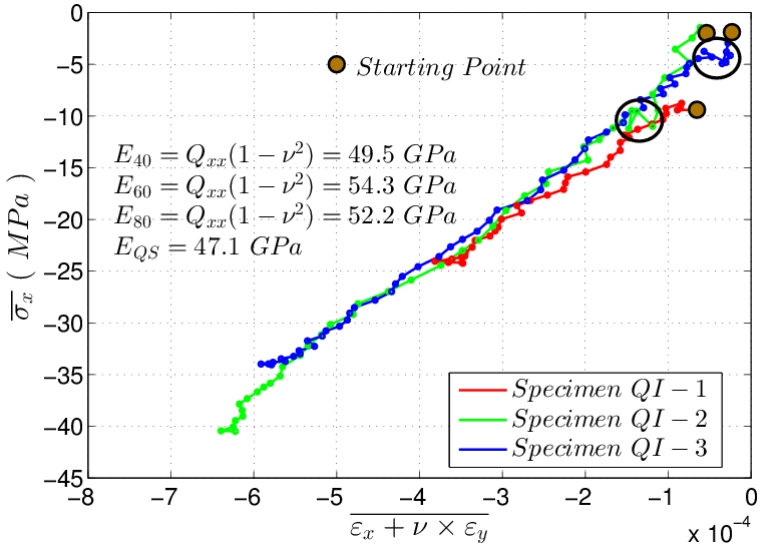

FIGURE 6.23: Stress-strain curves for the three specimens at $x = 17.7\ mm$. $\nu = 0.31$.

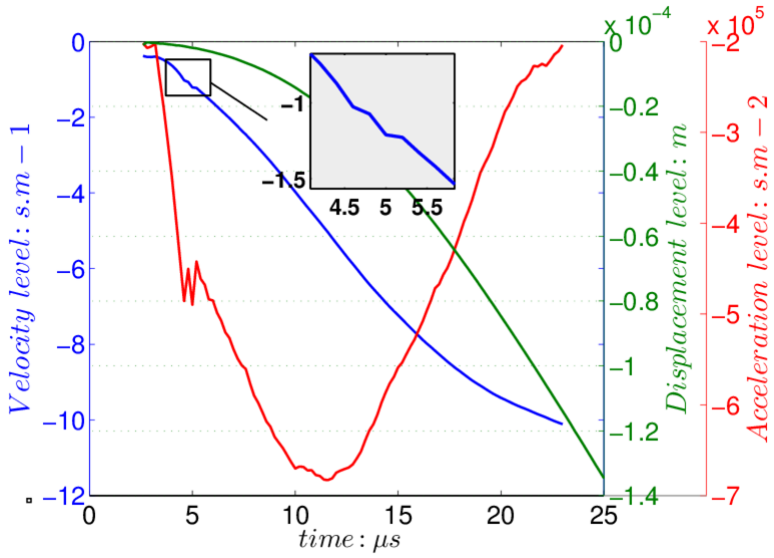

FIGURE 6.24: Profiles of longitudinal displacement, velocity and acceleration. Specimen QI-2.

variation (CV) of 3.6 %, whereas it is 54.2 GPa (CV of 1.7 %) for specimen QI-2 ($L = 60\ mm$) and 55.3 GPa (CV of 5.8 %) for specimen QI-3 ($L = 80\ mm$). Figure 6.27 reports the goodness of fit (R-square values) for all slices for each specimen. This figure first confirms that only a certain distance away from both ends is the behaviour linear, as already evidenced before. Moreover, the plot for specimen QI-1 shows oscillations certainly related to the significantly $3D$ nature of wave propagation, resulting in more perturbed stress-strain curves. Specimens QI-2 and QI-3 both exhibit excellent fit at a higher level than specimen QI-1, confirming the relevance of using longer specimens to mitigate for the $3D$ stress wave propagation. It is also interesting to note that for

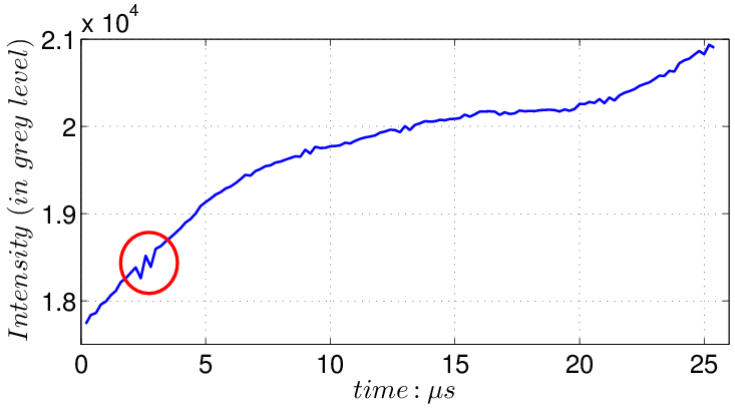

FIGURE 6.25: Profile of average grey level intensity of the raw images. Specimen QI-2.

both specimens QI-2 and QI-3, the identified Young's modulus is systematically larger than the value identified in quasi-static tests. This was not expected after the numerical results which showed unbiased estimation for E. However, these numerical simulations used the strains and accelerations directly from the FE model whereas as noted before, the full-field measurements provide significant low-pass filtering (both temporally and spatially) of the data. Temporal smoothing reduces the acceleration levels whereas spatial smoothing decreases the strain peaks. Since E results from a balance between two terms containing these data, positive or negative systematic errors can certainly be obtained. The only way to investigate this further would be to simulate the image processing as in the simulator presented in [124]. This is the next step to follow up on this work.

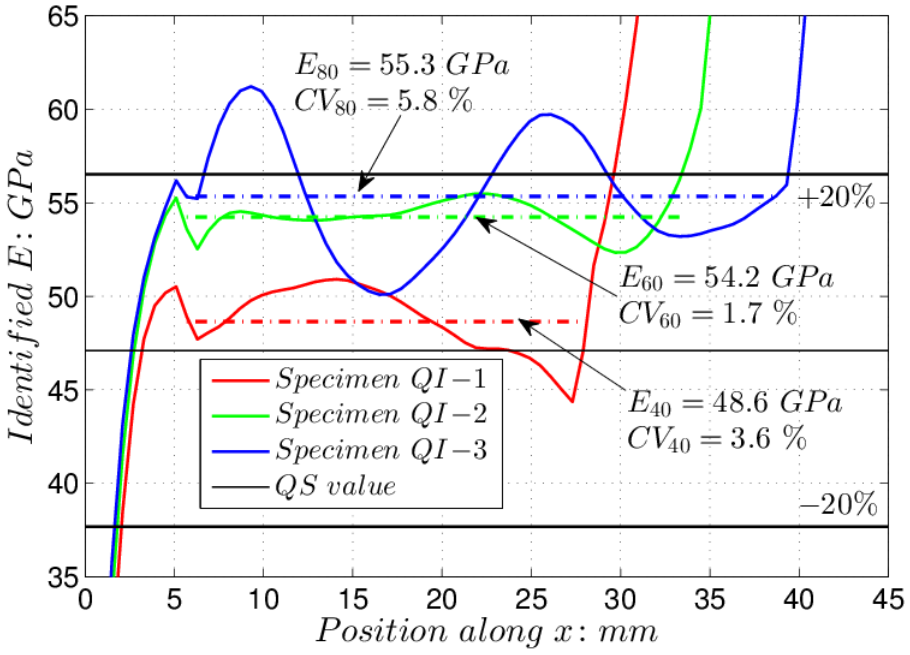

FIGURE 6.26: Identified Young's modulus for the three quasi-isotropic specimens.

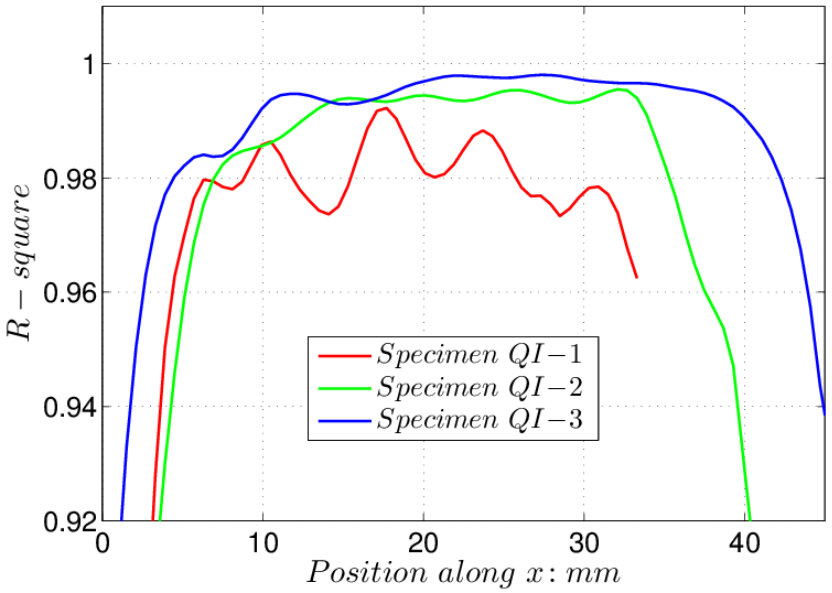

FIGURE 6.27: Correlation coefficient for the three quasi-isotropic specimens.

As seen in Figure 6.26, the identification in the central section of the field of view proved more stable. Therefore, a large over-determined system consisting of data in the central section has been built up frame by frame and used to identify the overall Young's modulus and Poisson's ratio. According to the identification in Figure 6.26, different regions of interests were selected. For specimen QI-1, 5 columns from the left (free) end and 2 columns from the right (impact) end of the field of view were removed from an initial data set of 56 columns by 44 rows. These were: for specimen QI-2, 4 columns from the left (free) end and 12 columns from the right (impact) end from a 68 columns by 47 rows data set, and for specimen QI-3, 3 columns from the left (free) end and 10 columns from the right (impact) end from a 76 columns by 46 rows data set. The identified results are shown in Table 6.1. It is clear that the identified ν is very bad. Thus, Young's modulus has been calculated with $\nu = 0.31$. The modulus from specimens QI-2 and QI-3 is closer to the expected reference, in spite of the large contact point offset for specimen QI-3, as seen in Figure 4.27. This illustrates again the benefit of longer specimens.

TABLE 6.1: Identification from the large over-determined system with experimental data for the three specimens. $E_{quasi-static} = 47.1\ GPa$. $\nu = 0.31$.

	E: GPa	ν
Specimen QI-1 (L=40 mm)	70.6	0.26
Specimen QI-2 (L=60 mm)	50.8	−0.14
Specimen QI-3 (L=80 mm)	51.9	−0.10

6.3 Full VFM identification

The last section presents the identified results with a simplified VFM approach based on the reconstruction of stress profiles from acceleration. This section presents the identification results using the full VFM. All experimental data described previously are now processed with the special optimised VFM described in Section 3.2. Not only does the VFM processing extract Young's modulus and Poisson's ratio from the heterogeneous kinematic fields, but this procedure also provides the coefficients variations of the identified stiffness components, indicating their sensitivity to noise.

6.3.1 Quasi-isotropic composite specimens

6.3.1.1 Cylindrical impactor tests

The experimental data obtained from the cylindrical quasi-isotropic impact tests were first processed. In the full VFM processing, a virtual mesh was used here to expand the virtual fields, with varying number of virtual elements: m in the x-direction and n in the y-direction. As previously discussed, the identification close to both ends of the specimen is not reliable, however, the identification in the central area is better, as shown in Figures 6.21 and 6.22. Therefore, the field of view used here discards 9 mm from the impact edge and 2.2 mm from the free edge. The virtual nodes located at both vertical boundaries are all constrained to zero virtual displacements to filter out the unknown stress distributions that would otherwise appear in the virtual work on external forces. Identification is performed at each time when an image is recorded. The results reporting E and ν obtained from Q_{xx} and Q_{xy}, which are the quantities delivered by the VFM, for $m = 10$ and $n = 2$ are shown in Figure 6.28. They are rather nice even though the data are bad for the early and late stages of the test. This is not surprising as strains are low at the beginning and at the end of the test. This is illustrated by the η_{ij}/Q_{ij} parameters in Figure 6.29. One can see high values at the beginning and end, reflecting bad signal-to-noise ratio then because of low strains. If one only keeps the data between 6 and 12 microseconds, then the average E is 47.2 GPa and the average ν is 0.28, which are very close to the reference. A legitimate question concerns the stability of the identification with respect to the virtual mesh. Figure 6.30 answers this question. Stability is excellent, with a slight convergence effect when the virtual mesh density is increased and a saturation after 8×2. If the density was increased further, instabilities would appear. This is consistent with previous results on this [28]. Globally, the stability of the VFM approach is good even though some oscillations in

stiffness parameters can be seen. Further work is required to investigate this issue in more depth, as well as the effect of the smoothing parameters.

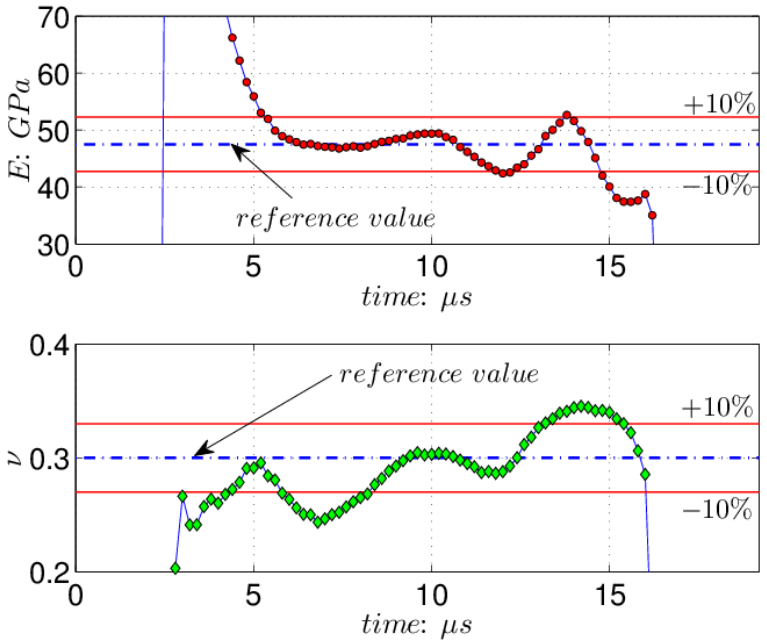

FIGURE 6.28: Identified results from the VFM with 10×2 virtual mesh, HPV-X camera. Quasi-isotropic specimen with the cylindrical impactor.

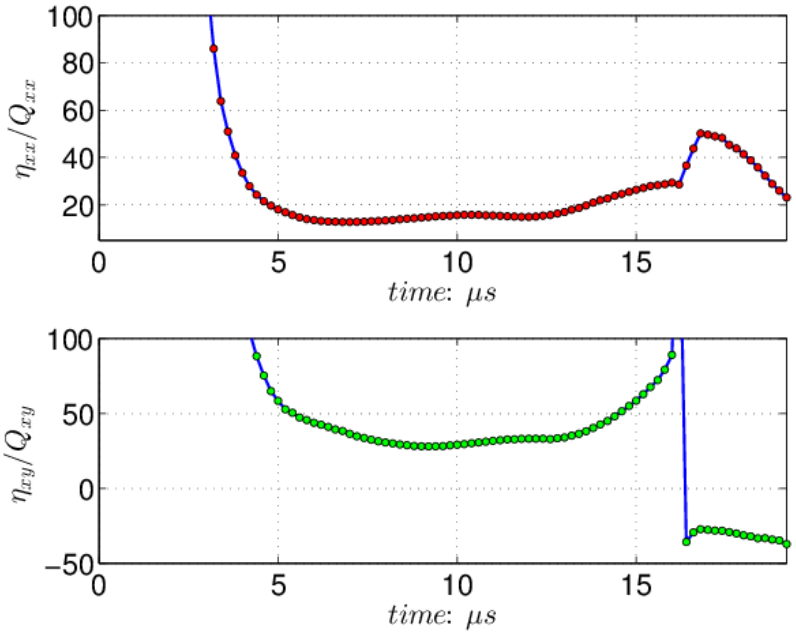

FIGURE 6.29: η_{ij}/Q_{ij} parameters for the VFM with 10×2 virtual mesh, HPV-X camera. Quasi-isotropic specimen with the cylindrical impactor.

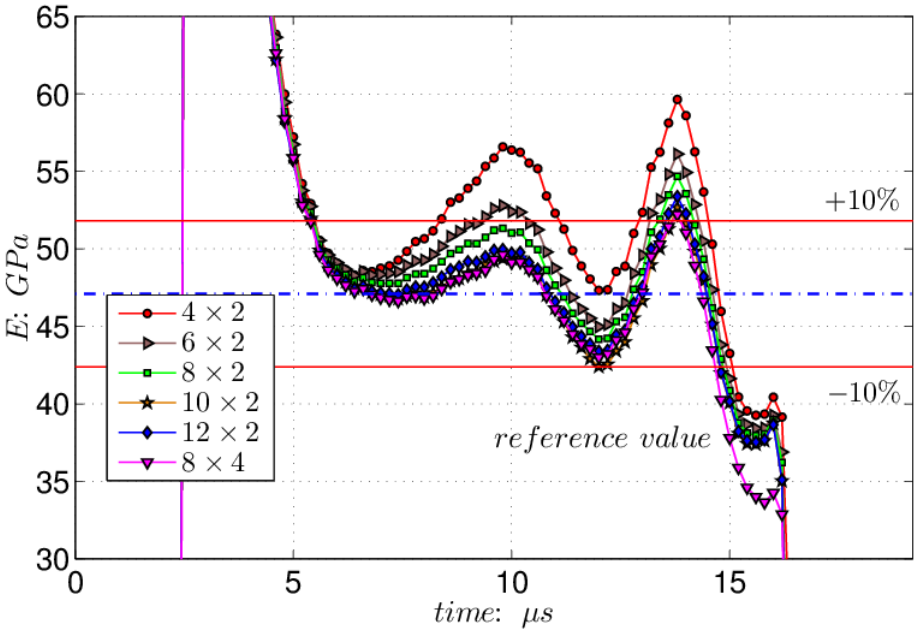

(A)

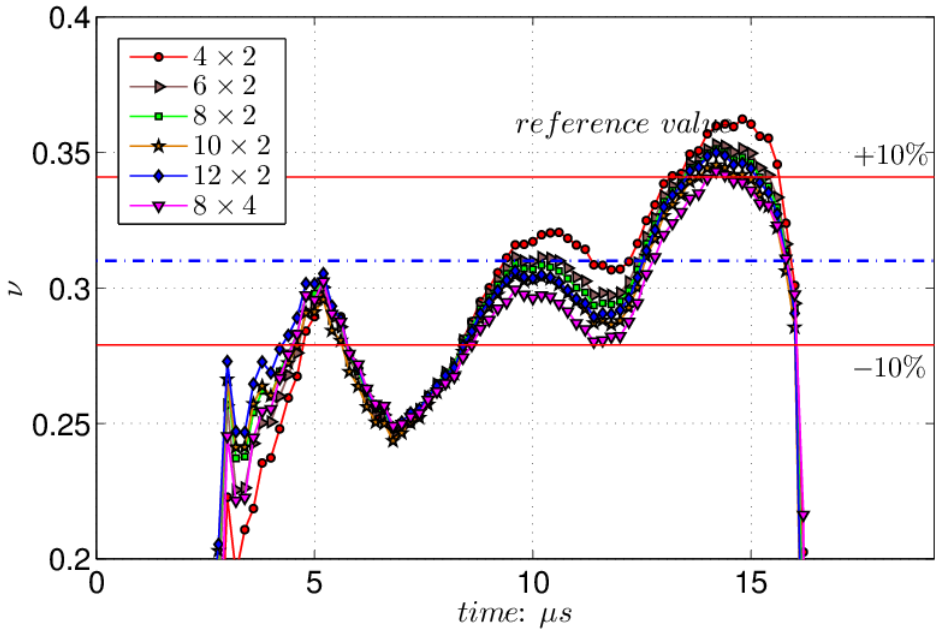

(B)

FIGURE 6.30: Identified results for the VFM with varied virtual mesh densities, HPV-X camera. Quasi-isotropic specimen with the cylindrical impactor. (A) Young's modulus. (B) Poisson's ratio.

6.3.1.2 Ball impactor tests

For the quasi-isotropic ball impact tests, the same data used to build up the large over-determined system in Section 6.2.2 was processed by the VFM. In this case, the virtual displacement components along the left and right boundaries of the region of interest

are necessarily set to zero so that the virtual work of the unknown stress distributions at both boundaries can be zeroed out. Following a convergence study on the virtual mesh density, the virtual mesh selected here is composed of 13 elements in the x-direction and 3 elements in the y-direction. The identified Young's modulus and Poisson's ratio are presented in Figure 6.31. Here again, Young's modulus has been calculated with $\nu = 0.31$, due to worse identification of Poisson's ratio. The identified values for E are consistent with the results from the over-determined system. The values are systematically lower for the 40 mm specimen and systematically higher for the other two, to about the same levels. Poisson's ratio was also reasonably estimated, particularly for the 60 mm specimen.

Finally, it is interesting to look at the ratios between the standard deviations and mean values of the identified stiffness components, denoted η_{xx}/Q_{xx} and η_{xy}/Q_{xy} in this paper and provided by the optimized virtual field procedure. The lower the η/Q values, the better the identification. As such, these parameters provide an indication of the quality of the identification. High values of these ratios indicate poor signal to noise ratios for the identification [148]. The values of these parameters are shown in Figure 6.32. As can be seen, the values of η_{xx}/Q_{xx} and η_{xy}/Q_{xy} for specimen QI-1 are systematically higher than for the other two specimens. This is consistent with the lower strain levels for this test, as seen in Figure 6.9. Also, the abnormally high values at the early and late stages are because of low signal to noise ratios, as explained before. Moreover, it is clear that the levels of η_{xy}/Q_{xy} are higher than that of η_{xx}/Q_{xx} for the three specimens. This is not surprising as Poisson's ratio has less influence on the actual strain field than Young's modulus and is always going to be more difficult to identify. Finally, the values are about one order of magnitude larger than for the cylindrical impact tests in Figure 6.29, as expected from the fact that strains are much lower here, which explains the lower quality of the identification.

Generally, the identified results are close to the quasi-isotropic reference values and the previous results from the cylindrical impactor tests. For instance, for specimen QI-3, the average E is 53.3 GPa (error of 13.2 %) and the average ν is 0.22 (error of 26.7 %) if only focusing on the results between 10 and 23 microseconds.

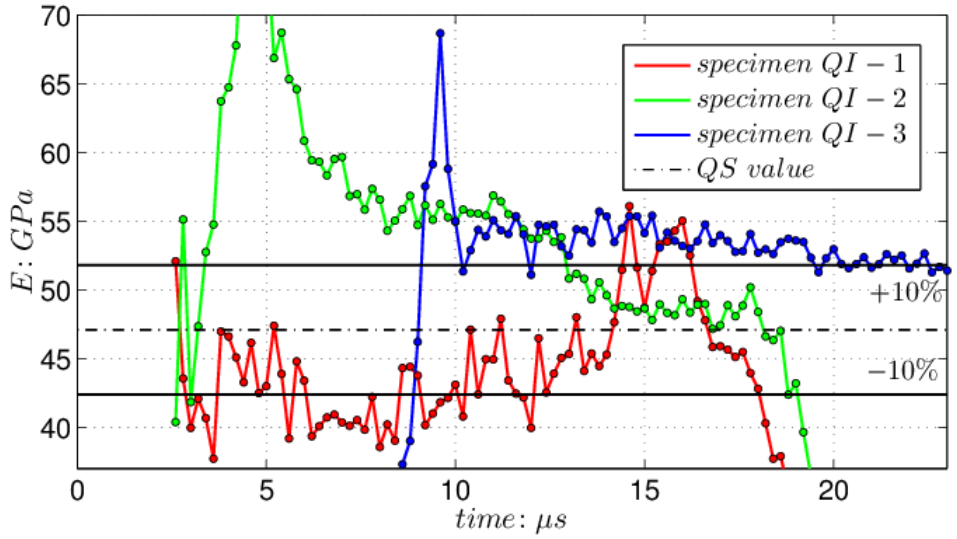

(A)

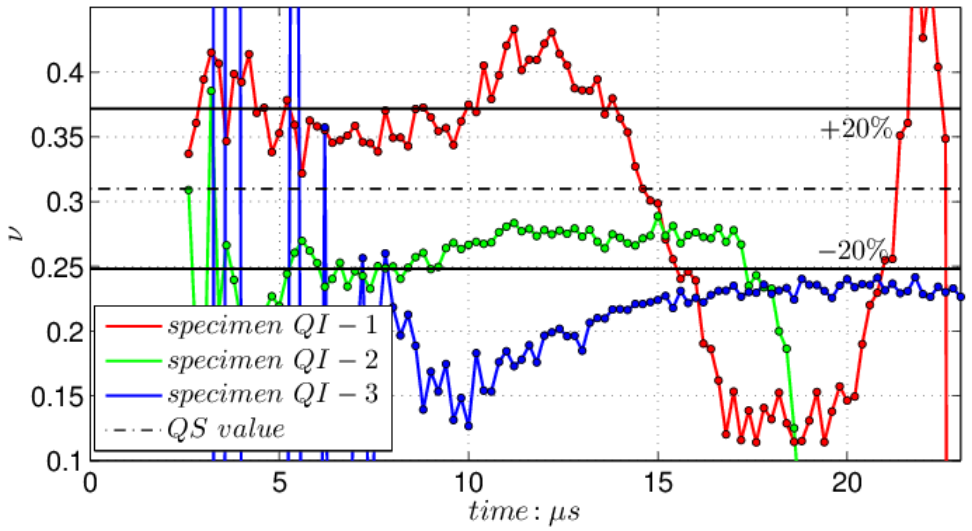

(B)

FIGURE 6.31: Identified Young's modulus and Poisson's ratios with the VFM for the three specimens. Virtual mesh: $m = 13$, $n = 3$. Quasi-isotropic specimen with the ball impactor. (A) Young's modulus. (B) Poisson's ratio.

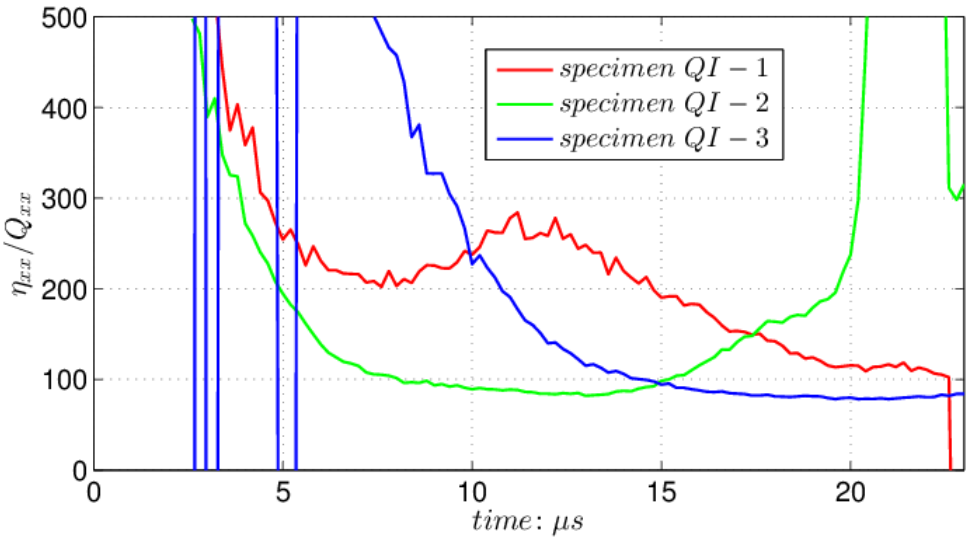

(A)

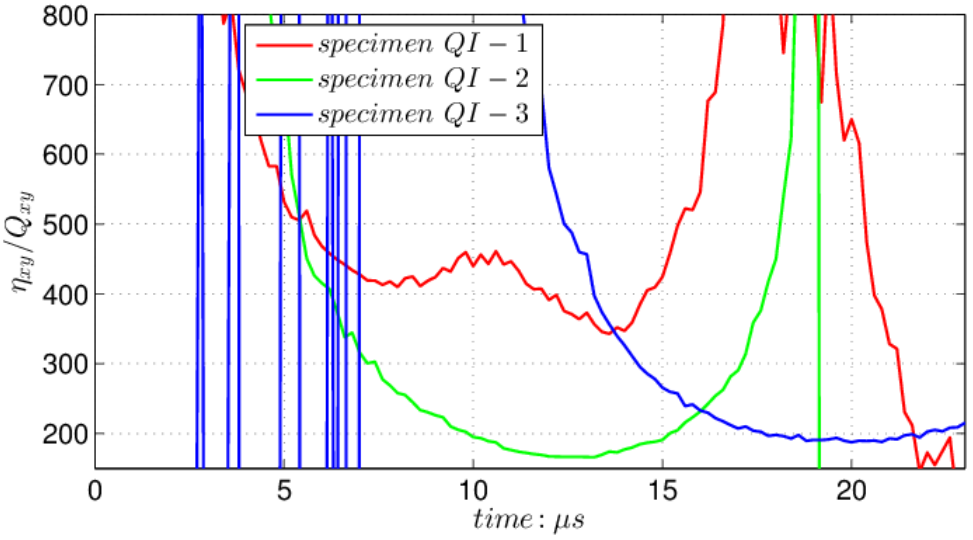

(B)

FIGURE 6.32: Coefficients of sensitivity to noise for the three specimens. Virtual mesh: $m = 13$, $n = 3$. Quasi-isotropic specimen with the ball impactor. (A) η_{xx}/Q_{xx}. (B) η_{xy}/Q_{xy}.

6.3.2 Unidirectional composite specimens

For the unidirectional impact tests, the full-field data were first processed using the VFM procedure without strain rate dependence described in Appendix C. However, as presented in Section 6.1.2, the strain rate levels in the cylindrical impactor tests are very high, over 3000 s^{-1}, which is significantly higher than that in the ball impactor tests. Therefore, the full-field data from the cylindrical impactor tests are used to initially identify the strain rate dependent parameters.

6.3.2.1 Cylindrical impactor tests

The full-field data obtained from the cylindrical impactor tests were processed by the full VFM routine. Here, the VFM procedure detailed in Appendix C was first used to identify the four independent stiffness components. In the processing, the virtual displacement vector along the right-hand side of the field of view was zeroed to cancel out the virtual work of impact forces. According to a convergence study on the virtual mesh density, the virtual mesh selected here is composed of 12 elements in the x-direction and 5 elements in the y-direction. The four identified stiffness components are presented in Figure 6.33. The references for Q_{22} and Q_{66} were extrapolated from the model and data in [32] based on the present average strain rate level (around 1300 s^{-1} and 400 s^{-1} for the shear and transverse strain rates, respectively). It can be seen that the identification of Q_{11} and Q_{66} is reasonably good, although the identification at the first few microseconds is unreliable because only a very small part of the field of view experiences significant strains. The mean value after 5 microseconds for the identified Q_{11} is around 96.8 GPa, and the relative error is 21.9 %. Similarly, for Q_{66} the mean value after 7 microseconds is around 5.9 GPa (error of 9.2 %). However, the identification of Q_{12} and Q_{22} is very bad. This is expected because at low off-axis fibre angles the transverse stress is very low, leading to lack of identifiability. As for Q_{12}, it was shown before that it can only be correctly identified if both Q_{11} and Q_{22} are correctly identified[28]. For the case of $\vartheta = 40°$, two sets of full-field maps were both processed using the same routine. For this off-axis angles, the identification of Q_{11} is bad due to the low longitudinal stress this time, and as explained before, Q_{12} cannot be identified successfully either is Q11 is not. Here only the identified Q_{22} and Q_{66} are presented, as shown in Figure 6.34. One can clearly see that the identifications of Q_{22} and Q_{66} from two independent impact tests are consistent. Specifically, from specimen UD 40-1, the mean value after 10 microseconds of identified Q_{22} is around 11.7 GPa, and the relative error is 4.5 %, the mean value of identified Q_{66} is about 5.0 GPa (error of 19.4 %). While from specimen UD 40-2, the mean value of Q_{22} between 5 and 20 microseconds is around 10.9 GPa (error of 2.7 %),

5.5 GPa (error of 11.3 %) for Q_{66}. This confirms the reproducibility of the experimental procedure even though a detailed analysis would be necessary to understand the results.

6.3.2.2 Ball impactor tests

As mentioned in Section 6.1.2.2, a couple of specimens with three different lengths and two off-axis fibre angles were employed in the ball impactor tests. For the off-axis case with $\vartheta = 15°$, the full-field data were processed by the VFM routine described in Appendix C. Similarly to the results in Section 6.3.2.1, Q_{22} and Q_{12} are not identifiable, for the same reason: the stress transverse to the fibre direction is too low for this off-axis configuration. On the other hand, the identification of Q_{11} and Q_{66} from the longest specimen ($L = 80\ mm$) is not good either. Therefore, only the identified Q_{11} and Q_{66} for the specimens of lengths 40 mm and 60 mm are presented here, as shown in Figure 6.35. Comparing with the results in the cylindrical impactor tests, it can be seen that the results in Figure 6.35 are worse than those in Figure 6.33. For one thing, as mentioned in Section 6.1.2.2, the strain levels in the ball impactor tests were much lower than those in the cylindrical impactor tests, leading to worse ratios of signal to noise. Another potential reason is that the through-thickness strain distribution in the ball impactor tests tends to be more heterogeneous, which introduces error when evaluating the volume integrals from surface measurements in the VFM equations, as mentioned previously. As seen in Figure 6.35, the identification from the specimen of length 60 mm is more stable and accurate than that from the short specimen, especially the identification of Q_{66}, confirming again that lengthening the specimens reduces the strain heterogeneity through the thickness at sections away from the impact end. For $\vartheta = 60°$ parameters Q_{11} and Q_{12} are not identified successfully as for the cylindrical impactor tests. The identified Q_{22} and Q_{66} are shown in Figure 6.36. It can be seen that the identification is reasonable, although it is worse than the counterpart in Figure 6.34.

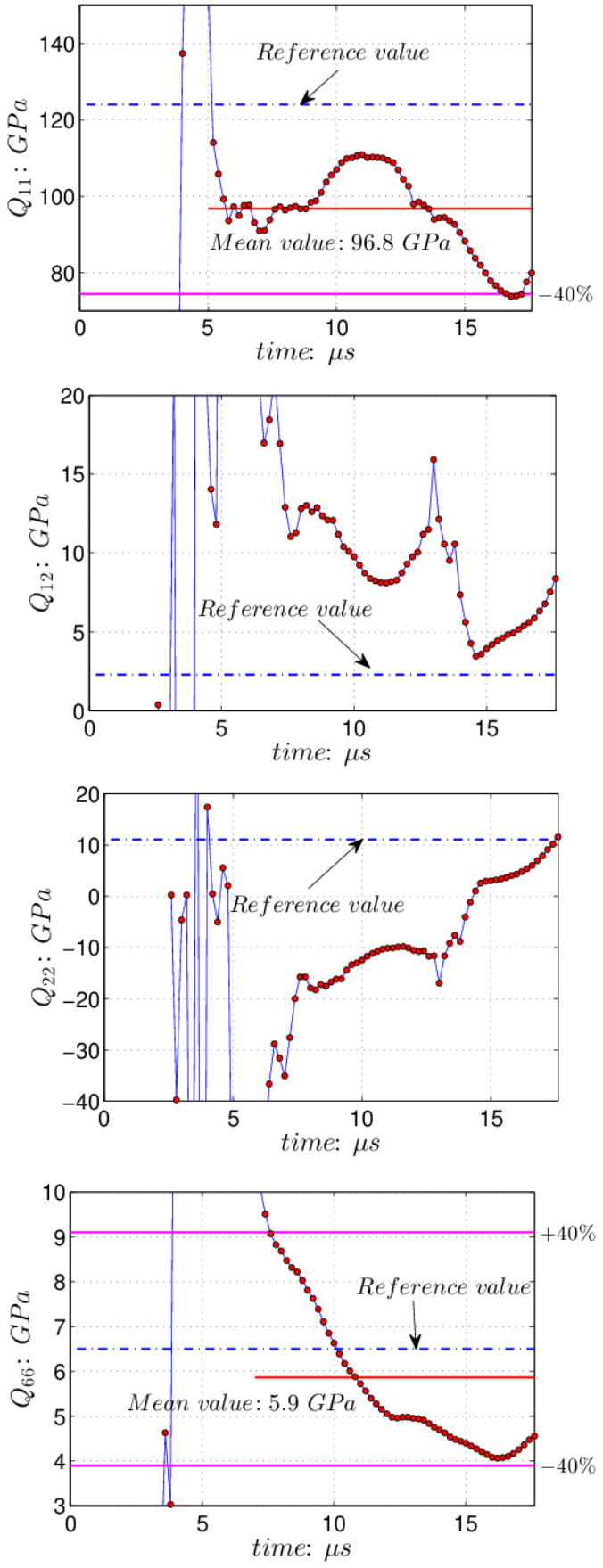

FIGURE 6.33: Identification of the four stiffness components without strain rate effect. Virtual mesh: 12×5. Data points: 55×42. Unidirectional specimen with the cylindrical impactor, $\vartheta = 15°$. Specimen length: $L = 40\ mm$.

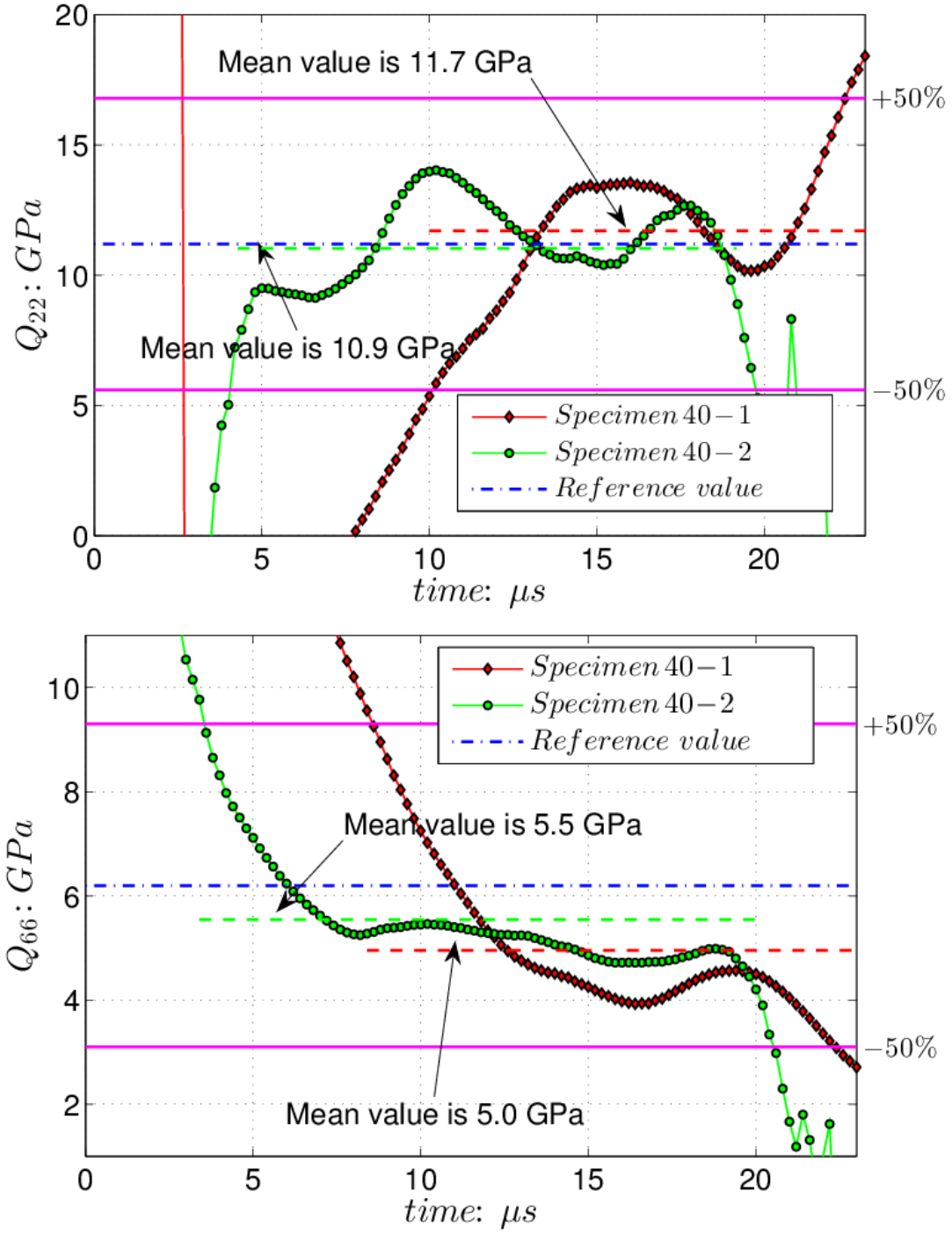

FIGURE 6.34: Identification of Q_{22} and Q_{66} without strain rate effect from two unidirectional specimens with the cylindrical impactor. $\vartheta = 40°$. Virtual mesh: 12×5. Data points: 55×45. Specimen length: $L = 40\ mm$.

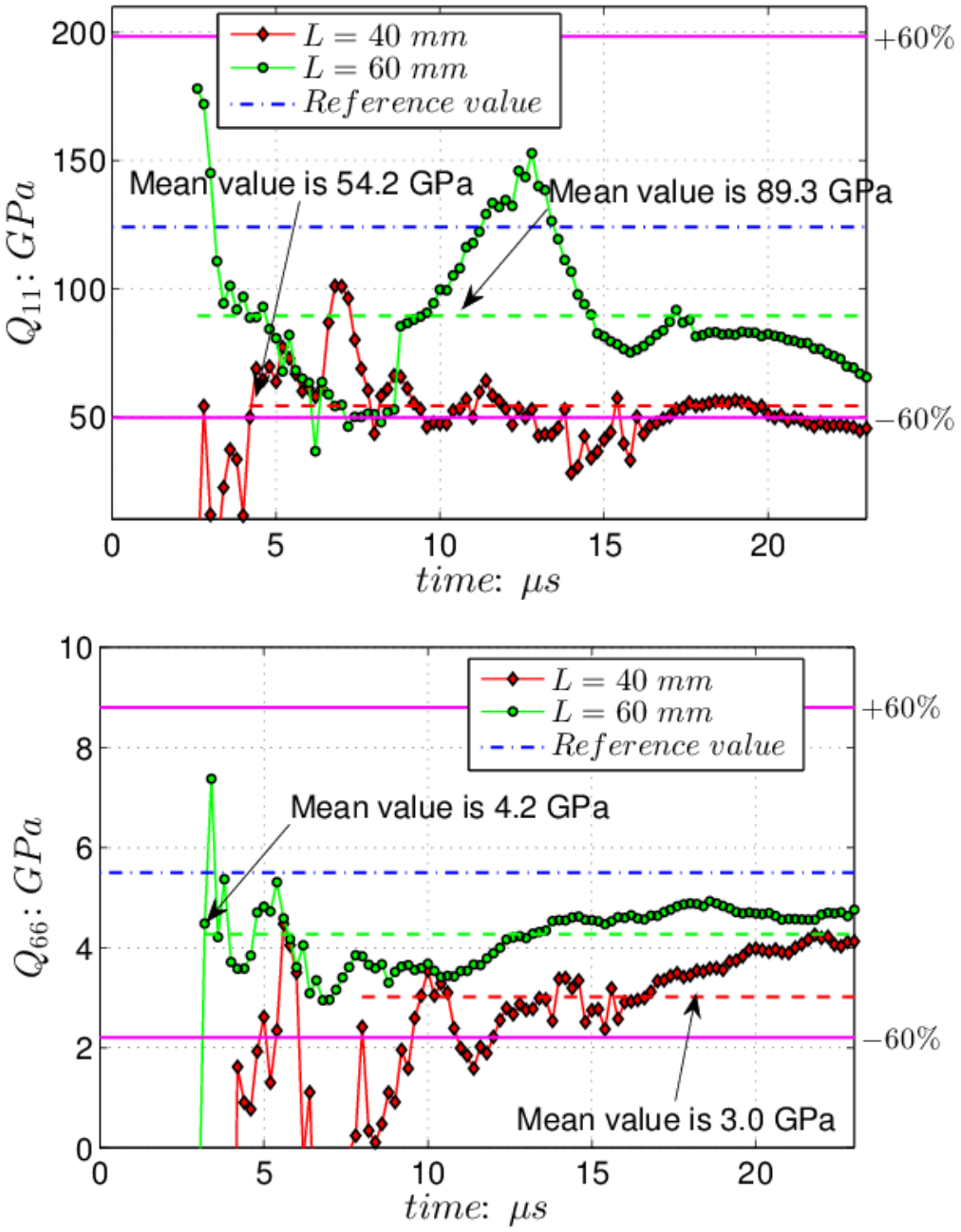

FIGURE 6.35: Identification of Q_{11} and Q_{66} without strain rate effect from two unidirectional specimens with different lengths in the ball impactor tests. $\vartheta = 15°$. Virtual mesh: 12×5.

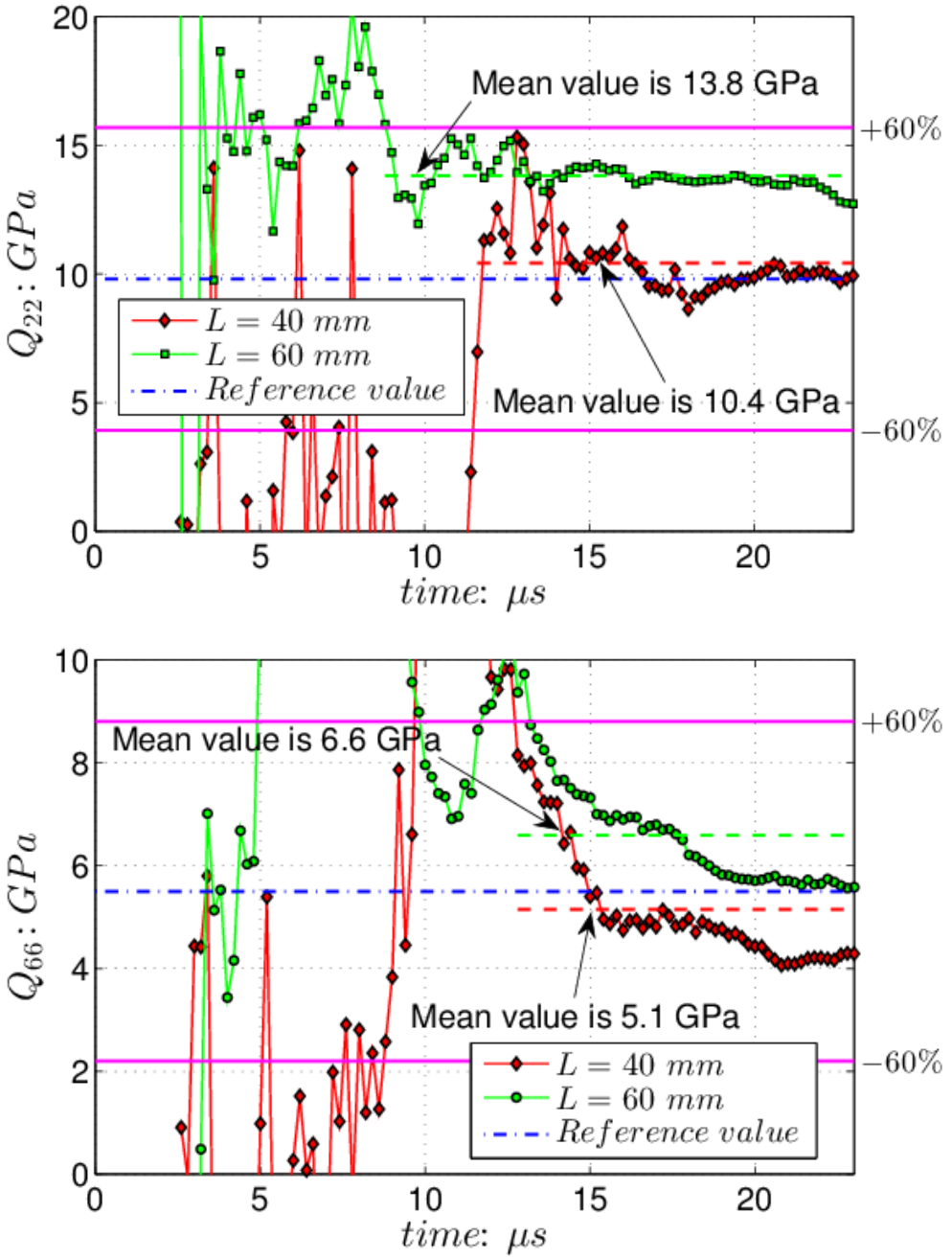

FIGURE 6.36: Identification of Q_{22} and Q_{66} without strain rate effect from two unidirectional specimens with different lengths in the ball impactor tests. $\vartheta = 60°$. Virtual mesh: 12×5.

6.3.2.3 Identification of strain rate dependent parameters

The previous identification did not consider an explicit strain rate dependence model. Since the strain rate maps are very heterogeneous, a strain rate dependence will lead to a spatial dependence of the modulus at each time step, and this will vary in time. The identification therefore results in a sort of weighted average of the strain rate dependent stiffness. This weighting depends on the VFM approach. However, even though the strain rate maps as seen for instance in Figure 6.10 contains continuous values between zero and the maximum strain rate (about 3000 s^{-1}), the areas where the strain rate is low also corresponds to areas where the strains are low. Therefore, the weight of these areas in the final stiffness value will be very small. This tends to kill the idea that a heterogeneous strain rate map has the potential to lead to the identification of the complete strain rate dependence model from zero to the maximum strain rate. In practice, this may only be done over a certain range of strain rates corresponding to large enough strain. This is even more true here as the strain rate heterogeneity only arises from the wave propagation. Introducing a strain concentrator (notches, holes) would increase the range of strain rate over which the strain rate dependence can be identified. The possibility to identify a strain rate dependence model over a certain range on a single test also depends on the severity of the strain rate dependence. Here, it is rather low, as shown in [32] so it is probable that even though the strain rate map is heterogeneous, the identified stiffness components correspond to the value that would be obtained from a homogeneous strain rate map tests at the corresponding average strain rate obtained from the heterogeneous maps. And therefore, the stain rate map heterogeneity can be ignored in the identification process. The objective of this section is to check this hypothesis by processing the heterogeneous strain rate map using an explicit strain rate dependence model and comparing the results with the identification without explicit strain rate dependence.

As discussed in Chapter 3 and 4, the strain rate dependence was considered only on the transverse and shear stiffness components. The model has been described as Equation 3.38. As a first step, only the experimental data from the off-axis test at $\vartheta = 15°$ are analysed. For this configuration, only the strain rate dependence on the shear stiffness component is investigated as a first step. The full-field data were processed using the VFM routine described in Appendix D, and only parameter β_6 is identified, supposing parameter Q_{66}^0 is known as the quasi-static stiffness. In the VFM processing, the virtual displacement vector was zeroed to cancel out the virtual work of the impact forces. The virtual mesh is composed of 12 elements in the x-direction and 5 elements in the y-direction. The identified β_6 is presented in Figure 6.37. It can be seen the profile of β_6 is very close to that of identified Q_{66} in Figure 6.33. In Equation 3.38, only considering

the shear component, parameter Q_{66} has been identified, as shown in Figure 6.33. Q_{66}^0 is known as the shear stiffness component under quasi-static conditions. From full-field information, it is possible to plot the average strain rate profiles ($\overline{|\dot{\varepsilon_6}|}$)over the field of view in the fibre orientation system with a threshold of 1.10^{-4} strain to remove small strains, as shown in Figure 6.38. Thus, in Equation 3.38, parameter β_6 can be extracted directly. The result is shown in Figure 6.37 as well. Comparing the results from the VFM routine and the direct resolution, one can clearly see that the profiles from the two routines are consistent. The mean value of identified β_6 after 6 microseconds is around 0.42 GPa. This is closed to the extracted value (0.35 GPa) from the data in [32] using the model in Equation 3.38. This confirms that for the current situation where strain rate heterogeneity is only caused by wave propagation, there is not enough information to extract a strain rate dependence information from just this test. However, this also means that it is not necessary to include a strain rate dependence model explicitly in the identification.

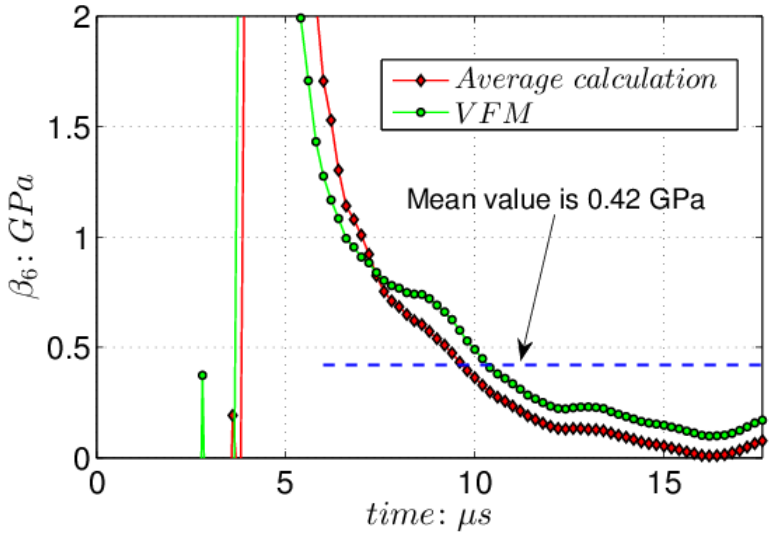

FIGURE 6.37: Identified β_6 from the VFM routine and the direct resolution. Virtual mesh: 12×5. Data points: 55×45. Unidirectional specimen with the cylindrical impactor, $\vartheta = 15°$.

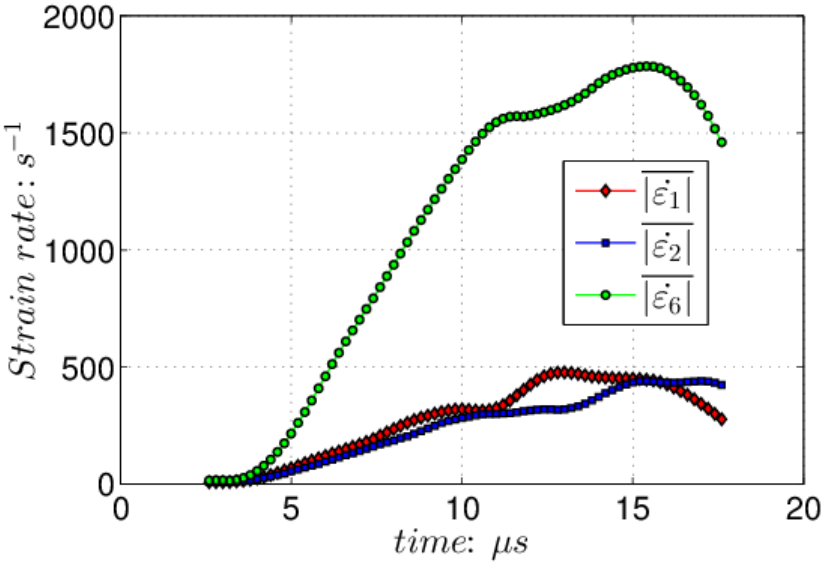

FIGURE 6.38: Average strain rate in the cylindrical unidirectional impact tests in fibre orientation system. Unidirectional specimen with the cylindrical impactor, $\vartheta = 15°$. Threshold of strain: 1.10^{-4}.

6.4 Summary

Chapter 5 and 6 described the experimental implementation of purely inertial impact tests and identification of the material parameters making use of inertial effects. The reasonably consistent identification from experimental tests confirms that inertial forces can be used to identify the constitutive parameters at high strain rates without the need for any external impact force measurement.

For the identification of isotropic constitutive parameters, a couple of quasi-isotropic composite specimens were tested using two different impact rigs. One uses a cylindrical impactor. In this set-up, two different UHS cameras were employed to record the full-field deformation of the specimens during the impact events. The patterns of full-field maps obtained from the two cameras are reasonably consistent, illustrating the reproducibility of the set-up which using a rigid foam stand for the specimen. The identification from the data obtained using the two cameras are also reasonably similar, confirming the feasibility of this experimental procedure. The other type of test was used a steel ball impactor to provide high rate loading. With this ball impactor, the stress/strain state in the specimen proved much more heterogenous than that with the cylindrical impactor. However, this also introduced an issue for the identification, *i.e.*, the through-thickness strain heterogeneity. This issue might happen in the cylindrical impactor tests as well. However, it is much more significant in the ball impactor tests. This has been numerically investigated in Chapter 4. The experimental results also

confirmed that lengthening the specimen can mitigate the through-thickness strain heterogeneity in sections away from the impact end, an example of Saint-Venant's principle in dynamics. Another issue in the ball impactor tests are the small strain levels. Indeed, the strain levels in this test were only one tenth of those in the cylindrical impact tests. However, the identified results were still reasonably consistent with that from the cylindrical impact tests and the reference values. This is even more remarkable as the strain levels were, systematically less than 1000 microstrains, together with the more complex $2D$ strain distributions arising from a point load and the $3D$ parasitic effects coming from the non-uniform through-thickness load distribution. This strengthens the fact that this new inertial testing approach already presented in a few papers in the past has great potential to become a practical tool for high strain rate identification in the future, even though plenty of work is still to be done to realize this potential.

For the identification of orthotropic constitutive parameters, the same impact rigs were used. In the cylindrical impactor tests, specimens with two off-axis fibre angles $\vartheta = 15°$ and $40°$ were tested. The full-field data were processed by the VFM without explicit strain rate dependent model. It was shown that the identifications of Q_{11} and Q_{66} were reasonably good when $\vartheta = 15°$, while the identification of Q_{22} and Q_{66} were better at the fibre angle of $40°$, which is consistent with the predominant stress levels. The identification of Q_{12} was always bad, as expected since both Q_{11} and Q_{22} could not be identified correctly at the same time with this test. In the ball impactor tests, specimens with three different lengths and two off-axis fibre angles $\vartheta = 15°$ and $60°$ were employed. The results were similar to that from the cylindrical impact tests. At the low off-axis fibre angle ($\vartheta = 15°$), the identification of only Q_{11} and Q_{66} was available, whereas at the fibre angle of $60°$, it was Q_{22} and Q_{66}. Comparing the identification from different specimen lengths (with the same off-axis fibre angles), it can be seen that the results from longer specimens proved more stable than those from short specimens, illustrating Saint-Venant effect in dynamics again. According to the results of the unidirectional impact tests, it was concluded that the strain state in the specimens was still not heterogeneous enough to activate all stiffness components, leading to incomplete identification of all stiffness components from a single test. Better experimental configuration should be developed in the future. Additionally, the strain rate dependent parameter was initially identified from experimental data. As a first step, only the strain rate effect on the shear stiffness component was considered. Parameter β_6 was identified either using an explicit strain rate dependent model taking into account the strain rate map heterogeneity, or considering an average strain rate without the explicit strain rate dependence. The results proved very close, which was expected because of the low strain rate dependence of the composite and the nature of the present test where the strain rate heterogeneity mainly arises from wave propagation.

Chapter 7

General conclusions and perspectives

In this work a novel general experimental procedure for high strain rate testing of materials has been proposed, although much work still has to be devoted to this new paradigm in the future to make it a fully operational tool. This procedure allows to identify the constitutive parameters of materials at high strain rates making use of inertial effects without the need for any external impact force measurements. Apart from simplifying the experimental set-up by removing the need for the cumbersome Hopkinson bars, the main advantage of this new paradigm is to relieve the stringent assumptions and limitations on which the standard split Hopkinson bars approaches rest. Indeed, the main idea is to use ultra-high speed imaging to record deformation maps as a function of time, using either speckle patterns and DIC or grids with phase shifting. From these data, time-resolved strain maps can be derived by spatial differentiation and acceleration maps by double temporal differentiation. Using integral mechanical equilibrium (weak form of equilibrium), it is possible to balance internal stresses calculated from strains and constitutive law with inertial forces obtained from the acceleration maps and the density. In this case, the need for external load measurement is relieved and all the required information is contained in the camera images, provided that the material density is known. Inertial effects, far from being a nuisance as in the standard SHPB approach, become an advantage by providing a volume distributed load cell. As a consequence of the above, the design space for test configurations opens up dramatically and needs to be explored as widely as possible in order to reach suitable new standard tests using this new paradigm.

7.1 General conclusions

The main conclusions of in the present work are as follows:

- It is possible to provide sufficient deformation and acceleration levels (over one million g's) with purely inertial impact tests as that shown in Figures 5.1 and 5.2.
- Recent progress in the technology of ultra-high speed cameras enables measurement of full-field deformation with unprecedented quality. With the increasing application of ultra-high speed cameras in high strain rate testing of materials and technological progress, ultra-high speed imaging will become nearly as common as high-speed imaging currently is.
- For the in-plane isotropic composite specimens tested here, the quality of the identification data is impressive at that level of strain rate, about 2000 s^{-1}. There is enough information to retrieve the two elastic parameters of the quasi-isotropic laminate with the current experimental configuration, and the results proved excellent, emphasising the previous point about camera progress. However, the identification of the four orthotropic parameters for unidirectional specimens was not successful. The main reason is because the stress/strain states in the specimen are not heterogenous enough; and some strain heterogeneity through the thickness occurring during the impact events may also have led to some discrepancies. Another thing is the strain rate dependence of orthotropic materials, making the identification of orthotropic parameters more difficult.
- According to the maps of full-field deformation in the cylindrical impactor tests, it is clear that these mechanical fields are very heterogeneous. In this case, conventional approaches such as the SHPB are invalid to perform the constitutive parameters identification.
- Comparing the experimental results from the two types of impactors, it can be see that the strain levels in the ball bullet impact tests were only one tenth of that in the steel cylindrical impact tests, however, the identification with the two projectiles proved reasonably consistent, verifying the feasibility and reproducibility of the procedure proposed in this thesis.
- This thesis proposes a new VFM-based methodology for analysing the strain rate dependence of materials at high strain rates. The identification of the strain rate dependent parameter with this new methodology was initially identified from experimental data. As a first step, only the strain rate effect on the shear stiffness component was considered. Parameter β_6 was identified either using an explicit strain rate dependent model considering the heterogenous strain rate map, or taking into account an average strain rate without the explicit strain rate dependence.

The results proved very close, which was expected due to the low strain rate dependence of the composite and the nature of the present test where the strain rate heterogeneity mainly arises from wave propagation.

- In the ball impactor tests, the point load impact configuration gives rise to heterogeneous distributions of stress and strain through the thickness which evolve in time and space as the waves propagate and bounce off the different specimen faces. The presence of a thin 1 *mm* steel tab slightly mitigates this problem, though its plastic deformation absorbs a significant amount of the impact energy which led to small experimental strain levels in the specimen. According to FE simulations with different offset impact models and specimen lengths, longer specimens provide more stable and precise identification. This was confirmed experimentally. As such, this has confirmed the existence of Saint-Venant effects in high rate dynamics, as already established by previous authors[166], with a fade away distance of around one to two times the width, similar to quasi-static situations. However, for orthotropic materials, this distance becomes much larger, as shown in [160].
- Finally, the results presented in this thesis confirm that the present alternative to classical Split Hopkinson Pressure Bar has potential to become a standard technique in the future.

7.2 Perspectives

This PhD work is very exploratory in nature. Many issues need to be addressed in the near future. A few of these are listed below:

- The identification is only elastic here, although the non-linear shear stress-strain behaviour was initially explored based on a simple non-linear law. This is justified at these early stages to validate the technique and test its robustness. There is a need for better constitutive models for high strain rate behaviour of materials. This has mainly been hindered by the poorer experimental evidence that could be collected compared to quasi-static situations. It is hoped that by improving test data, mechanics of materials researchers will be able to use this to develop better materials models to take full advantages of the current and future capacities of numerical simulation. For instance, a strain rate dependent constitutive model has been developed and implemented using the user subroutine (VUMAT) of ABAQUS/EXPLICIT. However, the time estimation in VUMAT proved unreliable, leading to erroneous calculation of strain rate. Therefore, more FE validations with suitable user subroutines are required to be developed. The real interest

lies in non-linear behaviour. Extension to elasto-visco-plasticity for metals is also underway and in the near future, more materials and constitutive models will be considered to widen the applicability of this technique.

- Finally, it will be necessary to delve into test configuration design by adapting recent tools developed for quasi-static to such inertial impact tests. There is a need for a more rational approach to test design. For instance, a special experimental set-up is required to produce more heterogeneous stress/strain states for the identification of orthotropic parameters. The identification simulator in [124] can be used for test design optimisation with an objective of minimal bias on the identified parameters, taking into accounts as many test parameters as needed to make it realistic. This is a long-term task and a difficult problem as the identification chain is very long and involves very many parameters.

Appendix A

List of Publications

Journal papers

- F. Pierron, H. Zhu, C. Siviour. Beyond Hopkinson's Bar. *Philosophical Transactions of the Royal Society A*, 372(2023) 2014: 1-24.
- H. Zhu, F. Pierron. Exploration of Saint-Venant's principle in inertial high strain rate testing of materials, submitted to *Experimental Mechanics*, 2014.

[1]International conferences papers & presentations

- H. Zhu, F. Pierron. Exploration of novel inertial tests for high strain rate testing of composites based on the Virtual Fields Method. 9^{th} *International Conference on Advances in Experimental Mechanics.* Sept 3∼5, 2013. Cardiff, UK. Finalist of the Young Stress Analyst Competition.
- H. Zhu, F. Pierron, C. Siviour. A methodology to identify materials constitutive parameters from inertial high strain rate tests: first results. 21^{st}*DYMAT Technical Meeting: High speed imaging for dynamic testing of materials and structures.* Nov 18∼20, 2013. London, UK.
- H. Zhu, F. Pierron, C. Sivour. A Novel Procedure to Identify the Strain Rate Dependence of the In-plane Shear Modulus of Composites Using Inertial Impact Tests. 16^{th}*International Conference of Experimental Mechanics.* July 7∼ 11, 2014. Cambridge, UK.
- H. Zhu, F. Pierron, C. Siviour. Strain Rate Dependence Identification From Full-field Heterogeneous Strain Rate Maps. 9^{th} *International Conference on Mechanics of Time Dependent Materials.* May 27∼ 30, 2014. Montréal, Canada.

- H. Zhu, F. Pierron, C. Siviour. Latest Results in Novel Inertial High Strain Rate Tests. Dynamic Behaviour of Materials. Volume I. *Proceedings of the 2014 Annual Conference of the SEM on Experimental and Applied Mechanics*, Greenville, USA. pp 21-26.

[1]Underlined name is the presenter of the paper.

Appendix B

Identification of the isotropic linear elastic model

Only considering the noise in the strain fields, for the $2D$ isotropic linear elastic model, with a particular virtual field Equation 3.14 can be expressed as:

$$\begin{aligned} Q_{xx}\int_S[(\varepsilon_x-\gamma\mathfrak{N}_x)\varepsilon_x^*+(\varepsilon_y-\gamma\mathfrak{N}_y)\varepsilon_y^*+\frac{1}{2}(\varepsilon_s-\gamma\mathfrak{N}_s)\varepsilon_s^*]dS+... \\ Q_{xy}\int_S[(\varepsilon_x-\gamma\mathfrak{N}_x)\varepsilon_y^*+(\varepsilon_y-\gamma\mathfrak{N}_y)\varepsilon_x^*-\frac{1}{2}(\varepsilon_s-\gamma\mathfrak{N}_s)\varepsilon_s^*]dS=-\int_S\rho a_i u_i^* dS \end{aligned} \tag{B.1}$$

where $\mathfrak{N}_i$'s represent the zero-mean Gaussian noise for three strain components, ε_i's the measured strains, γ the standard deviation of random variable of strain measurements. The noise in acceleration has been neglected as discussed in Chapter 3.

To identify two parameters in Equation B.1, two independent virtual fields satisfying the boundary conditions and special conditions are necessary. For instance, a special virtual field $u^{*(1)}$ provides Q_{xx}:

$$\begin{aligned} Q_{xx}=\gamma[Q_{xx}\int_S(\mathfrak{N}_x\varepsilon_x^{*(1)}+\mathfrak{N}_y\varepsilon_y^{*(1)}+\frac{1}{2}\mathfrak{N}_s\varepsilon_s^{*(1)})dS+... \\ Q_{xy}\int_S(\mathfrak{N}_x\varepsilon_y^{*(1)}+\mathfrak{N}_y\varepsilon_x^{*(1)}-\frac{1}{2}\mathfrak{N}_s\varepsilon_s^{*(1)})dS]-\int_S\rho a_i u_i^{*(1)}dS \end{aligned} \tag{B.2}$$

Similarly, Q_{xy} can be determined by another special field $u^{*(2)}$:

$$\begin{aligned} Q_{xy}=\gamma[Q_{xx}\int_S(\mathfrak{N}_x\varepsilon_x^{*(2)}+\mathfrak{N}_y\varepsilon_y^{*(2)}+\frac{1}{2}\mathfrak{N}_s\varepsilon_s^{*(2)})dS+... \\ Q_{xy}\int_S(\mathfrak{N}_x\varepsilon_y^{*(2)}+\mathfrak{N}_y\varepsilon_x^{*(2)}-\frac{1}{2}\mathfrak{N}_s\varepsilon_s^{*(2)})dS]-\int_S\rho a_i u_i^{*(2)}dS \end{aligned} \tag{B.3}$$

If the noise source is not taken into account in Equation B.2 and B.3, the stiffness components can be identified as approximate parameters Q_{xx}^{app} and Q_{xy}^{app}. According to Equation 3.19 and 3.22, these two components are defined by:

$$\begin{cases} Q_{xx}^{app} = -\int_S \rho a_i u_i^{*(1)} dS \\ Q_{xy}^{app} = -\int_S \rho a_i u_i^{*(2)} dS \end{cases} \tag{B.4}$$

Here Equation B.2 and B.3 can be rewritten as:

$$\begin{cases} Q_{xx} = \gamma[Q_{xx}\int_S(\mathfrak{N}_x\varepsilon_x^{*(1)} + \mathfrak{N}_y\varepsilon_y^{*(1)} + \frac{1}{2}\mathfrak{N}_s\varepsilon_s^{*(1)})dS + \\ \quad Q_{xy}\int_S(\mathfrak{N}_x\varepsilon_y^{*(1)} + \mathfrak{N}_y\varepsilon_x^{*(1)} - \frac{1}{2}\mathfrak{N}_s\varepsilon_s^{*(1)})dS] + Q_{xx}^{app} \\ Q_{xy} = \gamma[Q_{xx}\int_S(\mathfrak{N}_x\varepsilon_x^{*(2)} + \mathfrak{N}_y\varepsilon_y^{*(2)} + \frac{1}{2}\mathfrak{N}_s\varepsilon_s^{*(2)})dS + \\ \quad Q_{xy}\int_S(\mathfrak{N}_x\varepsilon_y^{*(2)} + \mathfrak{N}_y\varepsilon_x^{*(2)} - \frac{1}{2}\mathfrak{N}_s\varepsilon_s^{*(2)})dS] + Q_{xy}^{app} \end{cases} \tag{B.5}$$

The amplitude of noise γ is assumed to be far smaller than the norm of the strain components. Thus, the actual values of stiffness components can be substituted by their approximate counterparts. Thus,

$$\begin{cases} Q_{xx} = \gamma[Q_{xx}^{app}\int_S(\mathfrak{N}_x\varepsilon_x^{*(1)} + \mathfrak{N}_y\varepsilon_y^{*(1)} + \frac{1}{2}\mathfrak{N}_s\varepsilon_s^{*(1)})dS + \\ \quad Q_{xy}^{app}\int_S(\mathfrak{N}_x\varepsilon_y^{*(1)} + \mathfrak{N}_y\varepsilon_x^{*(1)} - \frac{1}{2}\mathfrak{N}_s\varepsilon_s^{*(1)})dS] + Q_{11}^{app} \\ Q_{xy} = \gamma[Q_{xx}^{app}\int_S(\mathfrak{N}_x\varepsilon_x^{*(2)} + \mathfrak{N}_y\varepsilon_y^{*(2)} + \frac{1}{2}\mathfrak{N}_s\varepsilon_s^{*(2)})dS + \\ \quad Q_{xy}^{app}\int_S(\mathfrak{N}_x\varepsilon_y^{*(2)} + \mathfrak{N}_y\varepsilon_x^{*(2)} - \frac{1}{2}\mathfrak{N}_s\varepsilon_s^{*(2)})dS] + Q_{12}^{app} \end{cases} \tag{B.6}$$

The variance of each stiffness components is expressed as follows:

$$V(Q_{ij}) = E([Q_{ij} - E(Q_{ij})]^2) \tag{B.7}$$

Thus,

$$\begin{cases} V(Q_{xx}) = \gamma^2 E([Q_{xx}^{app}\int_S(\mathfrak{N}_x\varepsilon_x^{*(1)} + \mathfrak{N}_y\varepsilon_y^{*(1)} + \frac{1}{2}\mathfrak{N}_s\varepsilon_s^{*(1)})dS + \\ \qquad Q_{xy}^{app}\int_S(\mathfrak{N}_x\varepsilon_y^{*(1)} + \mathfrak{N}_y\varepsilon_x^{*(1)} - \frac{1}{2}\mathfrak{N}_s\varepsilon_s^{*(1)})dS]^2) \\ V(Q_{xy}) = \gamma^2 E([Q_{xx}^{app}\int_S(\mathfrak{N}_x\varepsilon_x^{*(2)} + \mathfrak{N}_y\varepsilon_y^{*(2)} + \frac{1}{2}\mathfrak{N}_s\varepsilon_s^{*(2)})dS + \\ \qquad Q_{xy}^{app}\int_S(\mathfrak{N}_x\varepsilon_y^{*(2)} + \mathfrak{N}_y\varepsilon_x^{*(2)} - \frac{1}{2}\mathfrak{N}_s\varepsilon_s^{*(2)})dS]^2) \end{cases} \tag{B.8}$$

Because of the discrete nature of the measurement, the integrals above must be discretised. Thus, using for instance the rectangular method,

$$\begin{cases} V(Q_{xx}) \approx \gamma^2(\frac{S}{n})^2 E([Q_{xx}^{app}\sum_{i=1}^{n}(\mathfrak{N}_x(M_i)\varepsilon_x^{*(1)}(M_i)+\mathfrak{N}_y(M_i)\varepsilon_y^{*(1)}(M_i)+\frac{1}{2}\mathfrak{N}_s(M_i)\varepsilon_s^{*(1)}(M_i))+ \\ \qquad Q_{xy}^{app}\sum_{i=1}^{n}(\mathfrak{N}_x(M_i)\varepsilon_y^{*(1)}(M_i)+\mathfrak{N}_y(M_i)\varepsilon_x^{*(1)}(M_i)-\frac{1}{2}\mathfrak{N}_s(M_i)\varepsilon_s^{*(1)}(M_i))]^2) \\ V(Q_{xy}) \approx \gamma^2(\frac{S}{n})^2 E([Q_{xx}^{app}\sum_{i=1}^{n}(\mathfrak{N}_x(M_i)\varepsilon_x^{*(2)}(M_i)+\mathfrak{N}_y(M_i)\varepsilon_y^{*(2)}(M_i)+\frac{1}{2}\mathfrak{N}_s(M_i)\varepsilon_s^{*(2)}(M_i))+ \\ \qquad Q_{xy}^{app}\sum_{i=1}^{n}(\mathfrak{N}_x(M_i)\varepsilon_y^{*(2)}(M_i)+\mathfrak{N}_y(M_i)\varepsilon_x^{*(2)}(M_i)-\frac{1}{2}\mathfrak{N}_s(M_i)\varepsilon_s^{*(2)}(M_i))]^2) \end{cases} \tag{B.9}$$

where S is the area of the specimen, n the number of small rectangular elements used for the discretization of the specimen geometry and M_i the i^{th} discrete measurement data point. According to the nature of autocorrelation of function $\mathfrak{N}$, Equation C.8 can be rewritten as:

$$\begin{cases} V(Q_{xx}) = \gamma^2(\frac{S}{n})^2[((Q_{xx}^{app})^2+(Q_{xy}^{app})^2)\sum_{i=1}^{n}(\varepsilon_x^{*(1)}(M_i))^2+((Q_{yy}^{app})^2+(Q_{xy}^{app})^2)\sum_{i=1}^{n}(\varepsilon_y^{*(1)}(M_i))^2+ \\ \quad (\frac{1}{4}(Q_{xx}^{app})^2+\frac{1}{4}(Q_{xy}^{app})^2-\frac{1}{2}Q_{xx}^{app}Q_{xy}^{app})\sum_{i=1}^{n}(\varepsilon_s^{*(1)}(M_i))^s+4Q_{xx}^{app}Q_{xy}^{app}\sum_{i=1}^{n}(\varepsilon_x^{*(1)}(M_i)\varepsilon_y^{*(1)}(M_i))] \\ V(Q_{xy}) = \gamma^2(\frac{S}{n})^2[((Q_{xx}^{app})^2+(Q_{xy}^{app})^2)\sum_{i=1}^{n}(\varepsilon_x^{*(2)}(M_i))^2+((Q_{yy}^{app})^2+(Q_{xy}^{app})^2)\sum_{i=1}^{n}(\varepsilon_y^{*(2)}(M_i))^2+ \\ \quad (\frac{1}{4}(Q_{xx}^{app})^2+\frac{1}{4}(Q_{xy}^{app})^2-\frac{1}{2}Q_{xx}^{app}Q_{xy}^{app})\sum_{i=1}^{n}(\varepsilon_s^{*(2)}(M_i))^2+4Q_{xx}^{app}Q_{xy}^{app}\sum_{i=1}^{n}(\varepsilon_x^{*(2)}(M_i)\varepsilon_y^{*(2)}(M_i))] \end{cases} \tag{B.10}$$

Finally, the variances of Q_{xx} and Q_{xy} can be expressed as:

$$\begin{cases} V(Q_{xx}) = \gamma^2(\frac{S}{n})^2\mathbf{Q^{app}}.\mathbf{G^{(1)}}\mathbf{Q^{app}} \\ V(Q_{xy}) = \gamma^2(\frac{S}{n})^2\mathbf{Q^{app}}.\mathbf{G^{(2)}}\mathbf{Q^{app}} \end{cases} \tag{B.11}$$

where $\mathbf{G}^{(i)}(i=1,2)$ is the square matrix as:

$$\mathbf{G^{(i)}}: \begin{bmatrix} \sum_{i=1}^{n}(\varepsilon_x^{*(i)}(M_i))^2+\sum_{i=1}^{n}(\varepsilon_y^{*(i)}(M_i))^2+\frac{1}{4}\sum_{i=1}^{n}(\varepsilon_s^{*(i)}(M_i))^2 & 4\sum_{i=1}^{n}\varepsilon_x^{*(i)}(M_i)\varepsilon_y^{*(i)}(M_i)-\frac{1}{2}\sum_{i=1}^{n}(\varepsilon_s^{*(i)}(M_i))^2 \\ 4\sum_{i=1}^{n}\varepsilon_x^{*(i)}(M_i)\varepsilon_y^{*(i)}(M_i)-\frac{1}{2}\sum_{i=1}^{n}(\varepsilon_s^{*(i)}(M_i))^2 & \sum_{i=1}^{n}(\varepsilon_x^{*(i)}(M_i))^2+\sum_{i=1}^{n}(\varepsilon_y^{*(i)}(M_i))^2+\frac{1}{4}\sum_{i=1}^{n}(\varepsilon_s^{*(i)}(M_i))^2 \end{bmatrix} \tag{B.12}$$

Obviously, these variances are proportional to γ^2. Variables $\eta^{(i)}$ are defined as follows:

$$(\eta^{(i)})^2 = (\frac{S}{n})^2 \mathbf{Q^{app}}.\mathbf{G^{(i)}}\mathbf{Q^{app}} \tag{B.13}$$

Thus, the variances of Q_{xx} and Q_{xy} become:

$$\begin{cases} V(Q_{xx}) = (\eta^{(1)})^2\gamma^2 \\ V(Q_{xy}) = (\eta^{(2)})^2\gamma^2 \end{cases} \tag{B.14}$$

Obviously, the best virtual fields used to identify the parameters are the ones minimising the variances of identified stiffness components. This leads to solve a classical minimisation problem. The minimisation is implemented under constraints arising from the virtual boundary conditions, *i.e.*, zeroing the virtual work of unknown external forces and from the special conditions directly providing the constitutive parameters. In this thesis, the method of Lagrange multipliers is used to search for the minimum solution.

Appendix C

Identification of the orthotropic linear elastic model

Similarly, for the $2D$ orthotropic linear elastic model, with a particular virtual field Equation 3.14 can be expressed as (in the reference frame linked to the material directions):

$$\begin{aligned} Q_{11}\int_S(\varepsilon_1-\gamma\mathfrak{N}_1)\varepsilon_1^*dS+Q_{12}\int_S((\varepsilon_1-\gamma\mathfrak{N}_1)\varepsilon_2^*+(\varepsilon_2-\gamma\mathfrak{N}_2)\varepsilon_1^*)dS+... \\ Q_{22}\int_S(\varepsilon_2-\gamma\mathfrak{N}_2)\varepsilon_2^*dS+Q_{66}\int_S(\varepsilon_6-\gamma\mathfrak{N}_6)\varepsilon_6^*dS=-\int_S\rho a_iu_i^*dS \end{aligned} \tag{C.1}$$

To identify the four parameters in Equation C.1, four independent virtual fields satisfying the virtual boundary conditions and specialty conditions are necessary. Thus,

$$\left\{\begin{array}{l} Q_{11}=\gamma[Q_{11}\int_S\mathfrak{N}_1\varepsilon_1^{*(1)}dS+Q_{12}\int_S(\mathfrak{N}_1\varepsilon_2^{*(1)}+\mathfrak{N}_2\varepsilon_1^{*(1)})dS+ \\ \quad Q_{22}\int_S\mathfrak{N}_2\varepsilon_2^{*(1)}dS+Q_{66}\int_S\mathfrak{N}_6\varepsilon_6^{*(1)}dS]-\int_S\rho a_iu_i^{*(1)}dS \\ Q_{12}=\gamma[Q_{11}\int_S\mathfrak{N}_1\varepsilon_1^{*(2)}dS+Q_{12}\int_S(\mathfrak{N}_1\varepsilon_2^{*(2)}+\mathfrak{N}_2\varepsilon_1^{*(2)})dS+ \\ \quad Q_{22}\int_S\mathfrak{N}_2\varepsilon_2^{*(2)}dS+Q_{66}\int_S\mathfrak{N}_6\varepsilon_6^{*(2)}dS]-\int_S\rho a_iu_i^{*(2)}dS \\ Q_{22}=\gamma[Q_{11}\int_S\mathfrak{N}_1\varepsilon_1^{*(3)}dS+Q_{12}\int_S(\mathfrak{N}_1\varepsilon_2^{*(2)}+\mathfrak{N}_2\varepsilon_1^{*(3)})dS+ \\ \quad Q_{22}\int_S\mathfrak{N}_2\varepsilon_2^{*(2)}dS+Q_{66}\int_S\mathfrak{N}_6\varepsilon_6^{*(3)}dS]-\int_S\rho a_iu_i^{*(3)}dS \\ Q_{66}=\gamma[Q_{11}\int_S\mathfrak{N}_1\varepsilon_1^{*(4)}dS+Q_{12}\int_S(\mathfrak{N}_1\varepsilon_2^{*(2)}+\mathfrak{N}_2\varepsilon_1^{*(4)})dS+ \\ \quad Q_{22}\int_S\mathfrak{N}_2\varepsilon_2^{*(2)}dS+Q_{66}\int_S\mathfrak{N}_6\varepsilon_6^{*(4)}dS]-\int_S\rho a_iu_i^{*(4)}dS \end{array}\right. \tag{C.2}$$

If the identification in Equation C.2 is performed without considering the presence of noise, then the identified stiffness components are not exact and will denoted as approximate parameters Q_{11}^{app},Q_{12}^{app}, Q_{22}^{app} and Q_{66}^{app}. According to Equation 3.19 and 3.22, the

four components are defined by:

$$\begin{cases} Q_{11}^{app} = -\int_S \rho a_i u_i^{*(1)} dS \\ Q_{12}^{app} = -\int_S \rho a_i u_i^{*(2)} dS \\ Q_{22}^{app} = -\int_S \rho a_i u_i^{*(3)} dS \\ Q_{66}^{app} = -\int_S \rho a_i u_i^{*(4)} dS \end{cases} \tag{C.3}$$

Thus, Equation C.2 can be rewritten as:

$$\begin{cases} Q_{11} = \gamma[Q_{11}\int_S \mathfrak{N}_1\varepsilon_1^{*(1)}dS + Q_{12}\int_S(\mathfrak{N}_1\varepsilon_2^{*(1)} + \mathfrak{N}_2\varepsilon_1^{*(1)})dS + \\ \qquad Q_{22}\int_S \mathfrak{N}_2\varepsilon_2^{*(1)}dS + Q_{66}\int_S \mathfrak{N}_6\varepsilon_6^{*(1)}dS] + Q_{11}^{app} \\ Q_{12} = \gamma[Q_{11}\int_S \mathfrak{N}_1\varepsilon_1^{*(2)}dS + Q_{12}\int_S(\mathfrak{N}_1\varepsilon_2^{*(2)} + \mathfrak{N}_2\varepsilon_1^{*(2)})dS + \\ \qquad Q_{22}\int_S \mathfrak{N}_2\varepsilon_2^{*(2)}dS + Q_{66}\int_S \mathfrak{N}_6\varepsilon_6^{*(2)}dS] + Q_{12}^{app} \\ Q_{22} = \gamma[Q_{11}\int_S \mathfrak{N}_1\varepsilon_1^{*(3)}dS + Q_{12}\int_S(\mathfrak{N}_1\varepsilon_2^{*(2)} + \mathfrak{N}_2\varepsilon_1^{*(3)})dS + \\ \qquad Q_{22}\int_S \mathfrak{N}_2\varepsilon_2^{*(2)}dS + Q_{66}\int_S \mathfrak{N}_6\varepsilon_6^{*(3)}dS] + Q_{22}^{app} \\ Q_{66} = \gamma[Q_{11}\int_S \mathfrak{N}_1\varepsilon_1^{*(4)}dS + Q_{12}\int_S(\mathfrak{N}_1\varepsilon_2^{*(2)} + \mathfrak{N}_2\varepsilon_1^{*(4)})dS + \\ \qquad Q_{22}\int_S \mathfrak{N}_2\varepsilon_2^{*(2)}dS + Q_{66}\int_S \mathfrak{N}_6\varepsilon_6^{*(4)}dS] + Q_{66}^{app} \end{cases} \tag{C.4}$$

The standard deviation of noise γ is assumed to be far smaller than the norm of the strain components. Thus, the actual values of stiffness components can be substituted by their approximate counterparts. Therefore,

$$\begin{cases} Q_{11} = \gamma[Q_{11}^{app}\int_S \mathfrak{N}_1\varepsilon_1^{*(1)}dS + Q_{12}^{app}\int_S(\mathfrak{N}_1\varepsilon_2^{*(1)} + \mathfrak{N}_2\varepsilon_1^{*(1)})dS + \\ \qquad Q_{22}^{app}\int_S \mathfrak{N}_2\varepsilon_2^{*(1)}dS + Q_{66}^{app}\int_S \mathfrak{N}_6\varepsilon_6^{*(1)}dS] + Q_{11}^{app} \\ Q_{12} = \gamma[Q_{11}^{app}\int_S \mathfrak{N}_1\varepsilon_1^{*(2)}dS + Q_{12}^{app}\int_S(\mathfrak{N}_1\varepsilon_2^{*(2)} + \mathfrak{N}_2\varepsilon_1^{*(2)})dS + \\ \qquad Q_{22}^{app}\int_S \mathfrak{N}_2\varepsilon_2^{*(2)}dS + Q_{66}^{app}\int_S \mathfrak{N}_6\varepsilon_6^{*(2)}dS] + Q_{12}^{app} \\ Q_{22} = \gamma[Q_{11}^{app}\int_S \mathfrak{N}_1\varepsilon_1^{*(3)}dS + Q_{12}^{app}\int_S(\mathfrak{N}_1\varepsilon_2^{*(2)} + \mathfrak{N}_2\varepsilon_1^{*(3)})dS + \\ \qquad Q_{22}^{app}\int_S \mathfrak{N}_2\varepsilon_2^{*(2)}dS + Q_{66}^{app}\int_S \mathfrak{N}_6\varepsilon_6^{*(3)}dS] + Q_{22}^{app} \\ Q_{66} = \gamma[Q_{11}^{app}\int_S \mathfrak{N}_1\varepsilon_1^{*(4)}dS + Q_{12}^{app}\int_S(\mathfrak{N}_1\varepsilon_2^{*(2)} + \mathfrak{N}_2\varepsilon_1^{*(4)})dS + \\ \qquad Q_{22}^{app}\int_S \mathfrak{N}_2\varepsilon_2^{*(2)}dS + Q_{66}^{app}\int_S \mathfrak{N}_6\varepsilon_6^{*(4)}dS] + Q_{66}^{app} \end{cases} \tag{C.5}$$

The variance of each stiffness components is expressed as in Equation B.7. Thus, the variances of the stiffness components can be expressed as:

$$\begin{cases} V(Q_{11}) = \gamma^2 E([Q_{11}^{app}\int_S \mathfrak{N}_1\varepsilon_1^{*(1)}dS + Q_{12}^{app}\int_S(\mathfrak{N}_1\varepsilon_2^{*(1)} + \mathfrak{N}_2\varepsilon_1^{*(1)})dS + \\ \qquad Q_{22}^{app}\int_S \mathfrak{N}_2\varepsilon_2^{*(1)}dS + Q_{66}^{app}\int_S \mathfrak{N}_6\varepsilon_6^{*(1)}dS]^2) \\ V(Q_{12}) = \gamma^2 E([Q_{11}^{app}\int_S \mathfrak{N}_1\varepsilon_1^{*(2)}dS + Q_{12}^{app}\int_S(\mathfrak{N}_1\varepsilon_2^{*(2)} + \mathfrak{N}_2\varepsilon_1^{*(2)})dS + \\ \qquad Q_{22}^{app}\int_S \mathfrak{N}_2\varepsilon_2^{*(2)}dS + Q_{66}^{app}\int_S \mathfrak{N}_6\varepsilon_6^{*(2)}dS]^2) \\ V(Q_{22}) = \gamma^2 E([Q_{11}^{app}\int_S \mathfrak{N}_1\varepsilon_1^{*(3)}dS + Q_{12}^{app}\int_S(\mathfrak{N}_1\varepsilon_2^{*(3)} + \mathfrak{N}_2\varepsilon_1^{*(3)})dS + \\ \qquad Q_{22}^{app}\int_S \mathfrak{N}_2\varepsilon_2^{*(3)}dS + Q_{66}^{app}\int_S \mathfrak{N}_6\varepsilon_6^{*(3)}dS]^2) \\ V(Q_{66}) = \gamma^2 E([Q_{11}^{app}\int_S \mathfrak{N}_1\varepsilon_1^{*(4)}dS + Q_{12}^{app}\int_S(\mathfrak{N}_1\varepsilon_2^{*(4)} + \mathfrak{N}_2\varepsilon_1^{*(4)})dS + \\ \qquad Q_{22}^{app}\int_S \mathfrak{N}_2\varepsilon_2^{*(4)}dS + Q_{66}^{app}\int_S \mathfrak{N}_6\varepsilon_6^{*(4)}dS]^2) \end{cases} \tag{C.6}$$

Because of the discrete nature of the measurement, the integrals above must be discretised. Thus, using for instance the rectangular method,

$$\begin{cases} V(Q_{11}) \approx \gamma^2(\frac{S}{n})^2 E([Q_{11}^{app}\sum_{i=1}^n \mathfrak{N}_1(M_i)\varepsilon_1^{*(1)}(M_i) + Q_{22}^{app}\sum_{i=1}^n \mathfrak{N}_2(M_i)\varepsilon_2^{*(1)}(M_i) + ... \\ Q_{12}^{app}\sum_{i=1}^n(\mathfrak{N}_1(M_i)\varepsilon_2^{*(1)}(M_i) + \mathfrak{N}_2(M_i)\varepsilon_1^{*(1)}(M_i)) + Q_{66}^{app}\sum_{i=1}^n \mathfrak{N}_6(M_i)\varepsilon_6^{*(1)}(M_i)]^2) \\ V(Q_{12}) \approx \gamma^2(\frac{S}{n})^2 E([Q_{11}^{app}\sum_{i=1}^n \mathfrak{N}_1(M_i)\varepsilon_1^{*(2)}(M_i) + Q_{22}^{app}\sum_{i=1}^n \mathfrak{N}_2(M_i)\varepsilon_2^{*(2)}(M_i) + ... \\ Q_{12}^{app}\sum_{i=1}^n(\mathfrak{N}_1(M_i)\varepsilon_2^{*(2)}(M_i) + \mathfrak{N}_2(M_i)\varepsilon_1^{*(2)}(M_i)) + Q_{66}^{app}\sum_{i=1}^n \mathfrak{N}_6(M_i)\varepsilon_6^{*(2)}(M_i)]^2) \\ V(Q_{22}) \approx \gamma^2(\frac{S}{n})^2 E([Q_{11}^{app}\sum_{i=1}^n \mathfrak{N}_1(M_i)\varepsilon_1^{*(3)}(M_i) + Q_{22}^{app}\sum_{i=1}^n \mathfrak{N}_2(M_i)\varepsilon_2^{*(3)}(M_i) + ... \\ Q_{12}^{app}\sum_{i=1}^n(\mathfrak{N}_1(M_i)\varepsilon_2^{*(3)}(M_i) + \mathfrak{N}_2(M_i)\varepsilon_1^{*(3)}(M_i)) + Q_{66}^{app}\sum_{i=1}^n \mathfrak{N}_6(M_i)\varepsilon_6^{*(3)}(M_i)]^2) \\ V(Q_{66}) \approx \gamma^2(\frac{S}{n})^2 E([Q_{11}^{app}\sum_{i=1}^n \mathfrak{N}_1(M_i)\varepsilon_1^{*(4)}(M_i) + Q_{22}^{app}\sum_{i=1}^n \mathfrak{N}_2(M_i)\varepsilon_2^{*(4)}(M_i) + ... \\ Q_{12}^{app}\sum_{i=1}^n(\mathfrak{N}_1(M_i)\varepsilon_2^{*(4)}(M_i) + \mathfrak{N}_2(M_i)\varepsilon_1^{*(4)}(M_i)) + Q_{66}^{app}\sum_{i=1}^n \mathfrak{N}_6(M_i)\varepsilon_6^{*(4)}(M_i)]^2) \end{cases} \tag{C.7}$$

where S is the area of the specimen, n the number of small rectangular elements used for the discretization of the specimen geometry and M_i the i^{th} discrete measurement data point. According the properties of autocorrelation of function $\mathfrak{N}$, Equation C.7 can be rewritten as:

$$\begin{cases} V(Q_{11}) = \gamma^2(\frac{S}{n})^2[((Q_{11}^{app})^2 + (Q_{12}^{app})^2)\sum_{i=1}^n(\varepsilon_1^{*(1)}(M_i))^2 + (Q_{66}^{app})^2\sum_{i=1}^n(\varepsilon_6^{*(1)}(M_i))^2 + ... \\ ((Q_{22}^{app})^2 + (Q_{12}^{app})^2)\sum_{i=1}^n(\varepsilon_2^{*(1)}(M_i))^2 + 2(Q_{11}^{app} + Q_{22}^{app})Q_{12}^{app}\sum_{i=1}^n(\varepsilon_1^{*(1)}(M_i)\varepsilon_2^{*(1)}(M_i))] \\ V(Q_{12}) = \gamma^2(\frac{S}{n})^2[((Q_{11}^{app})^2 + (Q_{12}^{app})^2)\sum_{i=1}^n(\varepsilon_1^{*(2)}(M_i))^2 + (Q_{66}^{app})^2\sum_{i=1}^n(\varepsilon_6^{*(2)}(M_i))^2 + ... \\ ((Q_{22}^{app})^2 + (Q_{12}^{app})^2)\sum_{i=1}^n(\varepsilon_2^{*(2)}(M_i))^2 + 2(Q_{11}^{app} + Q_{22}^{app})Q_{12}^{app}\sum_{i=1}^n(\varepsilon_1^{*(2)}(M_i)\varepsilon_2^{*(2)}(M_i))] \\ V(Q_{22}) = \gamma^2(\frac{S}{n})^2[((Q_{11}^{app})^2 + (Q_{12}^{app})^2)\sum_{i=1}^n(\varepsilon_1^{*(3)}(M_i))^2 + (Q_{66}^{app})^2\sum_{i=1}^n(\varepsilon_6^{*(3)}(M_i))^2 + ... \\ ((Q_{22}^{app})^2 + (Q_{12}^{app})^2)\sum_{i=1}^n(\varepsilon_2^{*(3)}(M_i))^2 + 2(Q_{11}^{app} + Q_{22}^{app})Q_{12}^{app}\sum_{i=1}^n(\varepsilon_1^{*(3)}(M_i)\varepsilon_2^{*(3)}(M_i))] \\ V(Q_{66}) = \gamma^2(\frac{S}{n})^2[((Q_{11}^{app})^2 + (Q_{12}^{app})^2)\sum_{i=1}^n(\varepsilon_1^{*(4)}(M_i))^2 + (Q_{66}^{app})^2\sum_{i=1}^n(\varepsilon_6^{*(4)}(M_i))^2 + ... \\ ((Q_{22}^{app})^2 + (Q_{12}^{app})^2)\sum_{i=1}^n(\varepsilon_2^{*(4)}(M_i))^2 + 2(Q_{11}^{app} + Q_{22}^{app})Q_{12}^{app}\sum_{i=1}^n(\varepsilon_1^{*(4)}(M_i)\varepsilon_2^{*(4)}(M_i))] \end{cases} \tag{C.8}$$

Finally, the variances of Q_{11} and Q_{12} can be expressed as:

$$\begin{cases} V(Q_{11}) = \gamma^2(\frac{S}{n})^2 \mathbf{Q^{app}}.\mathbf{G^{(1)}}\mathbf{Q^{app}} \\ V(Q_{12}) = \gamma^2(\frac{S}{n})^2 \mathbf{Q^{app}}.\mathbf{G^{(2)}}\mathbf{Q^{app}} \\ V(Q_{22}) = \gamma^2(\frac{S}{n})^2 \mathbf{Q^{app}}.\mathbf{G^{(3)}}\mathbf{Q^{app}} \\ V(Q_{66}) = \gamma^2(\frac{S}{n})^2 \mathbf{Q^{app}}.\mathbf{G^{(4)}}\mathbf{Q^{app}} \end{cases} \tag{C.9}$$

where $\mathbf{G}^{(i)}$ $(i = 1, 2, 3 \; and \; 4)$ is the square matrix as:

$$\mathbf{G^{(i)}}: \begin{bmatrix} \sum_{i=1}^{n}(\varepsilon_1^{*(i)}(M_i))^2 & 0 & \sum_{i=1}^{n}(\varepsilon_1^{*(i)}(M_i)\varepsilon_2^{*(i)}(M_i)) & 0 \\ 0 & \sum_{i=1}^{n}(\varepsilon_2^{*(i)}(M_i))^2 & \sum_{i=1}^{n}(\varepsilon_1^{*(i)}(M_i)\varepsilon_2^{*(i)}(M_i)) & 0 \\ \sum_{i=1}^{n}(\varepsilon_1^{*(i)}(M_i)\varepsilon_2^{*(i)}(M_i)) & \sum_{i=1}^{n}(\varepsilon_1^{*(i)}(M_i)\varepsilon_2^{*(i)}(M_i)) & \sum_{i=1}^{n}(\varepsilon_1^{*(i)}(M_i))^2 + \sum_{i=1}^{n}(\varepsilon_2^{*(i)}(M_i))^2 & 0 \\ 0 & 0 & 0 & \sum_{i=1}^{n}(\varepsilon_6^{*(i)}(M_i))^2 \end{bmatrix} \tag{C.10}$$

Obviously, these variances are proportional to γ^2. The $\eta^{(i)}$ are defined as follows:

$$(\eta^{(i)})^2 = (\frac{S}{n})^2 \mathbf{Q^{app}}.\mathbf{G^{(i)}}\mathbf{Q^{app}} \tag{C.11}$$

Thus, the variances of Q_{11}, Q_{12},Q_{22} and Q_{66} become:

$$\begin{cases} V(Q_{11}) = (\eta^{(1)})^2\gamma^2 \\ V(Q_{12}) = (\eta^{(2)})^2\gamma^2 \\ V(Q_{22}) = (\eta^{(3)})^2\gamma^2 \\ V(Q_{66}) = (\eta^{(4)})^2\gamma^2 \end{cases} \tag{C.12}$$

Appendix D

Identification of the strain rate dependence parameters

For the sake of simplicity, only the strain rate dependence on the transverse and shear stiffness components are considered as:

$$\begin{cases} Q_{22} = Q_{22}^0 + \beta_2 ln(|\dot{\varepsilon_2}| + 1) \\ Q_{66} = Q_{66}^0 + \beta_6 ln(|\dot{\varepsilon_6}| + 1) \end{cases} \tag{D.1}$$

The noise of strain rate can be ignored in the present calculation because the logarithmic calculation in Equation D.1 reduces the noise effect. The noise on the acceleration fields can be neglected as discussed in section 3.2.1. So only the noise in the strain fields is considered and Equation 3.39 can be rewritten as:

$$\begin{aligned} Q_{11}\int_S(\varepsilon_1-\gamma\mathfrak{N}_1)\varepsilon_1^* dS + Q_{12}\int_S((\varepsilon_1-\gamma\mathfrak{N}_1)\varepsilon_2^* + (\varepsilon_2-\gamma\mathfrak{N}_2)\varepsilon_1^*)dS + ... \\ Q_{22}^0\int_S(\varepsilon_2-\gamma\mathfrak{N}_2)\varepsilon_2^* dS + Q_{66}^0\int_S(\varepsilon_6-\gamma\mathfrak{N}_6)\varepsilon_6^* dS + ... \\ \beta_2\int_S ln(|\dot{\varepsilon_2}|+1)(\varepsilon_2-\gamma\mathfrak{N}_2)\varepsilon_2^* dS + \beta_6\int_S ln(|\dot{\varepsilon_6}|+1)(\varepsilon_6-\gamma\mathfrak{N}_6)\varepsilon_6^* dS = ... \\ -\int_S \rho a_i u_i^* dS \end{aligned} \tag{D.2}$$

In Equation D.2, the parameters Q_{11}, Q_{12}, Q_{22}^0, Q_{66}^0, β_2 and β_6 can be identified from the dynamic full-field measurements. However, Q_{11} and Q_{12} are not strain rate dependent, and Q_{22}^0 and Q_{66}^0 in Equation D.1 are the stiffness components under quasi-static conditions. Therefore, for the sake of simplicity, the four variables are fixed here to their value under quasi-static conditions. Parameters β_2 and β_6 are the only two unknowns considered here.

To identify the two parameters in Equation D.2, the procedure is similar to that for the isotropic linear elastic model. Two independent virtual fields which fulfil specialty conditions provide parameters β_2 and β_6, respectively.

$$\begin{cases} \beta_2 = \gamma[\beta_2 \int_S ln(|\dot{\varepsilon_2}|+1)\mathfrak{N}_2\varepsilon_2^{*(1)}dS + \beta_6 \int_S ln(|\dot{\varepsilon_6}|+1)\mathfrak{N}_6\varepsilon_6^{*(1)}dS + Q_{11}\int_S \mathfrak{N}_1\varepsilon_1^{*(1)}dS + ... \\ \qquad Q_{12}\int_S(\mathfrak{N}_1\varepsilon_2^{*(1)} + \mathfrak{N}_2\varepsilon_1^{*(1)})dS + Q_{22}\int_S \mathfrak{N}_2\varepsilon_2^{*(1)}dS + Q_{66}\int_S \mathfrak{N}_6\varepsilon_6^{*(1)}dS] - W^{(1)} \\ \beta_6 = \gamma[\beta_2 \int_S ln(|\dot{\varepsilon_2}|+1)\mathfrak{N}_2\varepsilon_2^{*(2)}dS + \beta_6 \int_S ln(|\dot{\varepsilon_6}|+1)\mathfrak{N}_6\varepsilon_6^{*(2)}dS + Q_{11}\int_S \mathfrak{N}_1\varepsilon_1^{*(2)}dS + ... \\ \qquad Q_{12}\int_S(\mathfrak{N}_1\varepsilon_2^{*(2)} + \mathfrak{N}_2\varepsilon_1^{*(2)})dS + Q_{22}\int_S \mathfrak{N}_2\varepsilon_2^{*(2)}dS + Q_{66}\int_S \mathfrak{N}_6\varepsilon_6^{*(2)}dS] - W^{(2)} \end{cases} \tag{D.3}$$

with,

$$W = Q_{11}\int_S \varepsilon_1\varepsilon_1^* dS + Q_{12}\int_S(\varepsilon_1\varepsilon_2^* + \varepsilon_2\varepsilon_1^*)dS + Q_{22}\int_S \varepsilon_2\varepsilon_2^* dS + Q_{66}\int_S \varepsilon_6\varepsilon_6^* dS + \int_S \rho a_i u_i^* dS \tag{D.4}$$

If the noise source is not taken into account in Equation D.3, the strain rate dependence parameters β_2^{app} and β_6^{app} are identified and are approximations of the true values. According to Equation 3.19 and 3.22, these two components are defined by:

$$\begin{cases} \beta_2^{app} = -W^{(1)} \\ \beta_6^{app} = -W^{(2)} \end{cases} \tag{D.5}$$

Thus, Equation D.3 can be rewritten as:

$$\begin{cases} \beta_2 = \gamma[\beta_2 \int_S ln(|\dot{\varepsilon_2}|+1)\mathfrak{N}_2\varepsilon_2^{*(1)}dS + \beta_6 \int_S ln(|\dot{\varepsilon_6}|+1)\mathfrak{N}_6\varepsilon_6^{*(1)}dS + Q_{11}\int_S \mathfrak{N}_1\varepsilon_1^{*(1)}dS + ... \\ \qquad Q_{12}\int_S(\mathfrak{N}_1\varepsilon_2^{*(1)} + \mathfrak{N}_2\varepsilon_1^{*(1)})dS + Q_{22}\int_S \mathfrak{N}_2\varepsilon_2^{*(1)}dS + Q_{66}\int_S \mathfrak{N}_6\varepsilon_6^{*(1)}dS] + \beta_2^{app} \\ \beta_6 = \gamma[\beta_2 \int_S ln(|\dot{\varepsilon_2}|+1)\mathfrak{N}_2\varepsilon_2^{*(2)}dS + \beta_6 \int_S ln(|\dot{\varepsilon_6}|+1)\mathfrak{N}_6\varepsilon_6^{*(2)}dS + Q_{11}\int_S \mathfrak{N}_1\varepsilon_1^{*(2)}dS + ... \\ \qquad Q_{12}\int_S(\mathfrak{N}_1\varepsilon_2^{*(2)} + \mathfrak{N}_2\varepsilon_1^{*(2)})dS + Q_{22}\int_S \mathfrak{N}_2\varepsilon_2^{*(2)}dS + Q_{66}\int_S \mathfrak{N}_6\varepsilon_6^{*(2)}dS] + \beta_6^{app} \end{cases} \tag{D.6}$$

The amplitude of noise γ is assumed to be far smaller than the norm of the strain components. Thus, the actual values of the strain rate dependence parameters can be substituted by their approximate counterparts. Thus,

$$\begin{cases} \beta_2 = \gamma[\beta_2^{app}\int_S ln(|\dot{\varepsilon_2}|+1)\mathfrak{N}_2\varepsilon_2^{*(1)}dS + \beta_6^{app}\int_S ln(|\dot{\varepsilon_6}|+1)\mathfrak{N}_6\varepsilon_6^{*(1)}dS + Q_{11}\int_S \mathfrak{N}_1\varepsilon_1^{*(1)}dS + ... \\ \qquad Q_{12}\int_S(\mathfrak{N}_1\varepsilon_2^{*(1)} + \mathfrak{N}_2\varepsilon_1^{*(1)})dS + Q_{22}\int_S \mathfrak{N}_2\varepsilon_2^{*(1)}dS + Q_{66}\int_S \mathfrak{N}_6\varepsilon_6^{*(1)}dS] + \beta_2^{app} \\ \beta_6 = \gamma[\beta_2^{app}\int_S ln(|\dot{\varepsilon_2}|+1)\mathfrak{N}_2\varepsilon_2^{*(2)}dS + \beta_6^{app}\int_S ln(|\dot{\varepsilon_6}|+1)\mathfrak{N}_6\varepsilon_6^{*(2)}dS + Q_{11}\int_S \mathfrak{N}_1\varepsilon_1^{*(2)}dS + ... \\ \qquad Q_{12}\int_S(\mathfrak{N}_1\varepsilon_2^{*(2)} + \mathfrak{N}_2\varepsilon_1^{*(2)})dS + Q_{22}\int_S \mathfrak{N}_2\varepsilon_2^{*(2)}dS + Q_{66}\int_S \mathfrak{N}_6\varepsilon_6^{*(2)}dS] + \beta_6^{app} \end{cases} \tag{D.7}$$

The variance of each unknown is expressed as follows:

$$V(\beta) = E([\beta - E(\beta)]^2) \tag{D.8}$$

Thus,

$$\begin{cases} V(\beta_2) = \gamma^2 E[\beta_2^{app}\int_S ln(|\dot{\varepsilon_2}|+1)\mathfrak{N}_2\varepsilon_2^{*(1)}dS + \beta_6^{app}\int_S ln(|\dot{\varepsilon_6}|+1)\mathfrak{N}_6\varepsilon_6^{*(1)}dS + Q_{11}\int_S \mathfrak{N}_1\varepsilon_1^{*(1)}dS + ... \\ \qquad Q_{12}\int_S(\mathfrak{N}_1\varepsilon_2^{*(1)} + \mathfrak{N}_2\varepsilon_1^{*(1)})dS + Q_{22}\int_S \mathfrak{N}_2\varepsilon_2^{*(1)}dS + Q_{66}\int_S \mathfrak{N}_6\varepsilon_6^{*(1)}dS]^2 \\ V(\beta_6) = \gamma^2 E[\beta_2^{app}\int_S ln(|\dot{\varepsilon_2}|+1)\mathfrak{N}_2\varepsilon_2^{*(2)}dS + \beta_6^{app}\int_S ln(|\dot{\varepsilon_6}|+1)\mathfrak{N}_6\varepsilon_6^{*(2)}dS + Q_{11}\int_S \mathfrak{N}_1\varepsilon_1^{*(2)}dS + ... \\ \qquad Q_{12}\int_S(\mathfrak{N}_1\varepsilon_2^{*(2)} + \mathfrak{N}_2\varepsilon_1^{*(2)})dS + Q_{22}\int_S \mathfrak{N}_2\varepsilon_2^{*(2)}dS + Q_{66}\int_S \mathfrak{N}_6\varepsilon_6^{*(2)}dS]^2 \end{cases} \tag{D.9}$$

Because of the discrete nature of the measurement, the integrals above must be discretised. According to the nature of the autocorrelation of function $\mathfrak{N}$, Equation D.9 can be rewritten as:

$$\begin{cases} V(\beta_2) = \gamma^2(\frac{S}{n})^2[((Q_{11}^{app})^2 + (Q_{12}^{app})^2)\sum_{i=1}^{n}(\varepsilon_1^{*(1)}(M_i))^2 + ((Q_{22}^{app})^2 + (Q_{12}^{app})^2)\sum_{i=1}^{n}(\varepsilon_2^{*(1)}(M_i))^2 + (Q_{66}^{app})^2\sum_{i=1}^{n}(\varepsilon_6^{*(1)}(M_i))^2 + ... \\ (\beta_2)^2\sum_{i=1}^{n}(ln(|\varepsilon_2(\dot{M}_i)|+1))^2(\varepsilon_2^{*(1)}(M_i))^2 + (\beta_6)^2\sum_{i=1}^{n}(ln(|\varepsilon_6(\dot{M}_i)|+1))^2(\varepsilon_6^{*(1)}(M_i))^2 + 2\beta_2 Q_{22}\sum_{i=1}^{n} ln(|\varepsilon_2(\dot{M}_i)|+1)(\varepsilon_2^{*(1)}(M_i))^2 + ... \\ 2\beta_6 Q_{66}\sum_{i=1}^{n} ln(|\varepsilon_6(\dot{M}_i)|+1)(\varepsilon_6^{*(1)}(M_i))^2 + 2\beta_2 Q_{12}\sum_{i=1}^{n} ln(|\varepsilon_2(\dot{M}_i)|+1)\varepsilon_1^{*(1)}(M_i))\varepsilon_2^{*(1)}(M_i))] \\ V(\beta_2) = \gamma^2(\frac{S}{n})^2[((Q_{11}^{app})^2 + (Q_{12}^{app})^2)\sum_{i=1}^{n}(\varepsilon_1^{*(2)}(M_i))^2 + ((Q_{22}^{app})^2 + (Q_{12}^{app})^2)\sum_{i=1}^{n}(\varepsilon_2^{*(2)}(M_i))^2 + (Q_{66}^{app})^2\sum_{i=1}^{n}(\varepsilon_6^{*(2)}(M_i))^2 + ... \\ (\beta_2)^2\sum_{i=1}^{n}(ln(|\varepsilon_2(\dot{M}_i)|+1))^2(\varepsilon_2^{*(2)}(M_i))^2 + (\beta_6)^2\sum_{i=1}^{n}(ln(|\varepsilon_6(\dot{M}_i)|+1))^2(\varepsilon_6^{*(2)}(M_i))^2 + 2\beta_2 Q_{22}\sum_{i=1}^{n} ln(|\varepsilon_2(\dot{M}_i)|+1)(\varepsilon_2^{*(2)}(M_i))^2 + ... \\ 2\beta_6 Q_{66}\sum_{i=1}^{n} ln(|\varepsilon_6(\dot{M}_i)|+1)(\varepsilon_6^{*(2)}(M_i))^2 + 2\beta_2 Q_{12}\sum_{i=1}^{n} ln(|\varepsilon_2(\dot{M}_i)|+1)\varepsilon_1^{*(2)}(M_i))\varepsilon_2^{*(1)}(M_i))] \end{cases} \tag{D.10}$$

where S is the area of the specimen, n the number of small rectangular elements used for the discretization of the specimen geometry, and M_i the i^{th} discrete measurement data point. The rest of the procedure is the same as that for the isotropic linear elastic model.

Appendix E

VUMAT codes

E.1 VUMAT code for the strain rate dependent model

```
C************************************************************
C VUMAT FOR STRAIN RATE DEPENDENT STIFFNESS MODEL, ORTHOTROPIC
MATERIELS
C WRITTEN BY HAIBIN ZHU
C************************************************************
SUBROUTINE VUMAT(
C READ ONLY (UNMODIFIABLE)VARIABLES -
1 NBLOCK, NDIR, NSHR, NSTATEV, NFIELDV, NPROPS, LANNEAL,
2 STEPTIME, TOTALTIME, DT, CMNAME, COORDMP, CHARLENGTH,
3 PROPS, DENSITY, STRAININC, RELSPININC,
4 TEMPOLD, STRETCHOLD, DEFGRADOLD, FIELDOLD,
5 STRESSOLD, STATEOLD, ENERINTERNOLD, ENERINELASOLD,
6 TEMPNEW, STRETCHNEW, DEFGRADNEW, FIELDNEW,
C WRITE ONLY (MODIFIABLE) VARIABLES -
7 STRESSNEW, STATENEW, ENERINTERNNEW, ENERINELASNEW )
C
INCLUDE 'VABA_PARAM.INC'
C
DIMENSION PROPS(NPROPS), DENSITY(NBLOCK), COORDMP(NBLOCK,*),
1 CHARLENGTH(NBLOCK), STRAININC(NBLOCK,NDIR+NSHR),
2 RELSPININC(NBLOCK,NSHR), TEMPOLD(NBLOCK),
3 STRETCHOLD(NBLOCK,NDIR+NSHR),
4 DEFGRADOLD(NBLOCK,NDIR+NSHR+NSHR),
```

```
5 FIELDOLD(NBLOCK,NFIELDV), STRESSOLD(NBLOCK,NDIR+NSHR),
6 STATEOLD(NBLOCK,NSTATEV), ENERINTERNOLD(NBLOCK),
7 ENERINELASOLD(NBLOCK), TEMPNEW(NBLOCK),
8 STRETCHNEW(NBLOCK,NDIR+NSHR),
8 DEFGRADNEW(NBLOCK,NDIR+NSHR+NSHR),
9 FIELDNEW(NBLOCK,NFIELDV),
1 STRESSNEW(NBLOCK,NDIR+NSHR), STATENEW(NBLOCK,NSTATEV),
2 ENERINTERNNEW(NBLOCK), ENERINELASNEW(NBLOCK)
C CHARACTER*80 CMNAME
C


Q11 = PROPS(1)
Q12 = PROPS(2)
Q13 = PROPS(3)
Q23 = PROPS(4)
Q33 = PROPS(5)
Q220 = 75E8
Q660 = 4E9
B2 = 6E8
B6 = 3.5E8


DO NP = 1, NBLOCK
C Copy the values of strains into temp variables


ES1 = strainInc(NP,1)
ES2 = strainInc(NP,2)
ES3 = strainInc(NP,3)
ES4 = strainInc(NP,4)


C COMPUTE THE STRAIN RATE DEPENDENT STIFFNESS
C THE SHEAR STRAIN COMPONENT IS TENSORIAL STRAIN RATHER THAN
ENGINEERING SHEAR STRAIN


C TRANSVERSE STRAIN RATE
SR2=ABS(strainInc(NP,2)/DT)
```

```
C SHEAR STRAIN RATE (IN VUMAT THE SHEAR STRAIN IS TENSORIAL SHEAR
STRAIN)
SR4=2*ABS(strainInc(NP,4)/DT)


C STRAIN RATE EFFECT ON TRANSVERSE COMPONENT
Q22 = Q220+B2*LOG(SR2+1)
Q66 = Q660+B6*LOG(SR4+1)


stressNew(NP,1) = stressOld(NP,1)+Q11*ES1+Q12*ES2+Q13*ES3
stressNew(NP,2) = stressOld(NP,2)+Q12*ES1+Q22*ES2+Q23*ES3
stressNew(NP,3) = stressOld(NP,3)+Q13*ES1+Q23*ES2+Q33*ES3
stressNew(NP,4) = stressOld(NP,4)+Q66*ES4*2


C CHECK THE TIME INCREMENT
write(6,*) DT


END DO


RETURN
END
```

E.2 VUMAT code for the non-linear shear stress and strain behaviour

```
C**********************************************************
C VUMAT FOR NON-LINEAR SHEAR STRESS AND STRAIN BEHAVIOUR, OR-
THOTROPIC MATERIELS
C WRITTEN BY HAIBIN ZHU
C**********************************************************
SUBROUTINE VUMAT(
C READ ONLY (UNMODIFIABLE)VARIABLES -
1 NBLOCK, NDIR, NSHR, NSTATEV, NFIELDV, NPROPS, LANNEAL,
2 STEPTIME, TOTALTIME, DT, CMNAME, COORDMP, CHARLENGTH,
3 PROPS, DENSITY, STRAININC, RELSPININC,
```

```
4 TEMPOLD, STRETCHOLD, DEFGRADOLD, FIELDOLD,
5 STRESSOLD, STATEOLD, ENERINTERNOLD, ENERINELASOLD,
6 TEMPNEW, STRETCHNEW, DEFGRADNEW, FIELDNEW,
C WRITE ONLY (MODIFIABLE) VARIABLES -
7 STRESSNEW, STATENEW, ENERINTERNNEW, ENERINELASNEW )
C
INCLUDE 'VABA_PARAM.INC'
C
DIMENSION PROPS(NPROPS), DENSITY(NBLOCK), COORDMP(NBLOCK,*),
1 CHARLENGTH(NBLOCK), STRAININC(NBLOCK,NDIR+NSHR),
2 RELSPININC(NBLOCK,NSHR), TEMPOLD(NBLOCK),
3 STRETCHOLD(NBLOCK,NDIR+NSHR),
4 DEFGRADOLD(NBLOCK,NDIR+NSHR+NSHR),
5 FIELDOLD(NBLOCK,NFIELDV), STRESSOLD(NBLOCK,NDIR+NSHR),
6 STATEOLD(NBLOCK,NSTATEV), ENERINTERNOLD(NBLOCK),
7 ENERINELASOLD(NBLOCK), TEMPNEW(NBLOCK),
8 STRETCHNEW(NBLOCK,NDIR+NSHR),
8 DEFGRADNEW(NBLOCK,NDIR+NSHR+NSHR),
9 FIELDNEW(NBLOCK,NFIELDV),
1 STRESSNEW(NBLOCK,NDIR+NSHR), STATENEW(NBLOCK,NSTATEV),
2 ENERINTERNNEW(NBLOCK), ENERINELASNEW(NBLOCK)
C
CHARACTER*80 CMNAME
C


Q11 = PROPS(1)
Q12 = PROPS(2)
Q13 = PROPS(3)
Q23 = PROPS(4)
Q33 = PROPS(5)
Q22 = 7.5E9
Q66 = 4E9
K = 2E12


DO NP = 1, NBLOCK
C Copy the values of strains into temp variables
```

```
ES1 = strainInc(NP,1)
ES2 = strainInc(NP,2)
ES3 = strainInc(NP,3)
C In vumat the shear strain is tensorial strain
ES4 = 2*strainInc(NP,4)


stressNew(NP,1) = stressOld(NP,1)+Q11*ES1+Q12*ES2+Q13*ES3
stressNew(NP,2) = stressOld(NP,2)+Q12*ES1+Q22*ES2+Q23*ES3
stressNew(NP,3) = stressOld(NP,3)+Q13*ES1+Q23*ES2+Q33*ES3
stressNew(NP,4) = stressOld(NP,4)+Q66*ES4-K*ES4*ES4*ES4


C CHECK THE TIME INCREMENT
write(6,*) DT


END DO


RETURN
END
```

Bibliography

[1] M. Shokrieh and M. Omidi. Investigation of strain rate effects on in-plane shear properties of glass/epoxy composites. *Composite Structures*, 91(1):95–102, 2009.

[2] N. Dioh, P. Ivankovic, P. Leevers, and J. Williams. The high strain rate behaviour of polymers. *Journal de Physique IV*, 4:C8119–C8124, 1994.

[3] C. Gao and L. Zhang. Constitutive modelling of plasticity of FCC metals under extremely high strain rates. *International Journal of Impact Engineering*, 38:406–415, 2011.

[4] M. Shokrieh and M. Omidi. Investigating the transverse behavior of glass-epoxy composites under intermediate strain rates. *Composite Structures*, 93(2):690–696, 2011.

[5] Y. Han, D. Zou, Z. Chen, G. Fan, and W. Zhang. Investigation on hot deformation behavior of 00Cr23Ni4N duplex stainless steel under medium-high strain rates. *Materials Characterization*, 62(2):198–203, 2011.

[6] A. Gilat, R. Goldberg, and G. Roberts. Experimental study of strain-rate-dependent behavior of carbon/epoxy composite. *Composites Science and Technology*, 62(10-11):1469–1476, 2002.

[7] J. Field, S. Walley, W. Proud, H. Goldrein, and C. Siviour. Review of experimental techniques for high rate deformation and shock studies. *International Journal of Impact Engineering*, 30(7):725–775, 2004.

[8] B. Hopkinson. A method of measuring the pressure produced in the detonation of high explosives or by the impact of bullets. *Philosophical Transactions of the Royal Society A*, 213:437–456, 1914.

[9] H. Kolsky. An investigation of the mechanical properties of materials at very high rates of loading. *Philosophical Transactions of the Royal Society B*, 62:676–700, 1949.

[10] R. Gerlach, C. Kettenbeil, and N. Petrinic. A new split Hopkinson tensile bar design. *International Journal of Impact Engineering*, 50:63–67, 2012.

[11] S. Mousavi, K. Welch, U. Valdek, and B. Lundberg. Non-equilibrium split Hopkinson pressure bar procedure for non-parametric identification of complex modulus. *International Journal of Impact Engineering*, 31(9):1133–1151, 2005.

[12] M. Sutton, S. McNeill, J. Helm, and J. Yuh. Advances in two-dimensional and three-dimensional computer vision. *Photomechanics, Topic Applied Physics*, pages 323–372, 2000.

[13] Y. Surrel. Fringe analysis. *Photomechanics, Topics Applied Physics*, 77:55–99, 2000.

[14] A. Gilat, T. Schmidt, and A. Walker. Full field strain measurement in compression and tensile split Hopkinson bar experiments. *Experimental Mechanics*, 49(2):291–302, 2008.

[15] H. Koerber, J. Xavier, and P. Camanho. High strain rate characterisation of unidirectional carbon-epoxy IM7-8552 in transverse compression and in-plane shear using digital image correlation. *Mechanics of Materials*, 42(11):1004–1019, 2010.

[16] H. Luo, H. Lu, and N. Leventis. The compressive behavior of isocyanate-crosslinked silica aerogel at high strain rates. *Mechanics of Time-Dependent Materials*, 10(2):83–111, 2006.

[17] P. Ienny, A. Caro-Bretelle, and E. Pagnacco. Identification from measurements of mechanical fields by finite element model updating strategies. *European Journal of Computational Mechanics*, 18(3-4):353–376, 2009.

[18] J. Peirs, P. Verleysen, W. Van Paepegem, and J. Degrieck. Determining the stress-strain behaviour at large strains from high strain rate tensile and shear experiments. *International Journal of Impact Engineering*, 38:406–415, 2011.

[19] D. Notta-Cuvier, B. Langrand, E. Markiewicz, F. Lauro, and G. Portemont. Identification of Johnson-Cook's viscoplastic model parameters using the virtual fields method: application to titanium alloy Ti6Al4V. *Strain*, 49(1):22–45, 2013.

[20] F. Pierron, G. Vert, R. Burguete, S. Avril, R. Rotinat, and M. Wisnom. Identification of the orthotropic elastic stiffnesses of composites with the virtual fields method: sensitivity study and experimental validation. *Strain*, 43(3):250–259, 2007.

[21] M. Grédiac, N. Fournier, P. Paris, and Y. Surrel. Direct identification of elastic constants of anisotropic plates by modal analysis: experimental results. *Journal of Sound and Vibration*, 210(5):643–659, 1998.

[22] A. Giraudeau, B. Guo, and F. Pierron. Stiffness and damping identification from full field measurements on vibrating plates. *Experimental Mechanics*, 46(6):777–787, 2006.

[23] A. Giraudeau, F. Pierron, and B. Guo. An alternative to modal analysis for material stiffness and damping identification from vibrating plates. *Journal of Sound and Vibration*, 329(10):1653–1672, 2010.

[24] S. Aloui, R. Othman, A. Poitou, P. Guégan, and S. El-Borgi. Non-parametric identification of the non-homogeneous stress in high strain-rate uni-axial experiments. *Mechanics Research Communications*, 35(6):392–397, 2008.

[25] R. Othman, S. Aloui, and A. Poitou. Identification of non-homogeneous stress fields in dynamic experiments with a non-parametric method. *Polymer Testing*, 29(5):616–623, 2010.

[26] F. Pierron and P. Forquin. Ultra-high speed full-field deformation measurements on concrete spalling specimens and stiffness identification with the virtual fields method. *Strain*, 48(5):388–405, 2012.

[27] R. Moulart, F. Pierron, S. Hallett, and M. Wisnom. Full-field strain measurement and identification of composites moduli at high strain rate with the virtual fields method. *Experimental Mechanics*, 51(4):509–536, 2011.

[28] F. Pierron and M. Grédiac. *The Virtual Fields Method: extracting constitutive mechanical parameters from full-field deformation measurements.* Springer New-York, 2012.

[29] J. Ruiz-Herrero, M. Rodríguez-Pérez, and J. De Saja. Design and construction of an instrumented falling weight impact tester to characterise polymer-based foams. *Polymer Testing*, 24(5):641–647, 2005.

[30] H. Hsiao, I. Daniel, and R. Cordes. Strain rate effects on the transverse compressive and shear behavior of unidirectional composites. *Journal of Composite Materials*, 33(17):1620–1642, 1999.

[31] W. Hu. Development of experimental techniques for dynamic mechnical properties of materials (in Chinese). *Chinese Materials Science Technology & Equipment*, 3: 5–14, 2011.

[32] M. Longana. *Intermediate strain rate testing methodologies and full-field optical strain measurement techniques for composite materials characterisation.* PhD thesis, University of Southampton, 2014.

[33] M. Meyers. *Dynamic behavior of materials.* John Wiley & Sons, Inc., 1994.

[34] M. Stewart. Constant true strain rate compression: the cam plastometer. *Canadian Metallurgical Quarterly*, 13(3):503–509, 1974.

[35] E. Evangelista. *Hot Deformation and Processing of Aluminum Alloys.* CRC Press, 2011.

[36] G. Taylor. The use of flat-ended projectiles for determining dynamic yield stress I: theoretical considerations. *Proceedings of the Royal Society A*, 194(1038):289–299, 1948.

[37] A. Whiffin. The use of flat-ended projectiles for determining dynamic yield stress II: tests on various metallic materials. *Proceedings of the Royal Society A*, 194 (1038):300–322, 1948.

[38] W. Carrington and L. Gayler. The use of flat-ended projectiles for determing dynamic yield stress III: changes in microstructure caused by deformation under impact at high-striking velocities. *Proceedings of the Royal Society A*, 194(1038): 323–331, 1948.

[39] P. Maudlin, G. Gray, C. Cady, and G. Kaschner. High-rate material modelling and validation using the Taylor cylinder impact test. *Philosophical Transactions of the Royal Society A*, 357:1707–1729, 1999.

[40] S. Walley, P. Church, R. Townsley, and J. Field. Validation of a path-dependent constitutive model for FCC and BCC metals using "symmetric" Taylor impact. *Journal de Physique IV*, 10:PR9 69–74, 2000.

[41] L. Forde, W. Proud, and S. Walley. Symmetrical Taylor impact studies of copper. *Proceedings of the Royal Society A*, 465(2013):769–790, 2009.

[42] K. Ramesh. *High Strain Rate and Impact Experiments, in Handbook of Experimental Solid Mechanics.* Springer, 2008.

[43] J. Lewis and J. Campbell. The development and use of a torsional Hopkinson-bar apparatus. *Experimental Mechanics*, 12(11):520–524, 1972.

[44] H. Huh, W. Kang, and S. Han. A tension split Hopkinson bar for investigating the dynamic behavior of sheet metals. *Experimental Mechanics*, 42(1):8–17, 2002.

[45] G. Gray III. *High-Strain-Rate Testing of Materials: The Split-Hopkinson Pressure Bar*, pages 1–15. in Characterization of Materials. John Wiley & Sons, Inc., second edition, 2012.

[46] S. Osovski, Y. Nahmany, D. Rittel, P. Landau, and A. Venkert. On the dynamic character of localized failure. *Scripta Materialia*, 67(7-8):693–695, 2012.

[47] A. Hamouda and M. Hashmi. Testing of composite materials at high rates of strain: advances and challenges. *Journal of Materials Processing Technology*, 77 (1-3):327–336, 1998.

[48] R. Armstrong. On size effects in polycrystal plasticity. *Journal of the Mechanics and Physics of Solids*, 9(11):196–199, 1961.

[49] B. Song. Dynamic stress equilibration in split Hopkinson pressure bar tests on soft materials. *Experimental Mechanics*, 44(3):300–312, 2004.

[50] W. Chen, F. Lu, D. Frew, and M. Forrestal. Dynamic compression testing of soft materials. *Journal of Applied Mechanics*, 69(3):214–223, 2002.

[51] S. Rao, V. Shim, and S. Quah. Dynamic mechanical properties of polyurethane elastomers using a nonmetallic Hopkinson bar. *Journal of Applied Polymer Science*, 66(4):619–631, 1997.

[52] J. Liu, D. Salettib, S. Pattofattoc, and H. Zhao. Impact testing of polymeric foam using Hopkinson bars and digital image analysis. *Polymer Testing*, 36:101–109, 2014.

[53] J. Harrigan, B. Ahonsi, E. Palamidi, and S Reid. Experimental and numerical investigations on the use of polymer Hopkinson pressure bars. *Philosophical Transactions of the Royal Society A*, 372(2023):20130201, 2014.

[54] G. Owolabi, D. Odoh, A. Peterson, A. Odeshi, and H. Whitworth. Measurement of the deformation of aluminum alloys under high strain rates using high speed digital cameras. *World Journal of Mechanics*, 3:112–121, 2013.

[55] H. Koerber and P. Camanho. High strain rate characterisation of unidirectional carbon/epoxy IM7-8552 in longitudinal compression. *Composites Part A: Applied Science and Manufacturing*, 42(5):462–470, 2011.

[56] D. Radford, G. Willmott, S. Walley, and J. Field. Failure mechanism in ducile and brittle materials during Taylor impact. *Journal of Physique, IV, France*, 110: 687–692, 2003.

[57] M. Grédiac, F. Pierron, S. Avril, and E. Toussaint. The virtual fields method for extracting constitutive parameters from full-field measurements: a review. *Strain*, 42(4):233–253, 2006.

[58] Cordin. URL http://www.cordin.com/about.html.

[59] P. Reu and T. Miller. The application of high-speed digital image correlation. *The Journal of Strain Analysis for Engineering Design*, 43(8):673–688, 2008.

[60] J. Honour. A brief history of principles used in high speed cameras. *The Imaging Science Journal*, 57(6):303–316, 2009.

[61] P. Reu. High/ultra-high speed imaging as a disgnostic tool. *Applied Mechanics and Materials*, 70:69–74, 2011.

[62] F. Pierron, R. Cheriguene, P. Forquin, R. Moulart, M Rossi, and M. Sutton. Performances and limitations of three ultra-high speed imaging cameras for full-field deformation measurements. *Applied Mechanics and Materials*, 70:81–86, 2011.

[63] V. Tiwari, M. Sutton, and S. McNeill. Assessment of high speed imaging systems for 2D and 3D deformation measurements: methodology development and validation. *Experimental Mechanics*, 47(4):561–579, 2007.

[64] M. Elloumi, E. Fauvet, E Goujou, and P. Gorria. The study of a photosite for snapshot video. In *Proceedings of SPIE: International Congress on High Speed Imaging and Photonics (ICHSIP)*, pages 259–267, Taejon, Korea, Aug 1994.

[65] W. Kosonocky, G. Yang, C. Ye, L. Kabra, R.and Xie, J. Lawrence, V. Mastrocolla, F. Shallcros, and V. Patel. 360x360-element very-high frame-rate burst-image sensor. In *IEEE International Solid-State Circuits Conference (ISSCC)*, pages 182–183, San Francisco, CA, USA, Feb 1996.

[66] Shimadzu ultra-high speed camera HPV-2, . URL http://www.ssi.shimadzu.com/products/product.cfm?product=hpv2-3.

[67] T. Etoh and H. Mutoh. An image sensor of 1 Mfps with photon counting sensitivity. In *Proceedings of SPIE*, The 26th International Congress on High-Speed Photography and Photonics, pages 301–307, March 25 2005.

[68] T. Etoh, C. Vo Le, Y. Hashishin, N. Otsuka, K. Takehara, H. Ohtake, T. Hayashida, and H. Maruyama. Evolution of ultra-high-speed CCD imagers. *Plasma and Fusion Research*, 2:S1021, 2007.

[69] Y. Kondo, K. Takubo, H. Tominaga, R. Hirose, N. Tokuoka, Y. Kawaguchi, Y. Takaie, and A. Ozaki. Development of "hypervision HPV-X" high-speed video camera. *Shimadzu Review*, pages SR3–003E, 2013.

[70] Shimadzu ultra-high speed camera HPV-X, . URL http://www.ssi.shimadzu.com/products/product.cfm?product=hpv-x_3.

[71] Y. Tochigi, K. Hanzawa, Y. Kato, R. Kuroda, H. Mutoh, R. Hirose, H. Tominaga, K. Takubo, Y. Kondo, and S. Sugawa. A global-shutter CMOS image sensor with readout speed of 1-Tpixel/s burst and 780-Mpixel/s continuous. *IEEE Journal of Solid-State Circuits*, 48(1):329–338, 2013.

[72] S. Brankner and M. Hobson. *Synchronization and triggering with the ORCA-Flash 4.0 Scientific CMOS camera*. Hamamatsu Photonics, October 2013.

[73] J. Janesick, T. Elliott, J. Andrews, J. Tower, and J. Pinter. Fundamental performanece differences of CMOS and CCD imagers: Part V. *Proceedings of SPIE*, 8659:865902–1, 2013.

[74] D. Litwiller. CCD vs. CMOS: facts and fiction. *Photonics Spectra*, pages 1–4, 2001.

[75] D. Litwiller. CCD vs. CMOS: maturing technologies, maturing markets. *Photonics Spectra*, pages 1–4, 2005.

[76] J. Crooks, B. Marsh, R. Turchetta, K. Taylor, W. Chan, A. Lahav, and A. Fenigstein. Kirana: a solid-state megapixel uCMOS image sensor for ultra-high speed imaging. *Proceedings of SPIE*, 8659:865903–1, 2013.

[77] Kirana ultra-high speed camera. URL http://specialised-imaging.com/products/kirana-high-speed-video-camera.

[78] A. Lahav, J. Crooks, R. Turchetta, and A. Fenigstein. CMOS image sensor pixel with 2D CCD memory bank for ultra high speed imaging with large pixel count. In *Proceedings of International Image Sensors Workshop(IISW)*, Snowbird, Utah, USA, June 2013. International Image Sensor Society.

[79] J. Crooks, B. Marsh, R. Turchetta, K. Taylor, W. Chan, A. Lahav, and A. Fenigstein. Ultra-high speed imaging at megaframes per second with a megapixel CMOS image sensor. In *Proceedings of International Image Sensors Workshop(IISW)*, Snowbird, Utah, USA, June 2013. International Image Sensor Society.

[80] C. Vo Le, T. Etoh, H. Nguyen, V. Dao, H. Soya, M. Lesser, D. Ouellette, H. Kuijk, J. Bosiers, and G. Ingram. A backside-illuminated image sensor with 200,000 pixels operating at 250,000 frames per second. *IEEE Transaction on Electron Devices*, 56:2556–2562, 2009.

[81] D. Son, T. Etoh, M. Tanaka, N. Dung, V. Cuong, K. Takehara, T. Akino, K. Nishi, H. Aoki, and J. Nakai. Toward one Giga frames per second-evolution of *in situ* storage image sensors. *Sensors*, 13:4640–4658, 2013.

[82] Y. Surrel. Optique c1 18851, 2003.

[83] K. Stetson. A review of speckle photography and interferometry. *Optimical Engineering*, 14(5):482–489, 1975.

[84] P. Jacquot. Speckle interferometry: a review of the principal methods in use for experimental mechanics applications. *Strain*, 44(1):57–69, 2008.

[85] G. Fleming, H. Soto, and B. South. Projection moiré interferometry for rotorcraft application: deformation measurements of active twist rotor blades, 11-13 June 2002.

[86] D. Post and B. Han. *Moiré Interferometry, in Handbook of Experimental Solid Mechanics*. Springer, 2008.

[87] T Jeong. *Basic Principles and Applications of Holography*, chapter 1.10, pages 381–417. Fundamentals of Photonics. SPIE, 2008.

[88] B. Pan, K. Qian, Hu. Xie, and A. Asundi. Two-dimensional digital image correlation for in-plane displacement and strain measurement: a review. *Measurement Science and Technology*, 20(6):062001, 2009.

[89] Y. Surrel. Moiré and grid methods: a signal processing approach. *Phtomechanics*, 2342:118–127, 1994.

[90] K. Kim, H. Jung, K. Kang, and Y. Kang. Experimental analysis of vibration modes of plates using ESPI. *KSME International Journal*, 13(10):677–686, 1999.

[91] Y. Li, I. Yamaguchi, and J. Kato. ESPI vibration fringe enhancement by laser diode wavelength modulation. *Proceedings of SPIE 1553*, Laser Interferometry IV: Computer-Aided Interferometry:150–159, 1991.

[92] J. Bell. An experimental diffraction grating study of the quasi-static hypothesis of the split Hopkinson bar experiment. *Journal of the Mechanics and Physics of Solids*, 14(6):309–327, 1966.

[93] C. Siviour. A measurement of wave propagation in the split Hopkinson pressure bar. *Measurement Science and Technology*, 20(6):065702, 2009.

[94] M. Sutton, W. Wolters, W. Peters, W. Ranson, and S. McNeill. Determination of displacements using an improved digital correlation method. *Image and Vision Computing*, 1(3):133–139, 1983.

[95] P. Luo, Y. Chao, and M. Sutton. Application of stereo vision to three-dimensional deformation analyses in fracture experiments. *Optical Engineering*, 33(3):981–990, 1994.

[96] M. Sutton, J. Orteu, and H. Schreier. *Image Correlation for Shape, Motion and Deformation Measurements*. Springer, 2009.

[97] B. Pan, L. Yu, and D. Wu. High-accuracy 2D digital image correlation measurements with bilateral telecentric lenses: error analysis and experimental verification. *Experimental Mechanics*, 53(9):1719–1733, 2013.

[98] M. Kujawinska and J. Wojciak. Spatial-carrier phase-shifting technique of fringe pattern analysis. *Proceedings SPIE 1508, Industrial Applications of Holographic and Speckle Measuring Techniques*, 61, 1991.

[99] Y. Du, G. Feng, H. Li, J. Vargas, and S. Zhou. Spatial carrier phase-shifting algorithm based on principal component analysis method. *Optics Express*, 20(15): 16471–16478, 2012.

[100] M. D'Amico and G. Ferrigno. Technique for the evaluation of derivatives from noisy biomechanical displacement data using a model-based bandwidth-selection procedure. *Medical & Biological Engineering & Computing*, 28(5):407–415, 1990.

[101] G. Wood. Data smoothing and differentiation procedures in biomechanics. *Exercise and Sport Sciences Reviews*, 10:308–362, 1982.

[102] F. Pierron, B. Green, and M. Wisnom. Full-field assessment of the damage process of laminated composite open-hole tensile specimens. Part I: methodology. *Composites Part A: Applied Science and Manufacturing*, 38(11):2307–2320, 2007.

[103] S. Avril, P. Feissel, F. Pierron, and P. Villon. Estimation of the strain field from full-field displacement noisy data. Comparing finite elements global least squares and polynomial diffuse approximation. *European Journal of Computational Mechanics*, 17(5-7):857–868, 2008.

[104] S. Avril, P. Feissel, F. Pierron, and P. Villon. Comparison of two approaches for differentiating full-field data in solid mechanics. *Measurement Science and Technology*, 21(1):015703, 2010.

[105] R. Haddad and A. Akansu. A class of fast Gaussian binomial filters for speech and image processing. *IEEE Transactions on Acoustics, Speech and Signal Processing*, 39:723–727, 1991.

[106] Digital filters: Gaussian smoothing. URL http://homepages.inf.ed.ac.uk/rbf/HIPR2/gsmooth.htm.

[107] C. Badulescu, M. Grédiac, and J. Mathias. Investigation of the grid method for accurate in-plane strain measurement. *Measurement Science and Technology*, 20 (9):095102, 2009.

[108] F. Sur and M. Grédiac. Sensor noise modeling by stacking pseudo-periodic grid images affected by vibrations. *IEEE Signal Processing Letters*, 21(4):432–436, 2014.

[109] M. Grédiac, F. Sur, C. Badulescu, and J. Mathias. Using deconvolution to improve the metrological performance of the grid method. *Optics and Lasers in Engineering*, 51(6):716–734, 2013.

[110] C. Badulescu, M. Grédiac, J. Mathias, and D. Roux. A procedure for accurate one-dimensional strain measurement using the grid method. *Experimental Mechanics*, 49(6):841–854, 2008.

[111] M. Grédiac and F. Sur. Effect of sensor noise on the resolution and spatial resolution of displacement and strain maps estimated with the grid method. *Strain*, 50 (1):1–27, 2014.

[112] F. Pierron, H. Zhu, and C. Siviour. Beyond Hopkinson's bar. *Philosophical Transactions of the Royal Society A*, 372(2023):20130195, 2014.

[113] F. Pierron and S. Avril. Inverse problem in experimental solid mechanics. URL Encyclopedia:http://www.eolss.net/Eolss-sampleAllChapter.aspx.

[114] M. Grédiac. The use of full-field measurement methods in composite material characterization: interest and limitations. *Composites Part A: Applied Science and Manufacturing*, 35(7-8):751–761, 2004.

[115] F. Latourte, A. Chrysochoos, S. Pagano, and B. Wattrisse. Elastoplastic behavior identification for heterogeneous loadings and materials. *Experimental Mechanics*, 48(4):435–449, 2007.

[116] S. Avril, M. Bonnet, A. Bretelle, M. Grédiac, F. Hild, P. Ienny, F. Latourte, D. Lemosse, S. Pagano, E. Pagnacco, and F. Pierron. Overview of identification methods of mechanical parameters based on full-field measurements. *Experimental Mechanics*, 48(4):381–402, 2008.

[117] J. Cugnoni, T. Gmür, and A. Schorderet. Inverse method based on modal analysis for characterizing the constitutive properties of thick composite plates. *Computers & Structures*, 85(17-18):1310–1320, 2007.

[118] E. Pagnacco, D. Lemosse, F. Hild, and F. Amiot. Inverse strategy from displacement field measurement and distributed forces using FEA. In *SEM annual conference and Expostion on Experimental and Applied Mechanics*, Mariott, Portland, 2005.

[119] J. Cugnoni, J. Botsis, V. Sivasubramaniam, and J. Janczak-Rusch. Experimental and numerical studies on size and constraining effects in lead-free solder joints. *Fatigue & Fracture of Engineering Materials and Structures*, 30(5):387–399, 2006.

[120] E. Pagnacco, A. Moreau, and D. Lemosse. Inverse strategies for the identification of elastic and viscoelastic material parameters using full-field measurements. *Materials Science and Engineering: A*, 452-453:737–745, 2007.

[121] J. Kajberg, K. Sundin, L. Melin, and P. Ståhle. High strain-rate tensile testing and viscoplastic parameter identification using microscopic high-speed photography. *International Journal of Plasticity*, 20(4-5):561–575, 2004.

[122] J. Kajberg and B. Wikman. Viscoplastic parameter estimation by high strain-rate experiments and inverse modelling–speckle measurements and high-speed photography. *International Journal of Solids and Structures*, 44(1):145–164, 2007.

[123] M. Grédiac, E. Toussaint, and F. Pierron. Special virtual fields for the direct determination of material parameters with the virtual fields method. 2-Application to in-plane properties. *International Journal of Solids and Structures*, 39:2707–2730, 2002.

[124] M. Rossi and F. Pierron. On the use of simulated experiments in designing tests for material characterization from full-field measurements. *International Journal of Solids and Structures*, 49(3-4):420–435, 2012.

[125] F. Pierron and M. Grédiac. Identification of the through-thickness moduli of thick composites from whole-field measurements using the Iosipescu fixture: theory and simulations. *Composites Part A: Applied Science and Manufacturing*, 31:309–318, 2000.

[126] M. Rossi and F. Pierron. Identification of plastic constitutive parameters at large deformations from three dimensional displacement fields. *Computational Mechanics*, 49(1):53–71, 2011.

[127] F. Pierron, S. Avril, and V. The Tran. Extension of the virtual fields method to elasto-plastic material identification with cyclic loads and kinematic hardening. *International Journal of Solids and Structures*, 47(22-23):2993–3010, 2010.

[128] M. Grédiac and F. Pierron. Applying the virtual fields method to the identification of elasto-plastic constitutive parameters. *International Journal of Plasticity*, 22 (4):602–627, 2006.

[129] S. Avril, F. Pierron, M. Sutton, and J. Yan. Identification of elasto-visco-plastic parameters and characterization of Lüders behavior using digital image correlation and the virtual fields method. *Mechanics of Materials*, 40(9):729–742, 2008.

[130] T. Nguyen. *The Fourier Virtual Fields Method for the identification of material properties distributions.* PhD thesis, Loughborough University, 2013.

[131] D. Claire, F. Hild, and S. Roux. A finite element formulation to identify damage fields: the equilibrium gap method. *International Journal for Numerical Methods in Engineering*, 61(2):189–208, 2004.

[132] E. Toussaint, M. Grédiac, and F. Pierron. The virtual fields method with piecewise virtual fields. *International Journal of Mechanical Sciences*, 48(3):256–264, 2006.

[133] F. Amiot, F. Hild, and J. Roger. Identification of elastic property and loading fields from full-field displacement measurements. *International Journal of Solids and Structures*, 44(9):2863–2887, 2007.

[134] F. Amiot, F. Hild, and J. Roger. The equilibrium gap method with modeling parameters: identifiability conditions and sensitivity, 2008.

[135] S. Avril and F. Pierron. General framework for the identification of constitutive parameters from full-field measurements in linear elasticity. *International Journal of Solids and Structures*, 44:4978–5002, 2007.

[136] F. Al-Hazmi. *High strain rate bahaviour of carbon fibre composites.* PhD thesis, University of Loughborough, 1995.

[137] J. Harding and L. Welsh. A tensile testing technique for fibre-reinforced composites at impact rates of strain. *Journal of Materials Science*, 18:1810–1826, 1983.

[138] I. Daniel, H. Hsiao, and R. Cordes. Dynamic response of carbon/epoxy composites. In *High strain rate effects on polymer, metal and ceramic matrix composites and other advanced materials*, volume 48, pages 167–177, San Francisco, CA, USA, Nov 1995. ASME.

[139] H. Hsiao and I. Daniel. Strain rate behavior of composite materials. *Composites Part B: Engineering*, 29(5):521–533, 1998.

[140] M. Hosur, J. Alexander, U. Vaidya, and S. Jeelani. High strain rate compression response of carbon/epoxy laminate composites. *Composite Structures*, 52:405–417, 2001.

[141] L. Melin and L. Asp. Effects of strain rate on transverse tension properties of a carbon/epoxy composite: studied by moiré photography. *Composites Part A*, 30 (3):305–316, 1999.

[142] M. Wisnom. Size effects in the testing of fibre-composite materials. *Composites Science and Technology*, 59:1937–1957, 1999.

[143] R. Carriere. The effect of fibre diameter on the strength of composite materials. *Journal of Materials Science, Letters*, 6:5–6, 1971.

[144] N. Pan, H. Chen, J. Thompson, M. Inglesby, S. Khatua, X. Zhang, and S. Zeronian. The size effects on the mechanical behaviour of fibres. *Composites Science and Technology*, 32:2677–2685, 1997.

[145] J. Thomason. The influence of fibre properties of the performance of glass-fibre-reinforced polyamide 6,6. *Composites Science and Technology*, 59:2315–2328, 1999.

[146] T. Kim, K. Oshima, and H. Kawada. Impact tensile properties and strength development mechanism of glass for reinforcement fiber. *Journal of Physics*, 451: 1–6, 2013.

[147] M. Grédiac, E. Toussaint, and F. Pierron. Special virtual fields for the direct determination of material parameters with the virtual fields method. 1–Principle and definition. *International Journal of Solids and Structures*, 39:2691–2705, 2002.

[148] S. Avril, M. Grédiac, and F. Pierron. Sensitivity of the virtual fields method to noisy data. *Computational Mechanics*, 34(6):439–452, 2004.

[149] Lagrange multipliers. URL Wikipedia:http://en.wikipedia.org/wiki/Lagrange_multiplier.

[150] J. Falk. Lagrange multipliers and nonconvex programs. *SIAM Journal on Control and Optimization*, 7:534–545, 1969.

[151] N. Papadakis, N. Reynolds, M. Pharaoh, P. Wood, and G. Smith. Strain rate effects on the shear mechanical properties of a highly oriented thermoplastic composite material using a contacting displacement measurement methodology-Part A: elasticity and shear strength. *Composites Science and Technology*, 64(5):729–738, 2004.

[152] N. Papadakis, N. Reynolds, M. Pharaoh, P. Wood, and G. Smith. Strain rate dependency of the shear properties of a highly oriented thermoplastic composite material using a contacting displacement measurement methodology-Part B: shear damage evolution. *Composites Science and Technology*, 64(5):739–748, 2004.

[153] H. Chalal, S. Avril, F. Pierron, and F. Meraghni. Experimental identification of a nonlinear model for composites using the grid technique coupled to the virtual fields method. *Composites Part A: Applied Science and Manufacturing*, 37(2): 315–325, 2006.

[154] H. Chalal, F. Meraghni, F. Pierron, and M. Grédiac. Direct identification of the damage behaviour of composite materials using the virtual fields method. *Composites Part A: Applied Science and Manufacturing*, 35(7-8):841–848, 2004.

[155] M. Grédiac, F. Auslender, and F. Pierron. Applying the virtual fields method to determine the through-thickness moduli of thick composites with a nonlinear shear response. *Composites Part A: Applied Science and Manufacturing*, 32(12): 1713–1725, 2001.

[156] Strain rate calculation. URL https://polymerfem.com/showthread.php?1198-Strain-rate-calculation.

[157] M. Mashayekhi. Numerical methods in solid mechanics: comparison of implicit and explicit methods (courses document). URL http://mashayekhi.iut.ac.ir.

[158] H. Choi, S. Hwang, Y. Kang, J. Kim, and Kang B. Comparison of implicit and explicit finite-element methods for the hydroforming process of an automobile lower arm. *International Journal of Advanced Manufacturing Technology*, 20:407–413, 2002.

[159] I. Chowdhury and S. Dasgupta. Computation of Rayleigh damping coefficients for large systems. *The Electronic Journal of Geotechnical Engineering*, 8:Bundle C, 2003.

[160] Y. Arimitsu, N. Kazumi, and S. Toyomitsu. A study of Saint-Venant's principle for composite materials by means of internal stress fields. *Journal of Applied Mechanics, Transactions ASME*, 62(1):53–58, 1995.

[161] F. Pierron. Saint-Venant effects in the Iosipescu specimen. *Journal of Composite Materials*, 22:1986–2015, 1998.

[162] J. Piro and M. Grédiac. Producing and transferring low-spatial-frequency grids for measuring displacement fields with moiré and grid methods. *Experimental Techniques*, 28(4):23–26, 2004.

[163] F. Pierron, M. Sutton, and V. Tiwari. Ultra-high speed DIC and virtual fields method analysis of a three point bending impact test on an aluminium bar. *Experimental Mechanics*, 51(4):537–563, 2011.

[164] M. Rossi, F. Pierron, and P. Forquin. Assessment of the metrological performance of an in situ storage image sensor ultra-high speed camera for full-field deformation measurements. *Measurement Science and Technology*, 25(2):025401, 2014.

[165] M. Herráez, D. Burton, M. Lalor, and M. Gdeisat. Fast two-dimensional phase-unwrapping algorithm based on sorting by reliability following a noncontinuous path. *Applied Optics*, 41(35):7437–7344, 2002.

[166] B. Karp and D. Durban. Saint-Venant's principle in dynamics of structures. *Applied Mechanics Reviews*, 64(2):020801, 2011.

Résumé Français

Contexte

Le comportement mécanique des matériaux à moyennes et très hautes vitesses de déformation est extrêmement important dans de nombreuses situations en ingénierie telles que les essais d'impact, les crash-tests, les explosions, etc. Cependant, à de tels taux de déformation, les essais classiques à base d'états de contrainte et de déformation simples (uniforme, uniaxiale) ne fournissent pas assez d'informations expérimentales pour décrire le comportement complexe des matériaux. L'objectif principal de ce projet est d'explorer de nouvelles méthodes fondées sur la photomécanique (à l'aide de mesures des déformations plein champ obtenues par systèmes d'imagerie) pour traiter cette question.

Des modèles de matériaux fiables décrivant physiquement la réponse dynamique des matériaux sont requis pour réaliser les simulations numériques de ces structures. Le fait de considérer uniquement les modèles de matériaux en condition quasi-statique pourrait conduire à des solutions surdimensionnées ou rompant prématurément et inopinément [1], en raison du fait que le comportement mécanique de nombreux matériaux à hautes vitesses de déformation est sensiblement différent de celui sous charge quasi statique [2-6]. Par conséquent, il est essentiel de mener des essais expérimentaux à différentes vitesses de déformation. La plupart des matériaux ont déjà été caractérisés avec précision en condition quasi-statique. Cependant, la caractérisation dynamique encore un problème ouvert en raison des difficultés à mener des essais mécaniques fiables dans ces conditions. En pratique, à de telles vitesses, les effets d'inertie conduisent à la difficulté de mesurer les forces d'impact. En outre, à haut taux de déformation, il n'est pas facile de parvenir à un état de déformation homogène dans le spécimen. Les essais mécaniques à haute vitesse de

déformation sont également limités par des défis technologiques. Par exemple, il est difficile d'acquérir des champs de déformation en temps réel dans le spécimen comme en condition quasi-statique.

Néanmoins, différentes stratégies pour caractériser le comportement mécanique des matériaux à différents taux de déformation ont été développées par la communauté scientifique. Une revue des techniques expérimentales conventionnelles à haute vitesse de déformation est disponible dans [7]. Parmi ces techniques, la plus populaire est la barre de pression de Hopkinson, ou 'split Hopkinson pression bar' (SHPB). L'idée initiale a été proposée il y a un siècle par Hopkinson [8], tandis que le système de deux barres séparées actuel a été conçu par Kolsky [9]. Cette technique a été largement utilisée pour effectuer des essais à haute vitesse de déformation sur un certain nombre de matériaux. L'article de synthèse [7] cite de nombreuses utilisations de la SHPB. Cependant, le fonctionnement de la SHPB souffre d'un certain nombre de lacunes. Premièrement, il est basé sur la théorie de propagation des ondes unidimensionnelles; par conséquent, il dépend essentiellement de l'hypothèse d'état uniaxial et homogène des contraintes. Ensuite, une autre hypothèse importante vient de l'analyse de la barre SHPB standard, qui est basée sur la lecture de jauges de déformation placées sur les barres d'entrée et de sortie, et nécessite un chargement en condition quasi-statique, c'est-à-dire sans effets d'inertie. En conséquence, les éprouvettes doivent être très courtes pour minimiser le temps nécessaire à l'onde pour la traverser et disparaître. La situation est d'autant moins favorable pour les matériaux avec des vitesses d'onde plus faibles comme avec les matériaux mous et les tissus biologiques. Bien que certains auteurs aient proposé des solutions à certains de ces problèmes [10, 11], le traitement pour reconstruire l'onde de déformation et l'historique du chargement reste encore un point faible de la méthode.

Récemment, en raison des progrès spectaculaires en imagerie numérique et en technologie de stockage des données, associés aux algorithmes de traitement d'image numérique (par exemple la corrélation d'images numériques ou 'digital image correlation' (DIC) [12] et la méthode de la grille [13]), il est possible d'effectuer des mesures plein champ à ultra-haute vitesse, ou 'ultra-high speed' (UHS). Contrairement aux techniques de mesure classiques telles que les extensomètres ou les jauges de déformation, les mesures plein champ sont sans contact et peuvent fournir une déformation hétérogène sur la surface des éprouvettes. Les données plein champ permettent une analyse plus approfondie et des traitements tels que la caractérisation des paramètres constitutifs des matériaux. Au cours des dernières années, la DIC a été utilisée pour acquérir la déformation plein champ d'éprouvettes dans des essais SHPB [14-16]. Dans ces exemples, l'hypothèse d'état uniforme des contraintes/déformations dans l'éprouvette s'est avérée être raisonnablement vérifiée. Cependant, dans ces exemples, les mesures de déformation plein champ n'ont été utilisées que pour fournir une valeur moyenne des déformations dans une certaine zone, de manière similaire à l'utilisation d'une jauge de déformation sans contact. Ces exemples ne tirent pas pleinement avantage des mesures plein champs, en raison des limitations inhérentes au montage SHPB, en particulier la capacité de mesurer un état de déformation nominalement hétérogène.

Tous les exemples précédents impliquent uniquement des essais simples et uniformes nominalement. Dans le cas plus général, l'identification des paramètres des matériaux à partir d'essais hétérogènes est réalisée en utilisant des solutions inverses, par exemple, la méthode du recalage de modèle éléments finis 'finite element method updating' (FEMU) [17-19], la Méthode Des Champs Virtuels (MCV) autrement appelée 'Virtual Fields Method' (VFM) [20], etc. Cependant, il est important de noter

que dans ces exemples, la mesure de force extérieure est toujours requise. Sous condition quasi-statique, la force externe utilisée pour identifier les paramètres des matériaux est facile à mesurer grâce aux capteurs d'effort, comme dans [20], tandis qu'à haute vitesse de déformation, la mesure de la force d'impact est facilement corrompue par les effets d'inertie. C'est la raison pour laquelle les effets d'inertie représentent généralement un obstacle aux techniques courantes d'essai à haute vitesse de déformation.

Cependant, dans certains essais en vibration, il a été montré que les forces d'inertie peuvent être utilisées pour identifier les paramètres du matériau. Par exemple, Grédiac et al. [21] et Giraudeau et al. [22, 23] ont réalisé l'identification des paramètres de raideur et d'amortissement à l'aide de l'accélération de plaques vibrantes sans la nécessité de mesurer la force d'excitation. Dans ce cas en effet, l'accélération peut être obtenue simplement par mesure de la déformation dynamique de la plaque en sachant *a priori* que l'excitation imposée est harmonique. Plus récemment, Othman et al. [24, 25] a utilisé l'imagerie à haute vitesse ou 'high speed' (HS) pour obtenir l'accélération plein champ d'éprouvette en caoutchouc chargées à grande vitesse dans un système SHPB, en utilisant la dérivée seconde par rapport au temps du champ de déplacement, résolu temporellement, bien que leurs travaux impliquent encore la mesure de la force d'impact. Il est préconisé d'utiliser des caméras avec un taux d'échantillonnage important pour acquérir une accélération correcte avec les matériaux rigides, en raison de la très grande vitesse d'onde les traversant. Par exemple, Pierron et al. [26] a utilisé la MCV pour identifier le module d'Young d'un béton testé uniaxialement avec une caméra ultra-haute vitesse (UHS) en tenant compte de l'accélération mais sans la nécessité de mesurer la force externe. Tous ces exemples utilisent les forces d'inertie pour identifier les paramètres de

matériau à grands taux de déformation. Certains évitent complètement la nécessité de mesurer une force extérieure. Dans ces cas, les limites des techniques courantes d'essai (par exemple, aucun effet d'inertie, état uniforme de contrainte, etc.) à hautes vitesses de déformation peuvent être potentiellement dépassées. Cette avancée conduit à penser qu'une nouvelle ère d'essais à haute vitesse de déformation est à portée de main.

Objectifs

L'objectif principal de cette thèse est de développer une nouvelle procédure expérimentale en utilisant des mesures de déformation et d'accélération plein champ et la MCV pour identifier les paramètres constitutifs des matériaux à haute vitesse de déformation. Cette idée a été validée initialement par de simples essais uniaxiaux [26, 27], ce qui rend la méthode attrayante pour les essais à hauts taux de déformation des matériaux. Cependant, pour bénéficier pleinement du potentiel de cette méthode, beaucoup de travail est nécessaire (par exemple l'identification à partir d'essais nominalement hétérogènes, l'analyse de la dépendance au taux de déformation du matériau, la prise en compte de modèles constitutifs plus complexes, etc.). Dans ce travail, des caméras ultra-rapides (UHS) associées à la méthode de la grille sont utilisées pour exécuter des mesures de champ de déformation à haute vitesse. Pour atteindre l'objectif principal, les quatre étapes suivantes sont essentielles :

- Concevoir des essais avec imagerie à ultra-haute vitesse.
- Adapter la méthode des champs virtuels au cas des hautes vitesses de déformation en présence d'effets d'inertie
- Etudier l'incertitude d'identification des paramètres à haute vitesse de déformation.

- Explorer de nouvelles méthodologies pour identifier la dépendance au taux de déformation des matériaux en présence de carte de vitesses de déformation hétérogènes

Dans ce travail, deux défis principaux doivent être relevés. Le premier concerne les mesures de champ de déformation à très haute vitesse. Ce thème est encore en plein développement pour obtenir des données acceptables d'un point de vue métrologique. La prise en compte de l'éclairage, du temps de capture d'image, de la synchronisation du capteur d'image, de bruit et d'autres facteurs sont encore à l'étude. Le deuxième concerne l'utilisation des cartes de déformation dans la procédure d'identification inverse des propriétés mécaniques. Des essais hétérogènes sont considérés, menant à des cartographies hétérogènes de déformation et de vitesse de déformation, ce qui permet en principe d'identifier les paramètres constitutifs, mais il est nécessaire de disposer d'une technique d'identification inverse car il n'existe plus de lien simple a priori entre mesure et paramètres.

Dans ce projet, l'élasticité linéaire est principalement considérée dans un premier temps. Avant de passer aux essais, il a été nécessaire d'effectuer la validation des routines sur des données simulées et d'étudier différentes configurations expérimentales. La simulation a été exécutée en utilisant le code de calcul par éléments finis ABAQUS/EXPLICIT. Les essais ont été effectués sur des éprouvettes en composite pré-imprégnés carbone/époxyde. Deux configurations d'empilement ont été étudiées : un empilement $[0/45/-45/90]_s$ menant à des propriétés élastiques isotropes en membrane, l'idée étant ici de mener des essais élastiques avec seulement deux paramètres à identifier, afin de bien caractériser les performances de la mesure dans le cas d'un problème inverse plus simple. Dans un deuxième temps, un stratifié

unidirectionnel a été étudiée, orthotrope et non-linéaire en cisaillement, et présentant de surcroît une sensibilité significative à la vitesse de déformation.

Originalité et contribution scientifique

Une procédure expérimentale générale pour identifier les paramètres constitutifs des matériaux à haute vitesse de déformation est proposée dans cette thèse. Il doit être souligné que, dans les essais à haute vitesse de déformation réalisés ici, les forces d'inertie sont utilisées pour l'identification au lieu de la force d'impact externe mesurée au travers d'une barre ou de capteurs d'effort. C'est une idée complètement nouvelle, pouvant conduire à une simplification drastique des dispositifs d'essais dynamiques à l'avenir. Ce travail original couvre les aspects suivants :

- Champs virtuels optimisés en dynamique rapide (c'est-à-dire, en l'absence d'effets inertiels).

  Les champs virtuels optimisés ont été appliqués avec succès à l'identification de paramètres de matériau sous condition quasi-statique [28]. Dans cette thèse, cette procédure a pour la première fois été étendue en dynamique rapide.
- Utilisation de nouveaux essais sous chargement purement inertiel pour identifier la raideur en utilisant l'accélération comme une cellule de force alternative.

  Dans la Méthode Des Champs Virtuels (MCV, ou VFM en anglais), la résultante des forces est généralement utilisée comme information d'efforts extérieurs dans le principe des puissances virtuelles pour identifier les paramètres des matériaux en condition quasi-statique. Cependant, à haute vitesse de déformation, il est difficile de mesurer avec précision la force d'impact en raison des effets d'inertie. Dans ce travail, les forces d'inertie ont

été utilisées comme une 'cellule de force' alternative pour identifier les paramètres constitutifs à haute vitesse sans avoir besoin de mesure de la force d'impact. Ceci lève la nécessité de mesurer des forces extérieures et l'hypothèse d'état uniforme de contrainte des techniques d'essai actuelles à haut taux de déformation. Ceci doit permettre à terme une bien meilleure caractérisation du comportement mécanique à grandes vitesses de déformation des matériaux, en particulier pour les matériaux souples (faibles vitesses de propagation des ondes de contrainte) ou les matériaux fragiles (temps d'essais courts ne permettant généralement pas l'atteinte d'un équilibre quasi-statique avant rupture). .

- Validation numérique à partir de données simulées par éléments finis.

  L'idée d'identifier les paramètres en faisant usage des effets d'inertie a été validée numériquement avant de passer à la campagne expérimentale. Pour ce faire, des simulations par éléments finis ont d'abord été menées sur des éprouvettes composites quasi-isotropes, puis sur des composites unidirectionnels orthotropes.

- Mise en œuvre expérimentale sur les éprouvettes quasi-isotropes et unidirectionnelles en utilisant deux dispositifs d'impact différents et deux caméras ultra-rapides différentes.

  Lors des différentes campagnes d'essais, des états de contrainte/déformation à différent niveaux d'hétérogénéité ont été obtenus grâce à l'utilisation de deux projectiles différents, cylindrique et sphérique (bille). Les niveaux de déformation dans les essais d'impact par bille furent seulement d'environ un dixième de ceux des essais d'impact avec le projectile cylindrique, ceci en raison de la petite taille des billes utilisées. Cependant, l'identification avec les

deux types de projectiles s'est avérée assez cohérente. Deux caméras ultra-rapides ont été utilisées dans les essais avec projectile cylindrique. Les résultats obtenus avec les deux caméras sont comparables, bien que leurs performances respectives soient sensiblement différentes. La cohérence des résultats d'identification avec ces deux caméras aux performances très différentes confirme que la procédure expérimentale proposée dans cette thèse est reproductible et robuste.

- Identification des paramètres orthotropes à haute vitesse de déformation à partir d'un seul essai.

  Les résultats d'identification à partir de données obtenues par simulation par éléments finis montrent la possibilité d'identifier les quatre composantes orthotropes indépendantes des rigidités à partir de l'essai d'impact inertiel simple utilisé dans ce travail. Expérimentalement, les quatre paramètres n'ont cependant pas pu être identifiés correctement en raison du fait que l'essai est trop simple pour activer de manière équilibrée les différents paramètres de la loi plane orthotrope. Cela signifie qu'un essai plus complexe doit être mis en œuvre, dans un premier temps en jouant sur la forme de l'éprouvette (ajout d'un trou ou d'une entaille). Ce problème de conception d'essai est déjà difficile à résoudre en quasi-statique. Il nécessite une simulation plus réaliste des essais, comme dans [124].

- Première exploration de l'utilisation de cartes de déformation et de vitesse de déformation hétérogènes, numériquement et expérimentalement.

  Dans ce travail, les cartes pleins champs de taux de déformation présentent des distributions spatiales très hétérogènes. Elles conduisent à des valeurs de raideur variables spatialement dans l'éprouvette. Par conséquent, la routine

MCV précédente en élasticité linéaire basée sur l'hypothèse de raideur constante de l'éprouvette n'est plus valide. Une nouvelle méthodologie d'analyse de la dépendance à la vitesse de déformation a été explorée dans ce travail pour la première fois.

- Première exploration de lois non-linéaires.

  Le comportement mécanique des composites unidirectionnels est connu pour sa forte non-linéarité en cisaillement, même si cette non-linéarité s'atténue à grandes vitesses de déformation. Dans cette thèse, le comportement non-linéaire en cisaillement a d'abord été mis en œuvre numériquement puis été identifié avec la MCV l'aide des données simulées. Une première validation expérimentale a également été tentée.

Cette thèse a déjà conduit à un article dans une revue scientifique de premier plan (Transactions de the Royal Society A) et à présentation dans cinq conférences internationales. Un second article est en cours d'expertise (Experimental Mechanics, Springer). Une liste complète des publications est présentée dans l'annexe A de cette thèse.

Structure de la thèse

Chapitre 1

Ce chapitre présente l'introduction générale de cette thèse, y compris les principaux défis des essais à haute vitesse de déformation des matériaux et les réalisations principales de ce travail.

Chapitre 2

Une brève revue des principales techniques d'essai à hauts taux de déformation de matériaux est d'abord présentée dans le Chapitre 2. Les avantages et les inconvénients

de ces techniques y sont présentés en détail. Grâce aux progrès spectaculaires de la mesure plein champ et de l'imagerie ultra-rapide (UHS), il est possible d'effectuer des mesures plein champ à ultra-haute vitesse. Les caméras ultra-rapides et les techniques de mesures plein champ à haute vitesse de déformation sont ensuite respectivement comparées. La méthode de la grille présente un compromis sensiblement meilleur entre résolution spatiale et résolution en déformation. Les principales méthodes inverses utilisées pour identifier les paramètres de matériaux à partir de données plein champ hétérogènes sont ensuite passées en revue. Parmi ces techniques, la MCV est un excellent choix. En effet, la principale technique concurrente, le recalage par éléments finis, nécessite des calculs par éléments finis itératifs, ce qui en dynamique rapide, devient vite prohibitif en temps de calcul quand le nombre de paramètre augmente Les champs cinématiques mesurés, résolus spatialement et temporellement, y compris les déformations et l'accélération dérivées du déplacement mesuré, peuvent être traités à l'aide de la MCV afin d'identifier les paramètres des matériaux. Dans cette thèse, l'élasticité linéaire est considérée en premier lieu pour valider cette méthodologie. À cet effet, des composites à renfort de fibre de carbone ou 'carbon fibre reinforced polymer' (CFRP) ont été utilisés pour effectuer les essais à haute vitesse de déformation. Par conséquent, le comportement mécanique des composites CFRP à haute vitesse de déformation est brièvement passé en revue à la fin de ce chapitre. Les chapitres suivants expliquent la mise en œuvre des simulations et essais.

Chapitre 3

Le chapitre 3 détaille la MCV avec prise en compte des effets d'inertie à haute vitesse de déformation. Tout d'abord, il est expliqué pourquoi l'accélération peut être utilisée comme une 'cellule de force' alternative. Il est rappelé comment reconstruire les profils de contrainte dans chaque coupe transversale le long de l'axe longitudinal de

l’éprouvette à partir du champ d’accélération. Ce concept conduit à une méthode MCV simplifiée capable ici d'identifier les paramètres élastiques des matériaux. Cependant, cette méthode ne permet d’identifier qu’un seul paramètre élastique par section à chaque temps. Il est possible de l'étendre en utilisant une approche de système surdéterminé pour identifier plusieurs paramètres par section, en utilisant l’ensemble des données temporelles. Ceci peut être étendu à une loi en cisaillement non-linéaire. Deuxièmement, les procédures basées sur la MCV pour identifier les paramètres constitutifs de modèles élastiques linéaires isotropes et orthotropes sont détaillées. Les champs virtuels optimisés sont étendus au cas de la dynamique rapide non-harmonique pour la première fois. Pour le modèle orthotrope, du caractère hétérogène de la vitesse de déformation résultent des raideurs variables spatialement au sein de l’éprouvette. Par conséquent, la routine MCV basée précédemment sur l’hypothèse de raideur élastique spatialement constante de l’éprouvette n'est pas valide. Dans ce cas, une nouvelle méthodologie pour identifier la dépendance à la vitesse de déformation des matériaux à partir de cartes de vitesses de déformation hétérogènes est proposée. En outre, une procédure générale pour identifier les paramètres des matériaux basés sur un système surdéterminé est proposée à la fin de ce chapitre. L’approche surdéterminée est très attrayante en raison de sa simplicité. Ce chapitre décrit les éléments fondamentaux de la théorie de la MCV utilisant les forces d’inertie pour identifier les paramètres constitutifs des matériaux à hauts taux de déformation sans la nécessité des mesurer les forces d'impact. Différents modèles mentionnés ci-dessus seront validés numériquement et mis en œuvre expérimentalement dans les chapitres suivants.

Chapitre 4

Le chapitre 4 valide l'idée décrite dans le chapitre 3 à l'aide d'informations cinématiques simulées par éléments finis (EF). Des simulations en deux dimensions sont d'abord effectuées. Pour le modèle isotrope, deux projectiles avec différentes formes sont utilisés pour fournir des efforts d'impact dans le plan. L'un est cylindrique, utilisé pour produire un champ mécanique quasi-uniaxial en raison du contact uniforme entre l'éprouvette et le projectile. L'autre est un projectile sphérique (bille). En raison de la nature ponctuelle du contact, l'état de contrainte de ce modèle s'est avéré beaucoup plus hétérogène que le premier. Pour la simulation orthotrope, la dépendance des composantes de raideur transversale et de cisaillement au taux de déformation est mise en œuvre grâce à une sous-routine utilisateur (VUMAT) d'ABAQUS/EXPLICIT. Au final, une simulation EF en trois dimensions de l'essai avec projectile sphérique dans le plan a été effectuée. En pratique, un mauvais positionnement du point de contact est susceptible de se produire, ce qui conduit à une identification des paramètres des matériaux faussée. Différent cas de contact (parfait et excentré) ont donc été simulés. Dans tous les cas, contraintes et déformations sont hétérogènes dans l'épaisseur, ce qui génère un biais potentiel dans la MCV lors de l'approximation des intégrales de volumes à partir des mesures en surface.

Un modèle simple d'élasticité isotrope linéaire a d'abord été examiné. Les deux types de projectiles ont été simulés en 2D pour produire les déformations à haute vitesse et les champs d'accélération. Le module d'Young et le coefficient de Poisson de ce modèle isotrope ont été identifiés avec succès. Les erreurs relatives sont toutes deux à moins de 1 %.

Le modèle élastique linéaire orthotrope incluant l'effet du taux de déformation est présenté. Sans considérer la dépendance au taux de déformation, des séries de

modèles linéaires élastiques orthotropes avec différentes orientations de fibres par rapport à l'axe de l'éprouvette (impact 'hors-axes') ont été simulés. Les quatre composantes orthotropes indépendantes des rigidités ont été identifiées pour chaque angle hors-axes. La relation entre les coefficients de variation des composantes de raideur identifiées et l'orientation des fibres a montré que l'identification de la composante de raideur Q_{11} (resp. Q_{22}) selon l'axe des fibres (resp. transverse aux fibres) est moins bonne (resp. meilleure) quand l'angle hors-axes augmente. Ceci était prévisible, parce qu'aux faibles (resp. forts) angles hors-axes, la contrainte selon l'axe des fibres (resp. transverse aux fibres) est importante, ce qui mène à une meilleure identifiabilité des rigidités associées. Pour ce qui est de la raideur de cisaillement Q66, les coefficients de variation sont importants à des angles hors-axes proches de 0° et 90°, alors qu'à des angles de fibre intermédiaires, ces valeurs sont plus faibles, indiquant une meilleure identifiabilité, ceci en raison des niveaux de contrainte en cisaillement trop faibles aux angles proches de 0° ou 90°. La même tendance a été observée pour l'identification de Q_{12}. La dépendance au taux de déformation des composantes de raideur transversale et de cisaillement a été ensuite considérée. Le modèle de dépendance à la vitesse de déformation a été appliqué à l'aide de sous-routines utilisateur (VUMAT) d'ABAQUS/EXPLICIT pour produire des champs de déformation et d'accélération résolus temporellement. Différentes méthodologies ont été utilisées pour traiter les données plein champ et identifier les paramètres dépendant du taux de déformation. Les résultats identifiés en utilisant différentes méthodes se sont révélées cohérentes. Toutefois, des erreurs systématiques d'identification ont été mises en évidence. Cela est probablement causé par le calcul par élément finis. Ceci devra être exploré plus en détail à l'avenir mais il est

intéressant de noter que ma MCV peut aussi être un bon outil de validation de calculs par éléments finis.

Les techniques de mesure plein champ à haute vitesse de déformation actuelles sont uniquement capables d'acquérir des déformations à la surface des éprouvettes. Cependant, l'hétérogénéité des déformations dans l'épaisseur est susceptible de se produire au cours de l'impact, nuisant à l'identification correcte des paramètres du matériau. Par conséquent, une simulation EF tridimensionnelle détaillée du tir d'une bille en acier sur une éprouvette rectangulaire isotrope avec bords libres a été effectuée. Des modèles avec différents offsets du point d'impact et des éprouvettes de longueurs différentes ont été considérés, en lien avec la partie expérimentale. Les données plein champ des déformations et des accélérations ont été extraites pour les surfaces supérieure et inférieure de l'éprouvette puis traitées par différentes méthodes pour identifier les paramètres constitutifs. Les résultats avec différentes méthodes se sont révélés cohérents et ont montré que les effets parasites découlant du chargement non-uniforme dans l'épaisseur peuvent être atténués avec succès en utilisant des éprouvettes plus longues, en faisant usage du principe de Saint-Venant en dynamique.

Enfin, les composites unidirectionnels présentant une non-linéarité significative en cisaillement, ce chapitre a exploré cette situation à l'aide modèle constitutif non-linéaire simple sous la forme d'un adoucissement polynomial de degré trois à un paramètre. La simulation EF a été mise en œuvre à l'aide d'une routine VUMAT avec différentes orientations hors-axes des fibres. De même, les informations cinématiques résolues temporellement ont été extraites, puis traitées par la technique MCV simplifiée du système surdéterminé. Les résultats ont montré que l'identification aux angles de fibre intermédiaires par rapport à l'axe de l'éprouvette était meilleure qu'aux fibres à faibles et grands angles, comme pour le cas purement élastique.

Toutes ces simulations EF ont validé le fait que dans le traitement MCV les effets inertiels peuvent être utilisés pour identifier les paramètres des matériaux sans avoir besoin de mesure de force d'impact. Les chapitres suivants présentent la mise en œuvre expérimentale des configurations étudiées par simulation par éléments finis dans ce chapitre.

Chapitre 5 & 6

Les chapitres 5 et 6 présentent la mise en œuvre expérimentale des essais à haute vitesse de déformation. Une série d'essais d'impact a été menée sur différents types d'éprouvettes (composites quasi-isotropes stratifiés et unidirectionnels) en utilisant un projectile cylindrique en acier et une petite bille en acier. Le détail de la procédure expérimentale comprenant les dispositifs utilisés ainsi que la performance des mesures est décrite dans le chapitre 5. Le chapitre 6 détaille les résultats expérimentaux : d'abord que les cartes plein champ puis l'identification des paramètres des matériaux en utilisant les méthodes mentionnées dans les chapitres précédents. Dans le chapitre 6, le modèle de dépendance de la rigidité de cisaillement au taux de déformation a aussi été identifié..

Les résultats montrent sans surprise que la qualité de l'identification est d'abord liée à la qualité des images acquises par les caméras. Ainsi, la caméra SIMX16 de Specialized Imaging a montré ses limites, même si les résultats sont globalement cohérents avec les valeurs de référence. En revanche, la qualité des mesures obtenues avec la caméra HPV-X de Shimadzu est remarquable. Ces mesures ont permis l'établissement d'une courbe contrainte-déformation d'une linéarité spectaculaire à ce niveau de vitesse de déformation (près de 3000 s^{-1}), comme en atteste la Figure 6.19. On voit aussi que ce type d'essai permet d'effectuer essais de type charge/décharge

qui à l'avenir seront précieux pour explorer des lois d'endommagement pour ces matériaux.

Le deuxième point important est que même dans le cas de très faibles déformations, et d'une configuration d'impact plus complexe, les résultats restent remarquablement robustes, comme en attestent les courbes contrainte-déformation de la Figure 6.24 pour l'impact par bille. Les déformations restent ici inférieures à 1.10^{-3} mais la qualité des images est telle que les résultats restent cohérents. Ceci est très prometteur. Enfin, il est clair que la présence d'hétérogénéité des déformations dans l'épaisseur est un point critique pour la qualité de l'identification. Cependant, l'utilisation d'éprouvettes plus longues permet de s'affranchir un peu de ces problèmes, comme prévu par les simulations numériques.

Ensuite, et comme on pouvait s'y attendre, l'identification simultanées des quatre rigidités orthotropes est beaucoup plus difficiles et n'a pas pu être effectuée de mlanière satisfaisante. La raison principale est que l'essai utilisé ici n'est pas assez hétérogène. Il reste trop majoritairement uniaxial et ne permet pas d'obtenir des niveaux équilibrés des différentes composantes de contrainte. Ceci n'est pas surprenant car un essai de traction hors-axes ne permet pas d'identifier les quatre rigidités orthotropes d'un composite en quasi-statique. Ici, l'hétérogénéité supplémentaire introduite par la propagation d'onde permet l'identification à partir de données simulées 'exactes' mais elle n'est pas suffisante pour permettre cette identification à partir de mesures bruitée. A l'avenir, il faudra s'attaquer à la conception d'un essai d'impact inertiel permettant d'activer l'ensemble des rigidités orthotropes, avec une méthodologie similaire à celle décrite dans [124].

Finalement, il a été montré que même si la carte de vitesse de déformation de cisaillement est hétérogène, il n'y a pas suffisamment d'information pour identifier une loi de variation du module de cisaillement avec la vitesse. En effet, les endroits de l'éprouvette où la vitesse de déformation est faible à un temps donné sont aussi ceux où la déformation est faible et donc, on ne peut pas identifier une rigidité en dessous d'une vitesse de l'ordre de 500 s^{-1} dans le cas présent. Comme la sensibilité du module de cisaillement est faible sur une plage de 500 à 3000 s^{-1}, on ne peut donc identifier qu'un module à une vitesse de déformation 'moyenne' de l'ordre de 2000 s^{-1}. Ceci permet néanmoins de se passer de la paramétrisation explicite à la vitesse de déformation, ce qui simplifie la procédure d'identification. Cette conclusion sera néanmoins à revoir dans le cas d'un matériau présentant une sensibilité à la vitesse de déformation plus importante, ou dans le cas d'états de déformation plus hétérogènes (présence de concentrateurs de contrainte, comme trous ou entailles).

Chapitre 7

Les principaux résultats de cette thèse ainsi que des recommandations pour les travaux futurs sont présentés en Chapitre 7.

Conclusions

Dans ce travail, une nouvelle procédure expérimentale pour tester les matériaux à haute vitesse de déformation a été proposée. La principale nouveauté est que cette procédure permet d'identifier les paramètres constitutifs des matériaux à haute vitesse de déformation en faisant usage de l'effet d'inertie sans la nécessité de mesurer des forces d'impact. Au-delà de la simplification des dispositifs expérimentaux en supprimant la nécessité d'utiliser des barres de Hopkinson encombrantes, l'avantage principal de ce nouveau paradigme est de s'affranchir des hypothèses contraignantes sur lesquelles repose l'analyse des mesures sur montage de barres de Hopkinson. En

effet, l'idée principale est d'utiliser l'imagerie ultra-rapide pour enregistrer des cartes de déformation en fonction du temps, en utilisant soit des mouchetis sur la surface et la corrélation d'image numérique, soit des grilles avec traitement par décalage de phase spatial. Les cartes de déformation résolues temporellement peuvent être obtenues par dérivation spatiale et les cartes d'accélération par double dérivation temporelle. En utilisant l'équation d'équilibre mécanique sous forme intégrale, il est donc possible de trouver un équilibre entre d'une part les contraintes internes calculées à partir des déformations et paramètres constitutifs et d'autre part, les forces d'inertie obtenues à partir des cartes d'accélération, en supposant connue la masse volumique du matériau. Dans ce cas, la mesure du chargement externe n'est plus nécessaire et toutes les informations indispensables sont contenues dans les images numériques, à condition bien sûr que la masse volumique du matériau soit connue. L'effet d'inertie, au lieu d'être un désavantage comme dans l'approche SHPB standard, peut devenir un avantage en fournissant une cellule force distribuée dans le volume. En conséquence de ce qui précède, le champ des configurations d'essais possibles s'agrandit de façon spectaculaire et doit être exploré autant que possible, en vue de parvenir à un nouveau standard d'essai reposant sur ce nouveau paradigme. Les conclusions principales du présent travail sont les suivantes :

- Il est possible d'obtenir des déformations et accélérations suffisantes (plus d'un million de fois l'accélération de la pesanteur terrestre) avec des essais d'impact purement inertiels décrits dans la thèse, comme illustré dans les Figures 5.1 et 5.2.
- Les récents progrès des technologies de caméras ultra-rapides permettent à présent de mesurer des déformations plein champ avec une qualité sans précédent. Avec l'utilisation croissante de cameras ultra-rapides dans les

essais des matériaux à haute vitesse de déformation et le progrès technologique, l'imagerie ultra-rapide (comme définie par Reu et Miller, [59]) deviendra dans le futur presque aussi courante que peut l'être l'imagerie rapide actuellement.

- Pour les matériaux isotropes, la qualité de l'identification est impressionnante pour de telles vitesses de déformation, d'environ 2000 s^{-1}. Il y a assez d'information pour identifier les deux paramètres élastiques de composites quasi-isotropes stratifiés avec la configuration expérimentale actuelle, ce qui renforce la remarque précédente sur le progrès des caméras ultra-rapides. Cependant, l'identification simultanée des quatre paramètres orthotropes à partir d'un seul essai n'a pas été possible. Ceci est dû au fait que les états de contrainte/déformation dans l'éprouvette ne sont pas assez hétérogènes.
- En comparant les résultats expérimentaux obtenus avec les deux dispositifs d'impact, on peut voir que les niveaux de déformation dans les essais d'impact avec bille mènent à des niveaux de déformation environ dix fois plus faibles que ceux des essais d'impact par projectile cylindrique, ceci en raison de la petite taille de la bille par rapport au cylindre. Cependant, l'identification avec les deux projectiles s'est révélée assez cohérente.
- Cette thèse propose une nouvelle méthode pour analyser la dépendance au taux de déformation des matériaux à haute vitesse de déformation à partir de cartes de taux de déformation hétérogènes. Cependant, l'hétérogénéité des cartes de taux de déformation s'est révélée insuffisante ici pour tirer avantage de cette fonctionnalité.
- Dans les essais d'impact avec projectile bille, la position du point d'impact donne lieu à des contraintes et des déformations avec des distributions

hétérogènes dans l'épaisseur qui évoluent dans le temps et l'espace en même temps que les ondes se propagent et rebondissent sur les différentes faces de l'éprouvette. La présence d'un fin talon en acier d'épaisseur de 1 mm atténue légèrement ce problème, même si sa déformation plastique absorbe une quantité significative de l'énergie d'impact, ce qui conduit expérimentalement à de plus faibles niveaux de déformation. D'après les simulations EF avec différents offsets d'impact et différentes longueurs d'éprouvettes, les éprouvettes les plus longues fournissent une identification plus stable et précise, montrant que les effets tridimensionnels peuvent être atténués suffisamment pour obtenir une bonne identification mécanique. En tant que tel, ceci a confirmé l'existence d'un effet de Saint-Venant en dynamique rapide, effet bien connu en statique et qui conditionne l'utilisation d'éprouvette suffisamment longues lors d'essais de traction quasi-statique, par exemple. Ce résultat est une nouveauté supplémentaire de ce travail.

- Enfin, les résultats présentés dans cette thèse confirment le potentiel de cette nouvelle approche des essais dynamiques qui pourrait devenir une technique standard à l'avenir.

Perspectives

Cette thèse est de nature très exploratoire et n'a fait qu'entamer une partie du problème parce que beaucoup de questions doivent être abordées à l'avenir. Nous ne sommes encore qu'au début de cette nouvelle méthodologie et encore beaucoup de travail est nécessaire afin de la rendre pleinement opérationnelle comme technique d'essai de routine. Parmi ces travaux, quelques-uns sont énumérés ci-dessous :

- L'identification est ici seulement en élasticité, bien que le comportement non-linéaire en cisaillement ait été brièvement abordé par une loi simple qui bien que non-linéaire, est linéaire au sens de la MCV. Ceci est justifié à ces premiers stades pour valider la technique et tester sa robustesse. De nouveaux modèles constitutifs sont nécessaires pour le comportement à haute vitesse de déformation des matériaux. Ceci a principalement été entravé par la mauvaise qualité des données expérimentales qui pouvaient être recueillies comparées aux situations quasi- statiques. On peut espérer qu'en améliorant la qualité des données des essais, la recherche en mécanique des matériaux sera en mesure de les utiliser pour développer de meilleurs modèles de matériaux pour bénéficier pleinement des capacités actuelles spectaculaires de la simulation numérique. Le véritable intérêt des essais à haute vitesse de déformation est l'identification de comportements non-linéaire. L'extension à l'élasto-viscoplasticité des métaux est en cours actuellement au sein de l'équipe du professeur Pierron et dans un avenir proche, plus de matériaux et de modèles constitutifs seront examinés afin d'élargir l'applicabilité de la technique.
- Une approche plus rationnelle de la conception d'essai est nécessaire. Par exemple, un dispositif expérimental est nécessaire pour produire les états de contraintes/déformations plus hétérogènes dans les essais d'impact unidirectionnels. Le simulateur d'identification détaillé dans [124] est un outil idéal pour cela, Les simulations permettent d'optimiser des configurations d'essais avec pour objectif une erreur minimale sur les paramètres identifiés, en prenant en compte autant de paramètres expérimentaux que nécessaire pour rendre ces simulations réalistes. C'est une tâche à long terme et un problème difficile parce que la chaîne d'identification est très longue et implique

beaucoup de paramètres. Néanmoins, cette tâche est déjà en cours pour les essais quasi-statique et il devrait être raisonnablement aisé de l'adapté aux essais dynamiques. L'objectif à terme est la définition de nouveaux essais standards pour remplacer les procédures reposant sur les barres d'Hopkinson.

Note : La référence et les figures sont les mêmes que dans la thèse.

Haibin ZHU

Doctorat : Systèmes Mécaniques et Matériaux

Année 2015

Une méthodologie originale d'essai dynamique avec mesures plein champ et méthode des champs virtuels

Ce travail se concentre sur le développement d'une procédure expérimentale d'essai mécanique à haute vitesse de déformation de matériaux. La nouveauté de ce travail est l'utilisation de champs d'accélération mesurés comme cellule de force, évitant la nécessité des mesures des forces externes. Pour identifier les paramètres constitutifs des matériaux testés à partir des mesures de champs, la méthode champs virtuels (MCV) basé sur le principe des puissances virtuelles (PPV) est utilisée. En dynamique, avec la MCV, il est possible de définir des champs virtuels qui mettent à zéro les puissances virtuelles des forces externes. Au lieu de cela, l'accélération obtenue grâce à une double dérivation temporelle des déplacements peut être utilisée comme une cellule de force. Enfin, les paramètres élastiques peuvent être identifiés directement à partir d'un système linéaire qui se construit en réécrivant le PPV avec autant de champs virtuels indépendants que d'inconnues à identifier. Cette procédure est d'abord validée numériquement par des simulations éléments finis puis mise en œuvre expérimentalement en utilisant deux configurations d'impact différentes. Les résultats confirment que effets inertiels peuvent être utilisés pour identifier les paramètres des matériaux sans la nécessité de mesurer la force d'impact, et sans exigence de déformations uniformes comme dans les procédures actuelles basées sur le montage de barres d'Hopkinson. Ces nouveaux développement ont le potentiel de mener à de nouveaux essais standards en dynamique rapide.

Mots clés : mesures optiques - impact - déformations (mécanique) - inertie (mécanique) - matériaux, propriétés mécaniques.

A Novel Methodology for High Strain Rate Testing using Full-field Measurements and the Virtual Fields Methods

This work focuses on the development of a novel experimental procedure for high strain rate testing of materials. The underpinning novelty of this work is the use of the full-field acceleration maps as a volume distributed load cell, avoiding the need for impact force measurement. To identify the constitutive parameters of materials from the full-field data, the Virtual Fields Method (VFM) based on the principle of virtual work is used here. In dynamics, using the VFM, it is possible to define particular virtual fields which can zero out the virtual work of the external forces. Instead, the acceleration obtained through second order temporal differentiation from displacement can be used as a load cell. Finally, the elastic parameters can be identified directly from a linear system which is built up through rewriting the principle of virtual work with as many independent virtual fields as unknowns. Thus, external force measurement is avoided, which is highly beneficial as it is difficult to measure in dynamics. This procedure is first numerically validated through finite element simulations and then experimentally implemented using different impact setups. Both results confirm that inertial effects can be used to identify the material parameters without the need for impact force measurements, also relieving the usual requirements for uniform/uniaxial stress in SHPB like test configurations. This exciting development has the potential to lead to new standard testing techniques at high strain rates.

Keywords: optical measurements - impact - deformations (mechanics) - inertia (mechanics) – material, mechanical properties.

Thèse réalisée en partenariat entre :

Ecole Doctorale "Sciences et Technologies"